財團法人國家實驗研究院國家太空中心

全球定位科學應用研究委託案(3/3)

101年度「全球定位科學應用研究中心」

期末報告

工作項目(1.4)：SCI期刊論文電子檔

執行期間： 2012/2/18~2013/2/17

計畫主持人：黃清勇

參與人員： 黃成勇、蔡和芳、曾子榜、吳怡娟、翁佩芬、

吳靜美、謝涵蓁

中 華 民 國 1 0 2 年 2 月

Evaluating the impact of the COSMIC-RO bending angle data on predicting the heavy precipitation episode on 16 June 2008 during SoWMEX-IOP8

Yang[1*], Shu-Chih, Shu-Ya Chen[2], Shu-Hua Chen [3], Ching-Yuang Huang[1] and Ching-Sen Chen[1]
[1] Department of Atmospheric Sciences, National Central University, Taiwan
[2] University Corporation for Atmospheric Research, Boulder, Colorado, USA
3 University of California, Davis, USA

* Corresponding author:
Shu-Chih Yang
300 Jhong-Da Rd., JhongLi city, Taiwan
shuchih.yang@atm.ncu.edu.tw

Abstract

Global Positioning System (GPS) radio occultation (RO) data has been broadly used in global and regional numerical weather predictions. Although assimilation with the bending angle often performs better than refractivity that is inverted from the upstream bending angle under spherical assumption and is sometimes associated with negative biases at the lower troposphere, it also requires a higher model top as used in global models. This study furnishes the feasibility of bending-angle assimilation in the prediction of heavy precipitation systems.

The local RO operators for simulating bending angle and refractivity are implemented in the Weather Research and Forecasting (WRF)-Local Ensemble Transform Kalman Filter (LETKF) framework. The impacts of both RO data from the Constellation Observing System for Meteorology Ionosphere and Climate (COSMIC) are evaluated for predicting a heavy precipitation episode during SoWMEX-IOP8 in 2008. Results show that both the refractivity and bending angle give a positive contribution to the prediction of the heavy rainfall event.

In comparison with the refractivity data, the advantage of assimilating the bending angle is identified in the lower troposphere for moisture gradient as a direct effect, and for the wind field as an indirect effect. The convergence near the surface is better sustained from the offshore to coastal region of southwestern Taiwan and thus generates a favorable condition for the development of heavy precipitation. Therefore, the analysis leads to rainfall forecast with a location and intensity very close to the observations.

1. Introduction

Heavy rainfall frequently appears in Taiwan during the early summer rainy seasons (mid-May to mid-June, Chen and Chen 2003), especially over southwestern Taiwan (Chen et al. 2007). In order to investigate the mechanism of the heavy rainfall in this region with complex terrain (Fig. 1a), the Southwest Monsoon Experiment (SoWMEX) and the Terrain-Influenced Mesoscale Rainfall Experiment (TiMREX) were conducted jointly during the period of 15 May to 30 June 2008 in the northern South China Sea (SCS), western coastal plain and mountain slope regions of southern Taiwan (Jou et al., 2011). The objectives of SoWMEX/TiMREX are to improve understanding of physical processes associated with the terrain-influenced heavy precipitation systems and the monsoon environment in which they are embedded and, ultimately, to better forecast heavy rain-producing convective systems. For flash flooding prediction, the intensity and location of the heavy rainfall are particularly important for issuing the disaster warning (Lin et al., 2001). However, the flash flood warning becomes a challenging task in Taiwan due to the complex terrain and limited observations associated with the kinematic and thermodynamic fields. The availability of the Global Positioning System (GPS) radio occultation (RO) observations provides the possibility to depict the temperature and moisture profiles of the atmosphere. In this study, we investigate whether the upstream product of the RO observations, the bending angle, could provide additional benefits in predicting an extreme heavy rainfall episode during the SoWMEX/TiMEX period, when nature was characterized by warm and humid conditions.

During the recent years, the importance of the GPSRO observations has been well recognized in improving the global analysis and prediction with operational numerical weather prediction (NWP) systems (Healy and Thépaut, 2006; Healy, 2007, Cucurull, 2006, 2007; Cucurull and

Derber, 2008; Aparicio et al., 2009; Anlauf et al., 2011). Benefits are attributed to high accuracy and precision with high vertical resolution (2-60 m up to the stratosphere), all-weather capability with little shadowed by cloud, and an equal accuracy over either land or ocean. Mainly, improvements are identified in the temperature fields since the moisture concentrates in the low-troposphere where the amount of the RO data is limited. In terms of the available amount of observations in the operational NWP system, Baker (2011) demonstrates that the COSMIC RO data provides highly useful observation impact and effectively reduces the 1-day forecast error. Aiming to assimilate the upstream GPSRO data, Healy (2007, 2008) uses the European Centre for Medium-range Forecasts (ECMWF) operational global 4D-Var system to show that the GPSRO bending angle data has a positive impact on the temperature analysis and forecast in the mid-upper troposphere and stratosphere. Cucurull (2012) suggests that assimilation of the RO bending angle can be more beneficial than RO refractivity data in terms of the NWP forecast skill, with the challenge of vertical water vapor gradients and larger residual errors from the ionospheric correction. However, among these works, the impact of GPSRO data on the low-troposphere moisture is less clear.

For regional weather prediction, studies have shown that assimilating the RO retrieved refractivity data is beneficial for predicting the typhoon track and heavy precipitation (Chen et al. 2009; Kueh et al. 2009; Huang et al. 2005, 2010). Recently a case study by Liu et al. (2012) shows that the genesis of 2008 Hurricane Ernesto can be reproduced when the RO refractivity is assimilated and thus, enhances the moisture condition in the low troposphere. In addition to the impact on tropical cyclones, the impact of assimilating the RO refractivity data to improve the simulated Mei-Yu frontal systems is discussed in Huang et al. (2010). However, negative impacts are found in the moisture field at the 850-hPa level. As a consequence, the expected ability of the RO data to improve the moisture convergence and thus the heavy rainfall may be limited.

In most of the current data assimilation systems, assimilating the retrieved local RO refractivity data is commonly done for simplicity since one only needs to interpolate modeled pressure, water vapor and temperature values from the model grid points to the observation locations (Cucurull et al. 2007). However, the local refractivity operator with a spherically symmetric assumption will correctly simulate the refractivity only when the atmosphere was locally spherically symmetric. The use of climatology or auxiliary information to retrieve refractivities from bending angle profiles may also cause some inaccuracies (Kuo et al. 2000). Furthermore, an additional challenge arises under super-refraction conditions, which results in a negative bias below the height where super-refraction occurs (Sokolvskiy, 2005), such as boundary layer height. Although observations of bending angle are still retrieved under the assumption of local spherical symmetry, there is no need to use climatology information nor suffering from the negative bias in the lower troposphere caused by super-refraction condition. Because there is no use of an Abel inversion, bending angle is regarded as the upstream data and it is also expected that the measurement error is less correlated in bending angle than in refractivity profiles. Additionally, the bending angle accounts for the accumulated effect of horizontal gradient of the thermodynamic condition. With all these advantages, we can expect that the simulated bending angle in theory is more beneficial in regions with large gradient and may better reflect the variations in the lower atmopshere (Zou et al. 1999; Sokolovskiy et al. 2005; Chen et al. 2009; 2010). Therefore, it is preferable to assimilate the bending angle observation. However, it is too time-consuming in realistic applications to use a complicated observation operator to simulate the bending angle by solving the ray tracing equations (Zou et al. 1999). With more feasible local RO observation operators, studies show that most of the global atmospheric assimilating systems use the local operator to assimilate the RO bending angle and the advantage of using the upstream bending angle data can still be valid as compared with the refractivity data (Healy and Thépaut 2006; Cucurull et al. 2012). According to the results in Healy et al. (2007), both local and two-dimensional non-local bending angle operators obtain similar performance. Therefore, in this study an operator is used to derive the local bending angle from model local refractivity, which is then interpolated to the observation locations for data assimilation. The observation operator is further described in Section 3.2.

The gradient of the mesoscale moisture and temperature is important for generating heavy precipitation. The impact of the RO data for mesoscale weather prediction is investigated in previous studies. However, the local operator for simulating refractivity is used in most of these studies. With the experience of the global assimilation system, the upstream RO bending angle data may be expected to better represent the local variations. In this study, the RO products of refractivity and bending angle are assimilated with local operators in the Weather Research and Forecasting-Local Ensemble Transform Kalman Filter (WRF-LETKF) system (Yang et al. 2012). The error covariance in the WRF-LETKF system can represent the local flow-dependent dynamical uncertainties and naturally carries local properties of terrain. This helps better spread out the observation corrections for updating the model state during the assimilation. The impact from the RO data is investigated through a case study with heavy precipitation related to a Mei-Yu front in June 2008.

This manuscript is organized as the following. Section 2 introduces the synoptic conditions for producing the extreme heavy rain in Taiwan during the IOP-8 event (14th to 17th June 2008) of the SoWMEX/TiMREX experiment in 2008. The data assimilation system used in this study is discussed in Section 3, including the local observation operators for the assimilation of the RO refractivity and bending angle data. Section 4 describes the design of data assimilation and numerical experiments, while Section 5 presents the results of the analyses and forecasts in terms of factors leading to heavy precipitation. Finally, a summary and discussion are given in Section 6.

2. A brief overview of the characteristics of heavy rainfall on 16 June 2008 during SoWMEX /TiMREX IOP#8 event

Several studies (Davis and Lee, 2012, Lai et al., 2011, Xu et al. 2012, Chen et al. 2012) have investigated the heavy rainfall episodes during SoWMEX/TiMREX. At 0000 UTC 16 June, a mesocyclone over the northeastern SCS and Taiwan was embedded in a 500-hPa shortwave trough over the northern SCS (Fig. 5d of Xu et al. 2012). The south/southeasterly flow over Taiwan associated with the mesocyclone and the east-west oriented ridge of the subtropical high to the east of Taiwan might retard the movement of the precipitation system over the coast of the southwestern Taiwan. At the 850-hPa level, a mesocyclone was over southern China (Fig. 4d of Xu et al. 2012) and a strong southwesterly flow (or low-level jet, LLJ) with warm moist advection was observed over the northeastern SCS and southwestern Taiwan coast (Figs. 6 and 7 of Xu et al. 2012). The southwesterly LLJ over upstream ocean of southwestern Taiwan was deflected to southerly flow by Taiwan's topography (Fig. 8 of Xu et al. 2012) resulting in a low-level convergence over the coast of the southwestern Taiwan, and producing a favorable condition for the development of heavy precipitation systems. Due to the persistent rainfall over southwestern Taiwan and the adjacent coast from 14 to 15 June, a cold pool with a temperature depression of 2°-4°C in the lowest 500 m formed there (Davis and Lee, 2012, Xu et al. 2012). The cold pool over southwestern Taiwan and the adjacent ocean was further enhanced by the land breeze (Chen et al. 2012). Warm and moist air embedded in the southwesterly flow ascended over the cold pool and further lifted by the low-level convergence produced by orographic blocking is the key development of heavy rainfall over southwestern Taiwan (Chen et al. 2012). Because the low-level wind was from the south over southern Taiwan, the orographic lifting was not significant for producing rainfall over mountainous areas (Chen et al. 2012). Chen et al. (2012) suggest that as the convective systems propagated inland, the intensification takes place because of the warm, moist south/southwesterly flow interacting with the cool air associated with the land breeze. In addition, the low-level convergence between the deflecting southerly flow due to orographic blocking and the upstream southwesterly wind generate a favorable condition for the intensification of convection. Furthermore, the effect of orographic lifting aloft is absent due to the mountain-paralleling flow. These important factors result in orographic blocking and the convective cells being active in the coastal region.

In this study, the assimilation period is from 0000 UTC 13 June to 1800 UTC 16 June (IOP8). During the IOP8 period, Taiwan area is dominated by the southwesterly flow, which conveys abundant moisture to southern China and the Taiwan Strait, and sets up a favorable background for producing the heavy rainfall in southwestern Taiwan on 14 and 16 June. Before and after these events, strong deep southerly wind appears in southern Taiwan, meeting the prevailing southwesterly flow inducing a convergence zone over offshore of southwestern Taiwan. The heavy rainfall also leads to the cooling in the lowest 50 hPa on late 14 June and late 16 June. Whether heavy rainfall, in association with these features, can be captured by analyses and forecasts is investigated in Section 4.

Particularly, we further focus on the impact from the COSMIC-RO data on predicting the heavy precipitation on 16 June. The characteristic of this heavy precipitation episode is its coastal orientation and limited rainfall over the terrain slope (Fig. 1b and 1c). Compared to other heavy rainfall events during the SoWMEX/TiMREX field experiment, the rainfall intensity on 16 June is not only heavy but also long lasting (over 12 hours), as shown in Figure 1c (also see Fig. 2 in Davis and Lee. 2012). This leads to accumulated precipitation with a maximum over 300 mm within 24 hours. As discussed in Davis and Lee (2012), important features include that the heavy rainfall propagates from offshore to the coast, and the rainfall rate over the coastal region is always higher than the one over the terrain region (Fig. 1c). Before the overland precipitation starts, strong southerly jet appears offshore of southwestern Taiwan. As we show in later sections, the southerly is fundamental for localizing the rainfall over the coastal plain, given the humid environmental condition. The difficulty in predicting this event is the location of the heaviest rain, which is crucial for issuing warnings of flood, landslide or mudflow.

3. Data assimilation system and observation operators

3.1 The WRF-LETKF system

Yang et al. (2012) implemented the Local Ensemble Transform Kalman Filter (LETKF, Hunt et al. 2007) scheme in the Advanced Research WRF model version 3.2 (Skamarock et al. 2005) and applied this WRF-LETKF system to study the issues in typhoon assimilation and prediction. Below, the WRF-LETKF system is briefly described.

Unlike three-dimensional/four-dimensional variational analysis methods (3D/4D-Var), LETKF belongs to the class of sequential data assimilation that minimizes the analysis error variance. At each analysis grid point, LETKF performs data assimilation to update both the mean and perturbations of the ensemble according to the local information of the background (a short-range forecast) and regional observations. In LETKF, optimal weights are derived so that the linear combination of the ensemble perturbations minimizes the analysis error variance (in the local domain). With K background ensemble members at time t_n, the analysis ensemble perturbations (deviations from the mean) at the analysis time t_n are computed as:

$$\mathbf{X}_n^a = \mathbf{X}_n^b \mathbf{W}_n^a \tag{1}$$

Here, $\mathbf{X}_n^b$ is the matrix of the background perturbations whose columns are the vectors of ensemble perturbations from the ensemble mean: i.e., $\delta \mathbf{x}_n^{b,k} = \mathbf{x}_n^{b,k} - \overline{\mathbf{x}}_n^b$, where $\mathbf{x}_n^{b.k}$ is the k^{th} background ensemble member and $\overline{\mathbf{x}}_n^b$ is the background ensemble mean. Similar definitions are applied to the analysis ensemble mean ($\overline{\mathbf{x}}_n^a$) and perturbations ($\mathbf{X}_n^a$). In the WRF-LETKF system, $\mathbf{x}_n$ contains the WRF prognostic variables including horizontal and vertical velocity, perturbation potential temperature, geopotential height, water vapor mixing ratio, and perturbation surface pressure of dry air.

The analysis perturbation weight matrix, $\mathbf{W}_n^a$, is computed as:

$$\mathbf{W}_n^a = \left[(K-1)\hat{\mathbf{P}}_n^a \right]^{1/2} \tag{2}$$

where $\hat{\mathbf{P}}_n^a$ is the analysis error covariance matrix in the ensemble space, given by

$$\hat{\mathbf{P}}_n^a = \left[(K-1)I/\rho + \mathbf{Y}_n^{bT} \mathbf{R} \mathbf{Y}_n^b \right]^{-1}, \tag{3}$$

Here, $\mathbf{Y}_n^b$ is the matrix of the background ensemble perturbations in observation space in which the k^{th} column contains $\delta \mathbf{y}_n^{b,k} = h(\mathbf{x}_n^{b,k}) - \overline{h(\mathbf{x}_n^{b,k})}$, $\mathbf{R}$ is the observation error covariance matrix, $h(\bullet)$ is the observation operator that converts a variable from model to observation space and ρ is the multiplicative covariance inflation factor. The nonlinear observation operators for simulating the RO refractivity and bending angle will be discussed in the following subsection. The superscript T in (3) stands for matrix transpose, and the inflation coefficient ρ is a constant (1.15) throughout the assimilation experiments. Studies show that adaptively adjusting the inflation factor may further improve the overall performance of the LETKF system (Miyoshi and Kunii

2011; Miyoshi 2011). But this adaptive inflation method may not be suitable for varying observation locations like the RO data and requires further investigation (Miyoshi 2012, personal comm.).

The analysis ensemble mean at time t_n is obtained from

$$\bar{\mathbf{x}}_n^a = \bar{\mathbf{x}}_n^b + \mathbf{X}_n^b \bar{\mathbf{w}}_n^a \tag{4}$$

where

$$\bar{\mathbf{w}}_n^a = \hat{\mathbf{P}}_n^a \mathbf{Y}_n^{bT} \mathbf{R}^{-1} (\mathbf{y}_n^o - \bar{\mathbf{y}}_n^b) . \tag{5}$$

In (5), $\mathbf{y}_n^o$ and $\bar{\mathbf{y}}_n^b$ are the column vectors for the observations and the background ensemble mean in observation space, respectively. Equations (1) through (5) provide the basic formulas for deriving the LETKF analysis.

In addition to the covariance inflation, localization is used to avoid unrealistic correlation related to sampling issue and is important for optimizing the performance of LETKF. It is applied on the observation error covariance (Hunt et al. 2007) to increase the observation error with a Gaussian function in relating the distance between the observation and analysis grid point. The e-folding localization scale used in this study is 350 km and the cut-off scale is 1000 km.

In the WRF-LETKF system, a simple quality check (QC) procedure is applied to the observations before performing analysis. If the difference between the observation and background state (i.e. innovation) is five times larger than the observation error, this observation is rejected. This QC procedure is also referred to as QC-A in Table 1. To better use the bending angle data in the low atmosphere, such QC for COSMIC data is turned off below 1 km. This QC is referred to as QC-B. More discussions regarding QC-B are provided in the following sub-section. Further details about the experimental settings using the WRF-LETKF system is discussed in Section 4.

3.2 Local operators for the radio occultation

A local bending angle operator has been developed at National Central University (NCU), Taiwan (Chen et al. 2010) and implemented into WRF-LETKF system. An Abel transform is applied to this operator in order to inverse the model local refractivity profile to the "local" bending angle. Here, "local" means using the model local refractivity value at the occultation column, instead of the actual value following the ray by solving the ray-tracing equation, under the assumption of local symmetry. Following Kursinski et al. (1997), the observation operator is constructed to evaluate the bending angle integral given the observed impact parameter a

$$\alpha(a) = -2a\int_a^{\infty} \frac{d(\ln n)/dx}{\sqrt{(x^2-a^2)}}dx, \quad x = nr \tag{6}$$

where α is the bending angle, n is the refractive index derived from the model, and r is the radius value of a point on the ray path. And the atmospheric refractivity, defined as $N=(n-1)\times 10^6$, varies with the atmospheric pressure, temperature and the moisture. It can be calculated by

$$N = 77.6\frac{P}{T} + 3.73\times 10^5 \frac{P_w}{T^2}, \tag{7}$$

where T is the air temperature (K), P is the total air pressure (hPa), P_w is the water-vapor pressure (hPa). We note that the constants in (7) are empirically determined (Bean and Dutton, 1968). We use (7) to project the model variables T, P, P_w to refractivity and refractive index. To analyze (6), we do not use the approximations of ($\ln n \approx 10^{-6}N$) and ($\sqrt{x^2-a^2} \approx \sqrt{2a(x-a)}$) as those shown in Healy and Thépaut (2006, Equations (3)-(5)). Instead, we factor the equation directly. The denominator term $\sqrt{(x^2-a^2)}$ can be split into two terms ($\sqrt{(x+a)(x-a)}$). Then we assume that the x in $\sqrt{(x+a)}$ is an average in levels of i_{th} and $(i+1)_{\mathrm{th}}$. By approximating the gradient of $\ln n$ with respect to x (i.e., $d\ln n/dx$) and x+a ($=\bar{x}+a=\dfrac{x_i+x_{i+1}}{2}+a$) as constants for a profile the section of the ray path between the i_{th} to $(i+1)_{\text{th}}$ model levels can be written as

$$\Delta\alpha=-2a\frac{d\ln n}{dx}\frac{1}{\sqrt{x+a}}\int_{x_i}^{x_{i+1}}\frac{1}{\sqrt{x-a}}dx\,. \tag{8}$$

(8) is used to integrate from a to the model top. Above the model top, the bending angle is computed by extrapolating the uppermost model parameters as presented in Healy and Thépaut (2006).

$$\Delta\alpha_{top}=10^{-6}\sqrt{2\pi a k_i}N_{top}\exp\left[k_i(x_{top}-a)\right]\left[1-erf\left(\sqrt{k_i(x_{top}-a)}\right)\right] \tag{9}$$

where $k_i=\dfrac{\ln\left(N_i/N_{i+1}\right)}{x_{i+1}-x_i}$ and is assumed constant for a profile. And, erf represents the Gaussian error function. In (9), k_{i} is set to be a constant 1/6000 to simplify the calculation. In global models with a high domain top (e.g., 60 km or higher), error in contribution by (8) is very small. The error may increase for regional models with a lower top of 30 km, but this will not cause a problem as (9) has been used to account for the high atmosphere above 30 km in this study.

In the following, we refer this new local bending angle operator to as the NCU local operator. The NCU local operator is confirmed to have a comparable performance as the ECMWF ROPP[*] (Radio Occultation Processing Package) operator (Appendix A). Note that the assumption of exponential variation of the refractivity used in Healy and Thépaut (2006) is not applied in (8). Such assumption may not be valid with a low tangent point of the ray path when "super-refraction" occurs, especially at those low-atmospheric regions with a strong vertical gradient of moisture.

---

[*] The ROPP software is obtained from the ROM SAF (Radio Occultation Meteorology Satellite Application Facilities) of the EUMETSAT.

With the NCU local operator, large values of the bending angle can occur when the vertical gradient of the refractivity data below 1 km is large. This happens especially when the profiles are taken from the warm and humid region, like the region of southwesterly jet in the SCS. Figure 2 is an example of a profile taken from such a region showing high moisture and a sharp vertical gradient in the low troposphere, as in Fig. 2a. In comparison, the vertical gradient of the temperature is relatively linear. With such temperature and moisture profile, the refractivity has a very strong vertical gradient below 800 m (shown with ln(N) in Fig. 2b), resulting in a large bending angle greater than 0.05 rad near 500 m. Similar values are also obtained when derived using the ECMWF ROPP operator. With these usual values, the observations will be rejected with the regular QC-A check. To demonstrate that such large values are due to the moisture gradient, not the accuracy of the operator, the moisture below 1 km is linearly interpolated between the first and 8th model levels, indicated as the red line in Fig. 2a. After the modification of the moisture in the low levels, the logarithm of refractivity behaves more linearly and the large values of the bending angle are removed (the dashed line in Fig.2b). This also suggests the sensitivity of bending angle to the moisture, especially the vertical gradient near the boundary layer height. While the observed RO bending angles did not show such large values, the operator is applied to a dropsonde sounding near the RO location and a similar profile of local bending angle was obtained (figures were not shown), probably indicating an underestimation by observed bending angles in the lower atmosphere. Therefore, in the assimilation experiment of the local bending angle, the QC-A check below 1 km atmosphere is turned off. Following Healy and Thépaut (2006), the observation error of the local bending angle is assumed 10% at the surface and linearly decreases with height to 1% at 10 km. Above 10 km, the observation error is fixed to 1%. The observation error of the COSMIC refractivity follows Chen et al. (2011), varying from 3% near the surface to 0.3% at 14 km.

4. Data assimilation and forecast experiment design

In this section, we examine the differences between the assimilation of the local bending angle and local refractivity. The impact from assimilating the bending angle data is further investigated through the forecasts, focusing on the heavy rainfall on 16 June 2008.

The WRF-LETKF system is used for all assimilation and numerical experiments in this study. Domain 1 (the largest domain in Fig. 3), the only domain that performs LETKF assimilation, using a horizontal grid of 180 $\times$ 150 grid points with 27-km spacing. There are 27 vertically stretching layers, with the top at about 50 hPa. The physical parameterizations include the Rapid Radiative Transfer Model (RRTM) based on Mlawer et al. (1997) for longwave radiation, the Dudhia (1989) shortwave radiation scheme, the Yonsei University (YSU) PBL scheme (Hong et al. 2006), the Grell-Devenyi ensemble scheme (Grell and Dévényi, 2002) for the cumulus parameterization and the Goddard GCE microphysics scheme (Tao et al., 2003). Starting at 1800 UTC 11 June 2008, a set of 36 ensemble forecasts are generated with initial conditions centered at the National Centers for Environmental Prediction (NCEP) Global Forecasting System (GFS) final analysis (FNL 1° x 1° data). The ensemble perturbations are randomly drawn based on the 3D-Var background error covariance (Barker et al. 2004). The same procedure is used to perturb the NCEP FNL data every 6 hours until 0000 UTC 17 June; the tendencies are then computed at the boundaries according to these perturbed model states in order to obtain corresponding boundary conditions (Torn et al, 2006).

The WRF-LETKF analysis is performed every 6 hours at 0000, 0600, 1200, and 1800UTC, and the observations are collected with ±3-h windows. Observations used in this study include the wind and temperature from rawinsondes, upper air reports and flight dropsondes, surface pressure from the surface stations, and RO refractivity or bending angle from COSMIC (Constellation Observing System for Meteorology, Ionosphere and Climate; Anthes *et al.* 2008). Figure 3 shows all COSMIC observation locations for assimilation and the rest of observations at 0000UTC 15 June as a typical distribution. On average, six COSMIC RO profiles in a resolution of about 400 km are available at every analysis time within the model analysis domain. In this study, we also emphasize on the impact of the RO data in analysis on June 15 since the profiles are located in the range of the southwesterly jet, covering South China Sea and Taiwan. The RO data is preprocessed by interpolating the original atmprf data with a 3-meter vertical resolution to a profile with a 100-meter vertical resolution[*]. During this SoWMEX IOP period, the rawinsondes in Taiwan are launched every 6-hours (Ciesielski et al., 2011) but the flight dropsondes are available only at 0900-1200UTC 12 June (Davis and Lee, 2012). Moisture information from the sounding data is not assimilated on purpose in order to ensure that the moisture information is from the RO data.

Table 1 lists the assimilation experiments in this study. The CNTL experiment uses only the conventional observations, without any COSMIC RO data. In addition to the conventional data, the BANGLE and REF experiments use the COSMIC RO local bending angle and refractivity, respectively. Through these experiments, we investigate whether the dynamical and thermodynamical features associated with the extreme heavy rainfall events could be represented in the WRF-LETKF analysis and how this may determine the intensity and location of the heavy rainfall event on 16 June. Sensitivity experiments are also performed to validate the impact from the local bending angle and details are further discussed in Section 5.5.

[*] In order to resolve the high moisture in the lower troposphere, the RO data is thinned to have a vertical resolution of 100m, instead of the model vertical resolution.

The analysis ensemble means at 1200UTC 15 June from different experiments are used as initial conditions for 30-h forecast experiments, which are nested down to 3 km, as shown in Fig. 3. Note that all physical parameterizations used in the assimilation experiments with the 27-km domain are the same for the nested domains in the forecast runs, except that the cumulus parameterization is not activated in the finest (3km) domain.

5. Results

5.1 Error covariance and analysis increment in relationship to the RO data

In the local RO operator, same model information (T, Qv and P) is used to simulate the refractivity. By further using the information of the vertical gradient of the refractivity, the local bending angle is derived. This leads to different responses from the assimilation of refractivity and bending angle, in addition to the effect of using different observation errors. In this section, we explore the differences of assimilating bending angle and refractivity through the ensemble-based error covariance matrices between the background errors in the observation space and in the model space. This is the same as taking a particular column of the covariance matrix, of $\mathbf{HP}_f$, where **H** is the linearized observation operator that maps the model variables to observation space and $\mathbf{P}_f$ is the background error covariance (Kalnay, 2003). In the following, the covariance is constructed based on the same moisture field of the background ensemble from the BANGLE experiment at 0000 UTC 15 June co-varying with a set of simulated bending angles or refractivity ensemble, given a realistic observed RO point data at 1.2 km height taken from a COSMIC profile located at 121.4380°E and 19.4900 °N (north of Philippine).

Figures 4a and 4b are the corresponding covariance structures at the 850-hPa level, constructed with the simulated bending angle and refractivity ensemble, respectively. At this time (0000 UTC 15 June), the strong low-level southwesterly conveys high moisture from the

SCS to southwestern Taiwan. Comparing Fig. 4a with Fig. 4b, the horizontal scale of the background error covariance along line AB is broader with the simulated bending angle; positive covariance ranges from the location of the observation (indicated as point A) toward low-troposphere of the southwestern Taiwan and SCS. The negative covariance east of 123°E illustrates that this region is out of the boundary of the moisture transport and low-moisture is affected by the subtropical high. With the vertical cross section along the line AB in Fig. 4a, features with positive covariance in Fig. 5a mainly exhibit in the low-troposphere. In other words, any positive moisture increments derived with the bending angle at location A can increase the moisture in these regions. In comparison, negative correlations are obtained over the SCS and middle-Taiwan with the simulated refractivity ensemble (Fig. 4b) and such negative covariance can extend to mid-troposphere (Fig. 5b). Note that with observations at higher level, the $\mathbf{HP}_f$ covariance with the bending angle and refractivity exhibit very similar structures. This again supports that the additional benefit from the assimilation of the bending angle comes from the sensitivity to the vertical gradient of the moisture, especially in the lower atmosphere.

The simulated bending angle ensemble gets dispersive because of different “model” impact parameters and dln(n)/dx, according to (6). To detangle both effects, the operator for simulating bending angle is modified to fix either the impact parameters as the observed impact parameter or dln(n)/dx to a constant value of -3×10^{-8} (m^{-1}). These modified bending angles are referred to as BND-A and BND-B. Results suggest that by removing the effect of the vertical gradient of the refractivity (Fig. 4d) is very similar to REF (Fig. 4b), exhibiting negative correlations offshore of southwestern Taiwan, while limiting the spread of the impact parameters (Fig. 4c) still maintains the main features of the bending angle-related covariance (Fig. 4a). In other words, by ignoring the effect of dln(n)/dx, the derived analysis increment will be similar to the one obtained with the refractivity, losing the advantage (or disadvantage) of the bending angle. The same effect is seen in Fig. 5c and 5d. This confirms that the difference in assimilating the bending angle or refractivity data is attributed to the vertical gradient of the refractivity, which is strongly related to the vertical gradient of the moisture. This also explains why at higher levels, the covariance with the bending angle and refractivity show very similar structures and further implies that the bending angle is sensitive to the low-level moisture variations. This can be further illustrated with the relationship between the ensemble spread and the structure of the moisture field. As shown in Figs. 6a and 6b, the model state at this observation location is characterized by high moisture and a strong vertical moisture gradient below 1.5 km. Such characteristic is also reflected in the moisture ensemble, where the large ensemble spread of the moisture can extend toward the level of 3 km but the large spread of the vertical gradient is more concentrated in the low atmosphere (Fig. 6d). It is also evident that the spread of the bending angle ensemble capture the characteristics of the vertical gradient of the moisture, showing large spread in the low-atmosphere. In comparison, the ensemble spread of the refractivity resembles the behavior of the moisture spread. Results from Fig. 6 suggest that the simulated bending angle ensemble is sensitive to the uncertainties of the moisture gradient in vertical. We also note that in terms of the fraction, the refractivity spread (< 3%) is much smaller than the bending angle spread (> 15% below 1 km). This also justifies the RO observation errors used in this study.

5.2 Results from the analysis

We first evaluate the thermodynamical and wind conditions from WRF-LETKF analyses. Figure 7 shows the time-height series of the potential temperature at a model grid point near the Pingtung sounding station, located near the coast of southwestern Taiwan (Fig. 1a). With the heavy precipitation events during the assimilation period, significant difference appears in the lowest 50 hpa. As indicated in Fig.7c, by assimilating the bending angle, the near-surface cooling effect due to the passage of a decaying MCS system (Davis and Lee, 2012) is clearly shown at 1200 UTC 14 June while such cooling effect is less evident in the other two runs (Figs. 7a and 7b). On early 16 June, a similar cooling effect associated with the heavy rainfall on the same day can be seen in all three experiments. In both BANGLE and REF, the low-level high humid time period starts earlier and persists longer than that of CNTL. This is particularly apparent in the BANGLE analysis, showing a deep moisture layer of the after 1200 UTC 14th June. As for the wind, southwesterly dominates above the 900-hPa level most of the time in all three analyses, but stronger southerly exhibits near the surface at 1200 UTC 15 June in the BANGLE analysis. This sets up the condition of moisture transport toward the southwest of Taiwan.

Note that during the assimilation experiment, the moisture information from the sounding data is not assimilated and used for verification. Figure 8 is the mean Root-Mean-Square (RMS) of the differences of the water vapor mixing ratio between the observation and analysis, averaged from the last two days of the experiments (15 and 16 June). Given the accuracy of the sounding observation, this value can be used to approximate the RMS error. Results show that the RMS error from BANGLE is smaller especially near the surface and the 850-hPa level while the one with REF does not exhibit such advantage in the lower troposphere. This is because the air is relatively dryer in REF (Fig. 9d).

The surface map from the ECMWF reanalysis (figures not shown) shows that the Mei-Yu front at 1800 UTC 15 June extends from East China Sea, north of Taiwan, and to south of China. As shown in Fig. 9, the location and extension of the Mei-Yu front are well represented with all three analyses and indicates the boundary of the high moisture region. However, when comparing with the AIRS (Atmospheric Infrared sounder) and AMSU (Advanced Microwave sounder Unit) observations (Fig. 9a), the total precipitable water (TPW) computed from the BANGLE analysis at this time exhibits a more organized and high moisture region extending from the SCS, to the Taiwan Strait, and to northeast of Taiwan and the high TPW region is also confirmed with the in-situ measurements (dots). As shown in Fig. 9a, relatively high moisture appears in the southwestern Taiwan and south of the Guangdong province of China at the SCS (near 116.6°E, 20.6°N). Such a local high humid region is successfully reflected in the BANGLE analysis. In the REF analysis, high moisture occurs over the SCS and south of Taiwan, relatively low moisture appears offshore of the southwestern Taiwan (Fig. 9d). The validation of the local high moisture region in southwestern Taiwan is further justified later based on the precipitation forecasts. However, this also brings up the question about the key elements for correctly predicting the location and intensity of this heavy rain episode.

In addition to temperature and moisture, can the assimilation of the COSMIC data, especially the bending angle, modify other variables indirectly, such as the wind field? Figure 10 shows the mean RMS of the differences of winds between the observations and analysis. Observations are taken from the soundings launched at the research ships, which traversed a southwesterly path to the southwest of Taiwan (Davis and Lee, 2012). Overall, the REF analysis has the smallest RMS error for both zonal and meridional winds below the 600-hPa level. As for the BANGLE analysis, it improves the bias of the zonal wind below the 700-hPa level so that, on average, the eastward component is stronger. Also, the BANGLE analysis exhibits a smaller RMS error in the meridional wind below the 900-hPa level. The difference between the BANGLE and CNTL is further examined with Fig. 11 over the period of heavy precipitation. At 1200 UTC 15 June, the southwesterly is stronger in the BANGLE analysis (Figs. 11a and b); particularly the southerly wind over Bashi Channel and the waters offshore of southwestern Taiwan. Right before the heavy rain started (at 1800 UTC June 15), the stronger northward component is even more evident at the 850-hPa level and extend from the offshore of southwestern Taiwan to the western Taiwan (figure not shown). Also, at 1200 UTC and 1800 UTC 15 June, the westerly is stronger in the BANGLE analysis offshore of southwest Taiwan. As a result, moisture transport is stronger on June 15 at this location. As we discuss in the next sub-section, the differences in the wind fields result in the differences in convergence and vertical motion, which attributes the development of the heavy rainfall.

5.3 Impact on the forecast initialized at 1200 UTC 15 June 2008

The accumulated rainfall on 16 June is shown in Fig. 12a. The CNTL forecast shows that the heavily precipitated area is limited in the southern part of Taiwan. When the COSMIC RO data is assimilated, both the location and intensity of the heavy precipitation are improved, characterized by coastal rainfall at and offshore of the southwestern Taiwan (Figs. 12b and 12c). When the bending angle is used, the location and intensity of the precipitation are more similar to the observation (Fig. 1b) but the amount is somewhat excessive over the mountain region. From the time series of the hourly rainfall (Fig. 13c) and the hourly rainfall pattern (figure not shown), the peaks of rainfall rate are at 0100 LST, 0200 LST and 0400 LST for the offshore, coast and terrain regions, respectively, indicating that the simulated heavy rainfall from BANGLE propagates from the offshore region (blue line), toward the coast (black line) and then to the mountain region (red line). Such characteristics of the precipitation propagation are similar to the observation (Fig.1c). However, we should note that the peak time of the coastal rainfall rate in Fig. 13c is about 6-hours earlier than that in the observation (Fig. 1c). In comparison with the BANGLE forecast and observations, the CNTL forecast shows different rainfall characteristics, and the rainfall rate over the mountain region is always higher than the one over the coastal region (Fig. 13a). With the REF forecast, the rainfall over the mountain region starts too early around 2000 UTC June 15 (Fig. 13b).

Given the precipitation location and intensity shown in Fig. 12, the forecast skill of the Equitable Threat (ETS) and bias scores from the BANGLE forecast is significantly higher than the other two forecasts, as listed in Table 2a and b. A bias score larger than one is related to the excessive rainfall in the mountain. More importantly, positive impact from the COSMIC RO data is particularly apparent for the ETS score for the heavy rain, suggesting that the COSMIC RO data is beneficial for predicting the location of the heavy rain in this event. And, the bending angle data has even more impact on predicting both the location and intensity of the heavy rain.

The differences in the initial conditions (the analyses discussed in Section 5.2) show that when the bending angle is assimilated, the westerly wind at the low level over the SCS is enhanced at 1200 UTC 15 June, increasing the strength of southwesterly, and thus reenforces the moisture transport at the SCS. Also, the southerly along the coastal area of Taiwan and offshore is also strengthened (Fig. 11d). In other words, the southwesterly coming from the SCS slows down and turns into more southerly near the offshore of southwest of Taiwan. The associated convergence facilitates the development of the heavy precipitation, while the duration of the heavy rainfall is related to the maintenance of the convergence zone. Both are related to its dynamic and thermodynamic conditions. As shown in Fig. 14c, the convergence at the 950-hPa level appears offshore from the middle to the southwest of Taiwan in the BANGLE analysis. Therefore, the initial condition is set up for heavy rain starting offshore and propagating toward Taiwan, as shown in Fig. 13c. In contrast, weak divergence appears from the offshore to coastal region southwest of Taiwan in the CNTL analysis. From Fig. 14b, the convergence appears in a large area west of Taiwan in the REF analysis; however, there is no convergence near the coast of southwestern Taiwan, a condition less favorable for rainfall in the coastal region. Nevertheless, Figs. 14b and 14c both imply that the analyses incorporated with the RO data better represent the subsynoptic-scale, dynamical convergence as the prerequisite for the heavy precipitation.

Regarding the duration of the heavy precipitation, observations suggest that the low-level convergence is enhanced over the southwestern coast of Taiwan and the adjacent ocean by local convergence related to the local land-breeze (Chen et al., 2012). Starting at the early local hours on 16 June, the land cooling takes place at the slope of southwest Taiwan and results in the offshore flow (Figure 15). The southwesterly and southerly ranging from the offshore to coastal region encounters the offshore flow, causing the local convergence along the coast. Such features have been simulated in all three forecasts. Particularly, forecasts incorporated with the bending angle data show the evident and long-lasting convergence along the coast. As shown in Fig. 15c, it is clear that cold temperature (indicated by the blue and purple contours) and strong upward motion (indicated by gray shading) occurs at the coastal region and the interface of the cool air, and thus moist air is brought in and ascends at the coast. Although the CNTL forecast also shows significant cooling at this time (Fig. 15a), the moisture is much less and the updraft is weaker, compared to other forecasts with the information of the RO data.

Despite the location and intensity of the heavy rain being well predicted in the BANGLE forecast, most of the heavy rain occurs before 0800 LST 16 June (Fig. 13c) while the observations show that the heavy rain lasts until 2100 LST (Fig. 1c). Compared to the quasi-stationary observed rainfall system (Xu et al. 2012), the simulated rainfall system moves faster from the offshore to mountain. The movement is due to a southwest flow related to the northeast-southwest oriented ridge of the simulated subtropical high to the southeast of Taiwan (not shown), compared to the east-west oriented ridge of the subtropical high from observation (Section 2). Note that it may still be deficient in well representing the subtropical height with the limited-area model simulation.

In short summary, the bending angle data has the benefits to represent the important elements, in terms of the dynamic and thermodynamic states, for reproducing the heavy precipitation event on 16 June.

5.4 Results from sensitive experiments

To test the forecast sensitivity to the bending angle and its associated impact, we performed four more experiments as listed in table 1. The first two experiments (BANGLE_noTW and BANGLE_TW) focus on the bending angle near Taiwan at 1800 UTC 15 June and evaluate its importance on the moisture field. The other two experiments (NoBANGLE and BANGLE-QC) focus on the impact of the bending angle on predicting the heavy precipitation on 16 June.

The BANGLE_noTW and BANGLE_TW use the same setup as in the BANGLE analysis till 1200 UTC 15 June, but at 1800 UTC 15 June, the bending angle profile at 120.485°E, 20.537°N (south-southwest from Taiwan) is not assimilated for BANGLE_noTW. As for BANGLE_TW, only this bending profile is assimilated. At this time, right before the heavy rainfall begins, strong local moisture convergence is expected offshore of southwestern Taiwan. Figure 16 shows the total water vapor mixing ratio from surface to 500 hPa from different analyses. With the bending angle, it is evident that the high-moisture region is located southwest of Taiwan (Fig. 16b) and there is no moist region in the CNTL analysis (Fig. 16a). Without the bending angle profile near Taiwan, the amount of moisture is reduced (Fig. 16c). However, when assimilating only the bending angle profile near Taiwan, the high-moisture region can be reproduced (Fig. 16d) but extends less toward south of Taiwan. Results shown in Fig. 16 confirm the ability of the assimilation of the bending angle data to provide moisture corrections in the low atmopshere.

The NoBANGLE and BANGLE-QC experiments also use the same setup as the BANGLE experiment but until 1800 UTC 14 June. Starting from 0000 UTC 15 June, the NoBANGLE experiment stops assimilating the bending angle data and the BANGLE-QC switches back to use the original quality check that rejects the observations if the magnitude of the innovation is five times larger than the observation error. Results of the rain forecasts (initialized at 1200 UTC 15 June) are shown in Figure 17. As indicated in Fig. 17a, without the bending angle at 0000, 0600 and 1200 UTC 15 June, the location of the heavy precipitation is now shifted toward the mountainous region, and the intensity is largely reduced compared to Fig. 12c. In addition, there is excessive rain shown in the middle to northern Taiwan. In other words, this indicates that the wind field is now less favorable to maintain the convergence in the offshore region. As for the BANGLE-QC experiments, many of bending angle data in the low atmosphere below 1.5 km is rejected because of the quality check. Although the rainfall still dominates in southwestern Taiwan, the rainfall in the offshore and coastal region is reduced. This suggests that the bending angle available in the low atmosphere is important for correctly describing the amount of low-level moisture convergence, which contributes to the intensity of the precipitation.

These sensitivity tests confirm that assimilating the bending angle has the ability to provide beneficial information to depict the intensity and location of the heavy precipitation.

6. Summary and discussion

In this study, the NCU local bending angle operator is implemented in the WRF-LETKF system to evaluate the impact of the COSMIC RO bending angle for severe weather prediction with a case study of an extreme heavy rainfall episode during SoWMEX IOP8 in 2008. Three assimilation experiments are carried out with the WRF-LETKF system, without using the COSMIC data, with the COSMIC refractivity, and with the bending angle, respectively.

The difference between the assimilation of the refractivity or the bending angle data is examined by the structure of the ensemble-based $\mathbf{HP}_f$ error covariance, between the background state in the observation space and in the model space. Results suggest that the bending angle is more sensitive to the vertical gradient of the moisture, especially in the low atmosphere. Also, the ensemble spread of the simulated bending angle inherits the characteristic of the vertical gradient of the moisture. In comparison, the ensemble spread of the simulated refractivity is relatively small. Without the ensemble variations in the vertical gradient of the moisture, similar structures of the $\mathbf{HP}_f$ error covariance are obtained with either the refractivity or the bending angle and thus similar pattern of analysis correction are expected.

Based on the WRF-LETKF analyses, results suggest that positive influences are obtained with the COSMIC RO data by improving the moisture field. Particularly, the impact of the COSMIC RO bending angle is shown in the lower atmosphere, affecting the thermodynamic variables directly and the wind variables indirectly. As a result, the low-level moisture convergence is improved, giving a more favorable condition for generating heavy precipitation in the costal region of southwestern Taiwan on 16 June.

With the analyses at 1200 UTC 15 June, we focus on key elements for predicting the rainfall episode in Taiwan on 16 June. Results suggest that for this particular case study the COSMIC RO bending angle has a significant impact on improving the heavy precipitation forecast, including the location and intensity. Without the COSMIC data, the rainfall forecast in Taiwan is dominated by the terrain precipitation. With the COSMIC data, the location of the heavy rainfall is improved and moved toward the coastal region of southwestern Taiwan as seen in the observations. By assimilating the bending angle, the precipitation intensity is even more enhanced and the model simulation exhibits a feature that the heavy rain propagates from the offshore, coastal and toward the mountainous region. Results suggest that to be able to reproduce the location and intensity of the heavy precipitation event on 16 June, it is essential to generate and maintain the local convergence offshore of the southwestern Taiwan, with the moisture transport by the southwesterly from the ocean and the local convergence with the land-breeze. When only the RO bending angle is assimilated, the high moisture region is well depicted and the change of the low-level wind direction (from southwesterly to southerly) appears to support the local convergence. As a result, the analysis with the assimilation of the bending angle shows the highest forecast skill in representing the pattern and intensity of the heavy precipitation.

With the sensitivity experiments, we further confirm the impact of the bending angle. Results support that the bending angle can provide useful analysis corrections for depicting the high-moisture region and help represent the coastal rainfall. Most importantly, the bending angle in the low atmosphere affects the intensity of the moisture convergence and the following precipitation prediction.

In this study, we show the positive impact of assimilating COSMIC RO bending angles on heavy rainfall prediction over Taiwan with limited, available RO soundings using the WRF-LETKF system. The benefit is derived through the use of a local operator instead of a computationally high and complicated non-local operator, which is involved the use of a ray-tracing model. The second generation of the COSMIC project is expected to provide more bending angle profiles in time and space. This will provide great opportunities to further examine the influence of GPS RO data on severe weather prediction due to the advantage of retrieving the information of the vertical gradient of the moisture in the lower atmosphere.

Acknowledgement

The authors are very grateful to Dr. Y.-H. Kuo from NCAR and Dr. Healy from ECMWF for valuable discussions and suggestions. The authors also acknowledge the NSPO-TACC, EUMETSTAT for providing the RO data and the team of SoWMEX/TiMREX for providing valuable observations for assimilation and comparison. This work is sponsored by the National Space Organization grants No. NSPO-S-099010 and NSPO-S-101011 and partially supported by the National Science Foundation Award No. 100602-200912528. Shu-Ya Chen is sponsored by the National Science Foundation grant No. AGS-1033112.

Appendix A

The bending angle simulated from the NCU operator is compared with the one derived from the ECMWF Radio Occultation Processing Package (ROPP) operator used by Healy and Thépaut (2006), and both results are compared with observations as well. The verification data is collected from 31 RO profiles from Taiwan Analysis Center for COSMIC (TACC) during a period between 2230 UTC 16th July to 0130 UTC 17th July 2008, when tropical storm Kalmaegi located east of the Philippine. Two data formats of the TACC refractivity data (N) are used, including the NetCDF (atmprf) and BUFR (brfprf) data with a vertical resolution of 3-5 and 200 meters, respectively (Detail of the data format can be found in http://cdaac-www.cosmic.ucar.edu). The TACC refractivity with a coverage top of 60 km is provided as the inputs for the two local bending angle operators and the simulated bending angles are then compared with the retrieved (i.e. observed) bending angles from TACC. In the following the simulated bending angle with the NCU local operator is denoted as "NCU bending angle" (α_{NCU}) and same for the "ECMWF" bending angle (α_{ECMWF}).

Our results suggest that the simulated bending angles from both local operators are quite reliable compared to the observed values and the simulated errors can be as low as 0.1% below 30 km. Figure A shows the relative differences between the simulated bending angle and observations with the atmprf (left panel) and brfprf (right panel). With a very high resolution, the simulated bending angle by the NCU local operator is very accurate (<0.2%, about 10^{-5} rad) but the ECMWF operator provides a much larger positive bias (~10%) below 10 km. The amplitude of bending angles by using these two operators is about one order difference. With a lower vertical resolution, these differences with the observations are much larger now (10^{-3} rad). This suggests that the vertical resolution of the refractivity can significantly modify the accuracy of the computed bending angle. Nevertheless, the NCU and ECMWF operators show comparable accuracy (Figs. Ab,d). Healy (2011, personal communication) points out that the large positive bias shown in Fig. A-b may be related to the assumption of exponential variation of refractivity in vertical. If the profiles that violate such assumption are not used for verification, the positive bias resulted by using the ECMWF bending angle operator can be largely reduced (but cannot be completely removed) as shown in Figure Bb. With these selected profiles, the accuracy of the NCU bending angle is only 1~2% better (Fig. B-a).

We have to emphasize that the comparisons made above are using the "TACC refractivity" as the inputs. When using the bending angle operator in the assimilation system, the refractivity needs to be computed based on the model variables with Eq. (7). Also, the vertical resolution of the model and the assumption for a local operator would introduce errors in the simulated refractivity.

Reference:

Anlauf, H., D. Pingel, and A. Rhodin, 2011: Assimilation of GPS Radio Occultation data at DWD, *Atmos. Meas. Tech*., ***4***, 1105-1113.

Aparicio, J.M., G. Godelieve, L. Garand, and S. Laroche, 2009: Signature of the atmospheric compressibility factor in COSMIC, CHAMP, and GRACE radio occultation data, *J. Geophys. Res*., *114*, D16114, doi:10.1029/2008JD011159**.**

Anthes and the coauthors, 2008: The COSMIC/FORMOSAT-3 mission: early results. *Bull. Amer. Meteor. Soc.*, **89**, 313–333.

Baker, N. 2011: Overview of Navy atmospheric data assimilation activities, JCSDA 9th Workshop on Satellite Data Assimilation. College Park, Maryland, U.S.A., (http://www.jcsda.noaa.gov/meetings_Wkshp2011_Agenda.php).

Barker, D. M., W. Huang, Y.-R. Guo, A. J. Bourgeois, and Q. N. Xiao, 2004: A Three-Dimensional variational Data Assimilation System For Use With MM5: Implementation and Initial Results. *Mon. Wea. Rev*., **132**, 897-914.

Bean, B. and Dutton, E.,1968, *Radio Meteorology*. Dover Publications, New York, USA.

Chen, C.-S. and Y.-L. Chen, 2003: The rainfall characteristics of Taiwan. *Mon. Wea. Rev.*, **131**, 1323-1341.

Chen, C.-S., Y.-L. Chen, C.-L. Liu, P.-L. Lin, and W.-C. Chen, 2007: Statistics of heavy rainfall occurrences in Taiwan. *Wea. Forecasting*. **22**, 981-1002.

Chen, S.-Y., C.-Y. Huang, Y.-H. Kuo, Y.-R. Guo, S. Sokolovskiy, 2009: Typhoon predictions with GPS radio occultation data assimilations by WRF-VAR using local and nonlocal operators. *Terr. Atmos. Oceanic Sci.*, **20**, 133–154.

Chen, S.-Y., C.-Y. Huang, Y.-H. Kuo, and S. Sokolovskiy, 2011: Observational error estimation of FORMOSAT-3/ COSMIC GPS radio occultation data. *Mon. Wea. Rev.*, **139**, 853-865.

Chen, Y.-L., C.-C. Tu, C.-S. Chen, P.-L. Lin and P.-H. Lin, 2012: A comparison of two heavy rain events during the terrain-influenced monsoon rainfall experiment (TiMREX) 2008. Asia-Pacific natural hazard conference, 2012, Hawaii, USA.

Ciesielski, P. E and co-authors, 2011: Quality-Controlled upper-air sounding dataset for TiMREX/SoWMEX: development and corrections. *J. of Atmos. And Ocean. Tech.*, 27, 1802: 1821.

Cucurull, L., Y.-H. Kuo, D. Barker, SRH Rizvi, 2006: Assessing the impact of simulated COSMIC GPS radio occultation data on weather analysis over the Antarctic: a case study. *Mon. Wea. Rev.*., **134**, 3283–3296.

Cucurull, L., J.C. Derber, R. Treadon, R.J. Purser, 2007: Assimilation of global positioning system radio occultation observations into NCEP's global data assimilation system. *Mon. Wea. Rev.*, **135**, 3174–3193.

Cucurull, L., and J. C. Derber, 2008: Operational implementation of COSMIC observations into NCEP's global data assimilation system. *Wea. Forecasting.*, **23**, 702-711.

Cucurull, L., J.C. Derber, R.J. Purser, 2012: A bending angle forward operator for GPS Radio Occultation measurements, submitted. *J. Geophys. Res.*

Davis C. A. and W.-C. Lee, 2012: Mesoscale analysis of heavy rainfall episodes from SoWMEX/TiMREX. *J. of Atmos. Sci*., **69**, 512-537.

Dudhia, J., 1989: Numerical study of convection observed during the winter monsoon experiment using a mesoscale two-dimensional model, *J. Atmos. Sci*., **46**, 3077–3107.

Grell, G. A. and Dévényi D., 2002: A generalized approach to parameterizing convection combining ensemble and data assimilation techniques. *Geophy. Res. Lett*., **29**, 1693, 10.1029/2002GL015311.

Healy, S. B. and Thépaut J.-N., 2006: Assimilation experiments with CHAMP GPS radio occultation measurements. *Q. J. R. Meteorol. Soc.*, **132**, 605-623.

Healy, S. B., J. R. Eyre, M. Hamrud, J.-N. Thépaut, 2007: Assimilating GPS radio occultation measurements with two-dimensional bending angle observation operators. *Q. J. R. Meteorol. Soc.*, **626**, 1313-1327.

Healy, S. B., 2008: Forecast impact experiment with a constellation of GPS radio occultation receivers. *Atmos. Sci. Lett*., **9**, 111-118.

Huang, C.-Y., Y.-H. Kuo, S.-Y. Chen, C.-T. Terng, F.-C. Chien, P.-L. Lin, M.-T. Kueh, S.-H. Chen, M.-J. Yang, C.-J. Wang, and A. S. K. A. V. P. Rao, 2010: Impact of GPS radio occultation data assimilation on regional weather predictions. *GPS Solut*., **14**, 35–49.

Huang, C.-Y., Y.-H. Kuo, S.–H. Chen, F. Vandenberghe, 2005: Improvements on typhoon forecast with assimilated GPS occultation refractivity. *Wea Forecasting*, **20**, 931–953.

Hong, S.-Y., and Y. Noh, and J. Dudhia, 2006: A new vertical diffusion package with an explicit treatment of entrainment processes. *Mon. Wea. Rev*., **134**, 2318–2341.

Hunt, B.R., E. J. Kostelich, I. Szunyogh, 2007: Efficient data assimilation for spatiotemporal chaos: a Local Ensemble Transform Kalman Filter. *Physica D*, **230**, 112-126.

Jou, B. J.-D., W.-C. Lee, and R. H. Johnson, 2011: An overview of SoWMEX/TiMREX and its operation. The Global Monsoon System: Research and Forecast, 2nd ed. C.-P. Chang, Ed., *World Scientific*, 303–318.

Kanay, E., 2003: Atmospheric modeling, Data assimilation and predictability, *Cambridge Publications*. p341.

Kueh, M.-T, C.-Y. Huang, S.-Y. Chen, S.-H. Chen, C.-J. Wang, 2009: Impact of GPS radio occultation soundings on prediction of Typhoon Bilis (2006) landfalling Taiwan. *Terr.*

Atmos. Oceanic. Sci., **20**, 115–131.

Kuo, Y.-H. and S. Sokolovskiy, 2000: Assimilation of GPS radio occultation data for numerical weather prediction. *Terr., Atmos. Ocean. Sci*., **11**, 157–186.

Kursinski, E., G. Hajj, J. Schofield, R. Linfield and K. Hardy, 1997: Observing earth's atmosphere with radio occultation measurements using the Global Positioning System. *J. Geophys. Res.*, **102**, 23429–23465

Lai, H.-W., C. A. Davis and B. J.-D. Jou, 2011: A subtropical obceanic mesoscale convective vortex observed during SoWMEX/TiMREX. , *Mon. Wea. Rev*., **139**, 2367-2385.

Lin, Y.-H., S. Chiao, T.-A. Wang, M. L. Kaplan and R. P. Weglarz, 2001: Some common ingredients for heavy orographic rainfall. *Wea. Forecasting*, **16**, 633-660.

Liu, H., J. Anderson and Y.-H. Kuo, 2012: Improved Analyses and Forecasts of Hurricane Ernesto's Genesis Using Radio Occultation Data in an Ensemble Filter Assimilation System. *Mon. Wea. Rev*., **140**,151-166.

Melbourne, W., E. Davis, C. Duncan, G. Hajj, K. Hardy, E. Kursinski, T. Meehan and L. Young, 1994: The application of spaceborne GPS to atmospheric limb sounding and global change monitoring'. Publication 94-18, Jet Propulsion Laboratory, Pasadena, Calif., USA.

Miyoshi, T and M. Kunii, 2011: The local ensemble transform Kalman filter with the Weather Research and Forecasting model: experiments with real observations. *Pure and Appl. Geophys*., **169**, 321-333.

Mlawer, E. J., S. J. Taubman, P. D. Brown, M. J. Iacono, and S. A. Clough, 1997: Radiative transfer for inhomogeneous atmosphere: RRTM, a validated correlated-k model for the long-wave. *J. Geophys. Res*., **102** (D14), 16663–16682.

Skamarock, W. C., J. B. Klemp, J. Dudhia, D. O. Gill, D. M. Barker, W. Wang, and J. G. Powers, 2005: A description of the Advanced Research WRF version 2. NCAR Tech. Note TN-468_STR, 88 pp.

Sokolovskiy S., Y.-H. Kuo and W. Wang, 2005: Assessing the accuracy of a linearized observation operator for assimilation of radio occultation data: Case simulations with a high-resolution weather model. *Mon. Wea. Rev.* **133**: 2200–2212.

Tao, W.-K,, J. Simpson, D. Baker, S. Braun, M.-D. Chou, B. Ferrier, D. Johnson, A. Khain, S. Lang, B. Lynn, C.-L. Shie, D. Starr, C.-H. Sui, Y. Wang, and P. Wetzel, 2003: Microphysics, radiation and surface processes in the Goddard Cumulus Ensemble (GCE) model. *Meteor. and Atmos. Phys.*, **82**, 97–137.

Torn, R. D., G. J. Hakim, and C. Snyder, 2006: Boundary conditions for limited-area ensemble Kalman filters. *Mon. Wea. Rev.*, **134,** 2490–2502.

Xu, W., E. J. Zipser, Y.-L. Chen, C. Liu, Y.-C. Liou, W.-C. Lee, Ben J.-D. Jou, 2012: An Orography-Associated Extreme Rainfall Event during TiMREX: Initiation, Storm Evolution, and Maintenance. *Mon. Wea. Rev*., 120, 2555-2574.

Yang, S.-C., E. Kalnay and T. Miyoshi, 2012: Improving EnKF spin-up for typhoon assimilation and prediction, *Wea. Forecasting*, **27**, 878-897.

Zhang, F., Y. Weng, Y.-H. Kuo, J. S. Whitaker, B. Xie: 2010: Predicting typhoon Morakot's catastrophic rainfall with a convection-permitting mesoscale ensemble system. *Wea. Forecasting*, **25**, 1816-1825.

Zou, X., F. Vandenberghe, B. Wang, M.E. Gorbunov, Y.-H. Kuo, S. Sokolovskiy, J.C. Chang, J.G. Sela, R. Anthes, 1999: A ray tracing operator and its adjoint for the use of GPS/MET refraction angle measurements. *J. Geophys. Res* ., **104**, 22301–22318.

List of Tables

List of figures

Figure 1(a) Topography of Taiwan (in km) and the distribution of the automatic rain gauge stations. Three boxes denote the offshore, coastal, and terrain regions from the left to right, respectively. (b) Total accumulated rainfall from the observations in color scale (mm). (c) Average hourly rainfall from the automatic rain gauges on 16 June 2008. The red line denotes the average rainfall from the rain gauges collected over the coastal plain (the middle box in Fig. 1a) and the blue line is for the rain gauges over the terrain region (the right box in Fig. 1a). The star in Fig. 1a denotes the model grid point (120.2°E and 22.7°N) near the Pingtung sounding station.

Figure 2(a) Model temperature (T) and water vapor mixing ratio (Qv) for a profile located in the region of the southwesterly jet. The red line denotes the new water vapor mixing profile similar to the original one except that the values between the 1^{st} and level 8^{th} model levels are modified. (b) Model refractivity and bending angle profiles based on the information from Fig. 2a. The modified refractivity and bending angle derived with the modified moisture are denoted as red and dashed lines, respectively.

Figure 3. The WRF model domain and observations used in the assimilation and forecast experiments. The largest domain with a horizontal grid spacing of 27 km is used for performing the LETKF assimilation. Two additional nested domains, with horizontal grid spacing of 9 and 3 km respectively, are included for performing the 30-h forecasts.

Figure 4. Ensemble-based covariance between the water vapor mixing ratio at the model level near the 850-hPa level and (a) the bending angle, (b) the refractivity, (c) the BND-A and (d) the BND-B simulated at point A. Red contours denote the negative values. Point A is the location of

the COSMIC profile at 121.44°E and 19.49°N. Fig. 4(a)-(d) use the same ensemble from the background ensemble of the BANGLE experiment at 0000UTC 15 June.

Figure 5. Vertical cross-section of the ensemble-based covariance along line AB in Fig. 4 between the water vapor mixing ratio and (a) the bending angle, (b) the refractivity, (c) the BND-A and (d) the BND-B simulated at location A in Fig. 4.

Figure 6(a)The ensemble mean state of water vapor mixing ratio and (b) vertical gradient of the mean water vapor mixing ratio at the observation location (121.44°E, 19.49°N). Ensemble spread of the (c) water vapor mixing ratio, (d) vertical gradient of the water vapor mixing ratio, (e) refractivity and (f) bending angle at the same observation location.

Figure 7. Time-height series of the potential temperature (contours) and wind (arrows) at the location of the star in Fig. 1a. A full barb and a half barb represent 5 and 2.5 $m\ s^{-1}$, respectively. Gray shading denotes the water vapor mixing ratio larger than 18.5 g/kg.

Figure 8. Root mean square (RMS) of the differences of the water vapor mixing ratio between the observations and analysis. The observations are taken from all the rawinsondes located in the model domain during 15 and 16 June.

Figure 9. Total precipitable water in color scale from (a) the observation of AIRS and AMSU data at 1742 UTC 15 June and sounding data (scattered circles) at 1800UTC, and from the analysis of (b) CNT, (c) BANGLE and (d) REF at 1800 UTC 15 June.

Figure 10. The bias (dashed lines) and RMS (solid lines) of the differences between the observation and analysis of the (a) zonal and (b) meridional wind. The observations are the sounding data from the ships collected from 0000 UTC 15 June to 1800 UTC 16 June.

Figure 11. Differences of the zonal (upper panel) and meridional (lower panel) wind of the BANGLE and CNTL analyses (BANGLE minus CNTL) in color scale (m/s) at the 950-hPa level at 1200 UTC 15 June (left), 1800 UTC 15 June (middle) and 0000 UTC 16 June (right).

Figure 12. Total precipitation in color scale (mm) on 16 June (accumulated from 1600 UTC 15 to 1600UTC 16 June) from the forecasts initialized from (a) CNTL, (b) REF and (c) BANGLE analyses at 1200 UTC 15 June.

Figure 13. Time series (LST) of the hourly precipitation from the forecasts initialized from (a) CNTL, (b) REF and (c) BANGLE analyses at 1200 UTC 15 June.

Figure 14. 950-hPa wind vectors (m/s) and convergence (color shading; $10^{-4}s^{-1}$) of the (a) CNTL, (b) REF and (c) BANGLE analyses at 1200 UTC 15 June. The dashed line denotes the 500 m terrain height.

Figure 15. Wind vectors (m/s), vertical motion (shaded for amplitude larger than 0.2 m s^{-1}) and the 24°C (purple contour) and 25°C (blue contour) isotherm of the temperature at surface of the (a) CNTL, (b) REF and (c) BANGLE forecasts at 2200 UTC 15 June (0600LST 16 June). The green dashed line denotes the 500 m terrain height.

Figure 16. Total water vapor mixing ratio (g kg^{-1}) below the 500-hPa level from (a) CNTL, (b) BANGLE, (c) BANGLE_noTW and (d) BANGLE_TW analyses at 1800 UTC 15 June. Gray shading denotes the value larger than 13 g/Kg.

Figure 17. Same as Fig. 12 except the forecasts are initialized from (a) NoBANGLE and (b) BANGLE-A analyses at 1200 UTC 15 June.

Figure A (a) Relative difference of the simulated bending computed with the NCU local operator and the TACC atmprf data. (b) same as (a) but compared with the TACC brfprf data. (c) Same as

(a) but the simulated bending angle is computed with the ECMWF-ROPP local operator. (d) same as (c) but compared with the TACC brfprf data.

Figure B (a) Difference of the simulated bending angle computed with the NCU local operator and the TACC atmprf observations. The comparison is made only when the simulated refractivity fulfills the assumption of exponential variation in vertical. (b) same as (a), but the simulated value is computed with the ECMWF-ROPP operator.

Table 1 Settings in all the assimilation experiments

Exps. name	Observations	Quality control
CNTL	Convention[*]	QC-A
REF	Convention+ refractivity	QC-B
BANGLE	Convention + bending angle	QC-B
BANGLE_noTW	Same as BANGLE but the bending angle profile near Taiwan is not assimilated at 1800 UTC 15 June	QC-B
BANGLE_TW	Same as BANGLE but only the bending angle profile near Taiwan is assimilated at 1800 UTC 15 June	QC-B
BANGLE-QC	Convention+ bending angle	QC-A
NoBANGLE	Same as BANGLE but no bending angle assimilated at 1200U TC 15 June	QC-B

[*] Convention data used in this study includes the sounding from the rawinsondes and flight, upper air sounding from the air report, and surface station.

Table 2(a) ETS of quantitative precipitation forecast on 16 June.

threshold / observation	50mm/day	100mm/day	130mm/day
CNTL	0.11	0.04	0.00
Bending Angle	0.46	**0.73**	**0.59**
Refractivity	0.22	**0.30**	**0.18**

Table 2(b) Bias of quantitative precipitation forecast on 16 June.

threshold / observation	50mm/day	100mm/day	130mm/day
CNTL	0.63	0.41	0.37
Bending Angle	**1.20**	**1.07**	**1.18**
Refractivity	0.65	0.48	0.32

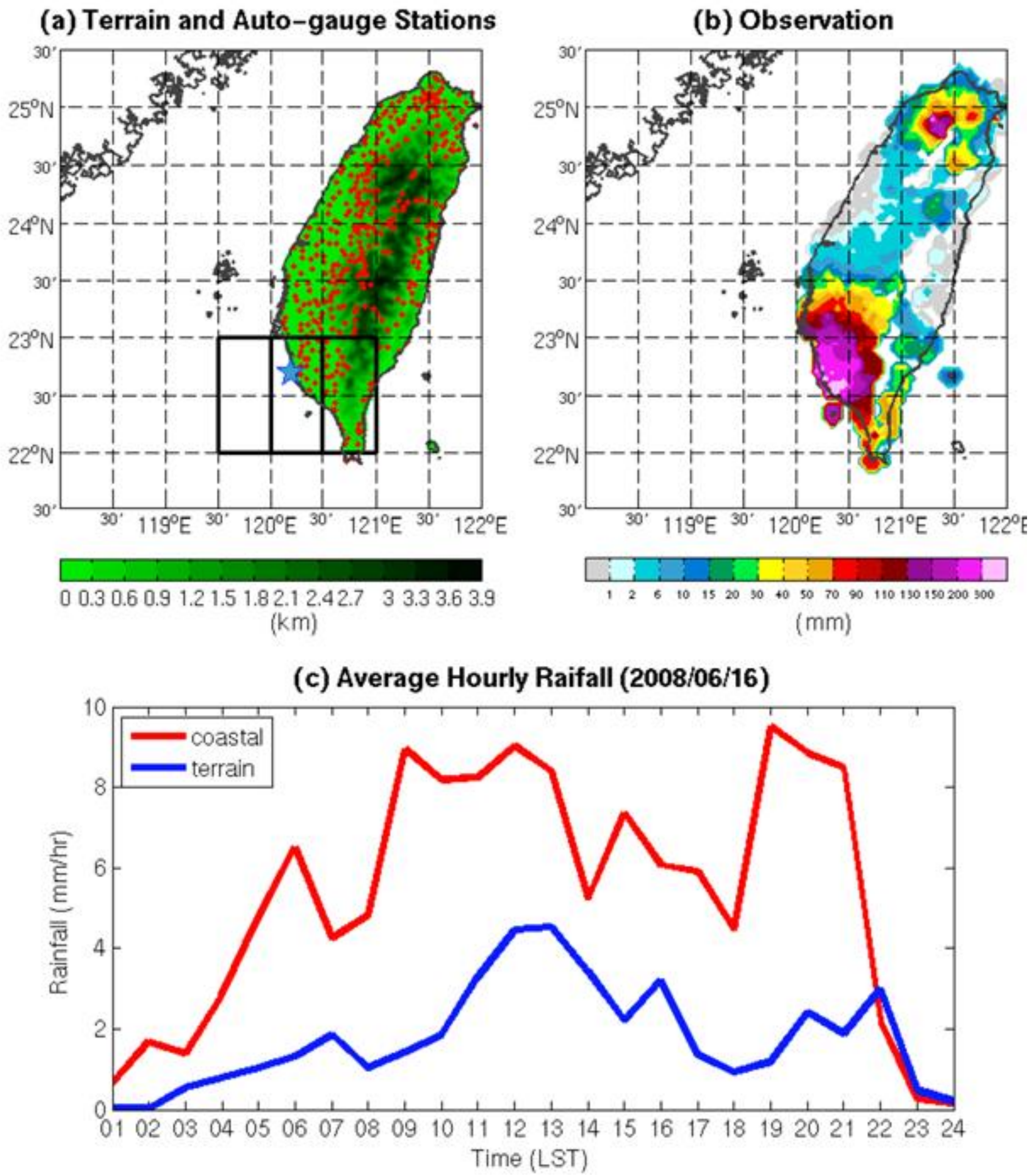

Figure 1(a) Topography of Taiwan (in km) and the distribution of the automatic rain gauge stations. Three boxes denote the offshore, coastal, and terrain regions from the left to right, respectively. (b) Total accumulated rainfall from the observations in color scale (mm). (c) Average hourly rainfall from the automatic rain gauges on 16 June 2008. The red line denotes the average rainfall from the rain gauges collected over the coastal plain (the middle box in Fig. 1a) and the blue line is for the rain gauges over the terrain region (the right box in Fig. 1a). The star in Fig. 1a denotes the model grid point (120.2°E and 22.7°N) near the Pingtung sounding station.

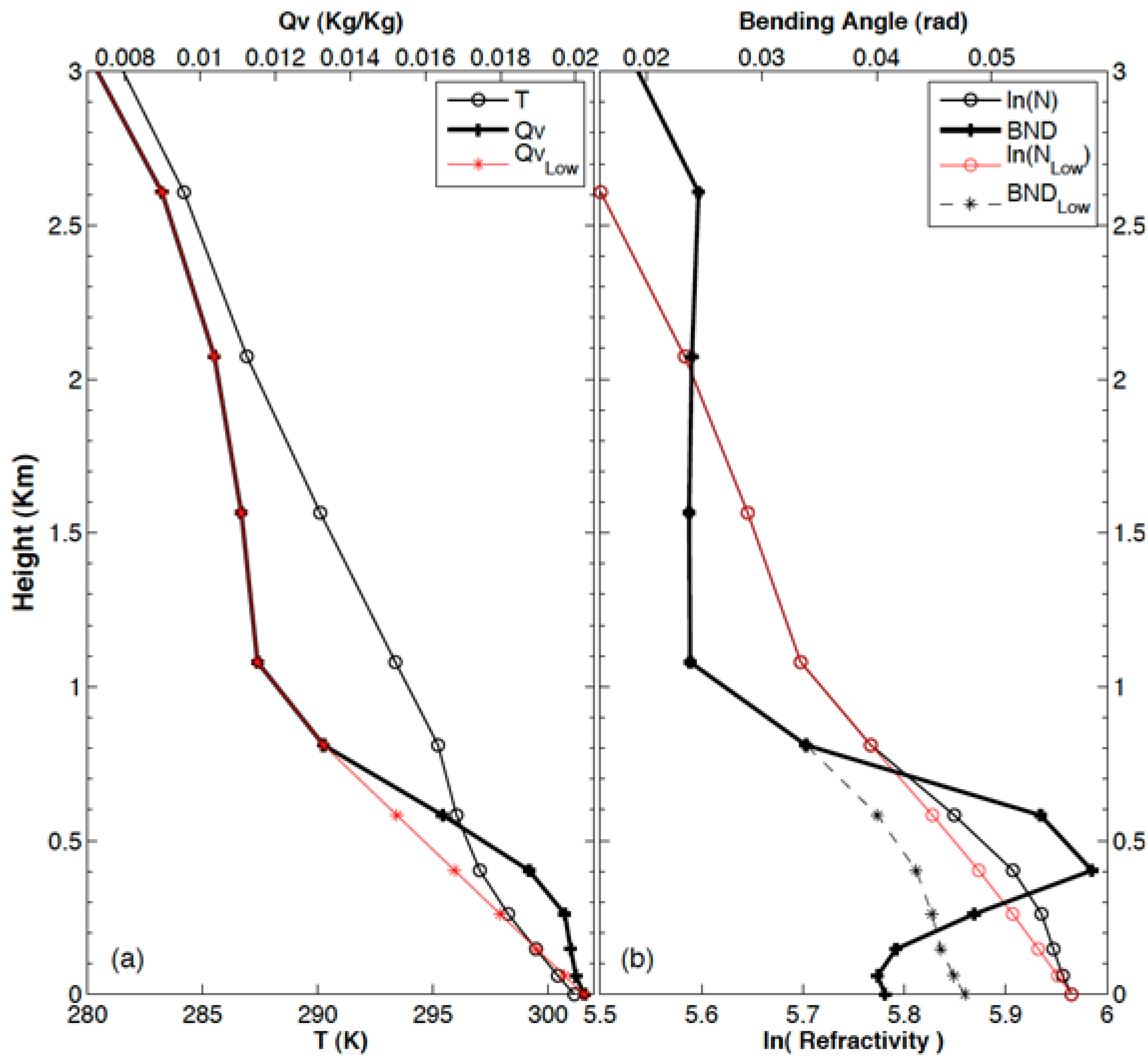

Figure 2. (a) Model temperature (T) and water vapor mixing ratio (Qv) for a profile located in the region of the southwesterly jet. The red line denotes the new water vapor mixing profile similar to the original one except that the values between the 1st and level 8th model levels are modified. (b) Model refractivity and bending angle profiles based on the information from Fig. 2a. The modified refractivity and bending angle derived with the modified moisture are denoted as red and dashed lines, respectively.

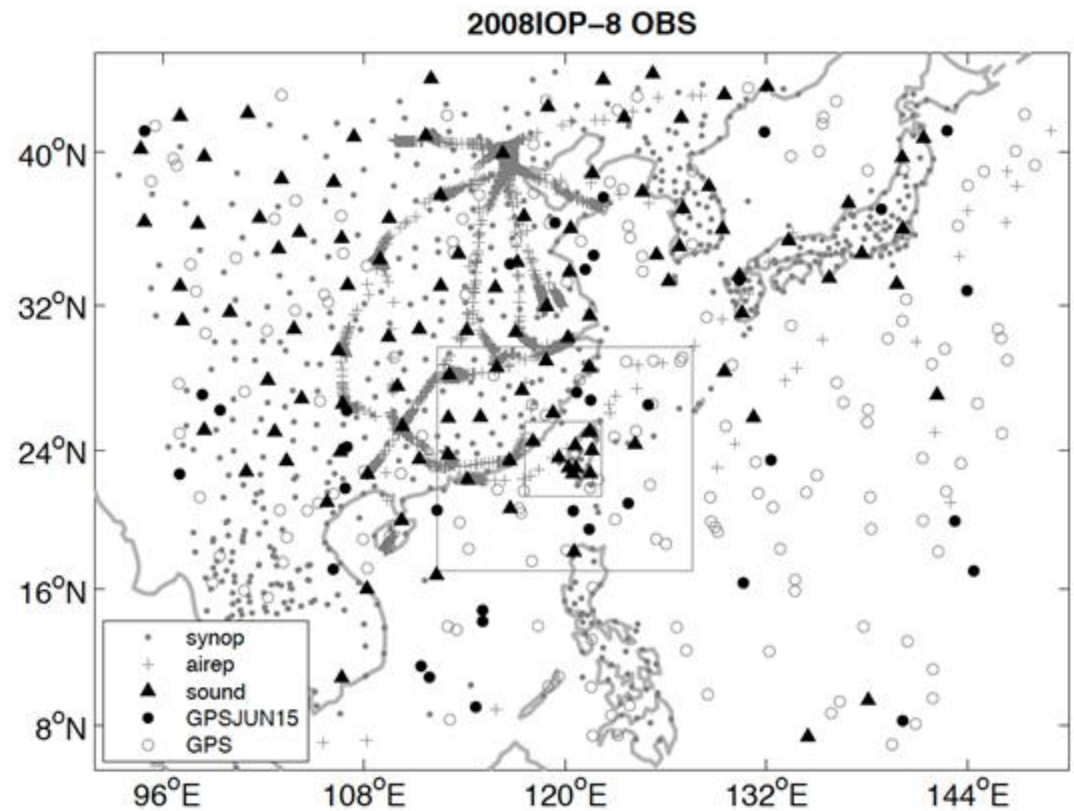

Figure 3. The WRF model domain and observations used in the assimilation and forecast experiments. The largest domain with a horizontal grid spacing of 27 km is used for performing the LETKF assimilation. Two additional nested domains, with horizontal grid spacing of 9 and 3 km respectively, are included for performing the 30-h forecasts.

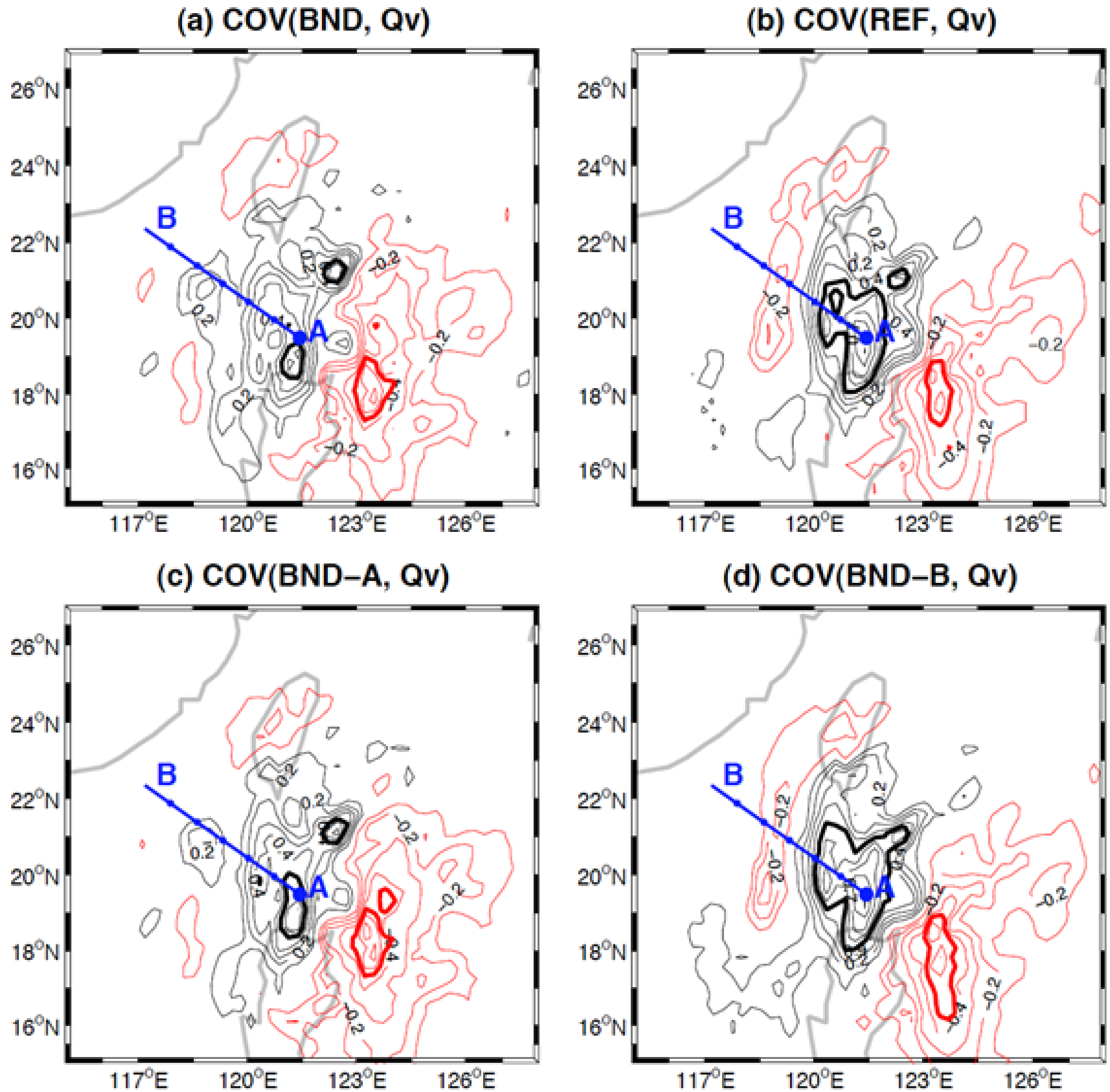

Figure 4. Ensemble-based covariance between the water vapor mixing ratio at the model level near the 850-hPa level and (a) the bending angle, (b) the refractivity, (c) the BND-A and (d) the BND-B simulated at point A. Red contours denote the negative values. Point A is the location of the COSMIC profile at 121.44°E and 19.49°N. Fig. 4(a)-(d) use the same ensemble from the background ensemble of the BANGLE experiment at 0000UTC 15 June.

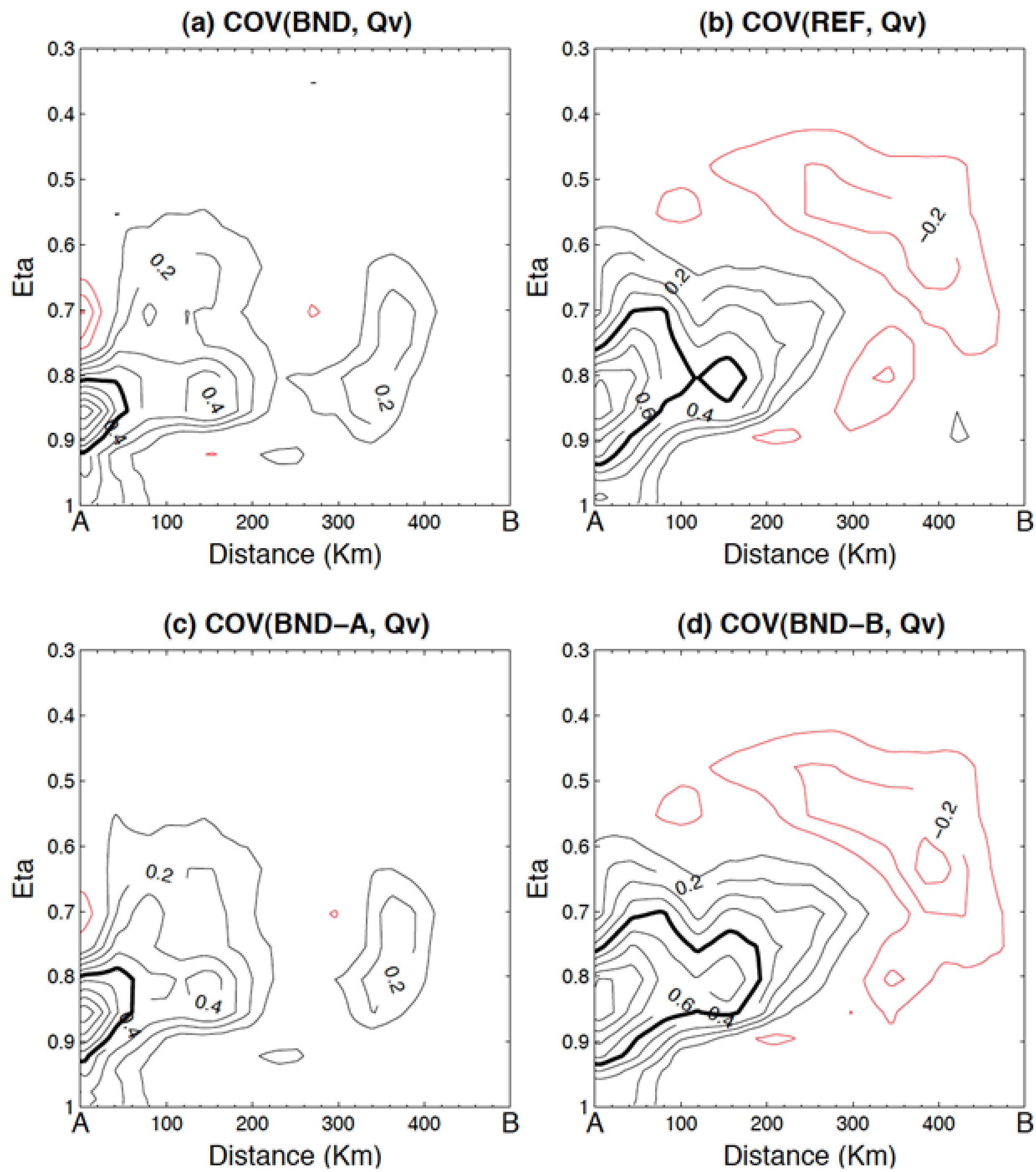

Figure 5. Vertical cross-section of the ensemble-based covariance along line AB in Fig. 4 between the water vapor mixing ratio and (a) the bending angle, (b) the refractivity, (c) the BND-A and (d) the BND-B simulated at location A in Fig. 4.

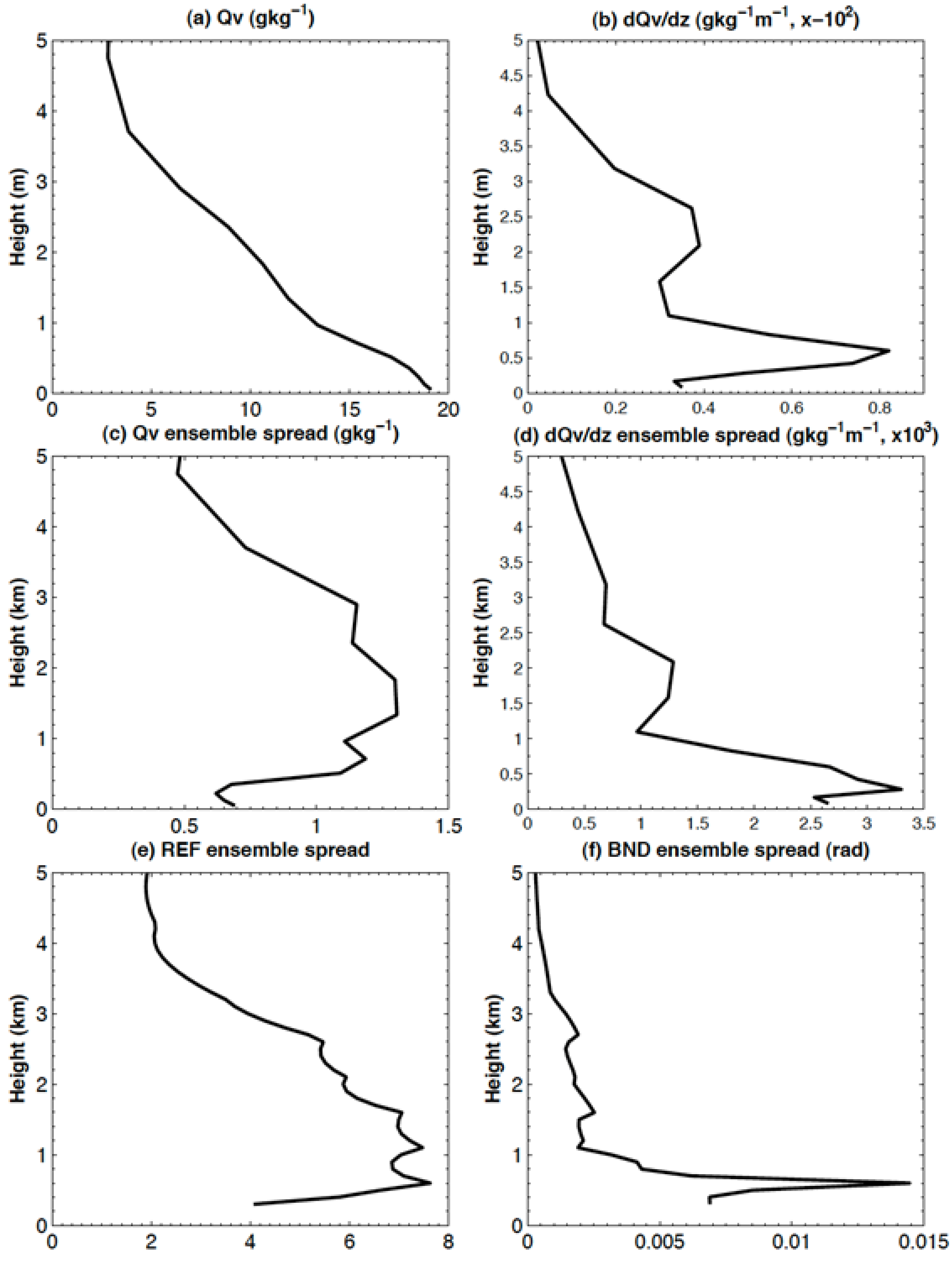

Figure 6. (a)The ensemble mean state of water vapor mixing ratio and (b) vertical gradient of the mean water vapor mixing ratio at the observation location (121.44°E, 19.49°N). Ensemble spread of the (c) water vapor mixing ratio, (d) vertical gradient of the water vapor mixing ratio, (e) refractivity and (f) bending angle at the same observation location.

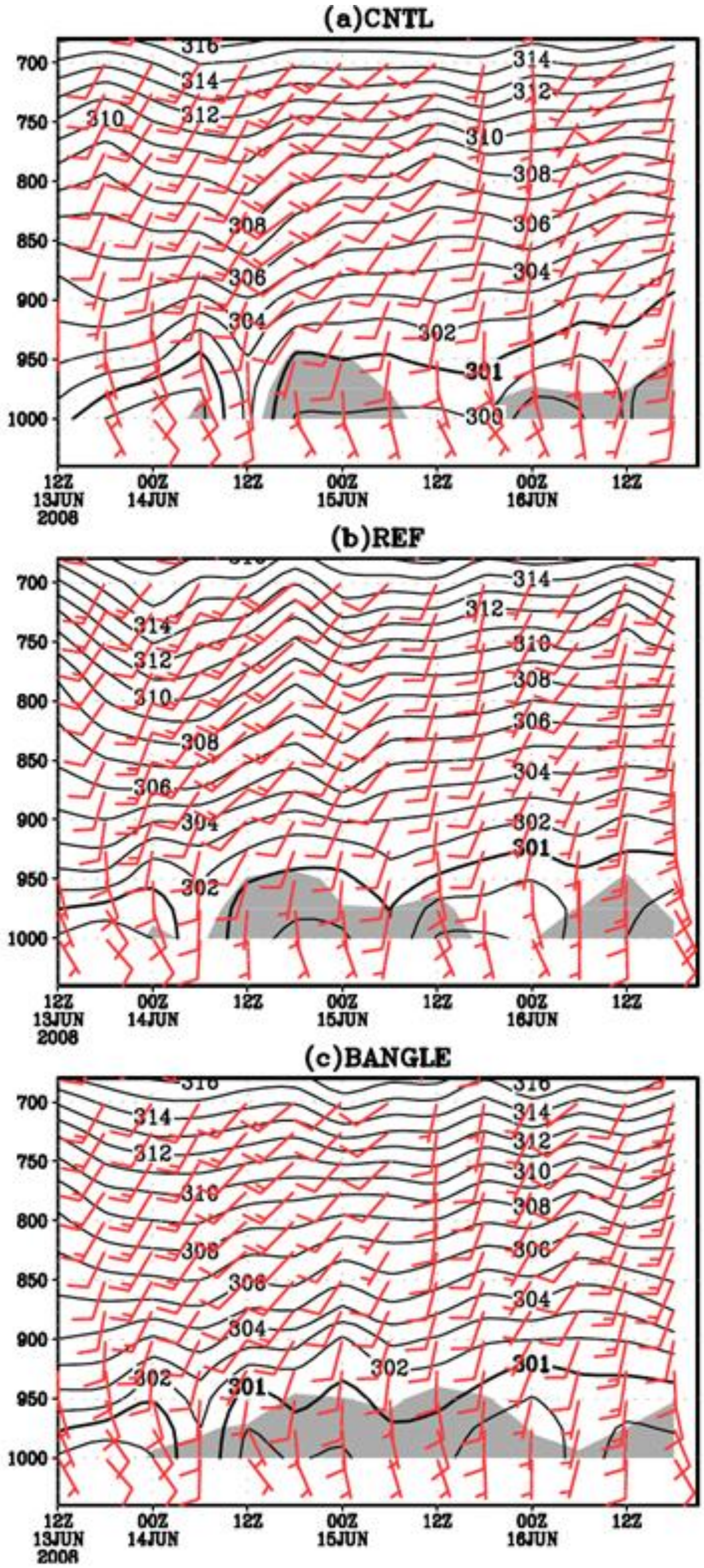

Figure 7. Time-height series of the potential temperature (contours) and wind (arrows) at the location of the star in Fig. 1a. A full barb and a half barb represent 5 and 2.5 m s^{-1}, respectively. Gray shading denotes the water vapor mixing ratio larger than 18.5 g/kg.

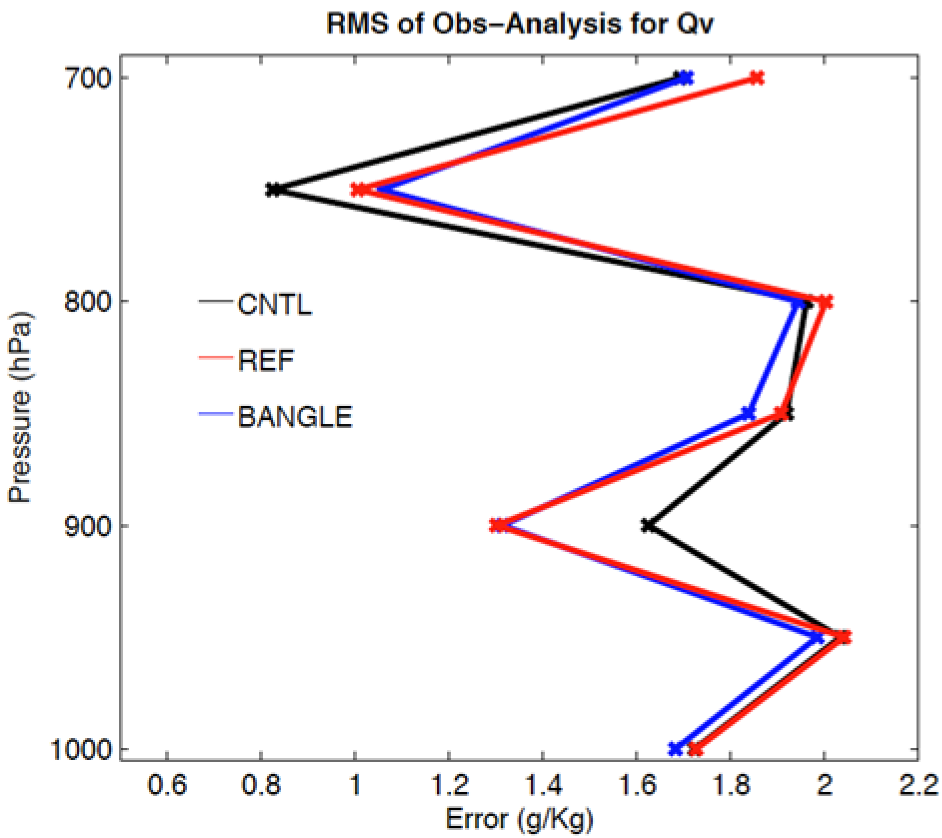

Figure 8. Root mean square (RMS) of the differences of the water vapor mixing ratio between the observations and analysis. The observations are taken from all the rawinsondes located in the model domain during 15 and 16 June.

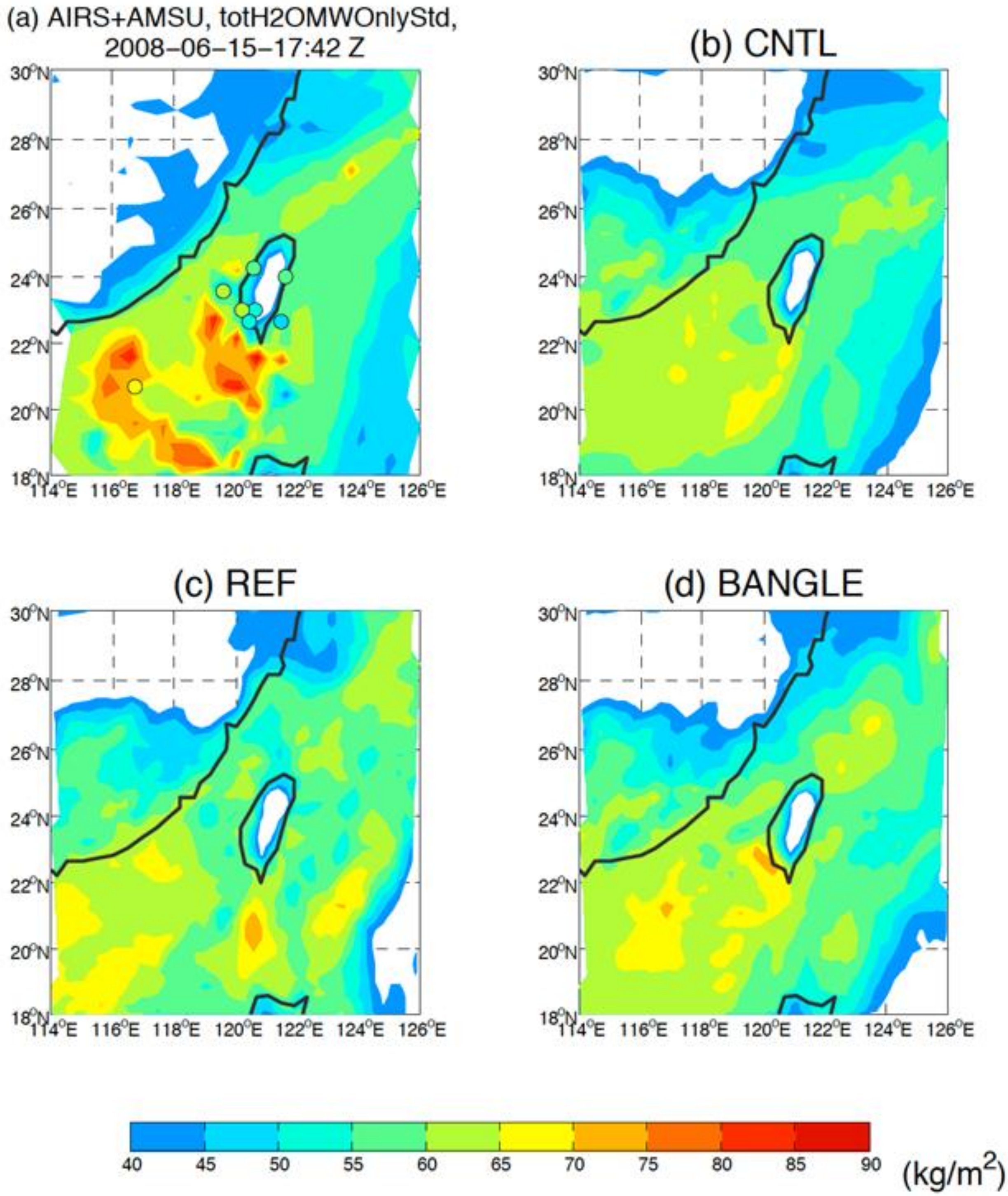

Figure 9. Total precipitable water in color scale from (a) the observation of AIRS and AMSU data at 1742 UTC 15 June and sounding data (scattered circles) at 1800UTC, and from the analysis of (b) CNT, (c) BANGLE and (d) REF at 1800 UTC 15 June.

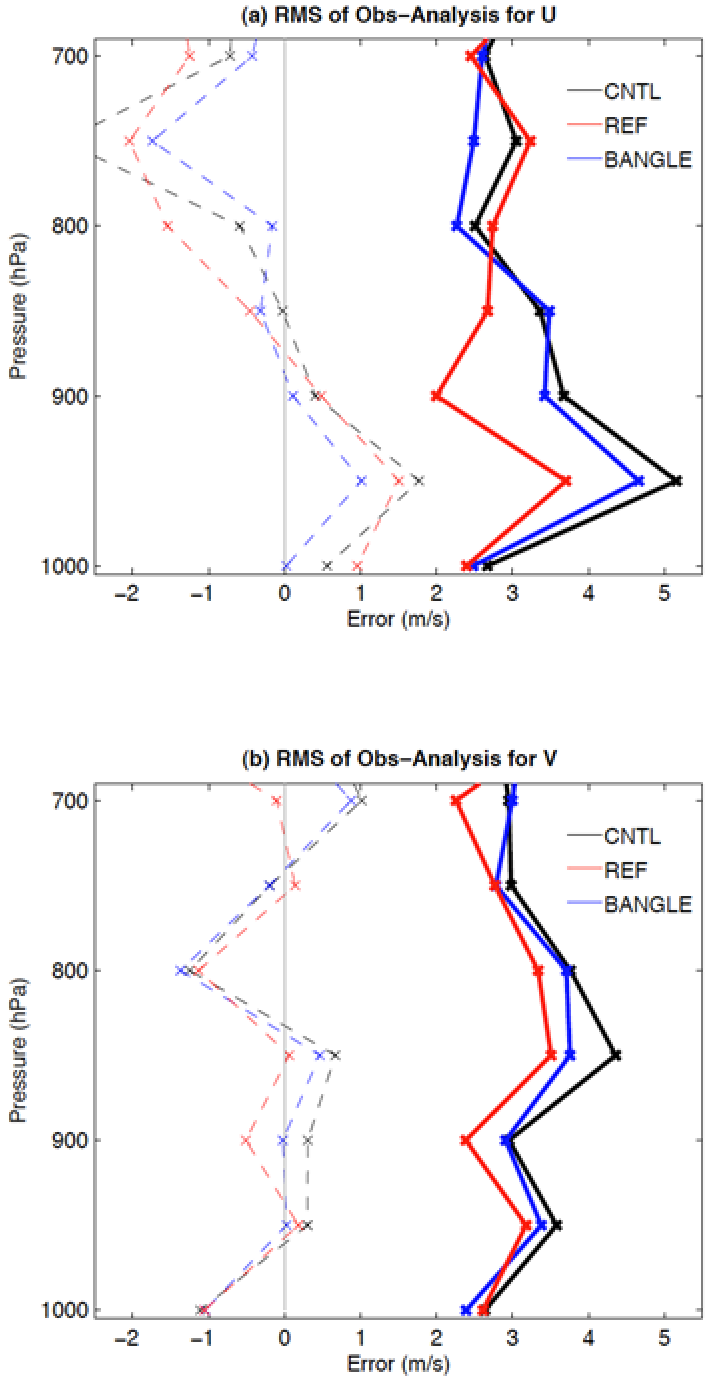

Figure 10. The bias (dashed lines) and RMS (solid lines) of the differences between the observation and analysis of the (a) zonal and (b) meridional wind. The observations are the sounding data from the ships collected from 0000 UTC 15 June to 1800 UTC 16 June.

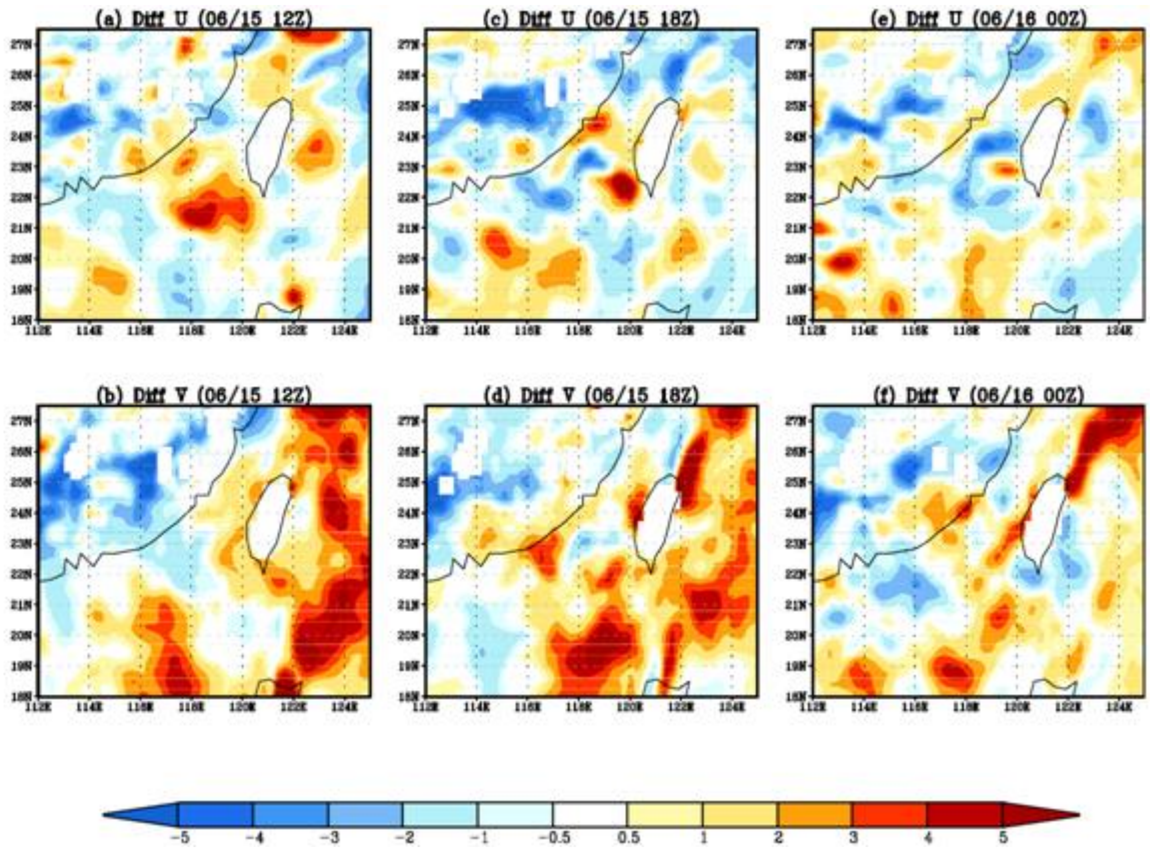

Figure 11. Differences of the zonal (upper panel) and meridional (lower panel) wind of the BANGLE and CNTL analyses (BANGLE minus CNTL) in color scale (m/s) at the 950-hPa level at 1200 UTC 15 June (left), 1800 UTC 15 June (middle) and 0000 UTC 16 June (right).

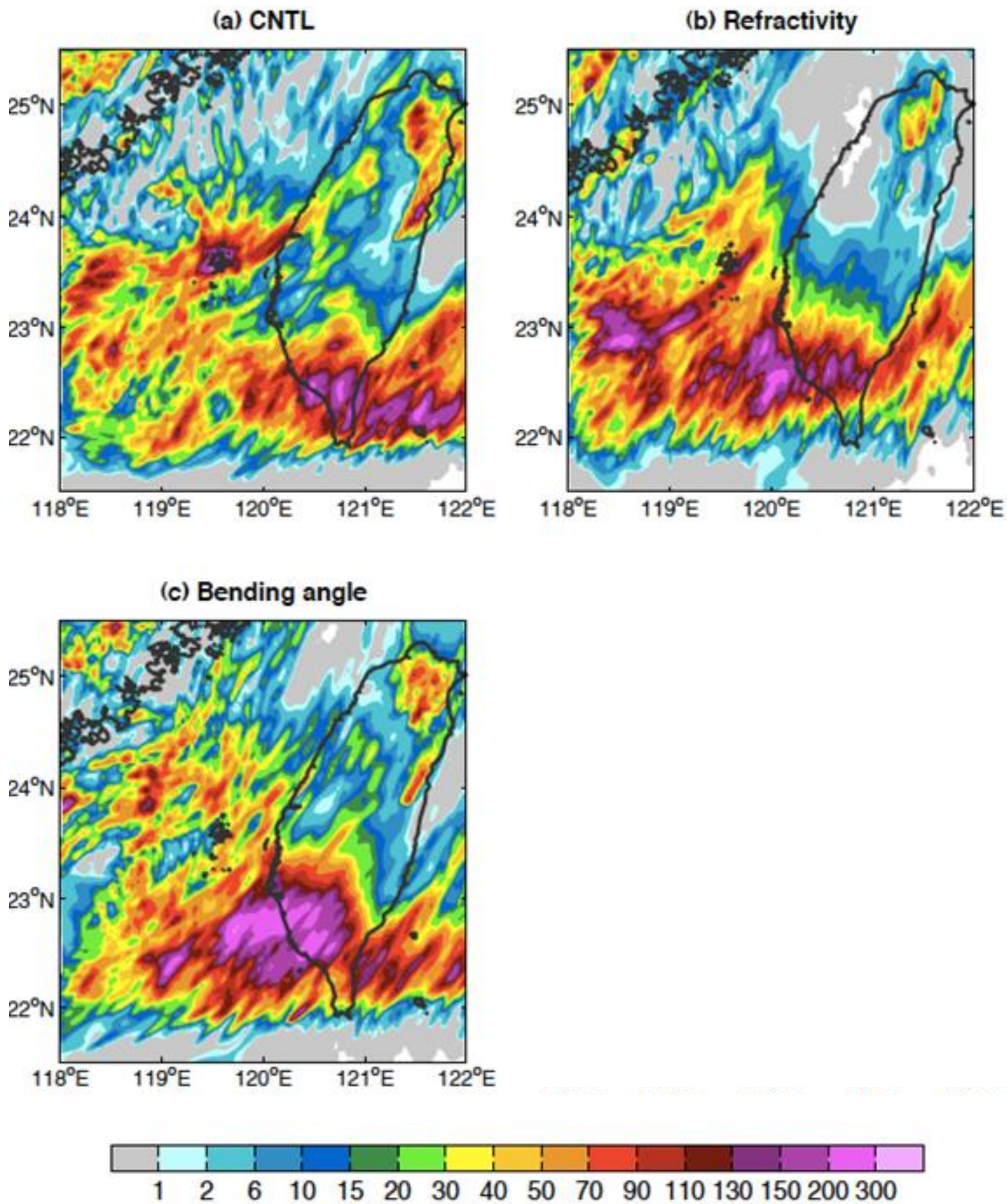

Figure 12. Total precipitation in color scale (mm) on 16 June (accumulated from 1600 UTC 15 to 1600UTC 16 June) from the forecasts initialized from (a) CNTL, (b) REF and (c) BANGLE analyses at 1200 UTC 15 June.

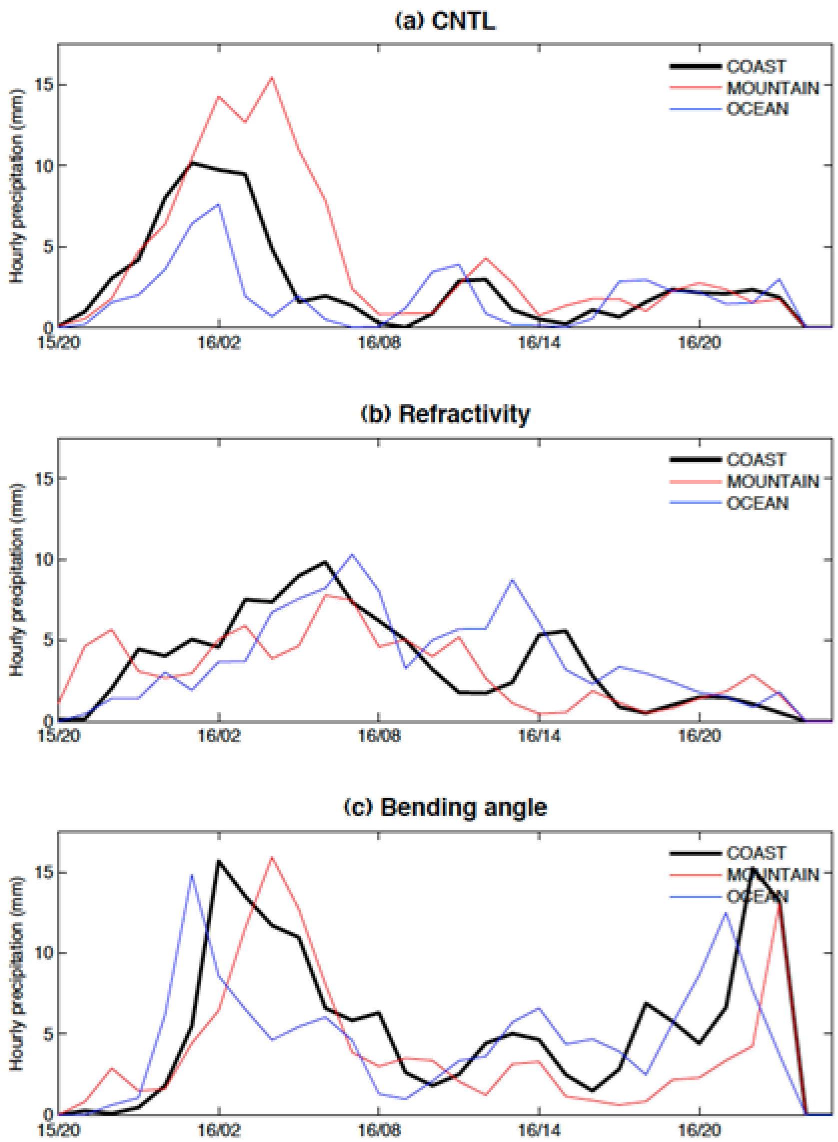

Figure 13. Time series (LST) of the hourly precipitation from the forecasts initialized from (a) CNTL, (b) REF and (c) BANGLE analyses at 1200 UTC 15 June.

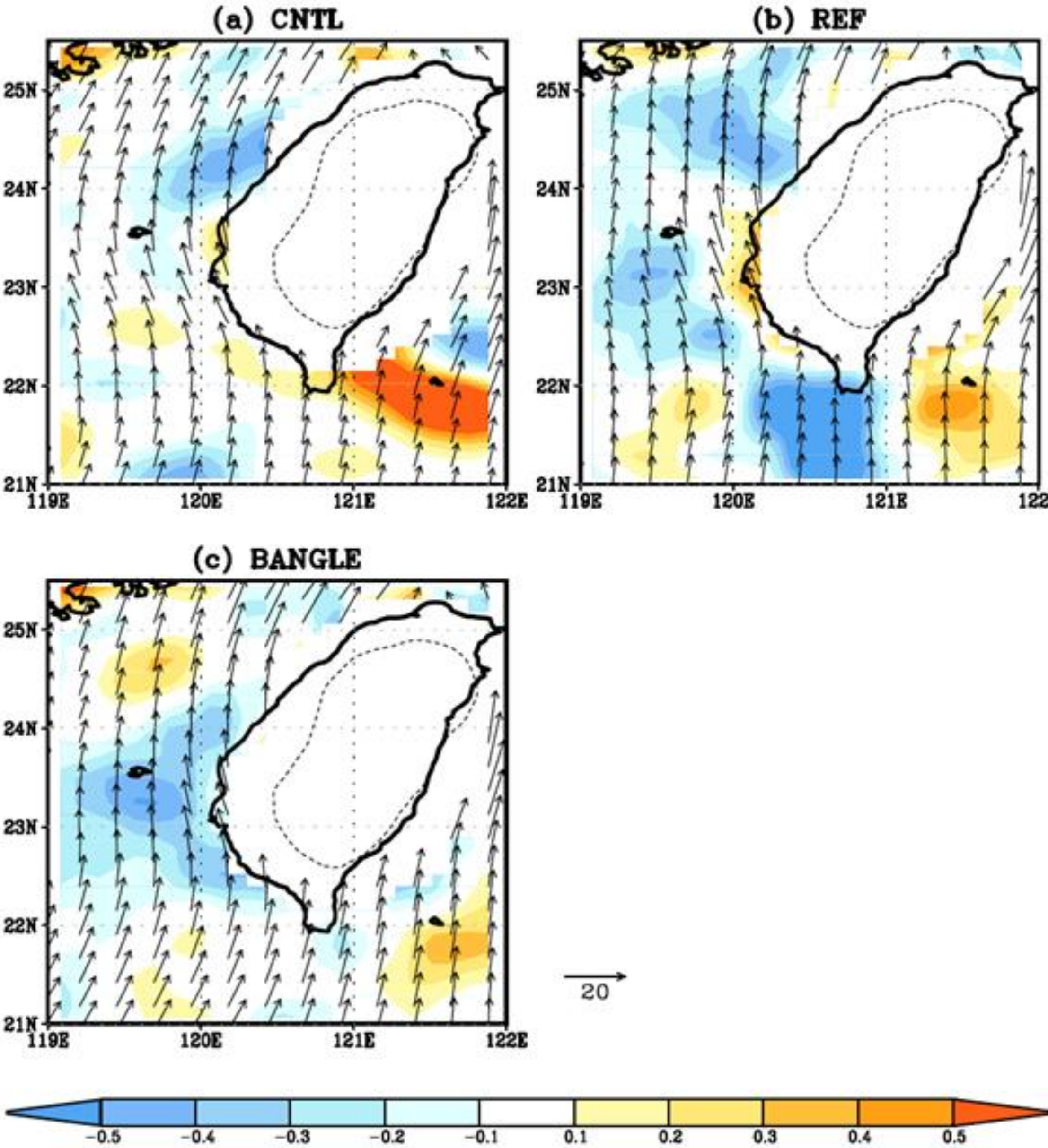

Figure 14. 950-hPa wind vectors (m/s) and convergence (color shading; $10^{-4}s^{-1}$) of the (a) CNTL, (b) REF and (c) BANGLE analyses at 1200 UTC 15 June. The dashed line denotes the 500 m terrain height.

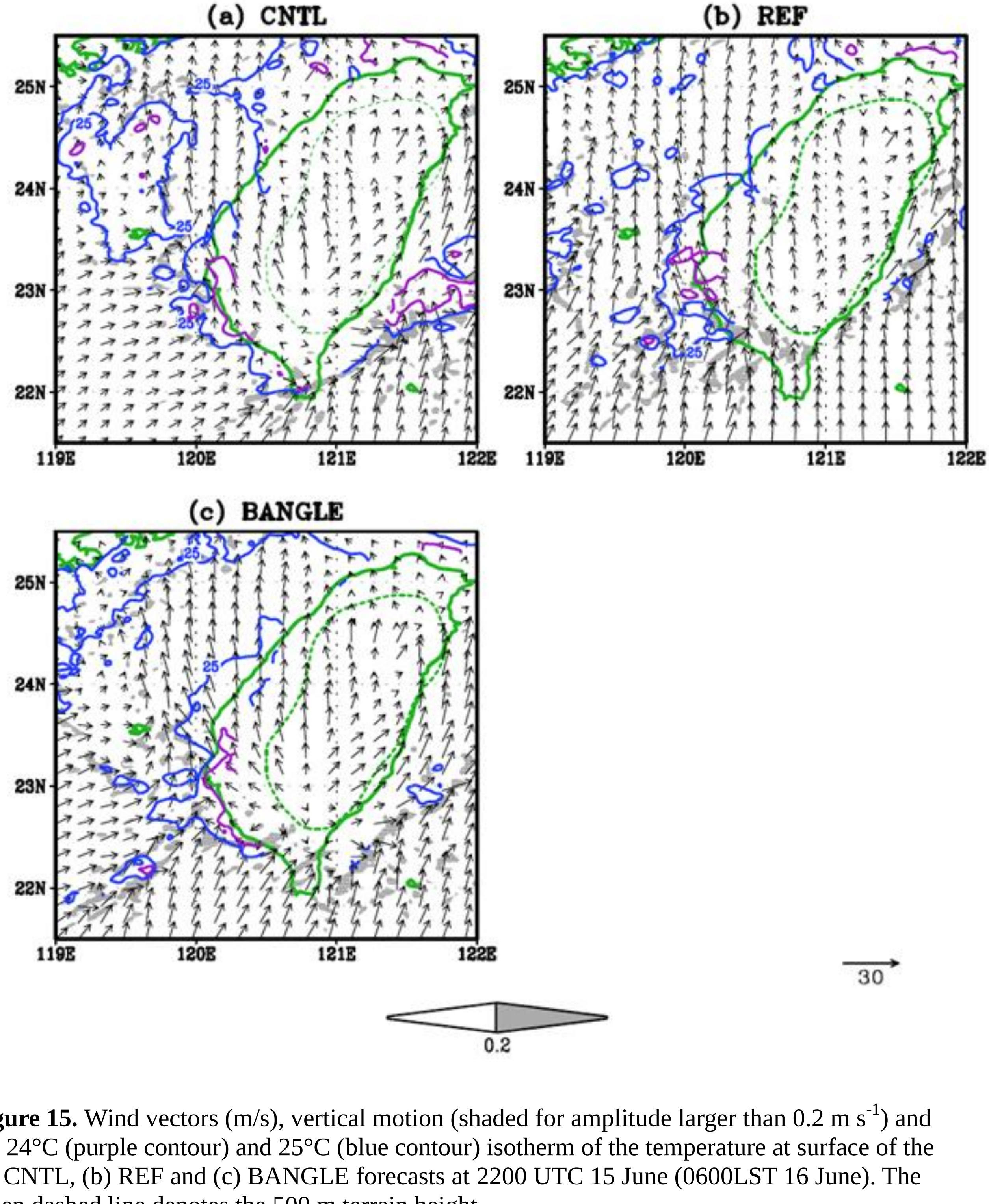

Figure 15. Wind vectors (m/s), vertical motion (shaded for amplitude larger than 0.2 m s^{-1}) and the 24°C (purple contour) and 25°C (blue contour) isotherm of the temperature at surface of the (a) CNTL, (b) REF and (c) BANGLE forecasts at 2200 UTC 15 June (0600LST 16 June). The green dashed line denotes the 500 m terrain height.

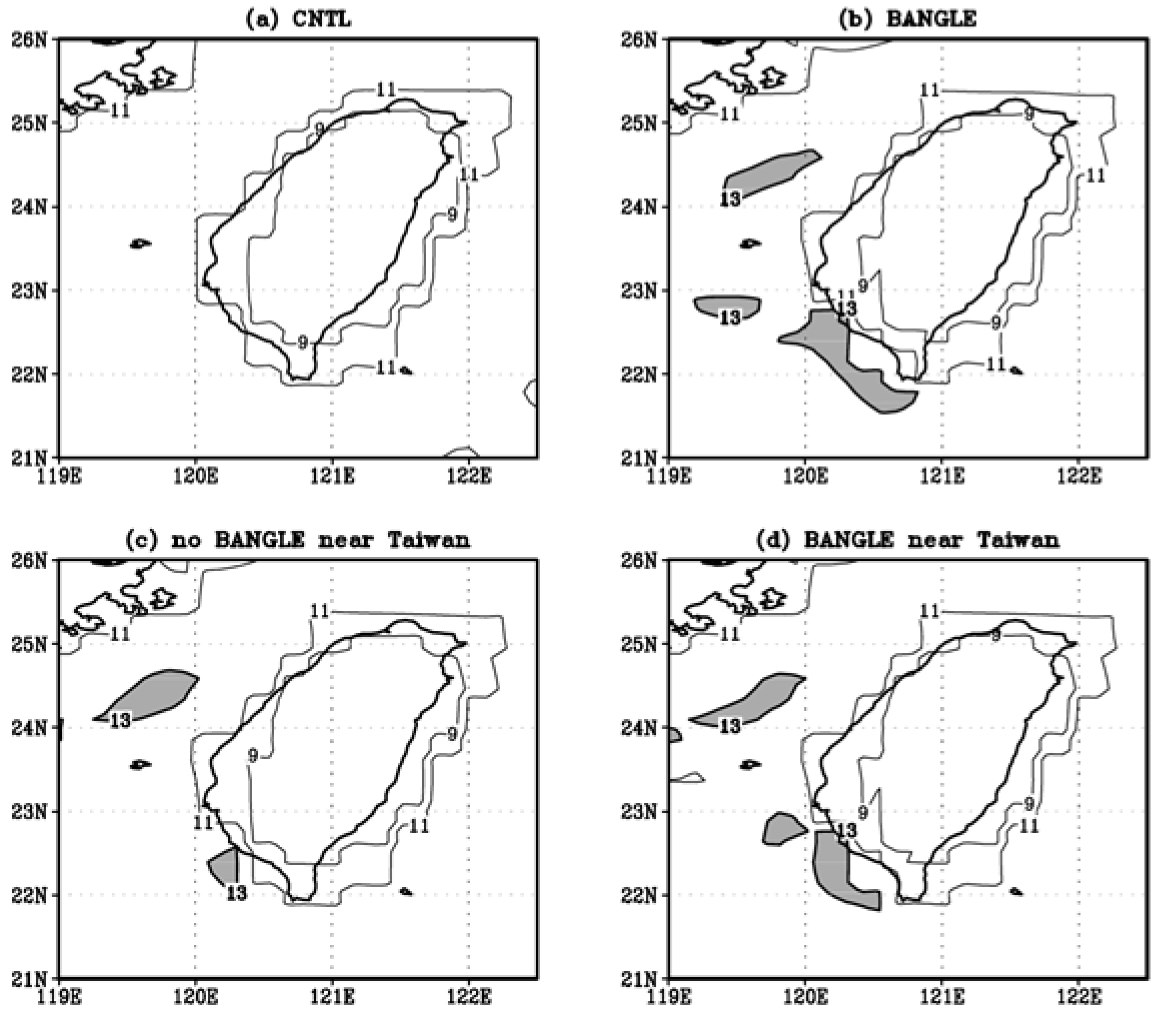

Figure 16. Total water vapor mixing ratio (g kg^{-1}) below the 500-hPa level from (a) CNTL, (b) BANGLE, (c) BANGLE_noTW and (d) BANGLE_TW analyses at 1800 UTC 15 June. Gray shading denotes the value larger than 13 g/Kg.

(a) NoBANGLE **(b) BANGLE-A**

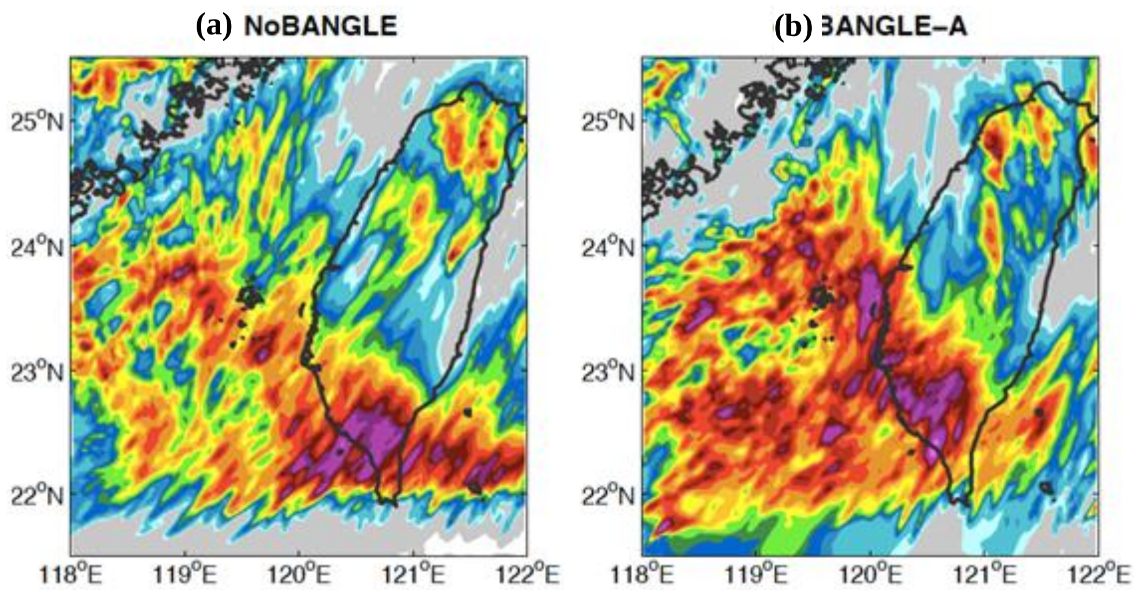

Figure 17. Same as Fig. 12 except the forecasts are initialized from (a) NoBANGLE and (b) BANGLE-A analyses at 1200 UTC 15 June.

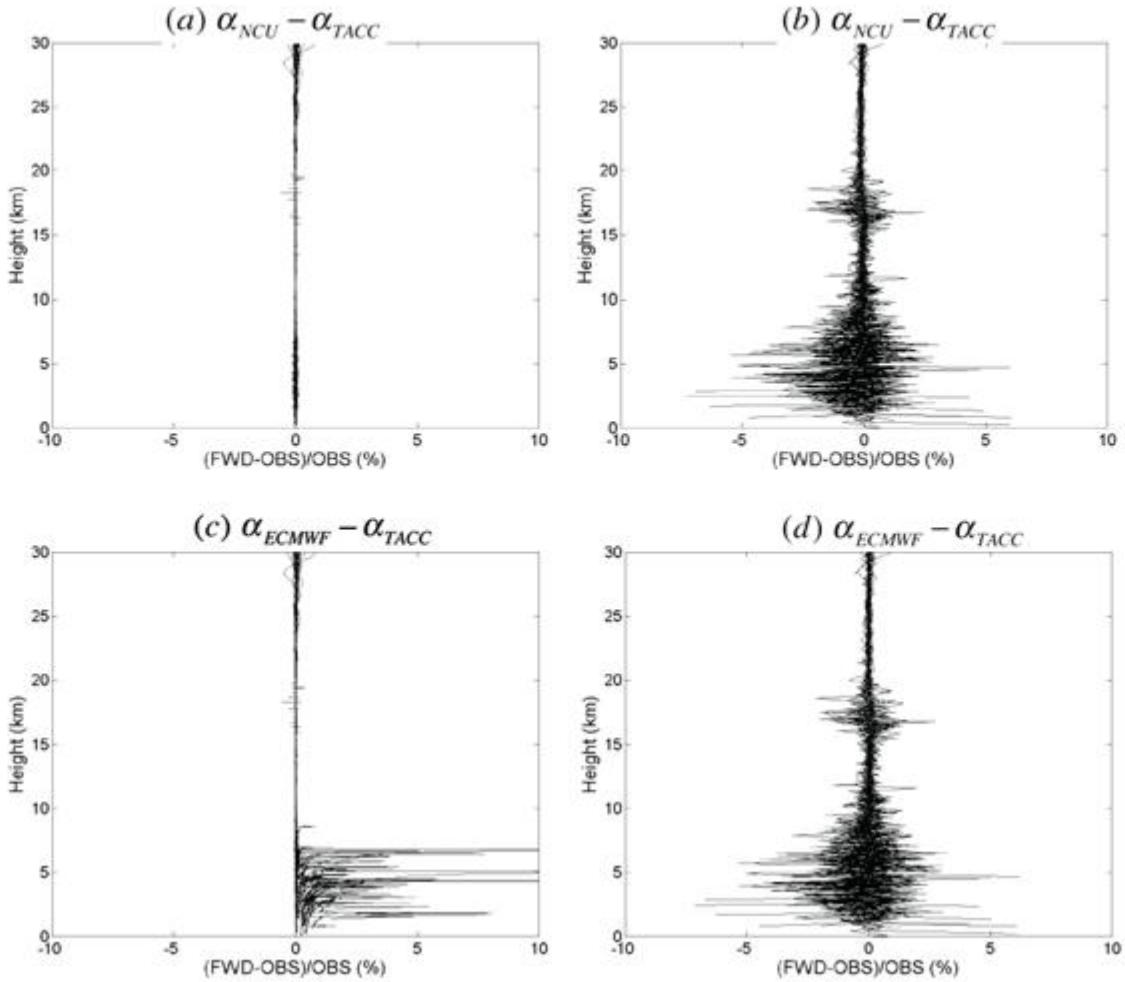

Figure A (a) Relative difference of the simulated bending computed with the NCU local operator and the TACC atmprf data. (b) same as (a) but compared with the TACC brfprf data. (c) Same as (a) but the simulated bending angle is computed with the ECMWF-ROPP local operator. (d) same as (c) but compared with the TACC brfprf data.

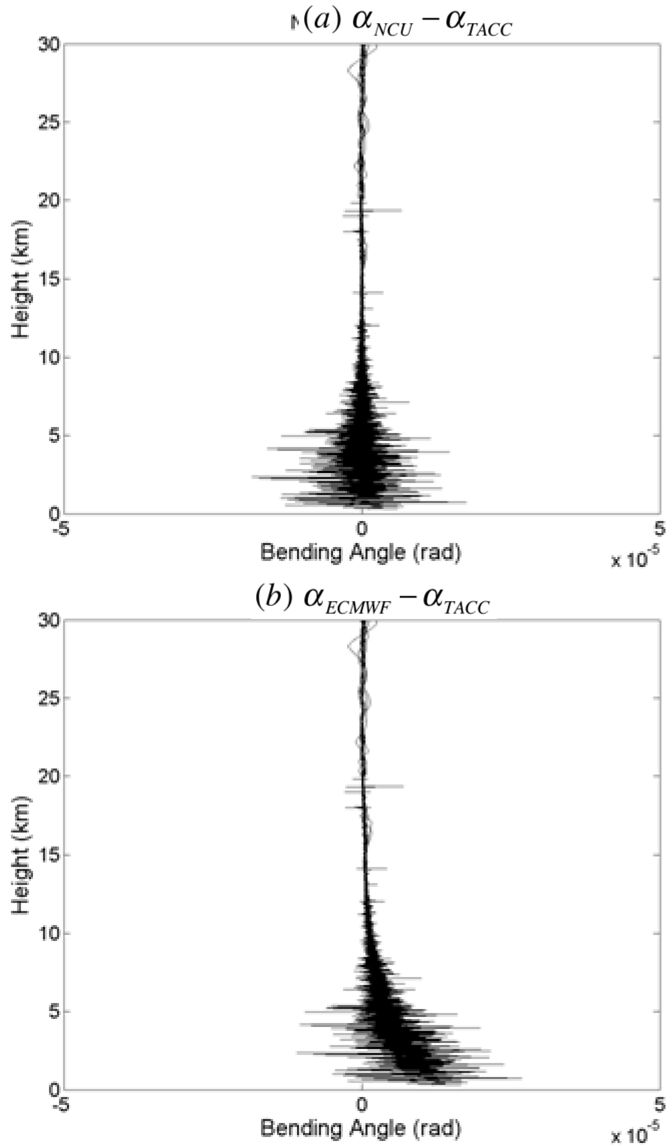

Figure B (a) Difference of the simulated bending angle computed with the NCU local operator and the TACC atmprf observations. The comparison is made only when the simulated refractivity fulfills the assumption of exponential variation in vertical. (b) same as (a), but the simulated value is computed with the ECMWF-ROPP operator.

Journal of Hydrology xxx (2012) xxx–xxx

Contents lists available at SciVerse ScienceDirect

Journal of Hydrology

journal homepage: www.elsevier.com/locate/jhydrol

Structure of precipitating systems over Taiwan's complex terrain during Typhoon Morakot (2009) as revealed by weather radar and rain gauge observations

Yu-Chieng Liou *, Tai-Chi Chen Wang, Yi-Chun Tsai, Yu-Shuang Tang, Pay-Liam Lin, Yung-An Lee

Department of Atmospheric Sciences, National Central University, 320 Jhongli City, Taiwan

ARTICLE INFO

Article history:
Available online xxxx

Keywords:
Typhoon Morakot
Doppler weather radar
Topographic effect
Quantitative precipitation estimation (QPE)

SUMMARY

This study documents from an observational perspective the structure of precipitation systems over the complex topography of Taiwan as Typhoon Morakot (2009) impinged on the island on 8 August 2009. An advanced multiple-Doppler radar synthesis technique particularly designed for dealing with non-flat surfaces is applied to analyze the three-dimensional wind fields over the ocean and terrain. In the northern and southern portion of the analysis domain where the mountain slope is relatively gentle and steep, respectively, the radar reflectivity measurements indicate that the precipitation systems exhibit very distinct features, namely, horizontal translation in the north and abrupt intensification in the south. While still far from the southern mountainous region, a north–south oscillation of an east–west-oriented band of strong radar reflectivity (>40 dBZ) with a horizontal span of 20 km is observed. Along the mountain slopes, the band of strong radar reflectivity has a much wider north–south extent. Both the radar and rain gauge observations show that the major precipitation is primarily confined to the windward side of the mountains. An analysis of the saturated Brunt–Väisälä frequency reveals that the upstream atmosphere is statically unstable, which implies that the lifting of the incoming convective cells by the topography will easily trigger precipitation. Thus, most of the moisture will be consumed before the air reaches the leeward side of the mountains. The long duration and the wide range of heavy precipitation in the mountainous regions resulted in a record-breaking average (over the gauges) rainfall amount of 2000 mm over 4 days.

The prevailing winds approaching the mountains are from the west. The cross-barrier wind speed has a maximum ($\sim$40 m s^{-1}) above the mountain crest that can be reasonably explained by a simplified shallow water model.

The capability of applying the weather radar to provide a reliable quantitative estimate of the rainfall over a large area with high temporal and spatial resolution is demonstrated using dual-polarimetric radar data. The potential applications of the knowledge of the wind and precipitation characteristics in hydrology and other fields are addressed in this manuscript.

1. Introduction

Tropical cyclones (TCs) are the most destructive weather systems threatening Taiwan. Every year, approximately 30 typhoons develop in the western North Pacific. On average, three to four TCs make landfall or affect Taiwan annually. Strong winds and heavy precipitation associated with these TCs often result in severe casualties and property loss.

The topography of Taiwan is dominated by the north–south-oriented Central Mountain Range (CMR, see Fig. 2), which has peaks reaching nearly 4000 m high and covers a distance of about 300 km from north to south. The CMR can significantly alter the structure and motion of a typhoon that crosses the island (Yang et al., 2008). The investigation of the interaction between the typhoon circulation and CMR is thus an important area of research. Chang et al. (1993) analyzed a 20-year data set (including 82 typhoons) recorded by 22 surface stations to describe the effects of the Taiwan topography on the surface structure of these typhoons. Yeh and Elsberry (1993a, 1993b), Lin et al. (2002, 2005), Jian and Wu (2008) and Huang et al. (2010) utilized numerical simulations to examine the rainfall distribution, track continuity, and track deflection induced by orographic effects as a typhoon passes over the CMR. Lee et al. (2006) examined observations from conventional surface stations and automatic rain gauges to study the correlation between the amount of rainfall and the elevation. Yang et al. (2008) applied a very high resolution (2 km) model to investigate the topographic effects on the typhoon track and intensity, and the rainfall pattern and amounts. Wu et al. (2002) and Chien et al. (2008) utilized the MM5 (Fifth-Generation NCAR/Penn State

* Corresponding author. Tel.: +886 3 4223287; fax: +886 3 4256841.
E-mail address: tyliou@atm.ncu.edu.tw (Y.-C. Liou).

0022-1694/$ - see front matter © 2012 Elsevier B.V. All rights reserved.
http://dx.doi.org/10.1016/j.jhydrol.2012.09.004

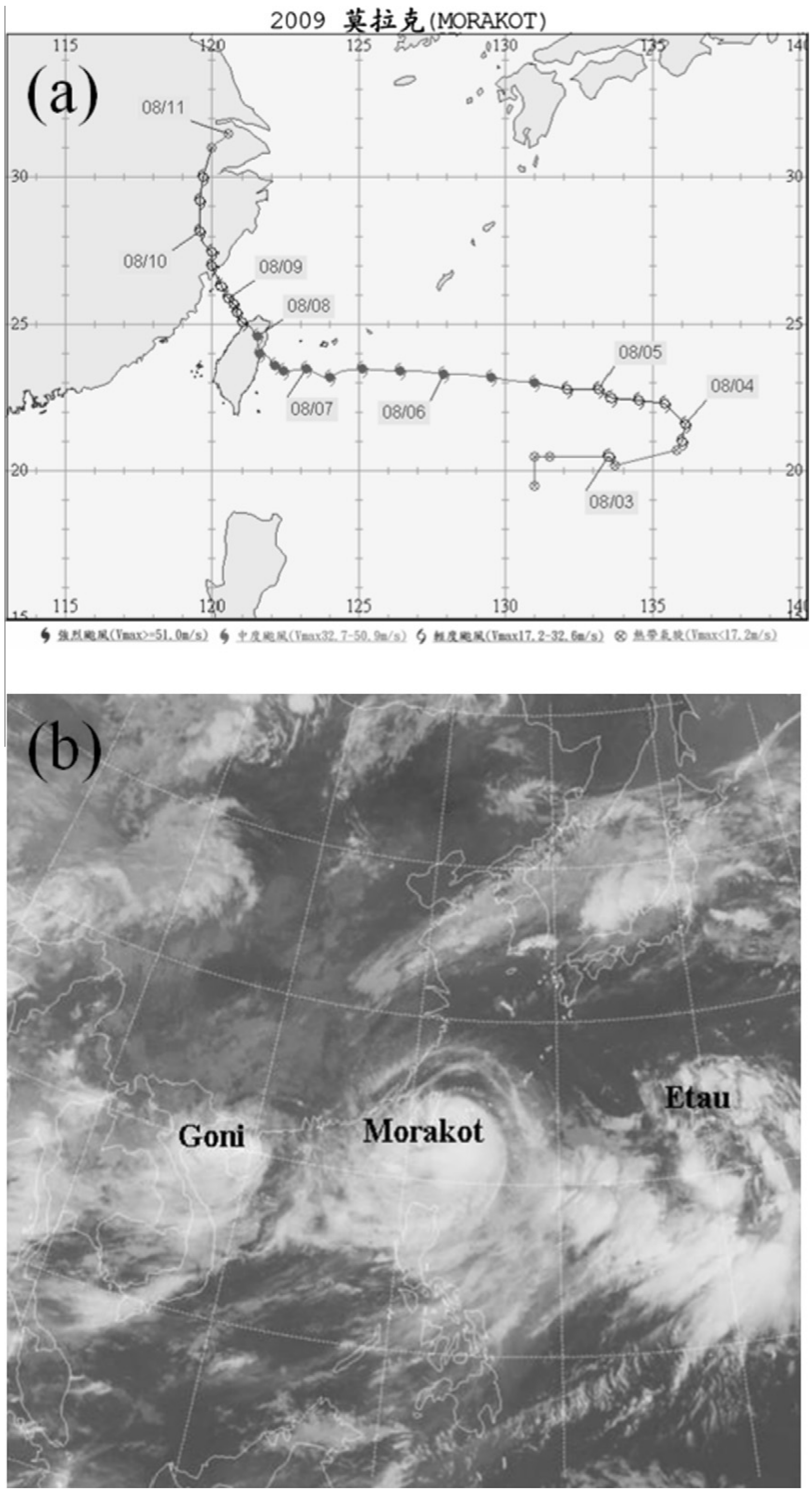

Fig. 1. (a) The track of Typhoon Morakot (2009) and (b) the satellite images of Tropical Storm Goni, Morakot and pre-typhoon Etau at 0030 UTC 07 August 2009.

Mesoscale Model) to assess the impact of the terrain on the occurrence of extreme typhoon rainfall events in Taiwan.

Weather radars around the globe have been utilized to study the interactions between typhoons/hurricanes and the topography. Willoughby and Black (1996), Geerts et al. (2000), Shun et al. (2003), and Nishiwaki et al. (2010) used ground-based and/or airborne Doppler radars to illustrate the characteristics of hurricanes (typhoons) in South Florida, Dominican Republic, Hong Kong, and Japan. Taiwan has an island-wide network of nine ground-based weather radars. New wind analysis techniques and the data collected by these radars have been widely used to diagnose the behavior and structure of typhoons affecting Taiwan (e.g., Wang and Tseng, 1999; Lee et al., 2000; Hor et al., 2005; Liou et al., 2006). Yu and Cheng (2008) documented the orographic precipita-

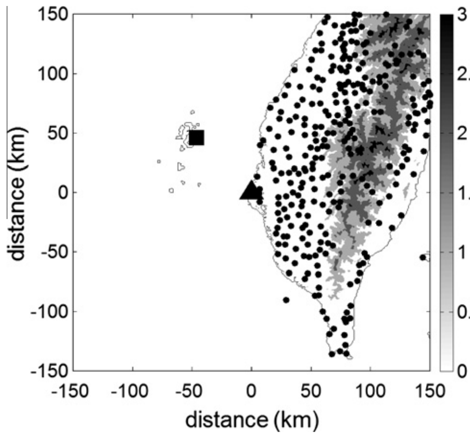

Fig. 2. Locations of surface rain gauges (solid circles) and the RCMK and RCCG weather radars (square and triangle, respectively). The height of the terrain is denoted by shading with an interval of 500 m.

tion characteristics associated with typhoon Xangsane (2000) using two ground-based Doppler radars in northern Taiwan. Their study described in detail the differences in the precipitation distributions near a three-dimensional mountain and a relatively lower, narrower two-dimensional barrier.

Typhoon Morakot (2009) is considered the most catastrophic meteorological event to strike Taiwan during the past five decades. The floods and mudslides triggered by its extreme torrential rainfall caused tremendous societal and economic impacts on this island. The purpose of this study is to document from an observational point of view the structure and variations of the precipitation systems within Typhoon Morakot over the complex topography when impinging on Taiwan on 8 August 2009. The possible applications of the information regarding wind and precipitation characteristics in hydrology and other fields are also addressed in this manuscript.

In the next section, a brief overview of the large-scale synoptic weather conditions associated with Typhoon Morakot is provided. The Doppler radar observations and the technique used in this study for analyzing the three-dimensional wind fields are described in Section 3. In Section 4, the structure and evolution of the precipitation systems over southern Taiwan are described based on the radar reflectivity. In Section 5, the rainfall distributions at different altitudes in the windward and leeward sides of the mountain are investigated using surface rain gauge measurements. Discussion of the kinematic structures of the typhoon rainbands is given in Section 6. The capability of using the advanced dual-polarimetric weather radar data to conduct quantitative precipitation estimation (QPE) is discussed in Section 7. Some conclusions and suggestions for future work are presented in Section 8.

2. Large-scale environmental conditions and a brief overview of Typhoon Morakot

Typhoon Morakot formed at 00 UTC 3 August over the western North Pacific (WNP) ocean near 20.0°N, 133.6°E and then moved steadily westward to make landfall on Taiwan at 16 UTC 7 August (Fig. 1a). At the same time, Tropical Storm Goni and a tropical depression that later intensified into Typhoon Etau were located to the southwest and east of Morakot, respectively. These three convective systems were within a much broader monsoon gyre that had a longitudinal span of about 5000 km (Fig. 1b). The southwest monsoon flow that expanded from the Bay of Bengal to the Philippine Sea transported warm and humid air to Taiwan and vicinity, which provided favorable environmental conditions for the maintenance and development of convection.

As Morakot approached Taiwan, its translation speed decreased substantially from 20 km h^{-1} to 10 km h^{-1}, and then further decreased to 5 km h^{-1} after landfall (Chien and Kuo, 2011). This slow movement of Morakot over Taiwan contributed a prolonged duration of rainfall. The maximum accumulated 4-day precipitation from 6 August to 10 August was a record-breaking 3000 mm at the Alishan station in the southern CMR. The rain gauge observations revealed that the heaviest rainfall occurred on 8 August, which is the target day for analysis in this study.

3. Observational data and methodology for wind field analysis

The locations of 146 surface rain gauges and two weather radars utilized in this study are shown in Fig. 2. Surface precipitation observations are available from 16 UTC 5 August to 16 UTC 10 August. The weather radar is a powerful instrument for monitoring severe weather since it provides information on the internal structures of the precipitating systems with high temporal (<10 min) and spatial (~1 km) resolution. Observations will be analyzed between 00 and 24 UTC 8 August from the RCCG and RCMK radars operated by the Central Weather Bureau (CWB) and Air Force of Taiwan, respectively. The RCCG is a S-band (10-cm wavelength) Doppler radar, while the RCMK is a C-band (5-cm wavelength) dual-polarimetric radar.

A Doppler radar detects the reflectivity and radial winds (V_r). The latter is the projected component of the complete three-dimensional wind field (u, v, w) along the radar beam, and can be expressed as follows:

$$V_r = \frac{x}{r}u - \frac{y}{r}v - \frac{z}{r}(w + W_T), \tag{1a}$$

$$r = \sqrt{x^2 + y^2 + z^2}, \tag{1b}$$

where r is the distance from the radar to the observed point (x,y,z), and W_T is the terminal velocity of the hydrometeors, which can be estimated from the radar reflectivity (Sun and Crook, 1997). In contrast, the dual-polarimetric radar transmits radio wave pulses with both horizontal and vertical orientations, which has been proved to be extremely useful in improving radar data quality control, precipitation classification, and rainfall estimation. The composite radar

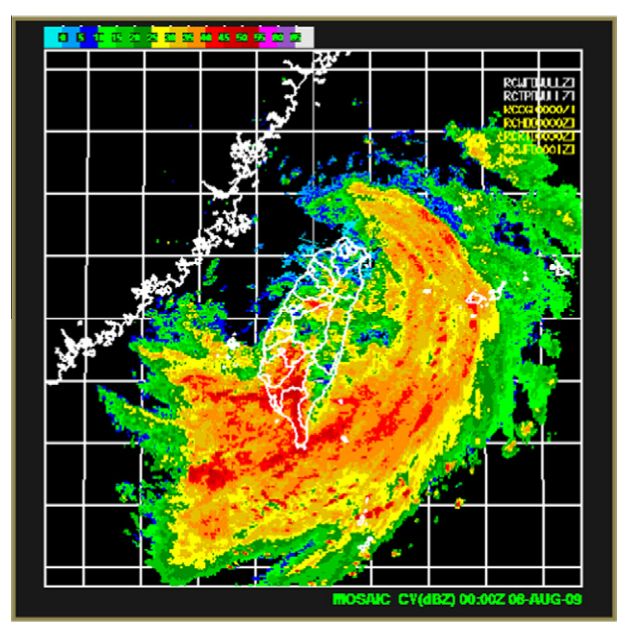

Fig. 3. Composite radar reflectivity (dBZ) of Typhoon Morakot at 00 UTC 8 August 2009.

reflectivity at 00 UTC 8 August (Fig. 3) indicates a highly asymmetric pattern of convection in Morakot, with the most intense convection concentrated in southern Taiwan. The center of the typhoon is nearly unidentifiable. The rainbands in southern Taiwan represented by the nearly east–west-oriented radar reflectivity will be studied in detail in the next section.

Using the radial winds detected by two or more radars, a multiple-Doppler radar wind synthesis can provide a complete three-dimensional wind field (u, v, w) based on an algebraic approach, a variational analysis, or a combination of the two (e.g., Armijo, 1969; Miller and Strauch, 1974; Doviak et al., 1976; Ray et al., 1978; Chong and Testud, 1983; Protat and Zawadzki, 1999; Chong and Bousquet, 2001; Gao et al., 2004). In this study, a newly designed algorithm developed by Liou and Chang (2009) and Liou et al. (2012) is employed for the first time to analyze the internal flow structure within the Typhoon Morakot precipitation systems.

In this new method, the solution of the three-dimensional wind is obtained by variationally adjusting the winds to satisfy a series of constraints in weak formats. Among them, the primary ones are the multiple-radar radial velocity observations, anelastic continuity equation, vertical vorticity equation, background wind field, top and bottom boundary conditions for the winds, and spatial smoothness terms. Liou and Chang (2009) demonstrated that this new method was capable of recovering the wind field along and near the radar baseline (an imaginary line connecting two radars), and performing vorticity budget analysis. Liou et al. (2012) further extended this algorithm to include the topographic effect by applying the immersed boundary method (Tseng and Ferziger, 2003), thus a wind synthesis immediately above the rugged mountain slopes can be obtained. These are the important advantages of this method over the traditional approaches cited above. Experiments using numerical and observational data in Liou and Chang (2009) and Liou et al. (2012) indicated that this method was able to retrieve accurate horizontal winds, and rather reasonable vertical velocity structure. However, it tends to underestimate the maximum vertical wind speed. This can be attributed to the relatively smaller geometric projection of w wind component to the Doppler radial wind observations (see Eq. (1a)), and is also a common problem to other dual/multiple Doppler radar synthesis algorithms.

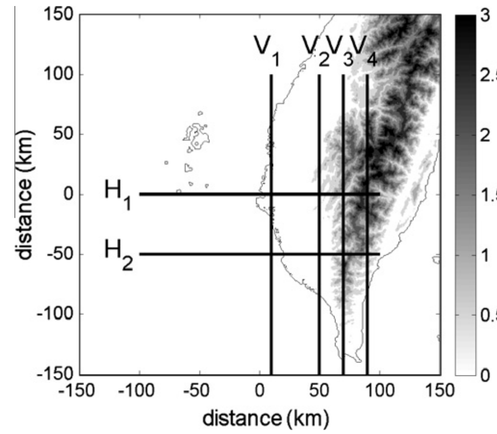

Fig. 4. Topography of Taiwan represented in gray scale with an interval of 500 m. Two east–west (H_1, H_2) and four north–south ($V_1 - V_4$) oriented cross-sections are selected for further analysis. The horizontal and vertical axes denote the distances (km) from the RCCG.

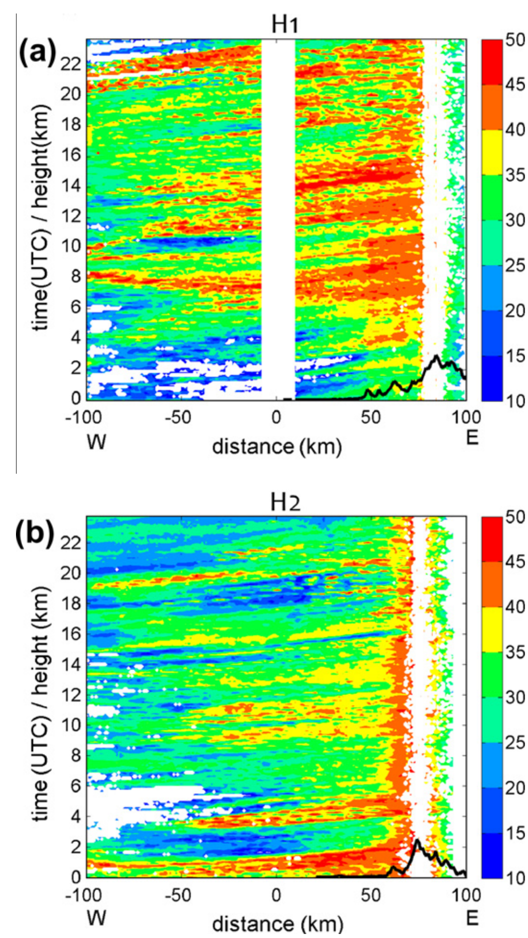

Fig. 5. Hovmöller diagram of radar reflectivity (5 dBZ interval) along east–west cross-sections (a) H_1, and (b) H_2. The horizontal coordinate is the distance along the east–west direction from RCCG. The vertical axis indicates UTC time on 8 August 2009. The solid curve at the lower-right corner depicts the topography. The characters E and W represent east and west directions, respectively.

4. Topographic effects on morakot precipitation systems revealed by radar reflectivity

Two east–west-oriented (H_1 and H_2 in Fig. 4) and four north–south-oriented (V_1–V_4 in Fig. 4) cross-sections are examined to display the vertical structure of the typhoon rainbands represented by radar reflectivity. The H_1 and H_2 represent two cross-sections extending from the ocean toward the land. The mountain crossed by H_1 (H_2) has a relatively gentle (steep) slope. Cross-sections V_1–V_4 are along vertical planes passing through the coastal plain, foothills, mountain slope, and mountain peak, respectively. To avoid using the data contaminated by surrounding ground/sea clutters, radar data within a horizontal distance of 5 km from the radar site are discarded. Furthermore, a criterion (radial wind $<2.0\ \mathrm{ms}^{-1}$ and reflectivity >45 dBZ) is given to filter out the data affected by mountain blockage. The removal of the radar data through the above procedures would generate data void regions, which are illustrated by the white stripes in the following Figs. 5 and 6.

The radar reflectivity at $Z = 3$ km along cross-sections H_1 and H_2 are shown in Fig. 5a and b. In these Hovmöller diagrams, the vertical axis denotes the time so that the temporal variation of the radar reflectivity at a certain location is described. Along cross-section H_1, most of the strong convection can be traced back to the ocean. In a few cases, the convection is strengthened above the gentle slope. At 08 UTC, the convection at approximately $X = -40$ km tends to move toward the ocean, which suggests the possibility of the formation of new convective cells on the upstream side that then merge with the old decaying cells. This process is referred to as back-building mechanism (Bluestein and Jain,

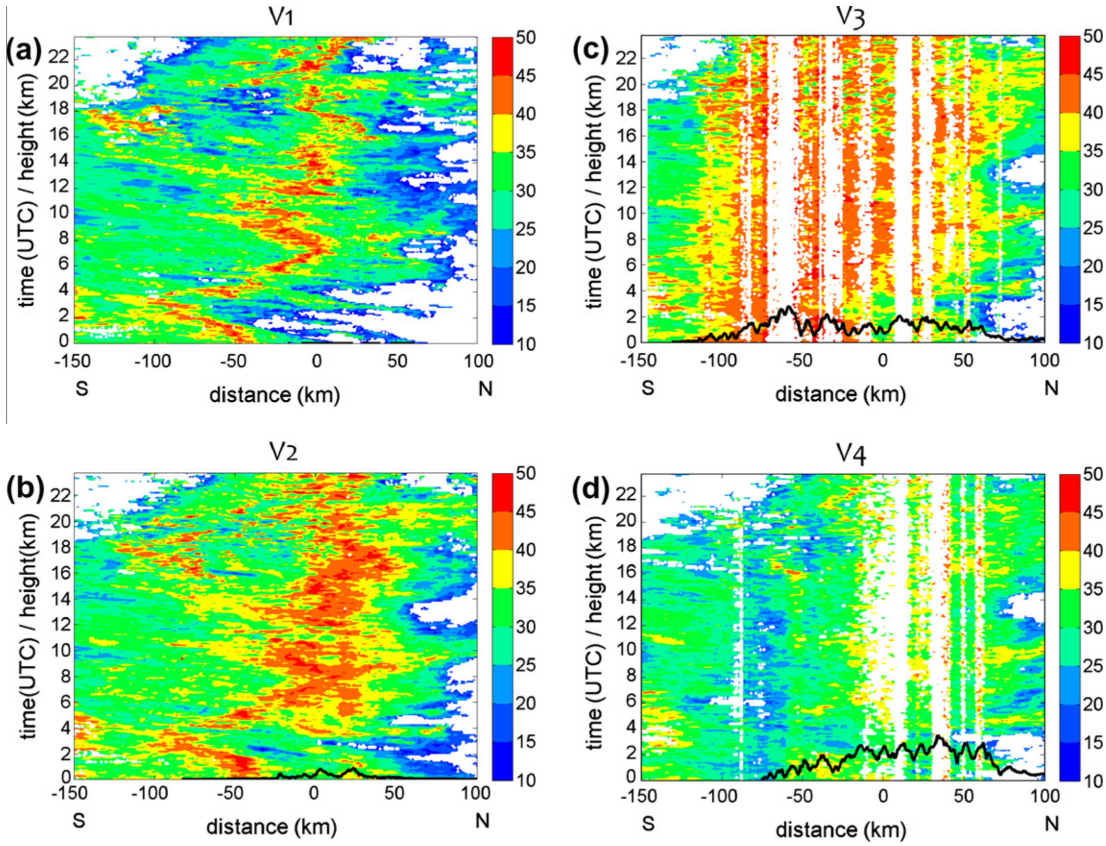

Fig. 6. Same as in Fig. 5, except the Hovmöller diagrams for north–south oriented cross-sections: (a) V_1; (b) V_2; (c) V_3, and (d) V_4. The horizontal coordinate is the distance along the north–south direction from the RCCG. The characters N and S represent north and south directions, respectively.

1985). Along H_2, the convection tends to intensify immediately in front of the steep mountains, especially after 04 UTC. In both H_1 and H_2, the regions of strong radar reflectivity seldom extend to the leeward side of the mountains, which is a clear indication of the impact of the topographic effects.

Hovmöller diagrams of the radar reflectivity at $Z = 3$ km are shown in Fig. 6 along four north–south cross-sections V_1–V_4. Where V_1 cross-section crosses the coastal plain area, the radar reflectivity has a prominent north–south-oriented oscillation from 00 to 12 UTC. This rainband oscillates over a distance of 100 km, with a period of approximately 8 h. This oscillation is proposed to be due to interaction between the northerly flow in the outer region of the typhoon and variations in the southerly flow. Since the Doppler radial wind is a measurement of the wind component parallel to the radar beam, a negative (positive) value indicates that the wind has a component toward (away from) the radar. An average of the radial wind within a sector south of the RCCG radar site with a radius of 60 km and an azimuth angle ranging from 166° to 194° is a good indicator of the strength of the southerly flow (Fig. 7). Note that in this plot positive (negative) velocity implies northerly (southerly) wind. Comparing Figs. 6a and 7, when the radar reflectivity band moves southward from 00 to 03 UTC, the northerly wind increases from 0 m s^{-1} to 6 m s^{-1} in a similar time interval. The magnitude of the northerly wind decreases gradually after 03 UTC, and the wind at 60 km radius from RCCG becomes southerly after 05 UTC. The increase in the southerly flow from 05 UTC to 12 UTC corresponds to the northward oscillation of the reflectivity band (Fig. 6a). The oscillatory movement of the rainband along V_1 was expected to reduce the accumulated rainfall over the ocean and near the coastal region. This feature was also verified by the surface rain gauge observations shown in the next section. When the southerly flow fluctuates at around 8 m s^{-1} from 12 to 24 UTC, the reflectivity band does become more stationary during this period of time.

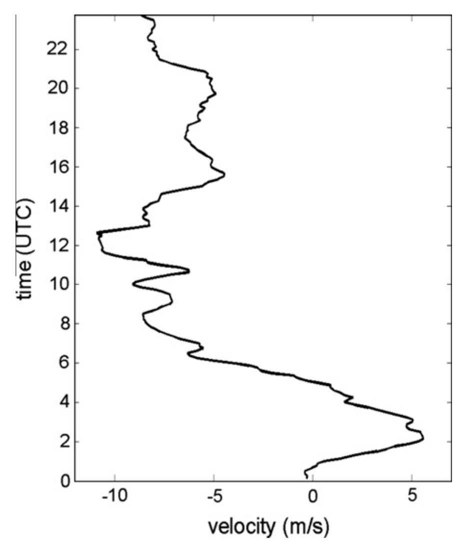

Fig. 7. Hovmöller diagram of the RCCG radial velocity averaged within a sector facing south. The positive (negative) value on the horizontal axis indicates a northerly (southerly) flow in m s^{-1}.

At V_2 (Fig. 6b), the radar reflectivity has a similar oscillatory movement as in V_1 from 00 to 10 UTC at the southern side of the mountains. After 10 UTC, the main band of strong radar reflectivity moves northward, spreads to a wider region, and remains almost stationary over the foothills. The north–south extent of the strong radar reflectivity (>40 dBZ) band increases from about 10 km at V_1 to 50 km at V_2. Along V_3, an even broader distribution of the strong radar reflectivity suggests the spread of heavy precipitation over a larger area along the mountain slopes, which persists for almost the entire 24 h. This prolonged duration resulted in record-breaking rainfall in this area. Finally, along where the V_4 cross-section falls above the mountain peaks, the intensity of the radar reflectivity decreases dramatically. This difference between V_3 and V_4 means that when the air flow, presumably unstable and very moist, ascends along the mountain slopes, most of the raindrops forming during this stage fall on the windward side before reaching the crest. The process that induces this type of orographic precipitation is categorized as the upslope-triggering mechanism (Houze, 1993).

5. Topographic effects on Morakot precipitation systems revealed by surface rainfall measurements

In this section, the topographic effects are examined utilizing surface rainfall measurements. Hourly rainfall intensity and accumulated amount recorded by rain gauges on the windward and leeward sides of the southern CMR are averaged (over the number of gauges) at different altitudes (0.0–0.2 km, 0.2–0.5 km, 0.5–1.0 km and >1.0 km MSL) in Figs. 8 and 9, respectively. On the windward side of the CMR (Fig. 8), the precipitation began at approximately 12 UTC 6 August, while on the leeward side (Fig. 9), the major rainfall did not occur until 00 UTC 7 August. On the windward side, relatively small precipitation is observed over the coastal plain area where the height of the terrain is below 0.2 km, and the accumulated rainfall in this region starts to level off after 06 UTC 9 August (Fig. 8a). However, the rainfall increases substantially close to the mountainous region. The strongest average rainfall intensity is about 63 mm h^{-1} and occurs at 0.2–0.5 km. The intensity decreases slightly to 50 mm h^{-1} at higher altitudes. The 4-day (12 UTC 6 August to 12 UTC 10 August) accumulation of precipitation reached 2000 mm at altitude >1.0 km. A significant amount of rainfall was recorded after 9 August (Fig. 8c, e, and g).

In contrast, a dramatic decrease in both the intensity and cumulative rainfall amount is observed on the leeward side of the CMR (Fig. 9). The accumulated precipitation observed by gauges located at 0.0–0.2 km, 0.2–0.5 km and 0.5–1.0 km MSL varies around 500 mm, but the differences are not very significant. The gauges at altitudes >1.0 km detect the heaviest 4-day accumulated rainfall and hourly rain rate on the lee side of CMR, but these values are only about 750 mm and 40 mm h^{-1} (Fig. 9g), respectively. Farther eastward over the mountain slopes near the east coast, the rainfall intensity decreases to less than 20 mm h^{-1} (Fig. 9c and e). The rain in this leeward area nearly stopped after 06 UTC 9 August. The accumulated 4-day precipitation on the leeward side is only about 30% of that on the windward side. Obviously, the CMR has a profound influence on the spatial distribution of the rainfall. These features revealed by the surface rainfall measurements are in good agreement with the radar reflectivity observations.

Lee et al. (2006) analyzed the data from conventional surface stations and automatic rain gauges for 58 typhoons affecting Taiwan during 1989–2001. They also found that the rainfall amount increased considerably with the station's elevation. However, it is worthwhile to note that although the increase of the rainfall with altitude appeared to be a frequently seen feature, yet it was not always the case. For example, using observational data and numerical model simulations, Chiao and Lin (2003) and Chen et al. (2007) all reported that the locations with maximum rainfall during the passage of a typhoon could be along the coastal region of Taiwan. Xu et al. (2012) presented that in a heavy precipitation event the rainfall was confined only over the ocean and southwestern coast of Taiwan during a period of 16 h, and never reached to the mountainous region.

6. Morakot's flow fields over complex terrain

The investigations by Westrick and Mass (2001), Ibbitt et al. (2001), Jasper et al. (2002) and Li et al. (2005) reveal promising results of applying meso-scale numerical weather prediction models for predicting regional rainfall characteristics, and the coupling of meteorological models with hydrological models for flood forecasting. Their studies show the crucial role played by a good model forecast of the precipitation. This leads to the requirement of a correct interpretation of the internal kinematic structure of the precipitation system, since accurate wind information will be needed for model initializing and/or data assimilation, if a reliable meteorological model forecast is desired. This is the main issue that is addressed in this section. In addition, the static stability of the atmosphere is an important parameter for understanding the sensitivity of the air to orographic lifting, which will also be evaluated in this section.

6.1. The wind field in a horizontal plane

The three-dimensional wind fields over the southern CMR are analyzed with the multiple-Doppler synthesis method developed by Liou and Chang (2009) and Liou et al. (2012) using the RCCG and RCMK observations at 1039 UTC and 1046 UTC. Several flow-related fields at $Z = 3.25$ km, at which the maximum vertical vorticity ($\partial v/\partial x - \partial u/\partial y$) occurs are depicted in Fig. 10. At this time, the typhoon center is well to the north outside the boundary of this diagram. The prevailing winds in this region are basically from due west, and impinge on the north–south-oriented CMR at a nearly perpendicular angle (Fig. 10a). The horizontal winds in the northern part of the analysis domain have a cyclonic curvature. An elongated band of strong winds that coincide closely with the large radar reflectivity (>40 dBZ) band extends from the ocean to the land (Fig. 10b). At this height, the maximum wind speed exceeds 38 m s^{-1} on the windward side of the terrain. Vertical velocities in the rainband indicate stronger (weaker) updrafts (downdrafts) with a highly variable spatial distribution, which implies vigorous convective motions inside the rainband. Comparing Fig. 10b and d, a strong positive vorticity is present near the foothills at $X \sim 50$ km, $Y \sim -10$ km, which is approximately at the radial-inward side of the wind speed maximum (see the thin horizontal line at $Y = -10$ km in Fig. 10b and d). This positive vorticity suggests an enhancement of the westerly winds within this rainband (Houze, 2010).

The vertical vorticity equation is:

$$\frac{\partial \xi}{\partial t} = -\left(u\frac{\partial \xi}{\partial x} + v\frac{\partial \xi}{\partial y} + w\frac{\partial \xi}{\partial z}\right) - (\xi + f)\left(\frac{\partial u}{\partial x} + \frac{\partial v}{\partial y}\right) - \left(\frac{\partial w}{\partial x}\frac{\partial v}{\partial z} - \frac{\partial w}{\partial y}\frac{\partial u}{\partial z}\right), \tag{2a}$$

$$\xi = \left(\frac{\partial v}{\partial x} - \frac{\partial u}{\partial y}\right), \tag{2b}$$

where ξ is the vertical vorticity, and f represents the Coriolis parameter. The first, second, and third terms on the right side of (2a) denote the advection, divergence, and tilting terms, respectively. Most of the temporal change in the vorticity can be attributed to the advection mechanism (Fig. 10e), which is not surprising in such a high wind speed region. As shown in Fig. 10f, the tilting term, which transfers the horizontal spin of the flow into the vertical, also has an important contribution to the rotational motion over the ocean and mountainous area. Over the coastal plain ($X = 0$–50 km, $Y = -50$ to

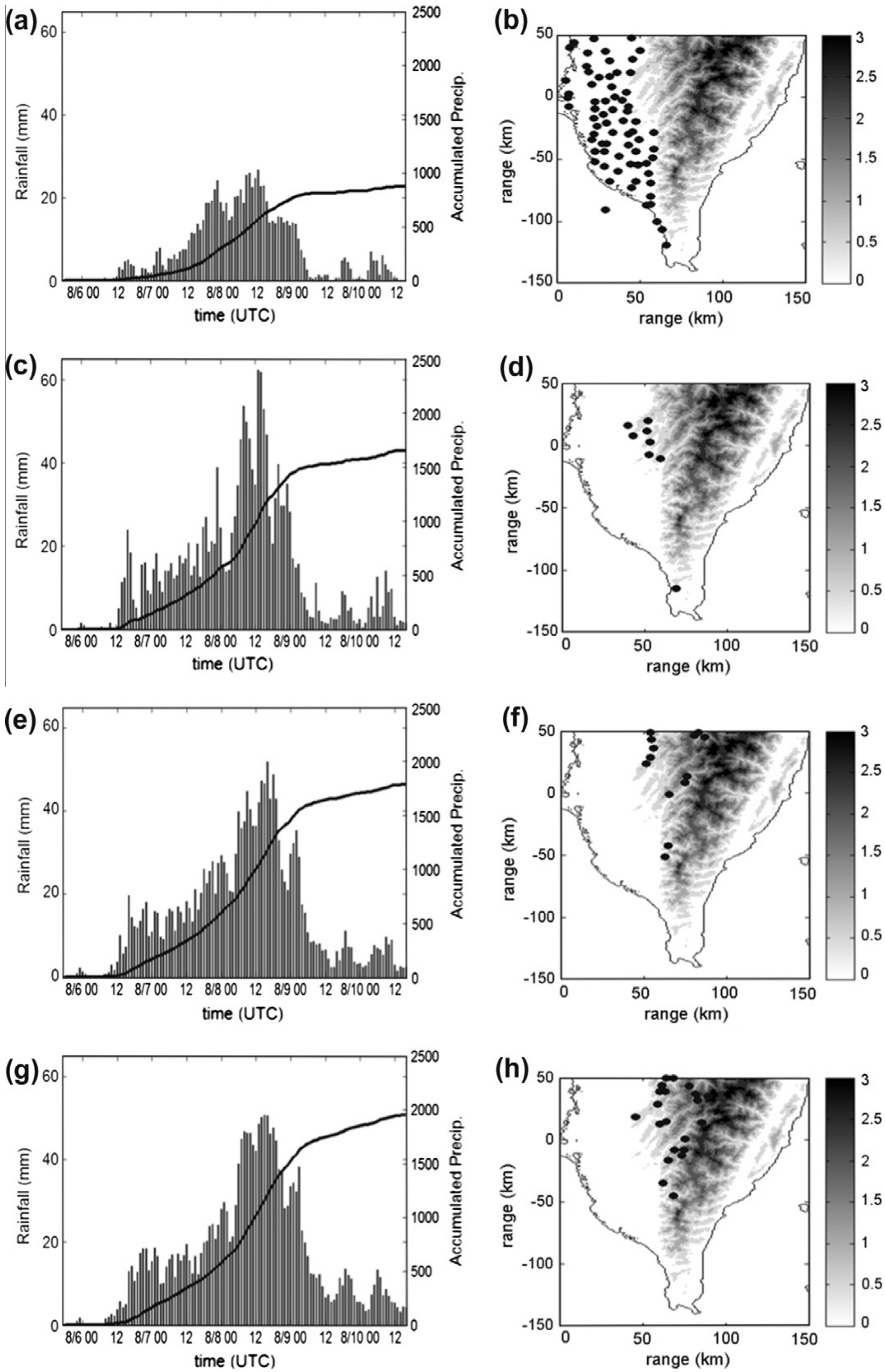

Fig. 8. Hourly rainfall rate histograms (mm h^{-1}; left axis) and accumulated precipitation (solid curve in mm; right axis) recorded by the gauges at different altitudes on the windward side of the CMR. The rain gauge data are grouped by altitudes: (a) and (b) 0.0–0.2 km; (c) and (d) 0.2–0.5 km; (e) and (f) 0.5–1.0 km, and (g) and (h) >1.0 km. The topography of Taiwan is illustrated in gray scale with an interval of 500 m.

0 km in Fig. 11f), the tilting term contribution at this height becomes less important. In this region, the horizontal gradients of w ($\partial w/\partial x$ and $\partial w/\partial y$; see w field in Fig. 11c) are relatively small. In addition, the convective mixing (to be discussed in the next section) likely diminishes the vertical wind shear ($\partial u/\partial z$ and $\partial v/\partial z$). As a result, the tilting term in (2a) may be reduced substantially in the coastal plain segment of the rainband. The contribution from the divergence term (not shown) is relatively insignificant at $Z = 3.5$ km.

Please cite this article in press as: Liou, Y.-C., et al. Structure of precipitating systems over Taiwan's complex terrain during Typhoon Morakot (2009) as revealed by weather radar and rain gauge observations. J. Hydrol. (2012), http://dx.doi.org/10.1016/j.jhydrol.2012.09.004

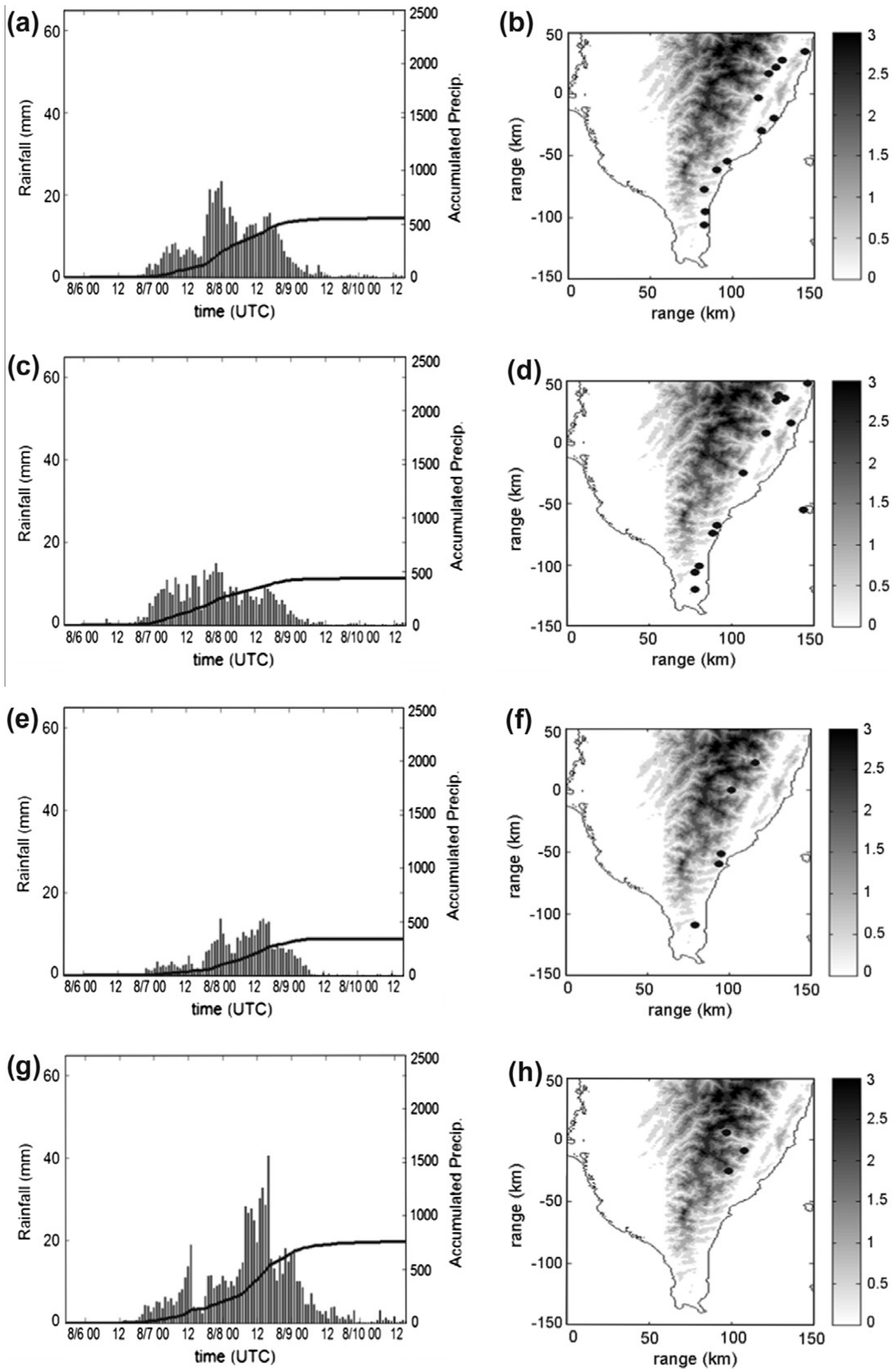

Fig. 9. As in Fig. 8, except for the rainfall measured at gauges on the leeward side of the CMR.

6.2. The wind field in a vertical plane

The wind field structure along a representative vertical cross-section passing through the CMR in southern Taiwan (Fig. 11) has several interesting features. As shown in Fig. 11a, the lower-tropospheric air ascends and flows over the mountain crest. The radar reflectivity begins to intensify, and increase to above 40 dBZ when reaching the first hill located at $X \sim 42$ km. The enhancement of the precipitation system on the windward side of the CMR is associated with vigorous up- and downdrafts (>4 m s^{-1}) in regions

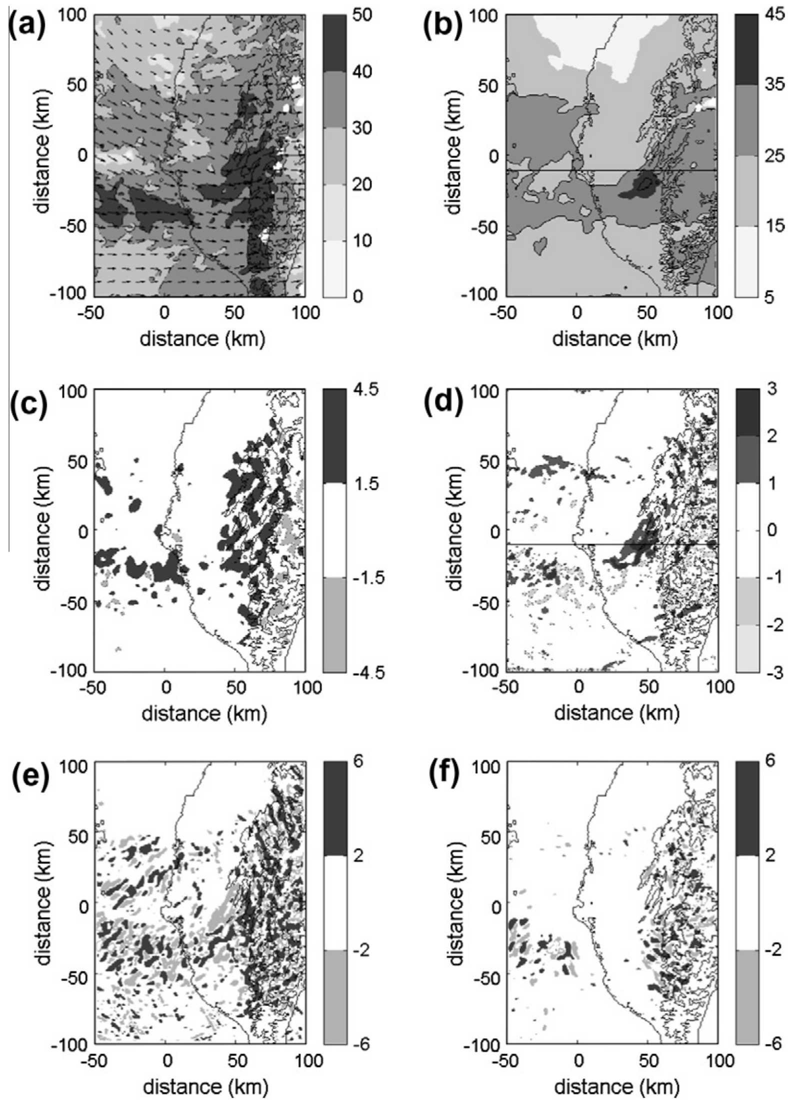

Fig. 10. Retrieved wind fields at Z = 3.25 km using radar observations from RCMK and RCCG between 1039 UTC and 1046 UTC 8 August 2009: (a) horizontal flow field (wind vectors) and radar reflectivity (gray scales in dBZ); (b) horizontal wind speed (m s^{-1}); (c) vertical velocity (m s^{-1}); (d) vertical vorticity ($\times 10^{-3}$ s^{-1}); (e) vorticity advection term ($\times 10^{-6}$ s^{-2}); and (f) vorticity tilting term ($\times 10^{-6}$ s^{-2}). Positive and negative distances on the coordinates are relative to the location of RCCG.

of strong radar reflectivity (>40 dBZ) that stretch from the foothills to the mountain peaks. The low-level vertical wind shear of the cross-barrier flow (i.e., u component) is weak, and the air decelerates near the surface at $X \sim 50$ km, where the effect of terrain begins (Fig. 11b).

A noticeable characteristic is the wind speed maximum exceeding 40 m s^{-1} above the mountain top. To explore the mechanism that causes this maximum, the static stability of the atmosphere is first evaluated, since the region of interest is filled with heavy precipitation. Instead of using the conventional dry or moist Brunt–Väisälä frequency, it is more appropriate to compute the saturated (N^2_{sat}) suggested by Durran and Klemp (1982):

$$N^2_{\text{sat}} = g\left\{\frac{1 + (\mathrm{L}q_sRT)}{1 + (\varepsilon L^2 q_s c_p RT^2)} \times \left(\frac{dln\theta}{dz} + \frac{L}{c_pT}\frac{dq_s}{dz}\right) - \frac{dq_w}{dz}\right\}, \tag{3a}$$

where g is the gravity, ε = 0.622, L is the latent heat of vaporization, R is ideal gas constant for dry air, T is the temperature, q_s denotes the saturation mixing ratio, C_p is the specific heat at constant pressure, θ represents the potential temperature, and q_w is the sum of q_s and the liquid water mixing ratio.

The National Centers for Environmental Prediction (NCEP) Final (FNL) analysis, and the liquid water mixing ratio estimates from the radar reflectivity (Sun and Crook, 1997, Liou et al., 2003), are used to estimate N^2_{sat}. Near the time of analysis, the upstream (west) side of the mountain value of N^2_{sat} is about -5.61×10^{-5} s^{-2}. A negative value implies that the saturated atmosphere is statically unstable, which creates a favorable condition for the development of convection, when proper external forcing such as orographic lifting is provided. Vigorous convective conditions are confirmed by the absence of a bright band in Fig. 11a, which would be an indicator of stratiform-type precipitation.

Vertical mixing processes in vigorous convection tend to smooth out vertical differences, and thus tend to generate an equivalent barotropic atmosphere. For such conditions, simplified steady-state, two-dimensional shallow water equations may be applied (Holton, 2004):

$$(1 - F_r^2)\frac{\partial u}{\partial x} = \frac{ug}{C^2}\frac{\partial H}{\partial x}, \tag{4a}$$

$$C^2 = g(h - H), \tag{4b}$$

$$F_r^2 = \frac{u^2}{C^2}, \tag{4c}$$

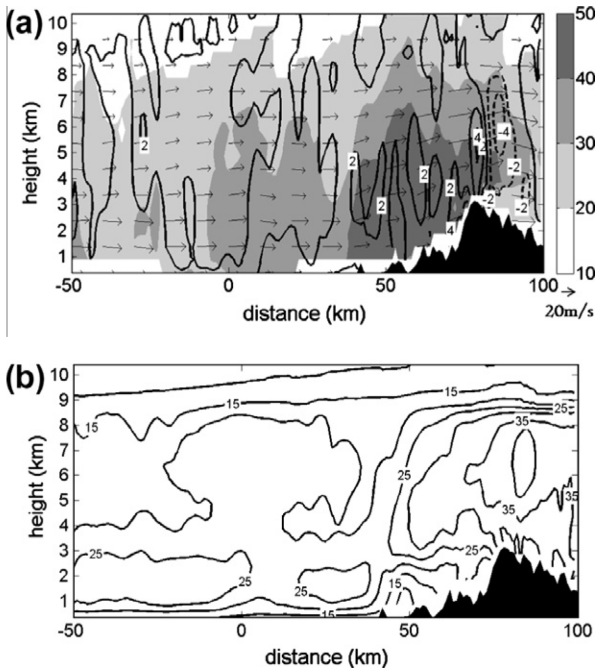

Fig. 11. Wind field along an east–west vertical cross-section 40 km south of RCCG. (a) u–w wind field (vectors), radar reflectivity (gray scales), and vertical velocity (positive (negative) indicated by solid (dashed) contours); (b) cross-barrier, or u component of wind. The intervals for radar reflectivity, vertical velocity, and u are 10 dBZ, 2 m s^{-1}, and 5 m s^{-1}, respectively.

where u (>0) is the cross-barrier wind component, h denotes the height of the shallow water interface, which in this case is the depth of the underlying barotropic atmosphere, and H represents the altitude of the mountain peak. The shallow water Froude number (F_r) is the ratio of the flow speed u and the shallow water gravity wave phase speed ($C = \sqrt{g(h-H)}$). For this case, the height (H) of the crests in the southern CMR is about 2000 m, and the upstream wind speed (u) is approximately 20 m s^{-1}. If it is assumed that h exceeds H owing to the strong vertical mixing, then F_r would be smaller than one, which is referred to as subcritical conditions (Durran, 1986, 1990). When $F_r < 1$ and $\partial u/\partial x > 0$ in (4a), then u would increase with distance x toward the east in upslope conditions (i.e., $\partial H/\partial x > 0$). The wind speed would then decrease after passing the mountain top as $\partial H/\partial x \sim 0$ at this position, so the result is a speed maximum above the mountain crest. The features described with this conceptual model are consistent with the observed wind speed distribution along the mountain slope shown in Fig. 11b.

7. QPE using RCMK dual-polarimetric radar data

An accurate representation of the temporal and spatial variation of rainfall is essential for computing and modeling runoff (Faures et al., 1995; Syed et al., 2003; Li et al., 2011). The dual-polarimetric radar has been recognized as a very effective instrument to improve QPE (Doviak and Zrnic, 1993; Zrnic and Ryzhkov, 1999; Bringi and Chandrasekar, 2001). In this study, dual-polarimetric radar data collected by the RCMK are utilized to conduct a QPE experiment for this extreme rainfall event. The relevant dual-polarimetric variables include the reflectivity factor (Z_H) and specific differential phase shift (K_{DP}). Basically, Z_H is the reflected power from horizontal polarization. Due to the oblate shape of a raindrop, the horizontally-polarized electromagnetic waves experience larger phase lags and thus propagate slower than the vertically-polarized waves. The K_{DP} is a measure of the resulting differential phase per unit distance, and is a parameter that is very sensitive to heavy precipitation. The extra information about the raindrop shape provided by these dual-polarimetric variables is crucial for accurate rainfall estimation. It is emphasized that compared with rain gauges, the RCMK radar is able to provide rainfall estimates over an area of several thousand square kilometers with high temporal (~7.5 min) and spatial (~1.0 km) resolutions.

It should be pointed out that the uncertainty of QPE by using weather radar was mainly from the variability of the rain drop size distribution (DSD). In order to reduce the errors of QPE, one can use a disdrometer to measure the DSD during a rainfall event, then merge this information with the data collected by a dual-polarimetric radar to perform QPE. However, in this Typhoon Morakot case, the disdrometer data were not available in the area of interest. In addition, it was our purpose to demonstrate the feasibility of using an operational dual-polarimetric radar to conduct QPE over an area with complex terrain at a routine basis. Thus, the rainfall was estimated only by a hybrid empirical scheme based on May et al. (1999) and data sets collected in previous case studies. The formulas adopted to estimate the rainfall using RCMK dual-polarimetric observations are:

$$Z_H < 30\,\mathrm{dBZ} \quad R = 6.56264 \times 10^{-2}(Z_H)^{0.637875}, \tag{5a}$$

$$Z_H \geqslant 30\,\mathrm{dBZ} \quad R = 34.6(K_{DP})^{0.83}, \tag{5b}$$

where R is the hourly rainfall rate (mm h^{-1}), Z_H denotes the radar reflectivity in mm^6 m^{-3}, and K_{DP} is in units of degrees km^{-1}. Accumulated precipitation from 06 to 12 UTC 8 August recorded by gauges and estimated by RCMK is displayed in Fig. 12. Although the correlation between the radar and gauge observations is 0.896, the radar tends to underestimate the heaviest precipitation (>400 mm 6 h^{-1}). The root-mean-square error normalized by the gauge-observed rainfall amount (i.e., the relative rms error) indicates that the difference between these two measurements for the heaviest precipitation is 24.7%.

Radar-derived hourly rainfall rates sampled at 7.5-min intervals from 06 to 12 UTC are compared in Fig. 13 with the hourly rates at two gauges selected to represent the precipitation at a low altitude (210 m MSL) and a mountain (1160 m MSL) site, respectively. Comparing these two sites, both the radar and gauge data indicate that the rainfall intensity begins to increase after 07 UTC, decrease after 09 UTC, and then increase again at about 12 UTC. Although the gauge-observed rainfall rates vary dramatically in time, both the tendency and magnitude are resolved quite well by the radar measurements. Due to the terrain blockage, higher radar elevation angles are usually required to collect data over mountainous area. A greater distance between the radar data point in the air and the ground often introduces large errors in radar QPE. Thus, the good

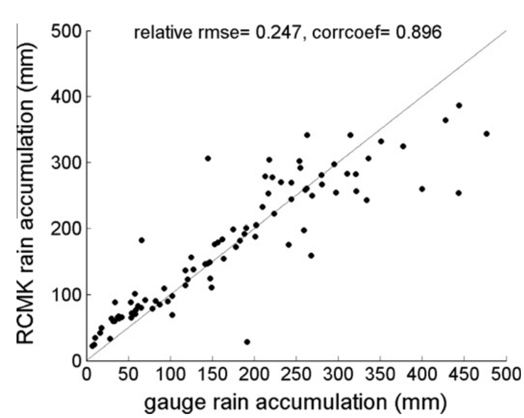

Fig. 12. Scatterplot of the 6-h (06–12 UTC 8 August) accumulated rainfall amounts observed by surface rain gauges and the RCMK dual-polarimetric radar.

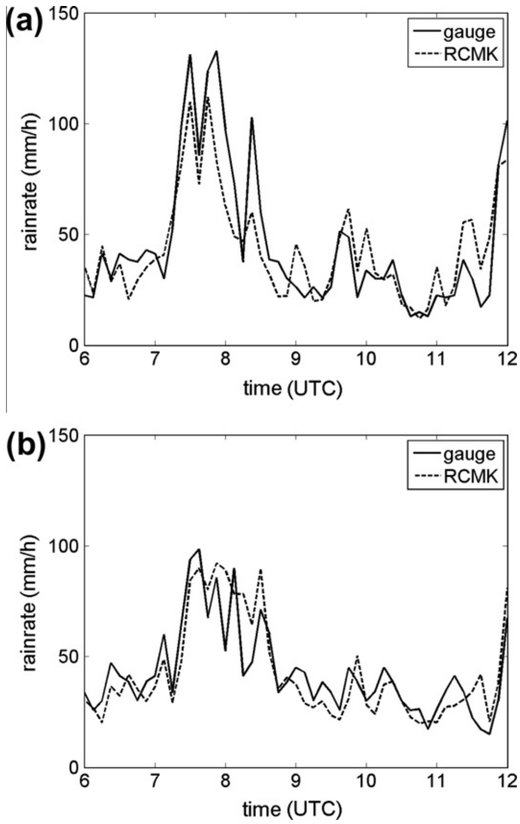

Fig. 13. Hourly rainfall rates (mm h^{-1}) sampled at 7.5-min intervals during 06–12 UTC 8 August as observed by gauges (solid line) and RCMK (dashed line) at: (a) a low altitude (210 m MSL) site; and (b) a mountain (1160 m MSL) site.

agreement between the gauge- and radar-observed rainfall rates at the mountain site (Fig. 13b) is particularly encouraging.

It is noted that Lin and Chen (2012) have derived a quantitative relationship between the rainfall kinetic energy (computed using gauge data) with landslides and sediment delivery based on a 15-year long data set collected in central Taiwan. They suggested that it was possible to predict the occurrence of these hazards through real-time monitoring of rainstorms. Their study is an example of the requirement for accurate rainfall measurements in various fields such as hydrology, water resource management, flash flood, landslide, and disaster prevention/mitigation. The results presented in this section demonstrate the capability of a dual-polarimetric weather radar to provide reliable and high temporal/spatial resolution precipitation information during a typhoon extreme rain event.

8. Conclusions and future work

The evolution and structure of the precipitation systems in Typhoon Morakot (2009) are documented in this study using ground-based weather radars and surface rainfall measurements. The existence of the CMR substantially alters the spatial distribution of the precipitation. On 8 August, 2009, the atmosphere in the upstream area was statically unstable. As a result, the local topography provided sufficient lifting of the incoming convective systems that led to heavy and uninterrupted precipitation on the windward side of the CMR. Most of the moisture in the air was consumed before reaching the crest, which contributed to a substantial decrease of the rainfall on the leeward side of the mountains. In other words, a near-continuous upslope-triggering process was the major mechanism in this precipitation event.

The generation of vertical vorticity can be primarily attributed to the advection mechanism. The tilting of the rotational motion from horizontal to vertical also plays an important role in producing the vorticity over the ocean and mountainous area. However, its contribution becomes less important in the coastal plain region. The positive vorticity embedded in the prevailing westerly wind helps to enhance the wind intensity inside the rainband. The wind speed reaches a maximum above the mountain peak. This phenomenon can be reasonably explained by a simplified shallow water model.

The capability of using dual-polarimetric radar data for reliable QPE over a large area with high temporal and spatial resolution in Morakot is demonstrated. The potential application of the knowledge of wind and rainfall characteristics and radar-derived QPE in hydrology and other fields is a topic worthy of further studies.

In the future, the relationship between the kinematic and thermodynamic fields will be investigated further by analyzing the internal temperature and pressure distributions of the precipitation systems by means of the so-called thermodynamic retrieval technique (Liou, 2001; Liou et al., 2003). Following Rowe et al. (2011), the dual-polarimetric radar data will also be utilized to identify the hydrometeor type, and help to understand the microphysical processes occurring inside the typhoon rainbands. All these efforts would lead to a better estimation and forecast of the precipitation, and eventually benefit the interdisciplinary research between meteorology and hydrology.

Acknowledgments

This research is supported by the National Science Council of Taiwan, under NSC 101-2625-M-008-003 and NSC 101-2119-M-008-019. The authors would like to thank the Central Weather Bureau and Air Force of Taiwan for providing the RCCG and RCMK radar data. Suggestions provided by Dr. Ming-Hsu Li are highly appreciated.

References

Armijo, L., 1969. A theory for the determination of wind and precipitation velocities with Doppler radars. J. Atmos. Sci. 26, 570–573.
Bluestein, H.B., Jain, M.H., 1985. Formation of mesoscale lines of precipitation: severe squall lines in Oklahoma during the spring. J. Atmos. Sci. 42, 1711–1732.
Bringi, V.N., Chandrasekar, V., 2001. Polarimetric Doppler Weather Radar: Principles and Applications. Cambridge Univ. Press, 636 pp.
Chang, C.-P., Yeh, T.-C., Chen, J.M., 1993. Effects of terrain on the surface structure of typhoons over Taiwan. Mon. Wea. Rev. 121, 734–752.
Chen, C.-S., Chen, Y.-L., Liu, C.-L., Lin, P.-L., Chen, W.-C., 2007. Statistics of heavy rainfall occurrences in Taiwan. Wea. Forecasting 22, 981–1002.
Chiao, S., Lin, Y.-L., 2003. Numerical modeling of an orographically enhanced precipitation event associated with tropical storm Rachel over Taiwan. Wea. Forecasting 18, 325–344.
Chien, F.-C., Liu, Y.-C., Lee, C.-S., 2008. Heavy rainfall and southwasterly flow after the leaving of Typhoon Mindulle (2004) from Taiwan. J. Metrorol. Soc. Jpn. 86, 17–41.
Chien, F.-C., Kuo, H.-C., 2011. On the extreme rainfall of typhoon Morakot (2009). J. Geophys. Res. 116, D05104. http://dx.doi.org/10.1029/2010JD015092.
Chong, M., Testud, J., 1983. Three-dimensional wind field analysis from dual-Doppler radar data. Part III: The boundary condition: An optimum determination based on a variational concept. J. Clim. Appl. Meteorol. 22, 1227–1241.
Chong, M., Bousquet, O., 2001. On the application of MUSCAT to a ground-based dual-Doppler radar system. Meteorol. Atmos. Phys. 78, 133–139.
Doviak, R.J., Ray, P., Strauch, R.G., Miller, L.J., 1976. Error estimation in wind fields derived from dual-Doppler radar measurement. J. Appl. Meteorol. 15, 868–878.
Doviak, R.J., Zrnic, D.S., 1993. Doppler Radar and Weather Observations. Academic Press, 562 pp.
Durran, D.R., Klemp, J.B., 1982. On the effects of moisture on the Brunt–Väisälä frequency. J. Atmos. Sci. 39, 2152–2158.
Durran, D.R., 1986. Another look at the downslope windstorms. Part I: The development of analogs to supercritical flow in an infinitely deep, continuously stratified fluid. J. Atmos. Sci. 43, 2527–2543.
Durran, D.R., 1990. Mountain waves and downslope winds. In: Bluemen, W. (Ed.), Atmospheric Processes Over Complex Terrain. American Meteorological Society, Boston, pp. 59–81.

Faures, J.M., Goodrich, D.C., Woolhieser, D.A., Sorooshian, S., 1995. Impact of small-scale spatial rainfall variability on runoff modeling. J. Hydrol. 173, 309–326.
Gao, J., Xue, M., Brewster, K., Droegemeier, K.K., 2004. A three-dimensional variational data analysis method with recursive filter for Doppler radars. J. Atmos. Oceanic Technol. 21, 457–469.
Geerts, B., Heymsfield, G.M., Tian, L., Halverson, J.B., Guillory, A., Mejia, M.I., 2000. Hurricane Georges's landfall in the Dominican Republic: detailed airborne Doppler radar imagery. Bull. Am. Meteorol. Soc. 81, 999–1018.
Holton, J.R., 2004. An Introduction to Dynamic Meteorology. Academic Press, 535 pp.
Hor, T.-H., Wei, C.-H., Chang, M.-H., Cheng, C.-S., 2005. Doppler radar analysis of typhoon Otto (1998) – characteristics of eyewall and rainbands with and without the influence of Taiwan orography. J. Metrorol. Soc. Jpn. 83, 1001–1023.
Houze Jr., R.A., 1993. Cloud Dynamics. Academic Press, 573 pp.
Houze Jr., R.A., 2010. Clouds in tropical cyclones. Mon. Wea. Rev. 138, 293–344.
Huang, C.-Y., Kuo, Y.-H., Chen, S.-Y., Terng, C.-T., Chien, F.-C., Lin, P.-L., Kueh, M.-T., Chen, S.-H., Yang, M.-J., Wang, C.-J., Prasad Rao, Anisetty S.K.A.V., 2010. Impact of GPS radio occultation data assimilation on regional weather predictions. GPS Solutions 14, 349–353.
Ibbitt, R.P., Henderson, R.D., Copeland, J., Wratt, D.S., 2001. Simulating mountain runoff with meso-scale weather model rainfall estimates: a New Zealand experience. J. Hydrol. 239, 19–32.
Jasper, K., Gurtz, J., Lang, H., 2002. Advanced flood forecasting in Alpine watersheds by coupling meteorological observations and forecasts with a distributed hydrological model. J. Hydrol. 267, 40–52.
Jian, G.-J., Wu, C.-C., 2008. A numerical study of the track deflection of supertyphoon Haitang (2005) prior to its landfall in Taiwan. Mon. Wea. Rev. 136, 598–615.
Lee, C.-S., Huang, L.-R., Shen, H.-S., Wang, S.-T., 2006. A climatology modal for forecasting typhoon rainfall in Taiwan. Nat. Hazards 37, 87–105.
Lee, W.-C., Jou, B.J.-D., Chang, P.-L., Marks, F.D., 2000. Tropical cyclones kinematic structure retrieved from single-Doppler radar observations. Part III: Evolution and structures of typhoon Alex (1987). Mon. Wea. Rev. 128, 3982–4001.
Li, M.-H., Sung, R.-T., Dong, J.-J., Lee, C.-T., Chen, C.-C., 2011. The formation and breaching of a short-lived landslide dam at Hsiaolin village, Taiwan. Part II: Simulation of debris flow with landslide dam breach. Eng. Geol. 123, 60–71.
Li, M.-H., Yang, M.-J., Soong, R., Huang, H.-L., 2005. Simulating typhoon floods with gauge data and mesoscale-modeled rainfall in a mountainous watershed. J. Hydrometeorol. 6, 306–323.
Lin, G.-W., Chen, H., 2012. The relationship of rainfall energy with landslides and sediment delivery. Eng. Geol. 125, 108–118.
Lin, Y.-L., Ensley, D.B., Chiao, S., Huang, C.-Y., 2002. Orographic influence on rainfall and track deflection associated with the passage of a tropical cyclone. Mon. Wea. Rev. 130, 2929–2950.
Lin, Y.-L., Chen, S.-Y., Hill, C.M., Huang, C.-Y., 2005. Control parameters for the influence of a mesoscale mountain range on cyclone track continuity and deflection. J. Atmos. Sci. 62, 1849–1866.
Liou, Y.-C., 2001. The derivation of absolute potential temperature perturbations and pressure gradients from wind measurements in three dimensional space. J. Atmos. Oceanic Technol. 18 (4), 577–590.
Liou, Y.-C., Chen Wang, T.-C., Chung, K.-S., 2003. A three-dimensional variational approach for deriving the thermodynamic structure using Doppler wind observations – an application to a subtropical squall line. J. Appl. Meteorol. 42, 1443–1454.
Liou, Y.-C., Chen Wang, T.-C., Lee, W.-C., Chang, Y.-J., 2006. The retrieval of asymmetric tropical cyclone structures using Doppler radar simulations and observations with the extended GBVTD technique. Mon. Wea. Rev. 134, 1140–1160.
Liou, Y.-C., Chang, Y.-J., 2009. A variational multiple-Doppler radar three-dimensional wind synthesis method and its impacts on thermodynamic retrieval. Mon. Wea. Rev. 137, 3992–4010.
Liou, Y.-C., Chang, S.-F., Sun, J., 2012. An application of the immersed boundary method for recovering the three-dimensional wind fields over complex terrain using multiple-Doppler radar data. Mon. Wea. Rev. 140, 1603–1619.
May, P.T., Keenan, T.D., Zrnić, D.S., Carey, L.D., Rutledge, S.A., 1999. Polarimetric radar measurements of tropical rain at a 5-cm wavelength. J. Appl. Meteorol. 38, 750–765.
Miller, L.J., Strauch, R.G., 1974. A dual-Doppler radar method for the determination of wind velocities within precipitating weather systems. Remote Sens. Environ. 3, 219–235.
Nishiwaki, N., Misumi, R., Maki, M., 2010. Relationship between orographic enhancement of rainfall rate and movement speed of radar echoes: case study of typhoon 0709. J. Meteorol. Soc. Jpn. 88, 931–936.
Protat, A., Zawadzki, I., 1999. A variational method for real-time retrieval of three-dimensional wind field from multiple-Doppler bistatic radar network data. J. Atmos. Oceanic Technol. 16, 432–449.
Ray, P.S., Wagner, K.K., Johnson, K.W., Stephens, J.J., Bumgarner, W.C., Mueller, E.A., 1978. Triple-Doppler observations of a convective storm. J. Appl. Meteorol. 17, 1201–1212.
Rowe, A.K., Rutledge, S.A., Lang, T.J., 2011. Investigation of microphysical processes occurring in isolated convection during NAME. Mon. Wea. Rev. 139, 424–443.
Shun, C.M., Lau, S.Y., Lee, O.S.M., 2003. Terminal Doppler weather radar observation of atmospheric flow over complex terrain during tropical cyclone passages. J. Appl. Meteorol. 42, 1697–1710.
Sun, J., Crook, N.A., 1997. Dynamic and microphysical retrieval from Doppler radar observations using a cloud model and its adjoint. Part I: Model development and simulated data experiment. J. Atmos. Sci. 54, 1642–1661.
Syed, K.H., Goodrich, D.C., Myers, D.E., Sorooshian, S., 2003. Spatial characteristics of thunderstorm rainfall fields and their relation to runoff. J. Hydrol. 271, 1–21.
Tseng, Y., Ferziger, J., 2003. A ghost-cell immersed boundary method for flow in complex geometry. J. Comput. Phys. 192, 593–623.
Wang, T.C., Tseng, C.H., 1999: The structure of Typhoon Herb (1996) during its landfall by dual Doppler analysis. In: Preprints, 29th Conf. on Radar Meteorology, Montreal, PQ, Canada, Am. Meteorol. Soc., pp. 364–365.
Westrick, K.J., Mass, C.F., 2001. An evaluation of a high-resolution hydrometeorological modeling system for prediction of a cool-season flood event in a coastal mountainous watershed. J. Hydrometeorol. 2, 161–180.
Willoughby, H.E., Black, P.G., 1996. Hurricane Andrew in Florida: dynamics of a disaster. Bull. Am. Meteorol. Soc. 77, 543–549.
Wu, C.-C., Yen, T.-H., Kuo, Y.-H., Wang, W., 2002. Rainfall simulation associated with typhoon Herb (1996) near Taiwan. Part I: the topographic effect. Wea. Forecasting 17, 1001–1015.
Xu, W., Zipser, E.J., Chen, Y.-L., Liu, C., Liou, Y.-C., Lee, W.-C., Jou, B.J., 2012. An orography-associated extreme rainfall event during TiMREX: initiation, storm evolution, and maintenance. Mon. Wea. Rev. 140, 2555–2574.
Yang, M.-J., Zhang, D.-L., Huang, H.-L., 2008. A modeling study of typhoon Nari (2001) at landfall. Part I: Topographic effects. J. Atmos. Sci 65, 3095–3115.
Yeh, T.-C., Elsberry, R.L., 1993a. Interaction of typhoons with the Taiwan orography. Part I: Upstream track deflections. Mon. Wea. Rev. 121, 3193–3212.
Yeh, Y.-C., Elsberry, R.L., 1993b. Interaction of typhoons with the Taiwan orography. Part II: Continuous and discontinuous tracks across the island. Mon. Wea. Rev. 121, 3213–3233.
Yu, C.-K., Cheng, L.-W., 2008. Radar observations of intense orographic precipitation associated with typhoon Xangsane (2000). Mon. Wea. Rev. 136, 497–521.
Zrnic, D.S., Ryzhkov, A., 1999. Polarimetry for weather surveillance radars. Bull. Am. Meteorol. Soc. 80, 389–406.

Please cite this article in press as: Liou, Y.-C., et al. Structure of precipitating systems over Taiwan's complex terrain during Typhoon Morakot (2009) as revealed by weather radar and rain gauge observations. J. Hydrol. (2012), http://dx.doi.org/10.1016/j.jhydrol.2012.09.004

極端高溫健康預警系統之國際文獻回顧

林于凱[1,5]　林沛練[2]　李明旭[3]　黃鈴雅[4]
宋鴻樟[4,5]　王玉純[6,*]

國內外研究顯示極端高溫及其連續數日事件顯著增加健康風險，本研究彙整2004-2012年間關鍵字為氣象、事件、高溫、預警及死亡等之國際主要文獻與報告，統整各國高溫預警準則及預警系統之架構，以作為本國未來相關系統建置之參考依據。都會區是氣象-健康預警系統之基本空間單位。建立預警系統前，需先了解溫度與敏感族群健康之相關性。目前熱預警系統定義之高敏感性族群以糖尿病、無行為能力者、藥癮酒癮者、腎臟疾病及腦血管、心肺疾病等慢性病病患為主。熱預警計畫由政府衛生單位、氣象單位及專家學者共同界定地區氣象預警項目及規範，氣象單位負責氣象預報並發布預警工作，衛生單位則負責熱應變計畫工作(如：建議敏感性族群提升個人主動防護及行為措施)及風險溝通工作。各地區採用之溫度指標及應變項目略有不同，宜因地制宜。研究證實熱預警系統建置可有效降低熱相關死亡及就醫。因此，在全球暖化趨勢下，我們應即早規劃適用本國之高溫預警應變系統。(台灣衛誌 2012；**31**(**6**)：512-522)

關鍵詞：熱浪、溫度、死亡、預警系統

前　言

全球氣候暖化[1]，自1950年來地球發生的極高溫事件(熱浪、乾旱)有顯著的上升趨勢[2,3]。根據近年台灣地區氣溫資料，不但平均溫度持續上升[4,5]，極端高溫事件發生強度及頻率亦逐年增加[6]。研究指出，不論是高溫或是連續極端高溫事件均會增加地區性的死亡、住院及急診就醫[7-13]。一份調查1994-2007年間台灣四大都會區(台北、台中、台南及高雄)年長者總死因、心血管及呼吸道疾病死亡與持續高溫事件研究，發現除了高溫會顯著增加死亡風險外，連續極端高溫(高於97百分位值連續9天)事件會額外增加年長者約5%的總死亡風險[14]。此外，由2000-2009年間上述四大都會區總病因、心血管及呼吸道疾病急診就醫與持續極端高溫之相關性，亦證實每年度第一次高溫事件會增加4-8%全病因及13%心血管急診就醫[15]。國內研究顯示，未來台灣高溫日數將大為增加，而低溫日數將逐漸減少[16]。國外經驗顯示，極端高溫預警系統的建立有助於降低因高溫所造成的額外死亡與就醫。因此，本研究蒐集並彙整國際上極端高溫預警系統之主要文獻與公部門報告，統整各國高溫預警準則及預警系統之架構，以作為本國未來相關系統建置之參考依據。

[1] 哈佛大學公共衛生學院環境衛生研究所環境與職業醫學及流行病學學程
[2] 國立中央大學大氣科學學系
[3] 國立中央大學水文與海洋科學研究所
[4] 中國醫藥大學公共衛生學院公共衛生學系
[5] 國立台灣大學公共衛生學院環境衛生研究所
[6] 中原大學工學院生物環境工程學系
[*] 通訊作者：王玉純
聯絡地址：桃園縣中壢市中北路200號
E-mail: ycwang@cycu.edu.tw
投稿日期：101年7月23日
接受日期：101年9月28日

材料與方法

蒐集2004到2012年高溫預警系統之相關文獻，主要字彙包括氣象關鍵字(weather, climate, heat, temperature)以及其他關鍵字(extreme, event, lag, warning, mortality, morbidity)。主要搜尋範圍為醫學電子資料庫(Medline及PubMed)，期刊以環境科學類及流行病學類期刊為主。並進一步蒐集國際組織(世界氣象組織(The World Meteorological Organization)及世界衛生組織(The World Health Organization)…等)、各國氣象、環境及健康公部門網頁之研究與執行報告書。

結果與討論

一、高溫健康預警系統定義[17]

極端高溫預警系統是在2003年歐洲熱浪造成重大健康衝擊後才被歐洲各國提出執行。目前國際上並無極端高溫之公認定義。然而，相較於一般氣候狀態之異常高溫連續數日，會造成族群負面健康危害的，均被定義為熱浪。而高溫健康預警系統即為用以警示決策者以及一般大眾認知高溫之健康危害，並提供對應高溫之減低健康危害之建議。高溫預警系統之設置包含準確之氣象預報、高溫預警之發布、敏感性族群界定、相關部門協調與互動、調適工作之執行與效益評估。高溫預警系統必須考量當地氣象、人口、族群文化特性與都市結構，沒有適用於各地區之預警系統。此外，預警系統必須是基於實際的氣象與健康相關性知識來建立，健康風險的溫度閥值(threshold temperature)會因設定的地區、發布時間及關注族群而異。預警發布內容應該採用一般大眾、相關單位及決策者可以理解的語言與說詞，因此，以國家層級來看，統一的用詞、大眾理解之說法、訊息將有助於風險溝通。預警系統並應與調適反應機制配合運行，兩者個別及整合之成效亦應被評估。

二、健康風險分析模式[17,18]

建立極端溫度預警系統前，必須先了解溫度對族群健康之相關性。氣象因子對族群就醫或死亡乃符合波以松機率分配(Poisson distribution)，因此，研究多會採用時間序分析之一般廣義線性模式(generalized linear models)、廣義累加模式(generalized additive model)或是大氣氣團(air masses)空間概要法(spatial synoptic approach)來進行溫度對族群健康風險相關性分析[18,19-22]。亦有部分研究使用多變項複迴歸(multiple linear regression)進行分析[23-26]。上述統計模式各有其對應之模式適用性判斷準則，在此略述。

三、高溫敏感性族群

目前熱預警系統定義之高敏感性族群[18,27]，包含：糖尿病及內分泌系統疾病(diabetes mellitus, other endocrine disorders)、器質性精神疾病(organic mental disorders)、癡呆(dementia)、阿茲海默症(Alzheimer's disease)、藥癮及酒癮導致精神及行為異常者、精神分裂症(schizophrenia)、錐体外系及運動障礙疾病(extrapyramidal and movement disorders，如：帕金森氏症)、心血管疾病(cardiovascular disease)、高血壓(hypertension)、腦血管疾病(coronary artery disease)、心傳導系統疾病(heart conduction disorders)、呼吸系統疾病(diseases of the respiratory system)、慢性肺部疾病(chronic lower respiratory disease)、腎臟系統疾病(diseases of the renal system)、腎衰竭(renal failure)及腎結石(kidney stones)等。性別的影響目前並未有定論，歐洲地區女性年長族群風險高於男性，但在美國地區卻為相反趨勢。若觀察全年齡人口族群，男女無差異。獨身及獨居(未婚、未有伴侶等)是危險因子，增加社會接觸可有效減低高溫對健康的風險。此外，目前並無足夠證據顯示都會區內的低社經族群有較高風險。

四、國際極端高溫預警系統基本架構與流程[17,18]

表一簡單摘要各地區明列之熱預警分

表一　各國因應極端高溫之氣象健康預警系統統整表

國家 / 地區	預警分類	應變單位/措施	參考文獻
英國	•溫度閥值(threshold temperature)：日最高溫30°C，日最低溫15°C •層級一 預備(awareness)：每年6/1-9/15特別觀測熱氣候；層級二 警報(alert)：預期2-3天後將會有60%機率出現高溫；層級三 熱浪(heatwave)：大於一個以上地區會出現高於溫度閥值；層級四 緊急(emergency)：熱浪發生在兩地區以上並持續4天以上，除健康及社會照護系統單位之外，如：供電及供水系統可能吃緊或受到衝擊 •明列短期(0-5年)、中期(10-30年)及長期(30年上)之調適目標	•高風險族群：75歲以上、女性、獨居、身障或精障、藥癮酒癮者、服用多種藥物者、嬰兒及幼童 •不同層級有其對應之準備、應變工作 •提出警戒、找出高風險族群、監測室內溫度4次/日、提供涼爽避難處	[36]
法國	•溫度閥值：日最高溫31°C，日最低溫21°C (依地區略微差異) •1.警戒(vigilance)：6/1-10/1加強溫度監測；2.警報(alert)：當預警溫度將於3天內達到時；3.干預(intervention)：當已達預警溫度，4.緊急(emergency)：持續熱浪，或是乾旱、停電伴隨熱浪發生	•當有達到警戒3級以上的地區時，法國當局將立即成立緊急應變委員會，並立即啟動社區老人照護之家(nursing home)、醫療體系、消防體系，並對年長者及風險較高族群提出警告、開放公共空調空間	[37,38]
匈牙利	•1.注意(attention)：政府內部警戒，日均溫高於25°C；2.準備(readiness)：日均溫高於27°C，日均溫25°C連續3日以上；3.警報(alarm)：日均溫27°C連續3日以上	•大眾教育文宣	[39]
澳洲	•酷熱指數(heat index)及平均溫度均被採用。昆士蘭地區採用體感溫度。 •國家警報建議：白警報-熱浪前3-4天提出，政府單位準備；黃警報-熱浪前1-2天提出，由媒體告知民眾；紅警報-熱浪前24小時提出，理應準備完善；綠警報-熱浪結束。 •布里斯班：酷熱指數>36°C連續2天發布熱預警；酷熱指數>40°C連續2天發布極端熱預警 •安柏利：預警溫度為酷熱指數>37°C •柏斯：預警溫度為平均溫度>32°C •墨爾本：預警溫度為平均溫度>30°C	•高風險族群：65歲以上、獨居、身障或精障者、藥癮或酒癮者、慢性病患、嬰兒及幼童 •熱預警系統工作擴及衛生單位、氣象單位、緊急救護單位、農業單位及地球科學單位…等，各單位工作項目文件請逕至網路下載	[40,41]
加拿大			
大多倫多地區	•每年5/15-9/30加強觀測與預警 •早期遵循Environment Canada的濕熱指數建議值：每日濕熱指數超過40°C以及/或超過36°C持續3天以上。現主要以大氣氣團空間概要法之分析結果發布熱預警	•應變單位：加拿大紅十字會、緊急醫療服務、避難所、社福單位、公共衛生單位、警察局、老年之家、公共圖書館	[42-44]

表一　各國因應極端高溫之氣象健康預警系統統整表(續)

國家 / 地區	預警分類	應變單位/措施	參考文獻
加拿大			
蒙特婁熱預警系統	• 溫度閥值：日最高溫33°C，日最低溫20°C	• 各單位文件請至網路下載	[42]
漢彌頓公共衛生服務系統	• 遵循Environment Canada的濕熱指數建議值40°C	-	[45]
美國			
國家氣象預報辦公室(National Weather Service Forecast Office)	• 1.觀測期(outlook statement)：熱浪警報將在未來的3-7天發生，2.過量熱觀測(excessive heat watch)：接下來的24 至72小時內可能有熱浪發生，3.過量熱警告(excessive heat warning)：於熱浪事件發生前36小時提出 • 熱浪定義為酷熱指數超過105-110°F，連續兩天以上。各地定義不同，請逕至網頁查詢 • 特別加強說明艷陽下停放汽車內之熱危害	• 當有地區發生警戒層級二以上時，美國當局將立即展開應變，包括：熱傷害主動調查、24小時內啟動熱觀測小組、開放避難所、危險族群每日將派專人確認健康狀況以及資源需求	[46,47]
大氣氣團空間概要法熱觀測預警系統	• 利用演算模式建立地區別每日總死亡人數與大氣氣團特徵(溫度/露點/氣壓/風速及雲覆率)相關性，進而由每日氣象條件預測額外死亡人數 • 實施地區：費城、華盛頓特區、鳳凰城、芝加哥、達拉斯、西雅圖、紐奧良…等城市	• 建立“Buddy System”、啟動公部門電話服務(heatline)、針對求助heatline群眾進行家戶拜訪、家戶護理介入、熱預警期間水電供應系統人員停止休假、增加緊急醫護人員服務、提供遊民協助、延長老年服務中心開放時間、提供空調避難所	[48]
中國上海	• 溫度指標：大氣氣團 • 一級預警：預測會有40-59名額外死亡；二級預警：預測會有60-79名額外死亡；三級預警：預測會有>80名額外死亡 • 於熱浪發生前48小時提出預警	• 上海市衛生局(Shanghai Municipal Health Bureau)及其他單位 • 媒體公告(報紙、廣播、電視)、大眾健康教育、公共服務/醫療設施準備、穩定提供飲水/電力/空調避難所	[24]
日本	• 溫度指標：綜合溫度熱指數(wet bulb globe temperature, WBGT） • 日本體育學會公告標準：1.安全：WBGT<21°C，2.注意：WBGT介於21~25°C，3.警戒：WBGT介於25~28°C，4.嚴重警戒：WBGT介於28~31°C，5.運動中止：WBGT>31°C • 日本氣象學會公告標準：1.注意：WBGT<25°C，2.警戒：WBGT介於25~28°C，3.嚴重警戒：WBGT介於28~31°C，4.危險：WBGT>31°C	• 請高齡者居家自我預防，建議戶外活動多補充水分	[34]

類及應變措施。有關發布預警的極端高溫定義，各個國家處理過程並不相同，有些國家依照溫度與死亡的相關性，如：法國定義都會區50%額外死亡、義大利定義10-20%額外死亡之溫度值為預警溫度閥值(threshold temperature)[20,21]，有些國家(如：英國)則是由氣象單位依照該地區之溫度機率來定義發布預警之溫度[17,18]。預警之空間尺度，有城市等級及國家等級(內部再細分區域)，都會區是最基本的高溫預警空間單位。

熱預警計畫由政府衛生單位、氣象單位及專家學者共同界定各地區氣象預警分級項目及規範，氣象單位負責氣象預報並發布預警工作，衛生單位則依據熱預警應變計畫執行緊急應變項目(mitigation) (圖一)，應變工作項目因地制宜，由各地政府制定之。風險溝通由衛生單位協同醫護單位執行。預警訊息主要透過媒體(如：電視、電台及新聞報紙等)傳播，或經由公告，以提升各地警戒。此外，應針對特殊敏感族群(如：長期照護單位及社福單位)另設有應變計畫。預警地區除了開放公共空間以供避難，亦應提升醫療供給需求(含相關用藥指示)，衛生單位應主動建議敏感性族群提升個人主動防護及行為措施。部分國家熱預警系統內設風險族群主(互)動聯絡網，或是建立熱線(heatline)服務，可即時提供大眾居家防範熱危害之諮詢與協助。

基本上，各地區依氣溫與健康之相關性，先由(城市)氣象單位預測未來1週內氣象參數，緊接由衛生單位來預測未來3天左右各都會區之死亡及就醫人數[18-22,24-26,28]。在氣象對健康的預警上，各國系統都面臨到一項艱鉅的挑戰，所有的未來健康預測均受限於氣象預測準確度，在考量發布熱預警(啟動應變機制)需要付出的社會成本下，多數國家會採取較保守穩當的3天以內做為極高溫預警期。

五、各國預警系統使用之比較

評估氣象與族群健康相關性上，各國政府使用的溫度指標彙整於表二。由於氣溫對健康衝擊分析多採用歷史資料，所以多

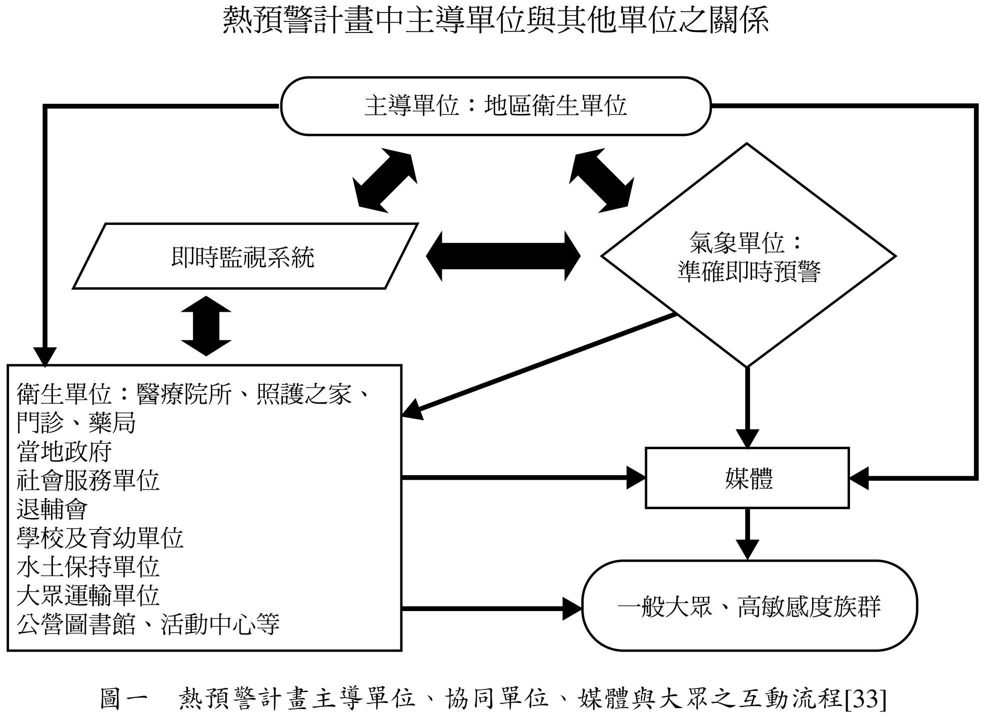

圖一　熱預警計畫主導單位、協同單位、媒體與大眾之互動流程[33]

表二　各國使用之高溫預警參數[17]

國家	熱預警系統之溫度參數	使用死亡檔為評估健康資料	預測額外死亡	考量極端高溫連續天數	模式中校正季節性或考量調適作用	地區溫度參數閥值
澳洲(昆士蘭)	體感溫度			2天		◎
比利時	日最高溫/日最低溫/臭氧			3天		
法國	日最高溫/日最低溫	◎		3天		◎
德國	體感溫度(perceived temperature)			2天	◎	◎
希臘	日最高溫			◎		
匈牙利(布達佩斯)	日平均溫	◎				
義大利	大氣氣團/體感溫度	◎	◎	◎	◎	◎
荷蘭	日最高溫			◎		
波蘭	日最高溫/日最低溫					
西班牙	日最高溫/日最低溫	◎				◎
瑞士	酷熱指數					
英國(英格蘭/威爾斯)	日最高溫/日最低溫	◎		◎		◎
美國						
空間概要法(實施地區請見表一)	大氣氣團	◎	◎	◎	◎	◎
其他	酷熱指數			2天		◎
加拿大						
多倫多	大氣氣團	◎	◎	◎	◎	◎
蒙特婁	日最高溫/日最低溫			◎		
其他	濕熱指數			◎		
中國						
香港	有效溫度(effective temperature)	不明	不明	不明	不明	
上海	大氣氣團	◎	◎	◎	◎	

註：大氣氣團(air mass)：特定地區每日監測四次之溫度/露點溫度/氣壓/風速及雲覆率統整之氣團特徵。

使用鄰近的都會區的氣象測站資訊來做相關分析。選擇溫度指標必須關注幾點[29]：(1)指標是否能準確的代表當地天候狀況？；(2)指標計算方式，是否能夠由一般民眾簡易計算？；(3)天氣預報上哪些氣象指標較為為準確？；(4)指標的變化是否能夠準確預測出地區族群的健康衝擊程度？目前以日平均溫度、日最高溫度、日最低溫度、日體感溫度(apparent temperature)及每日大氣氣團(air masses)最常被應用於慢性病死亡及全死因死亡的討論[18-22,24-26]。為顧及夜間溫度對健康的衝擊，比利時、加拿大(蒙特婁)、英國、法國、波蘭及西班牙等國均採用日最高溫及日最低溫做為預警溫度指標。美國則採用酷熱指數(heat index)，適用於溫度高於26°C、相對濕度高於40%以上的環境，其中，熱浪廣泛定義為酷熱指數為超過105-110°F，連續兩天以上。加拿大則使用溫濕指數(humidex)。研究指出，使用不同的溫度指標評估高溫健康風險將會有些微差異，台灣地區較適用平均溫度及體感溫度做高溫對死亡相關分析[30]。溫度指標定義及相關計算公式可參閱世界氣象組織及世界衛生組織之報告[17]。

公共衛生在氣象資訊上屬於末端使用者，其相關性是在近10年內才受到重視，研究比例上，多數仍屬於風險評估階段，僅少數文章有比較不同預測模式上的差異。Hajat

表三　熱預警系統效益評估

研究地區/健康資料	氣候資訊項目	使用氣候資訊時間	氣候資訊空間解析度	風險評估方法	可能效益	參考文獻
法國/死亡率	日最高溫、日最低溫及對應之10日移動平均、一天之內超過27°C之總度數。除了溫度，其他氣象參數可參考	預警系統：0-3天~1週	測站	波以松迴歸模式	降低法國2006年境內熱相關死亡人數。 需額外考慮其他熱調適機制的影響。未量化經濟效應。	[22]
急診就醫數 (本篇為文獻回顧)	日溫度、季節參數、日期(時間、季節)	最短為1-2週內之日資料	測站	1. 逐步線性迴歸 2. 時間序列模式 3. 複立葉轉換 4. 模式解釋率：線性迴歸(65-87%)優於時間序列模式(31-42%)，因研究方法而異 5. 最佳解釋因子為「日期」，部分研究發現氣象無助於預測	各醫院急診醫學部可預先規畫醫療人力調配。 亦可用於消防局(急診救護單位人力規劃)。 未量化經濟效應。	[23]
美國費城/死亡率	日溫度、露點溫度、連續高溫持續日數、日期(時間、季節)	0-3天，最短為1週內之日資料	測站	多變項線性迴歸(R^2=0.04)	三年成本$200,000，效益 $468百萬，減少117名人員死亡	[32]
美國密爾沃基/死亡率、急診就醫	3小時酷熱指數值、夜間(7 PM-7 AM)酷熱指數值、日間酷熱指數值	預警系統：0-3天	測站	波以松迴歸模式	死亡(最多-83%)及急診就醫數(最多-73%)均有減少，但是，無法完全歸功於氣象預測，公衛體系準備及應變工作同等重要。未量化經濟效應。	[28]
上海/死亡率	大氣氣團(2 AM、8 AM、2 PM及8 PM之地表空氣溫度、露點溫度、覆雲百分比、海平面氣壓、風速及風向)、日最高溫、日最低溫	預警系統：0-2天	測站	1. 空間概要法 2. 逐步線性迴歸	準確預測上海市未來兩天的高溫死亡人數(某一熱浪事件預測331名死亡，實測294人死亡)。未量化經濟效應。	[24]
香港/死亡率(缺血性心臟病、腦中風)	淨有效溫度指數(net effective temperature)-考量日溫度、相對溼度及風速	(未註明)	測站	逐步線性迴歸	啟動預警制度顯著降低65歲以上缺血性心臟病死亡0.97人/天、腦中風1.23人/天。	[26]

等人評比目前各國使用的氣象預警評估法：(1)大氣氣團空間概要法，(2)波以松迴歸模式，(3)溫度溼度指數(temperature-humidity index)及(4)環境生理反應分類參數(environmental stress index)在倫敦、蒙特婁、芝加哥及馬德里四大城市的預警表現。結果發現使用不同的評估方法會得到不同的極端高溫事件日的結果。此外，冷氣候及熱氣候城市適用的氣象預警系統不同，倫敦及蒙特婁以一般常見時間序列波以松迴歸模式分析方法所得結果最佳，未適應熱的城市(如：芝加哥)較需考量露點溫度、大氣壓力、風速、風向及覆雲率等氣象參數，所以建議採用大氣氣團空間概要法，但一般統計分析方法表現亦佳。已適應熱城市(如：馬德里)不論用哪一套評估方式均無法有效預測死亡發生情形[31]。研究人員[31,32]一致認為一個城市若只使用單一熱預警系統，很可能會低估或高估熱事件之影響，因此不斷的評估與驗證熱預警系統相形重要，同時也必須對沒有發布警報時我們錯失補救的健康損失進行估算。

六、熱預警系統評估與亞洲發展

依照統計模式所建立之風險模式會包含解釋率，如：相關係數(R square)等，部分國家預警模式及部分研究以此為評判依據[21,22,25]。法國特別分析執行氣象預警系統後3年內之死亡人數觀測值(observed)與模式預測期望值(expected)之比較[22]，預測值均較觀測值來的高，推論預警發布及公衛體系立即應變與降低的死亡人數有關。預警溫度閥值的適當性或是應變機制運作成效均需要每個年度進行檢討[17]。葡萄牙、法國、義大利、西班牙、及英國亦建立即時健康監視系統，用以監視即時高溫預警及對應預測健康危害之成效[33]。表三整理近年各國採取熱預警計畫所產生的健康效益，現今仍少見評估相關經濟效益之報告[32]。

在亞洲地區中國上海使用預警模式與美國、加拿大、義大利相同的大氣氣團空間概要法。而日本則採用與歐美國家不同的「綜合溫度熱指數」(wet bulb globe temperature, WBGT)做為指標[34]。目前無任何正式報告針對亞熱帶海島型氣候城市做氣象預警系統適用性分析，或提出相關建議。

台灣位處亞熱帶地區，雖然本國室內風扇使用及冷氣空調設備安裝率相較歐美地區高[35]，但是，經過台北、台中、台南及高雄四大都會區的氣溫與死亡資料分析[14]，相較於最適平均溫度26°C，平均溫度30°C將顯著增加7-8%的額外死亡，連續極端高溫事件更增加5%額外死亡，顯示國人並未完全調適熱危害，相形之下，更顯政府相關單位之預警公告及應變項目工作之重要性。

結　論

根據2001年的國政研究報告[5]，中央氣象局分析台灣氣象資料，發現過去100年台北氣象站的平均溫度上升1.31°C，台中上升1.11°C，台南上升1.39°C，比聯合國氣候變化政府間專家委員會(Intergovernmental Panel on Climate Change)所估計全球百年來溫度上升0.6°C還高出1倍，顯現台灣溫暖化的情況較全球嚴重。全球氣候暖化趨勢下，世界各國均已設置相關熱預警公告及應變計畫機制，不但行之有年且已顯現成效。本研究建議台灣應儘速進行基礎研究分析，建立本土之溫度與健康效應關聯，並參考歐美等國經驗以建立台灣適用之高溫預警應變系統。

致　謝

本研究由國科會(NSC 101-2918-I-033-002、NSC 99-2621-M-039-001及NSC 100-2621-M-039-001)及氣象局(計畫名稱：具風險管理概念之氣候預測應用架構一開發具有風險管理概念的氣候預測應用方法)經費補助完成，特此致謝。

參考文獻

1. Intergovernmental Panel on Climate Change (IPCC). Climate Change 2007: The Physical Science

Basis- Summary for Policymakers (Work Group I). Cambridge: Cambridge University Press, 2007.
2. Guha-Sapir D, Hargitt D, Hoyois P. Thirthy Years of Natural Disasters 1974-2003: The Numbers. Louvain-la Neuve: Presses Universitaires de Louvain, 2004.
3. Munich GR. Topics Geo Annual Review: Natural Catastrophes. Germany: F-Media Druck GmbH, 2005.
4. 王玉純、宋鴻樟：綜論氣象變化對心血管、呼吸道及腸胃道之健康衝擊。台灣衛誌 2006；**25**：256-65。
Wang YC, Sung FC. The impact of weather conditions on cardiovascular, respiratory, and gastroenteric health. Taiwan J Public Health 2006;**25**:256-65. [In Chinese: English abstract]
5. 蔡動雄、郭博堯：全球氣候變遷加劇的現象。http://old.npf.org.tw/PUBLICATION/SD/090/SD-R-090-030.htm。引用2012/11/09。
Tsai HH, Kuo PY. Rapid changes in the global climate. Available at: http://old.npf.org.tw/PUBLICATION/SD/090/SD-R-090-030.htm. Accessed November 9, 2012. [In Chinese]
6. 林于凱、吳祐誠、黃鈴雅等：極端氣溫對台灣都會區65歲以上族群心肺疾病死亡之風險趨勢分析。台灣衛誌 2011；**30**：277-89。
Lin YK, Wu YC, Huang LY, et al. A chronological study of mortality risks associated with extreme temperature for elderly populations in metropolitan areas of Taiwan. Taiwan J Public Health 2011;**30**:277-89. [In Chinese: English abstract]
7. Huynen MM, Martens P, Schram D, Weijenberg MP, Kunst AE. The impact of heat waves and cold spells on mortality rates in the Dutch population. Environ Health Perspect 2001;**109**:463-70.
8. Anderson BG, Bell ML. Weather-related mortality: how heat, cold, and heat waves affect mortality in the United States. Epidemiology 2009;**20**:205-13.
9. Hajat S, Armstrong B, Baccini M, et al. Impact of high temperatures on mortality: is there an added heat wave effect? Epidemiology 2006;**17**:632-8.
10. D'Ippoliti D, Michelozzi P, Marino C, et al. The impact of heat waves on mortality in 9 European cities: results from the EuroHEAT project. Environ Health 2010;**9**:37.
11. Gasparrini A, Armstrong B. The impact of heat waves on mortality. Epidemiology 2011;**22**:68-73.
12. Mastrangelo G, Fedeli U, Visentin C, Milan G, Fadda E, Spolaore P. Pattern and determinants of hospitalization during heat waves: an ecologic study. BMC Public Health 2007;**7**:200.
13. Theoharatos G, Pantavou K, Mavrakis A, et al. Heat waves observed in 2007 in Athens, Greece: synoptic conditions, bioclimatological assessment, air quality levels and health effects. Environ Res 2010;**110**:152-61.
14. Lin YK, Ho TJ, Wang YC. Mortality risk associated with temperature and prolonged temperature extremes in elderly populations in Taiwan. Environ Res 2011;**111**:1156-63.
15. Wang YC, Lin YK, Chuang CY, et al. Associating emergency room visits with first and prolonged extreme temperature event in Taiwan: a population-based cohort study. Sci Total Environ 2012;**416**:97-104.
16. 宋鴻樟：氣候變遷對台灣公共衛生的衝擊及脆弱度評估與因應策略。台北：行政院國家永續發展委員會，2009。
Sung FC. Public Health Impact, Vulnerability Assessment and Strategies for Response to Climate Change in Taiwan. Taipei: National Council for Sustainable Development, Executive Yuan, R.O.C. (Taiwan), 2009. [In Chinese]
17. The World Meteorological Organization and The World Health Organization, Heat Waves and Health. Guidance on warning system development. Available at: http://www.wmo.int/pages/prog/wcp/ccl/opags/documents/HeatWavesandHealthGuidance_26July2010.pdf. Accessed September 1, 2012.
18. Matthies F, Menne B. Prevention and management of health hazards related to heatwaves. Int J Circumpolar Health 2009;**68**:8-22.
19. EuroHeat. Climate information decision support tool for healt in Europe. Available at: http://www.euroheat-project.org/dwd/flyer_guide.pdf. Accessed July 13, 2012.
20. Michelozzi P, de' Donato FK, Bargagli AM, et al. Surveillance of summer mortality and preparedness to reduce the health impact of heat waves in Italy. Int J Environ Res Public Health 2010;**7**:2256-73.
21. Pascal M, Laaidi K, Ledrans M, et al. France's heat health watch warning system. Int J Biometeorol 2006;**50**:144-53.
22. Fouillet A, Rey G, Wagner V, et al. Has the impact of heat waves on mortality changed in France since the European heat wave of summer 2003? A study of the 2006 heat wave. Int J Epidemiol 2008;**37**:309-17.
23. Wargon M, Guidet B, Hoang TD, Hejblum G. A systematic review of models for forecasting the number of emergency department visits. Emerg Med J 2009;**26**:395-9.
24. Tan J, Kalkstein LS, Huang J, Lin S, Yin H, Shao D. An operational heat/health warning system in

Shanghai. Int J Biometeorol 2004;**48**:157-62.
25. Kim J, Ha JS, Jun S, Park TS, Kim H. The weather watch/warning system for stroke and asthma in South Korea. Int J Environ Health Res 2008;**18**:117-27.
26. Chau PH, Chan KC, Woo J. Hot weather warning might help to reduce elderly mortality in Hong Kong. Int J Biometeorol 2009;**53**:461-8.
27. Kovats RS, Hajat S. Heat stress and public health: a critical review. Annu Rev Public Health 2008;**29**:41-55.
28. Weisskopf MG, Anderson HA, Foldy S, et al. Heat wave morbidity and mortality, Milwaukee, Wis, 1999 vs 1995: an improved response? Am J Public Health 2002;**92**:830-3.
29. Smoyer-Tomic KE, Rainham DG. Beating the heat: development and evaluation of a Canadian hot weather health-response plan. Environ Health Perspect 2001;**109**:1241-8.
30. Lin YK, Chang CK, Li MH, Wu YC, Wang YC. High-temperature indices associated with mortality and outpatient visits: characterizing the association with elevated temperature. Sci Total Environ 2012;**427-428**:41-9.
31. Hajat S, Sheridan SC, Allen MJ, et al. Heat-health warning systems: a comparison of the predictive capacity of different approaches to identifying dangerously hot days. Am J Public Health 2010;**100**:1137-44.
32. Ebi K, Teisberg T, Kalkstein L, Robinson L, Weiher R. Heat watch/warning systems save lives: estimated costs and benefits for Philadelphia 1995 - 1998. Bull Amer Meteorol Soc 2004;**85**:1067-74.
33. Matthies F, Bickler G, Marín NC, Hales S. Heat-Health Action Plans. Denmark: World Health Organization Regional Office for Europe, 2008.
34. 日本環境省：熱中症預防情報。http://www.nies.go.jp/health/HeatStroke/。引用2012/07/13。
Ministry of the Environment Government of Japan. Prevention of hyperthermia. Available at: http://www.nies.go.jp/health/HeatStroke/. Accessed July 13, 2012. [In Japanese]
35. 內政部營建署：台閩地區住宅狀況調查。台北：內政部營建署，2006。
Construction and Planning Agency, Ministry of the Interior. Survey on Housing Conditions in the Taiwan-Fukien Area. Taipei: Construction and Planning Agency, Ministry of the Interior, 2006. [In Chinese]
36. National Health Service. Heatwave plan: 2011. Available at: http://www.nhs.uk/Livewell/Summerhealth/Documents/dh_HeatwavePlan2011.pdf. Accessed July 13, 2012.
37. Bosch X. France makes heatwave plans to protect elderly people. Lancet 2004;**363**:1708.
38. Adaptation and Mitigation - An Integrated Climate Policy Approach. Heat wave warning system. Available at: http://www.amica-climate.net/406.html. Accessed July 13, 2012.
39. Kishonti K, Páldy A, Bobvos J. Heat health watch warning system and communication in Hungary. Available at: http://isee.zuova.cz/past_budapest/Bud_24.pps. Accessed July 13, 2012.
40. Health Protection Branch, Department of Health, Victorian Government. Heatwave Plan for Victoria: Protecting Health and Reducing Harm from Heatwaves. Melbourne, Victoria: Health Protection Branch, Department of Health, Victorian Government, 2011.
41. Queensland Government. Heatwave. Available at: http://www.emergency.qld.gov.au/emq/css/heatwave.asp. Accessed July 13, 2012.
42. Greater Toronto Area Clean Air Council. A scan of municipal heat/health watch warning systems and hot weather response plans. Available at: http://www.cleanairpartnership.org/pdf/heat_report.pdf. Accessed July 13, 2012.
43. Toronto's Medical Officer of Health. Heat alerts and extreme heat alerts. Available at: http://www.toronto.ca/health/heatalerts/. Accessed July 13, 2012.
44. Toronto Public Health. Hot weather response plan, 2012. Available at: http://www.toronto.ca/health/heatalerts/pdf/hwr_plan_2012.pdf. Accessed July 13, 2012.
45. Hamilton Public Health. City of hamilton's heat response. Available at: http://www.hamilton.ca/HealthandSocialServices/PublicHealth/TipsToBeatTheHeat?WT.mc_id=heat&WT.hamilton_redirect_friendly=1. Accessed July 13, 2012.
46. NOAA's National Weather Service. Heat index. Available at: http://www.weather.gov/om/heat/index.shtml. Accessed July 13, 2012.
47. National Weather Service Weather Forecast Office-Milwaukee/Sullivan. NWS heat wave program. Available at: http://www.crh.noaa.gov/mkx/?n=heat_wave. Accessed July 13, 2012.
48. Sheridan SC, Kalkstein LS. Progress in heat watch - warning system technology. Available at: http://www.climateknowledge.org/heat_waves/Doc1005_Sheridan_Kalkstein_HWWS_%20BAMS_2004.pdf. Accessed July 13, 2012.

A literature review of action plans for the impact of heat waves on health

Yu-Kai Lin[1,5], Pay-Liam Lin[2], Ming-Hsu Li[3], Ling-Ya Huang[4], Fung-Chang Sung[4,5], Yu-Chun Wang[6,*]

Many studies have associated episodes of extremely high temperature and prolonged heat waves with increased risks in terms of mortality and morbidity. This study investigated the various health warning systems regarding heat waves that had been proposed by Western countries and reviewed worldwide publications and reports available from 2004 to 2012. Temperature-health associations should be identified before establishing a heat wave warning system. Patients with diabetes mellitus, renal diseases, disabilities, and chronic cardiopulmonary diseases are highly vulnerable to extremely high temperatures. A national weather system is expected to disseminate the heat warning accurately and in a timely fashion. The regional health authority is the lead agency responsible for public health responses to heat and the communication of risks to the public. Application of the temperature index and responses to heat wave warnings vary among areas depending on weather conditions and socio-demographic status. Based on our evaluation, a heat wave warning system would be expected to significantly reduce the impact on health from extremely high temperatures. Studies of temperature-health associations and heat wave warning systems should be established in Taiwan to mitigate the impact of global warming. (*Taiwan J Public Health. 2012;**31**(**6**):512-522*)

Key Words: heat wave, temperature, mortality, warning system

[1] Environmental and Occupational Medicine and Epidemiology Program, Department of Environmental Health, Harvard School of Public Health, Boston, MA, U.S.A.
[2] Department of Atmospheric Sciences, National Central University, Taoyuan, Taiwan, R.O.C.
[3] Graduate Institute of Hydrological & Oceanic Sciences, National Central University, Taoyuan, Taiwan, R.O.C.
[4] Department of Public Health, College of Public Health, China Medical University, Taichung, Taiwan, R.O.C.
[5] Institute of Environmental Health, College of Public Health, National Taiwan University, Taipei, Taiwan, R.O.C.
[6] Department of Bioenvironmental Engineering, College of Engineering, Chung Yuan Christian University, No. 200, Chung-Pei Rd., Chung Li, Taoyuan, Taiwan, R.O.C.
[*] Correspondence author.　E-mail: ycwang@cycu.edu.tw
Received: Jul 23, 2012　Accepted: Sep 28, 2012

The DOI for this manuscript is doi: 10.1175/JAMC-D-12-0109.1

The final published version of this manuscript will replace the preliminary version at the above DOI once it is available.

If you would like to cite this EOR in a separate work, please use the following full citation:

Cheng, F., Y. Hsu, P. Lin, and T. Lin, 2012: Investigation of the effects of different land use and land cover patterns on mesoscale meteorological simulations in the Taiwan area. J. Appl. Meteor. Climatol. doi:10.1175/JAMC-D-12-0109.1, in press.

Investigation of the effects of different land use and land cover patterns on mesoscale meteorological simulations in the Taiwan area

Fang-Yi Cheng [a], Yu-Ching Hsu [a], Pay-Liam Lin [a], Tang-Huang Lin [b]

[a] Department of Atmospheric Sciences, National Central University, Taiwan

[b] Center for Space and Remote Sensing Research, National Central University, Taiwan

Corresponding Author: Fang-Yi Cheng

Email: bonniecheng18@gmail.com

Address: No. 300, Chun-Da Rd., Chung-Li City, Tao-Yuan County, Taiwan.

Telephone: +886-3-4227151-65508

Fax number: +886-3-425-6841

Abstract

The U.S. Geological Survey (USGS) land use (LU) data employed in the Weather Research Forecasting (WRF) model classifies most LU types in Taiwan as mixtures of irrigated cropland and forest, which is not an accurate representation of current conditions. The WRF model released after version 3.1 provides an alternative LU dataset retrieved from 2001 Moderate Resolution Imaging Spectroradiometer (MODIS) satellite products. The MODIS data correctly identifies most LU type distributions, except that it represents the western Taiwan as being extremely urbanized. A new LU dataset, obtained using the 2007 Système Probatoire d'Observation de la Terre (SPOT) satellite images (namely NCU), accurately shows the major metropolitan cities as well as other land types. Three WRF simulations were performed, each with a different LU dataset. Owing to the overestimation of urban area in MODIS data, WRF-MODIS overpredicts daytime temperatures in western Taiwan. Conversely, WRF-USGS underpredicts daytime temperatures. The temperature variation estimated by WRF-NCU falls between those estimated by the other two simulations. Over the ocean, WRF-MODIS predicts the strongest onshore sea breezes, owing to the enhanced temperature gradient between land and sea, while WRF-USGS predicts the weakest onshore flow. The intensity of onshore breeze predicted by WRF-NCU is in between those predicted by WRF-MODIS and WRF-USGS. Over Taiwan Island, roughness length is the key parameter influencing wind speed. WRF-USGS significantly overpredicts the surface wind speed owing to the shorter roughness length of its elements, while the surface wind speeds estimated by WRF-NCU and WRF-MODIS are in better agreement with the observed data.

Keywords: land use data; land–sea breeze; surface energy budget; urbanization; WRF

1. Introduction

The twin processes of urbanization and deforestation occurring over the past few decades have slowly changed the land surface characteristics of Taiwan; these changes modify the local circulation and boundary layer structures. For example, the urbanization process increases temperature due to changes in land surface characteristics, such as increased paving, rooftops, buildings, and other urban infrastructure. Meanwhile, deforestation will affect evapotranspiration processes.

Over the past few decades, land use (LU) and land cover (LC) characteristics in Taiwan have changed substantially. Major cities such as Taipei, Taichung, and Kaohsiung have evolved into megacities, accompanied by the removal of croplands and trees on the outskirts and further urbanization in different parts of the metropolitan area. Such changes have modified local weather conditions, including the land–sea breeze (LSB) circulation and urban heat island effects (Tai et al. 2008).

Taiwan is an island, with the Central Mountain Range (CMR) running from the north of the island to the south. When synoptic-scale forcing is weak, the local circulation is normally dominated by the LSB flow. It has been found that the locally produced high ozone events in Taiwan are typically associated with the LSB circulation (Liu et al. 2002; Cheng et al. 2012). To adequately simulate such locally induced circulations and the atmospheric dynamic and thermodynamic processes, a meteorological model requires a LU/LC dataset that accurately represents present surface characteristics.

LU type is an important land surface parameter describing the exchange of heat and momentum between the land and air. It has been demonstrated that LU/LC data can have a significant effect on meteorological simulations. For example, Cheng and Byun (2008) found that the update of the LU/LC data using LANDSAT-derived datasets successfully improved the prediction of transport and mixing processes in the planetary boundary layer (PBL). Grossman-Clarke et al. (2005) divided the U.S. Geological Survey (USGS) urban category into three classes (urban built-up, urban mesic residential, and urban xeric residential) based on the distribution of vegetation and irrigation. The new LU classification had an apparent impact on turbulent heat fluxes and PBL evolution, and improved the prediction of daytime and nighttime temperatures. Similar studies have also been conducted by Lam et al. (2006), Lo and Quattrochi (2003), and Civerolo et al. (2007).

For applications in the Taiwan area, Tai et al. (2008) performed Weather Research and Forecasting (WRF) simulations by replacing the original USGS 25-category LU data with a new LU dataset prepared by China Technical Consultants, Inc. (CTCI). The new LU data was retrieved from aerial photographs collected from 1999 to 2001. This CTCI LU/LC data correctly identifies the urbanization processes in the cities of Taipei, Taichung, and Kaohsiung; however, most parts of the CMR area were assigned to the mixed forest type LU category without additional detailed classification. The simulation result showed that the model was able to produce a reasonable response to the improved LU data set in terms of ground temperature, latent heat flux, and sensible heat flux. The use of different LU data also contributed to the differences in simulated precipitation, surface temperature, and wind field. One major concern regarding this dataset is that aerial photographs collected from 1999 to 2001 may have failed to capture very recent urban expansion. Another study conducted by Lin et al. (2011) coupled a WRF model with an urban canopy model and reclassified the LU types from 1999 Moderate Resolution Imaging Spectroradiometer (MODIS) satellite images. The simulation results improved predictions of the patterns of accumulated rainfall when compared to the simulation performed using the USGS LU data. Compared to the LU data prepared by CTCI, the 1999 MODIS LU data better represents mountainous areas as a mixture of deciduous and needleleaf forest types while the western side of the country is extremely urbanized.

The current USGS 25-category LU/LC data available for WRF models have a resolution of roughly 1 km (reference year 1990), with some of the components originating from a dataset compiled in the 1970s. This problems introduced by the use of the outdated LU/LC data currently available for WRF meteorological modeling have been remedied with support from the Center for Space and Remote Sensing Research (CSRSR) at National Central University (NCU). New LU/LC data have been derived using 2007 Système Probatoire d'Observation de la Terre (SPOT) satellite images; we refer to these updated LU datasets as NCU.

The objectives of this study are as follows: (1) to demonstrate the effects of using different LU/LC datasets on the simulated meteorological fields; (2) to establish the importance of using accurate LU/LC datasets in the simulated temperature, wind speed, and surface heat flux components and in LSB dynamics; and (3) to improve weather prediction capability in Taiwan through the update of the LU/LC datasets.

The episode characterization and model configuration is described in Section 2. The classification of the NCU LU data and comparison with other LU datasets are described in Section 3. The meteorological simulation results are reviewed in Section 4 and some conclusions are summarized in Section 5.

2. Episode characterization and model configuration

In this study, WRF version 3.2.1 was selected for the meteorological simulation. The WRF model is a mesoscale numerical weather prediction system designed to serve both operational forecasting and atmospheric research needs (Michalakes et al. 2001; Klemp et al. 2007) and it has been widely used in the meteorological modeling community. The simulation episode runs from May 7 to May 11 2007. On May 7, a continental anticyclone originating from Mainland China moved to the South China Sea and Taiwan was under the influence of northeasterly to easterly flow. On May 8, a cold pressure system moved eastward and the wind direction in Taiwan changed to southeasterly. On May 9, the cold high-pressure system left Taiwan and, with the weak influence of the synoptic forcing, the local circulation was dominated by LSB flow in western Taiwan. Figure 1a shows the surface weather map generated by the Japan Meteorology Agency at 0800 local standard time (LST) on May 9 2007. On May 10 and 11, Taiwan was under the weak influence of a cold pressure system that was situated at the northern end of the country. Northern Taiwan was affected by easterly wind, while other areas in Taiwan were affected by weakly southeasterly flow.

The simulation domain is shown in Figure 1b. The coarse domain was set to have a resolution of 81 km, ranging down to resolutions of 27, 9, and 3 km. The finest domain covers Taiwan and the surrounding ocean. The vertical layer was composed of 35 full sigma levels, 16 of them within the lowest 1.5 km, with the lowest layer at around 16 m. The model top was at 100 hPa. The initial and boundary conditions were acquired from the National Center for Environmental Prediction's (NCEP) Final Analysis (FNL) of global data. The analysis nudging approach was applied above the boundary layer for wind, temperature, and water vapor through domains 1 to 3 to allow for larger scale forcing to be used to nudge the model simulation toward the reanalysis field.

The WRF physical options include the following: Kain–Fritsch cumulus schemes (Kain and Fritsch 1993) (not used at the 9- and 3-km domains), a Dudhia shortwave radiation scheme (Dudhia 1989), the Rapid Radiative Transfer Model (RRTM) longwave radiation scheme (Mlawer et al. 1997), a Yonsei University (YSU) PBL scheme (Hong et al. 2006), and the Noah (N: NCEP; O: Oregon State University; A: Air Force; and H: Office of Hydrologic Development) land surface model (LSM) (Chen and Dudhia 2001). The Noah

LSM incorporates the evapotranspiration process, and soil moisture is updated with recent precipitation and evapotranspiration through the initialization data. To fully exploit the new land surface data, a LSM incorporating sufficient physical processes (such as the Noah LSM) is required for meteorological simulation.

Figure 1c illustrates the locations of the Central Weather Bureau (CWB) stations in Taiwan that are used to evaluate model performance. Regions of sloping terrain can be identified based on the topographic height distribution, as shown by the contour line in Figure 1c. The observed data includes temperature and wind speed and direction. In particular, data from the flux tower located at Chiayi is used to evaluate surface flux components. The locations of major metropolitan cities (Taipei, Taoyuan, Taichung, Chiayi, Tainan, Kaohsiung, Ilan, Hualien, and Taitung) are also identified.

3. Land use and land cover data

The NCU LU data was retrieved from SPOT satellite images with resolution of 10 m, which was collected on October 14 2007. There are 11 LU classifications, which had to be remapped to the corresponding USGS type. Table 1 is the corresponding mapping table. Most of the classifications from the NCU data could be assigned directly, as they corresponded to the USGS types; however, classification for croplands and fallow land was not straightforward. Cropland could be remapped either as dry/irrigated cropland or irrigated land depending on the style of cultivation. Taiwan's main crops are rice, sugar cane, fruits, and vegetables. Rice paddy areas were assigned to the irrigated cropland LU; all other crops were classified as dry/irrigated cropland. Information on crop varieties was obtained from the land-use program under the Ministry of the Interior. Area where fallow land was recognized was reclassified. In this study, the episode studied was from May 7 to 11 2007, i.e., during a period where the land was being cultivated. Consequently, the areas classified as fallow land were assigned to the mixed dry/irrigated cropland category if the land was under cultivation; otherwise, they were identified as dry cropland.

Figure 2a shows the LU types at 3-km resolution; from left to right, they are the USGS, MODIS, and NCU classifications. In the USGS data, almost all of the western side of the country was classified as irrigated cropland, a completely outdated classification that does not take into account urbanization processes over recent decades. Additionally, the coverage of forestlands has been erroneously located. The MODIS LU classifications were retrieved from the 2001 MODIS satellite products and were provided from the WRF model released after version 3.1. Compared to the USGS data, the 2001 MODIS LU data more accurately identified the distribution of forestlands; however, urbanization (indicated by the red color in the figure) was overestimated on the western side of the country. In the NCU LU data, the major metropolitan cities were identified accurately, as were irrigated croplands and forested areas. Figure 2b is similar to Figure 2a, but has been enlarged to encompass the area of northern Taiwan.

Table 2 lists the percentages of each LU distribution class by area over the land surface of Taiwan. The major differences in LU distribution among the three LU datasets are reflected in the urban, cropland, and forestland categories. For the USGS data, the coverage of urban areas was very small (<0.2%); 56% of the area was classified as irrigated cropland and 25% as forestlands. Conversely, for the 2001 MODIS data, 17% was classified as urban area, 14% as cropland, and 66% as forestlands. Based on the NCU dataset, 5% was classified as urban, 22% as cropland, and 65% as forestlands.

One disadvantage of the NCU data is that the majority of the LU types over the mountainous regions are classified as mixed forest types without consideration of detailed characteristics, such as whether they are deciduous or needleleaf forests. This limitation is due to the spectral resolution of the onboard satellite sensors, such as the SPOT High Resolution Stereo or the LANDSAT Thematic Mapper, which is too coarse to provide sufficient radiometric features for discrimination. Furthermore, the slope and aspect of the terrain and non-Lambertian surface reflectance create geometric variations from the forest reflectivity, particularly over mountainous areas.

Three WRF sensitivity studies were designed to investigate the impact of different LU datasets (the original USGS, MODIS, and new NCU datasets) on meteorological simulations; we refer to these as WRF-USGS, WRF-MODIS, and WRF-NCU, respectively. The NCU LU data correctly represented the major metropolitan cities as urban LU type. Conversely, the USGS data represented these highly populated regions as underdeveloped rural areas. This difference between the WRF-USGS and WRF-NCU results can be used to study the impact of enhanced anthropogenic activity due to urbanization processes on local-scale meteorological simulation. We focused mainly on a comparison between the WRF-USGS and WRF-NCU simulations, while the results from the WRF-MODIS served as additional information to understand the effects of extreme urbanization processes on meteorological simulations.

4. Simulation results

a. Spatial comparison of the simulations (temperature, wind fields, roughness length and Bowen ratio)

Figures 3 illustrate the 2-m temperature distributions. The upper panel is for the temperature fields averaged from hour 1000 to 1600 LST on 9 May as representative of daytime average. The bottom panel is for the data averaged from hour 2200 LST on 9 May to the 0400 LST on 10 May as representative of nighttime average. During the day, the major temperature difference between WRF-USGS and WRF-NCU appeared in urban areas, particularly in the cities of Taipei, Taichung, and Kaohsiung. WRF-MODIS predicted the highest temperatures in western Taiwan due to the overly urbanized surface structures distributed in that area. Through the night, the temperature was also raised in these cities in the WRF-NCU simulation compared to the WRF-USGS run, while WRF-MODIS still predicted the highest temperatures in western Taiwan. Near the mountainous regions, even though the LU distribution was distinct among the three datasets, the simulated temperature fields behaved similarly in all model results. In fact, the temperature distribution over the CMR region was affected more by topographical height than by LU/LC changes. The comparison indicated that, even though the NCU LU data could not distinguish detail in the mountainous regions, this did not have a significant impact on temperature comparisons in the CMR region, as it was the terrain height that played the major role in the determination of the temperature distribution.

Figure 4 shows a comparison of wind fields averaged from hour 1000 to 1600 LST on 9 May (upper panels) and from hour 2200 LST on 9 May to the 0400 LST on 10 May 2007. The leftmost plot is from the WRF-NCU run. The center plot shows the difference of wind fields, with WRF-USGS subtracted from WRF-NCU and the rightmost plot the difference with WRF-MODIS subtracted from WRF-NCU. During the day, the local circulation was dominated by the onshore sea breeze flow. WRF-NCU predicted stronger onshore flow than WRF-USGS in the offshore areas of western Taiwan, particularly near the coastline of Taoyuan (just south of Taipei) and the Tainan region, that was caused by the enhanced land–sea temperature gradient from WRF-NCU simulation. Among the three simulations, WRF-MODIS predicted the strongest onshore flow in coastal regions of western Taiwan. Over Taiwan Island, WRF-NCU predicted lower wind speeds than WRF-USGS, owing to the specification of longer roughness length (Z_0) elements (urban structures and forestlands). Through the night, the land breeze flow was formed over the land and offshore areas of western Taiwan. WRF-NCU predicted weaker offshore flow than WRF-USGS over the areas of megacities such as Taipei and Taichung due to the reduced temperature gradient between the land and the sea. WRF-MODIS predicted the weakest offshore flow of all the runs, especially near the coastal areas on the northwestern side of Taiwan. The differences in urban regions were higher during the nighttime than the daytime.

Figure 5 shows the distribution of Z_0 utilized for each individual WRF simulation. In the WRF model, the specified value of Z_0 was obtained from a look-up landuse table (Chen and Dudhia 2001) (i.e., by knowing the underlying LU type, land surface parameters such as Z_0 were set accordingly); as a result, Z_0 distribution was in accordance with the patterns of LU type. Clearly, the lowest value of Z_0 was used in the WRF-USGS run. In the NCU LU data, most of the LU types were replaced with urban and forestlands, which possess higher Z_0 than the classifications of the USGS LU data. The higher Z_0 would slow the wind flow, as indicated in the center plot of Figure 4. The major difference of Z_0 between the simulations using MODIS and NCU LU data was in western Taiwan, where a higher Z_0 value was used in the WRF-MODIS run. WRF-NCU predicted higher wind speed than WRF-MODIS in the area where urban type was identified in MODIS LU data but not in NCU LU data (rightmost plot of Figure 4).

Figure 6 shows the distribution of the Bowen ratio, which is defined as the ratio of the sensible heat flux (SHF) to the latent heat flux (LHF), at 1200 LST on May 9 2007. As expected, the Bowen ratio was smaller over vegetated surfaces where most of the energy goes into transpiration and evaporation, and larger over dry surfaces where most of the energy goes into SHF (Stull 1988). At 1200 LST, the Bowen ratios were consistently higher (above 5) in the urban areas where higher SHF and lower LHF were simulated. The distribution of the Bowen ratio exhibited a strong correspondence to patterns of LU type. WRF-MODIS predicted the highest Bowen ratio in western Taiwan, while the distributions predicted by WRF-USGS and WRF-NCU were similar, except in areas where an urban LU type was classified from NCU LU data. The Bowen ratio from WRF-USGS was less than one in western Taiwan, indicating that most of the energy was used for evapotranspiration from the croplands. The distribution of the Bowen ratio behaved similarly in the CMR region for all three simulations. This indicates that the change of the LU types over the mountainous regions does not have significant effect in surface sensible and latent heat fluxes predictions. As mentioned before, the terrain height affects the temperature fields more than the LU/LC changes; besides, the land surface parameters supplied from the look-up landuse table does not differ much for different forest types.

b. Vertical cross-sectional analysis

Figure 7a shows a vertical cross-sectional plot across the Taipei metropolitan area (refer to Figure 2b for the location) at 1200 LST on May 9 2007 from the WRF-NCU simulation. Across this line, the dominant LU type in the USGS data was irrigated cropland, while the NCU data classified it as a mixture of urban, cropland, and forests, and the MODIS data as completely urbanized area. At that time, onshore and upslope flow was simulated in the WRF-NCU simulation. Over the ocean, the onshore sea breeze flow exhibited a smooth and consistent pattern with very weak vertical motion. Over the landside, due to the effects of surface heating processes, a strong upward motion was simulated at the hilltop and over Taipei City (near longitude 121.5°E) with a compensating downward movement simulated adjacently. Figure 7b shows the difference in the wind vectors and vertical wind speed simulated by WRF-USGS and WRF-NCU (positive means higher from WRF-NCU). WRF-

NCU showed a stronger onshore sea breeze flow in offshore areas than the WRF-USGS run. Over the land areas, WRF-NCU predicted stronger convergent flow and upward motion than WRF-USGS, particularly near longitude 121.5°E, where the major metropolitan area of Taipei is located. The analysis indicated that, with the updated LU/LC data, the underlying surface was replaced with impervious structures such as roads, parking lots, and buildings, which increased surface heating processes and induced stronger upward motions in Taipei.

c. Time series comparison (temperature, wind fields, surface heat fluxes and soil moisture)

Figures 8a and 8b show a time series comparison of 2-m temperature from the WRF simulations averaged for urban and non-urban areas, respectively. The urban areas refer to grid points where an urban LU type was specified, while non-urban areas are otherwise indicated. As shown in Figure 2 and Table 2, the distributions of urban areas were distinct for the three simulations. The difference was more apparent for urban areas than non-urban areas. WRF-MODIS predicted the highest temperatures in urban areas, while WRF-USGS predicted the lowest. The temperature distribution from WRF-NCU was in between the other two simulations. For non-urban areas, WRF-NCU predicted higher temperatures during the day and slightly lower temperatures during the night compared to the other simulations.

Figure 9 illustrates the surface wind speed comparison. In the urban areas, WRF-USGS predicted the strongest wind speed, with differences between this simulation and the others reaching 2 m s^{-1}; WRF-NCU predicted the lowest wind speeds. For non-urban areas, the difference between the three simulations was small, with WRF-NCU predicting slightly lower wind speeds than the other simulations.

Figure 10 shows a comparison with the observed surface data at Taipei station. This station was classified as urban type in both MODIS and NCU LU data, which represented actual conditions correctly; however, the USGS data treated this site as a type of shrubland. WRF-MODIS predicted the highest 2-m temperatures, while predictions from the other two were similar. For wind speed comparison, there was significant overprediction by WRF-USGS but the other two runs were in better agreement with the observed data. For the comparison of wind direction, the flow was mostly dominated by northeast to easterly flow, except for a time when LSB flow was observed on May 9. All three runs captured the variations of flow patterns and the turning of the LSB circulation quite well.

Figure 11 shows a comparison of the simulated surface energy fluxes at Taipei station on May 9. All the simulations predicted higher SHF than LHF. The components of the surface energy fluxes from the shrubland type behaved similarly to those of the urban type. The similarity can be attributed to the use of a high canopy resistance (R_c), which is an important factor determining the rate of evaporation and transpiration from inside the vegetation canopy to the air; this parameter was calculated according to the formulations of Noilhan and Planton (1989) with the corresponding parameters given from the look-up landuse table. R_c was calculated according to equation (1) (Chen and Dudhia, 2001).

$$R_c = \frac{R_{c\,\min}}{LAIF_1F_2F_3F_4} \quad (1)$$

Here, LAI is the leaf area index, F_1 represents the effects of solar radiation, F_2 takes into account the effect of water stress on surface resistance, F_3 represents the effects of vapor pressure deficit of the atmosphere, and F_4 represents air temperature dependence on surface resistance. R_{cmin} is the minimum stomatal resistance. In fact, the default R_{cmin} defined for shrubland from the look-up table is large (currently 300 s m^{-1}), which would inhibit evapotranspiration processes. As a result, higher SHF and lower LHF were simulated by WRF-USGS at the Taipei site. The verification of the surface heat flux at this urban site was not possible due to the lack of the observed datasets.

Figures 12 and 13 are similar to Figures 10 and 11 but for the Chiayi site, which is located in a rural area. The site was classified as an urban type from the MODIS data and as irrigated land from the NCU and USGS datasets. WRF-MODIS showed the highest temperatures and a consistent overestimation, while the other two runs agreed better with the observed data. The wind speed comparison was similar for all three runs, with WRF-MODIS showing the lowest wind speed most of the time. For wind direction, unlike the Taipei site, there was a clear turning of the LSB circulation throughout the whole episode at the Chiayi site. This also indicated the distinct atmospheric conditions in northern and southern Taiwan during this episode. As shown in Figure 13, WRF-MODIS predicted higher SHF than LHF, with very small LHF simulated, while the other two runs behaved similarly with higher LHF than SHF predicted. WRF-MODIS produced the highest estimated values of downward ground heat flux (GHF) among the three simulations.

Fortunately, a flux measurement site located near the Chiayi station was available for comparison. The site is surrounded by rice paddies and was classified as an urban type from the MODIS data and as irrigated lands from both the USGS and NCU data. Figure 14 compares the simulated SHF and LHF with the observed components. All three runs consistently overpredicted the daytime SHF, with the highest bias from WRF-MODIS. The overprediction from WRF-MODIS contributed to the high temperature bias at the Chiayi site.

The consistent overprediction of SHF can be attributed to the reason that the soil moisture content is too low. Figure 15 shows a comparison of the simulated soil moisture in different soil layers obtained from the three WRF simulations. In the WRF modeling, the soil moisture was initially provided from the reanalysis fields (NCEP FNL data) and updated with recent precipitation and runoff processes. In the rice paddy areas, the underlying soil fields are damp due to high water quantities supplied for irrigation; however, this localized feature is not reflected in the NCEP FNL data due to the coarse spatial resolution (one-degree). As a result, all three runs showed the similar distributions of soil moisture throughout the whole period, regardless of the differences in LU type (urban vs. irrigated cropland) specified for different WRF simulations. Due to the lack of the observed datasets, the evaluation and comparison of the soil moisture content is not possible. However, Tsai et al. (2007) found that the maximum soil moisture could reach 0.68 in a rice paddy site in central Taiwan. The simulated soil moisture at the Chiayi site was lower than 0.45 throughout the study period and significantly lower than the observed data based on Tsai et al. (2007). The issues of soil moisture availability are currently under investigation, so we offer no further discussion on this matter at this time.

For LHF, both WRF-USGS and WRF-NCU agreed well with the measured flux; however, WRF-MODIS showed generally quite low LHF.

The analysis of the surface heat flux components revealed distinct characteristics of surface energy partition processes at the Taipei and Chiayi sites. The land surface was mostly paved with concrete and asphalt in Taipei but covered by irrigated cropland at the Chiayi site. The misrepresentation of LU type could have erroneously predicted the surface heat flux components, which in turn could have caused the temperature biases near the surface layer.

d. Hodograph analysis

The hodograph plot was generated to demonstrate the LSB circulation. Figure 16 shows the comparison at the Taipei site on May 9. The observed data clearly showed a southeasterly flow during the night and morning hours that became stagnant from 0800 to 1000 LST and turned to northwesterly flow along with the onset of the onshore sea breeze flow from 1000 to 1100 LST. The simulations all show a clockwise turning of the wind direction on May 9. Compared to the observed data, the turning of the wind direction occurred one to two hours earlier in both the WRF-USGS and WRF-MODIS simulations (around 0800 to 1000 LST) (Figures 16b, 16c). The turning of the wind direction was better simulated by WRF-NCU, where it took place between 1000 and 1100 LST, close to the onset time of the sea breeze flow. The nighttime wind shifted slightly toward the northeasterly direction in the WRF-MODIS and WRF-NCU simulations. The southeasterly offshore flow was better simulated by WRF-USGS; however, the nighttime wind speed was overestimated.

e. Statistical analysis

Table 3 shows the root mean square error (RMSE) comparison for temperature and wind speed at the Taipei and Chiayi sites. At the Taipei site, the WRF-NCU run exhibited the best performance for both temperature and wind speed. At the Chiayi site, WRF-NCU showed good statistical scores for temperature, while WRF-MODIS produced the worst comparison. Both WRF-MODIS and WRF-NCU exhibited better statistical scores for wind speed than WRF-USGS. The RMSE value of wind speed from the WRF-USGS run was large, particularly at the Taipei site.

Table 4 shows the bias and RMSE comparison of the temperature and wind speed for all the CWB surface sites, the locations of which are illustrated in Figure 1c. WRF-MODIS (WRF-USGS) overpredicted (underpredicted) temperature, while WRF-NCU agreed best with the observed data. For the wind speed comparison, WRF-USGS showed the least agreement, while the other two runs were comparable. The calculation of the bias and RMSE values for all the surface sites indicated that surface temperature and wind speed prediction could be improved with the updated and accurate NCU LU/LC data.

5. Summary and conclusions

The default USGS data currently utilized in WRF modeling systems classifies most of the LU types in Taiwan as irrigated croplands and erroneously locates forestlands. An alternative LU dataset retrieved from 2001 MODIS satellite products correctly identified the majority of LU type distributions, except the extremely urban nature of the western side of the country. Both USGS and MODIS datasets misrepresented the LU/LC types in Taiwan, while the new NCU LU data correctly reflected the recent development of urban structures as well as the distributions of croplands and forestlands.

The WRF simulation results with respect to different LU/LC datasets demonstrated that the usage of different LU/LC data modified surface energy fluxes, surface meteorological parameters, and LSB circulation. For a typical day dominated by the local LSB circulation on May 9 2007, WRF-MODIS predicted the highest temperature in western Taiwan; WRF-USGS predicted the lowest, while WRF-NCU results fell between the other two simulations. The onshore sea breeze flow was the strongest in the WRF-MODIS simulation due to the enhanced temperature gradient predicted in western Taiwan. Over land areas, the wind speed was strongest in WRF-USGS but was reduced significantly in WRF-MODIS and WRF-NCU due to the specification of longer roughness length elements that would have increased the surface drag and slowed wind flow. The onset time of the onshore sea breeze flow was better simulated by the WRF-NCU simulation at Taipei site.

Comparison with the observed surface datasets indicated overprediction of the temperature by WRF-MODIS, underprediction by WRF-USGS, and best agreement with WRF-NCU. For the wind speed comparison, WRF-USGS consistently overpredicted throughout the whole episode, while WRF-MODIS and WRF-NCU were in better agreement with the observed data. The statistical analysis demonstrated that WRF-NCU outperforms the other simulations. In addition, a flux measurement site located at Chiayi site allowed us to evaluate the simulated surface flux components. All three runs overpredicted SHF, with the highest bias from WRF-MODIS. Both WRF-USGS and WRF-NCU showed good agreement of the simulated LHF with the observed value.

The NCU LU/LC data lies between two extreme and apparently incorrect LU/LC data from the USGS and MODIS classifications. The more accurate representation of the NCU LU/LC databases in the area of Taiwan successfully improved local-scale meteorological simulations, particularly for the wind speed and temperature fields. The results indicate the need for accurate LU data to adequately simulate the surface energy budget, surface meteorological fields, and LSB dynamics in Taiwan. The application of the correct LU/LC datasets is expected to improve numerical weather simulations and enhance weather forecasting capability in the Taiwan area.

Acknowledgments

This study was supported by the research project “Study effect of land surface processes on boundary layer meteorological simulation in Taiwan” supported by the National Science Council, Taiwan, under grant number NSC-98-2111-M-008-024-MY2.

References:

Chen, F., and J. Dudhia, 2001: Coupling an advanced land surface-hydrology model with the Penn State-NCAR MM5 modeling system. Part I: model implementation and sensitivity. *Mon. Wea. Rev.*, **129**, 569–585.

Cheng, F.-Y., and D.W. Byun, 2008: Application of high resolution land use and land cover data for atmospheric modeling in the Houston-Galveston metropolitan area: part I, meteorological simulation results. *Atmos. Environ.*, **42**, 7795–7811.

Cheng, F.-Y., S.-C. Chin, and T.-H. Liu, 2012: The role of boundary layer schemes in meteorological and air quality simulations of the Taiwan area. *Atmos. Environ.*, **54**, 714–727.

Civerolo, K., C. Hogrefe, B. Lynn, J. Rosenthal, J. Ku, W. Solecki, J. Cox, C. Small, C. Rosenzweig, and R. Goldberg, 2007: Estimating the effects of increased urbanization on surface meteorology and ozone concentrations in the New York City metropolitan region. *Atmos. Environ.*, **41**(9), 1803–1818.

Dudhia, J., 1989: Numerical study of convection observed during the winter monsoon experiment using a mesoscale two-dimensional model. *J. Atmos. Sci.*, **46**, 3077–3107.

Grossman-Clarke, S., J. A. Zehnder, W. L. Stefanov, Y. Liu, and M. A. Zoldak, 2005: Urban modifications in a mesoscale meteorological model and the effects on near-surface variables in an arid metropolitan region. *J. Appl. Meteor.*, **44**, 1281–1297.

Hong, S.-Y., Y. Noh, and J. Dudhia, 2006: A new vertical diffusion package with explicit treatment of entrainment processes. *Mon. Wea. Rev.*, **134**, 2318–2341.

Kain, J. S., and J. M. Fritsch, 1993: Convective parameterization for mesoscale models: The Kain-Fritsch scheme. *The representation of cumulus convection in numerical models, Meteor. Monogr,,* No. 24, Amer. Meteor. Soc., 165–170.

Klemp, J. B., W. C. Skamarock, and J. Dudhia, 2007: Conservative split-explicit time integration methods for the compressible nonhydrostatic equations, *Mon. Wea. Rev.*, **135**, 2897–2913.

Lam, J.S.L., A.K.H. Lau, and J.C.H. Fung, 2006: Application of refined land-use categories for high resolution mesoscale atmospheric modeling. *Bound. Layer Meteor.*, **119**, 263–288.

Lin, C.Y., W. C. Chen, P.-L. Chang, and Y.F. Sheng, 2011: Impact of the urban heat island on precipitation over a complex geographic environment in northern Taiwan. *J. Appl. Meteorol. Climatol.*, **50**, 339–353.

Liu, K.-Y., Z. Wang, and L.F. Hsiao, 2002: A modeling of the sea breeze and its impacts on ozone distribution in northern Taiwan. *Environ. Modell. Softw.,* **17**, 21–27.

Lo, C.P., and D.A. Quattrochi, 2003: Land Use and land cover change, urban heat island phenomenon, and health implications: a remote sensing approach. *Photogram. Eng. Remote Sensing*, **69**, 1053–1063.

Michalakes, J., S. Chen, J. Dudhia, L. Hart, J. Klemp, J. Middlecoff, and W. Skamarockm, 2001: Development of a next generation regional weather research and forecast model, in Developments in Teracomputing, *Proc. of the Ninth ECMWF Workshop on the Use of High Performance Computing in Meteorology*, Singapore, World Sci., 269–276.

Mlawer, E. J., S. J. Taubman, P. D. Brown, M. J. Iacono, and S. A. Clough, 1997: Radiative transfer for inhomogeneous atmospheres: RRTM, a validated correlated-k model for the longwave. *J. Geophys. Res.*, **102**, 16663-16682.

Noilhan, J., and S. Planton, 1989: A simple parameterization of land surface processes for meteorological models. *Mon. Wea. Rev.*, **117**, 536–549.

Stull, R. B., 1988: *An Introduction to Boundary Layer Meteorology*. Atmospheric Sciences Library, Kluwer Academic Publishers, Dordrecht, 670 pp.

Tai, L.-H., J.-S. Hong, B.-J. Tsuang, J.-L. Tsai, and P.-J. Ni, 2008: Update of Taiwan landuse data in WRF model. *J. Atmos. Sci.*, **36**(1), 43–61.

Tsai, J.-L., B.-J. Tsuang, and P.-S. Lu, 2007: Surface energy components and land characteristics of a rice paddy. *J. Appl. Meteor.*, **46**, 1879–1900.

Lists of figure caption:

Figure 1. (a) Surface weather map at 0800 LST on 9 May 2007, (b) model simulation domain, and (c) observation monitoring stations (circles) with dashed contour line representing the terrain height (unit: m).

Figure 2. (a) LU distribution from USGS (left), MODIS (center) and NCU data (right) at 3-km resolution, (b) enlarge to encompass the area of northern Taiwan.

Figure 3. Comparison of 2-m temperature (^{0}C) averaged from hour 1000 to 1600 LST on 9 May (upper panels) and from hour 2200 LST on 9 May to the 0400 LST on 10 May (lower panels) obtained from simulations using USGS (left), MODIS (middle) and NCU (right) LU data.

Figure 4. Comparison of surface wind fields (m s^{-1}) averaged from hour 1000 to 1600 LST on 9 May (upper panels) and from hour 2200 LST on 9 May to the 0400 LST on 10 May (lower panels). Leftmost plot is from WRF-NCU and color bar is shown in the top. Center plot is the difference with WRF-USGS subtracted from WRF-NCU. Rightmost plot is the difference with WRF-MODIS subtracted from WRF-NCU. For the difference plot, the color bar is shown in the bottom.

Figure 5. Distribution of roughness length utilized for WRF-USGS (left), WRF-MODIS (center), and WRF-NCU (right) simulations.

Figure 6. Bowen ratio distribution at 1200 LST on 9 May 2007 from WRF-USGS (left), WRF-MODIS (center), and WRF-NCU (right) simulations.

Figure 7. Vertical cross-sectional analysis at 1200 LST on 9 May 2007 from (a) WRF-NCU simulation. Shaded color is for vertical wind speed greater than 0.5 cm s^{-1}. Contour line is for equivalent potential temperature. Wind arrows represent the wind vectors of the $\tilde{u}$ and $\tilde{w}$ wind components (m s^{-1}) ($\tilde{u}$: wind vector along the cross-section line, $\tilde{w}$: 10 times of the vertical wind speed). (b) is difference plot with WRF-USGS subtracted from WRF-NCU. The shaded color is for the difference of vertical wind speed greater than 0 cm s^{-1}.

Figure 8. Time series comparison of the temperature from WRF simulations averaged over space for (a) urban areas and (b) non-urban areas.

Figure 9. Similar to Figure 8 but for wind speed.

Figure 10. Time-series comparison of 2-m temperature (top), wind speed (middle) and wind direction (degree) (bottom) at Taipei station.

Figure 11. Comparison of simulated sensible heat flux (SHF), latent heat flux (LHF), ground heat flux (GHF) and net radiation (NET) at Taipei site from WRF-USGS (top), WRF-MODIS (middle) and WRF-NCU (bottom) simulations.

Figure 12. Time-series comparison of 2-m temperature (top), wind speed (middle) and wind direction (degree) (bottom) at Chiayi station.

Figure 13. Comparison of simulated sensible heat flux (SHF), latent heat flux (LHF), ground heat flux (GHF) and net radiation (NET) at Chiayi site from WRF-USGS (top), WRF-MODIS (middle) and WRF-NCU (bottom) simulations.

Figure 14. Comparison of the SHF (top) and LHF (bottom) near the Chiayi station.

Figure 15. Comparison of the simulated soil moisture at Chiayi station from WRF simulations using USGS (top), MODIS (middle) and NCU (bottom) LU data at different soil layers. Z1, Z2, Z3 and Z4 represent thickness of each soil layer and are 0.1, 0.3, 0.6, and 1.0 m respectively from the ground surface to the bottom.

Figure 16. Hodograph comparison at Taipei site on May 9 2007 from (a) observation, (b) WRF-USGS, (c) WRF-MODIS and (d) WRF-NCU. The arrows pointing from the center to the location of number identifier (0~23) represents where the wind comes at the corresponding hour. The distance between the center and the location of number identifier indicates the wind speed (m s^{-1}).

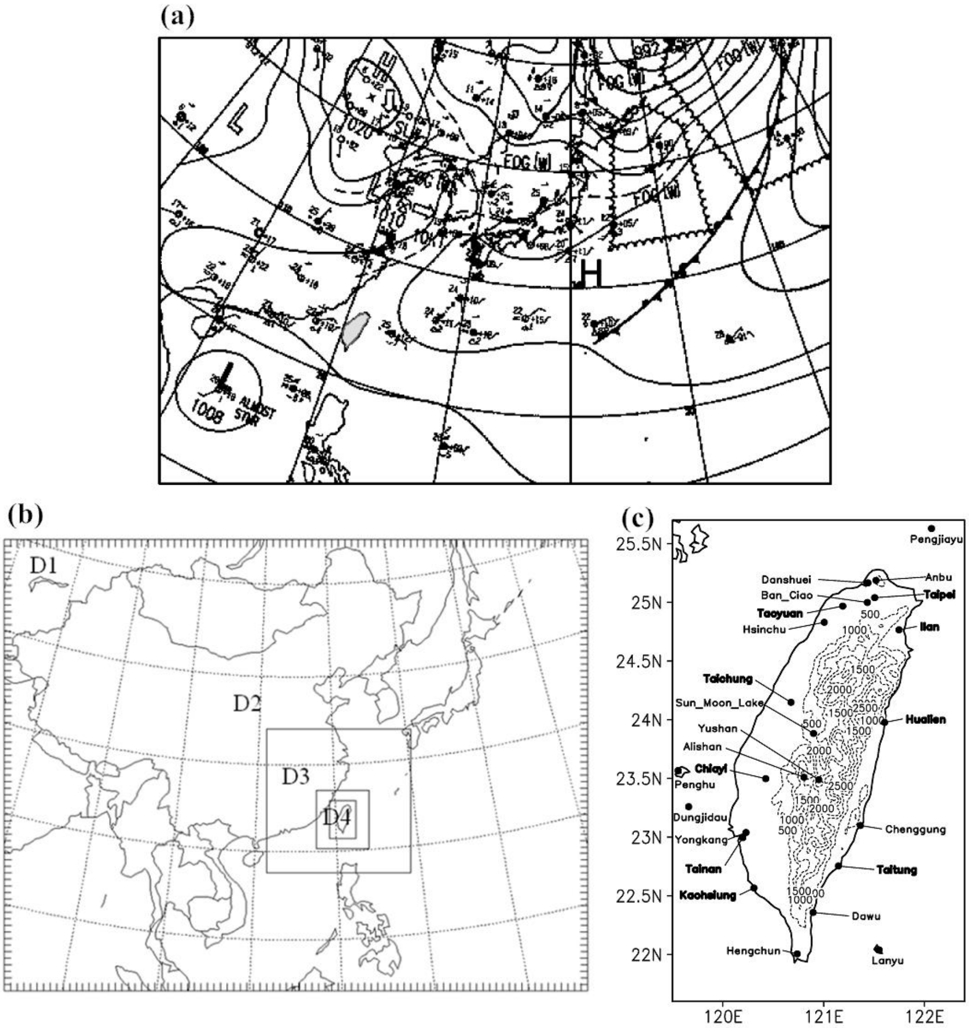

Figure 1. (a) Surface weather map at 0800 LST on 9 May 2007, (b) model simulation domain, and (c) observation monitoring stations (circles) with dashed contour line representing the terrain height (unit: m).

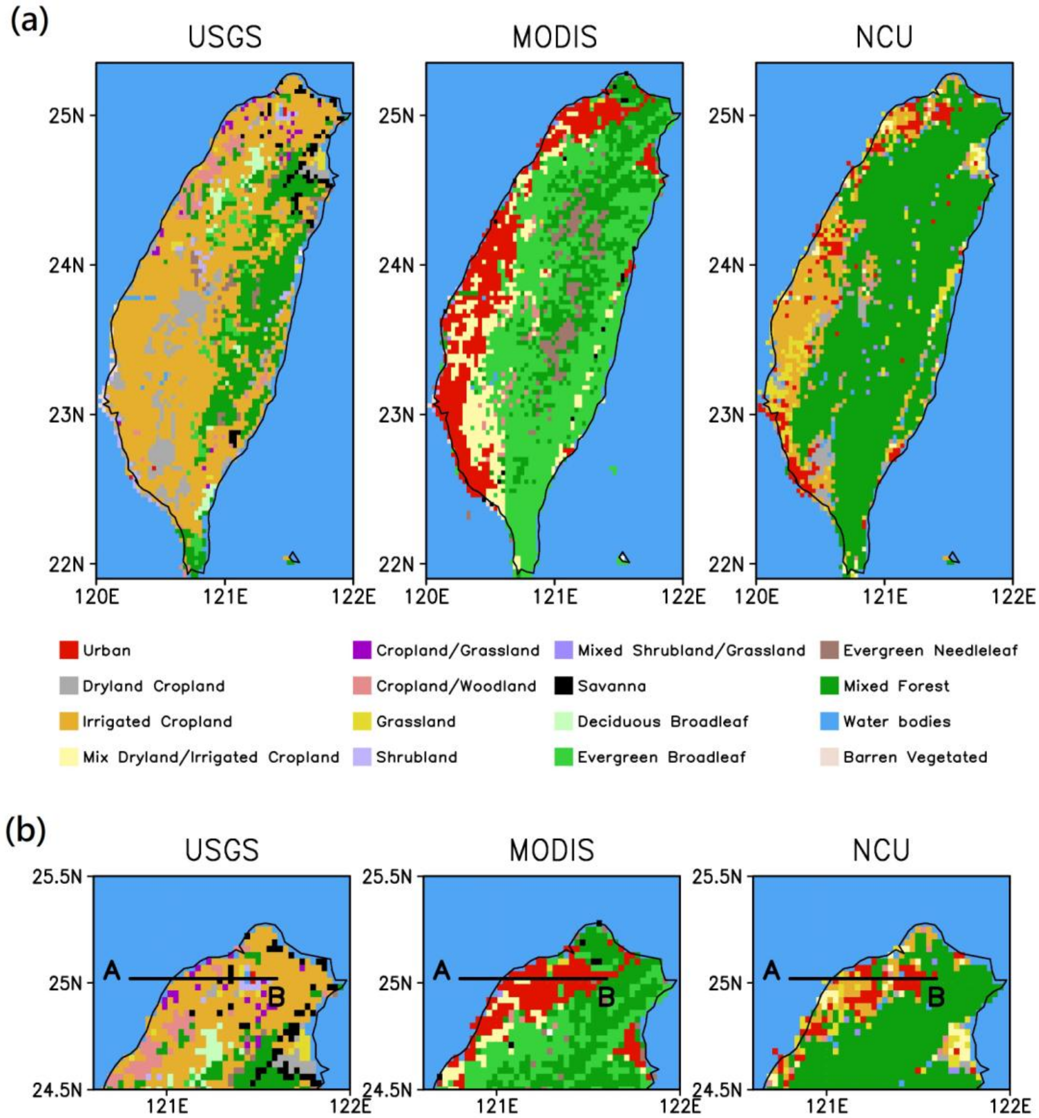

Figure 2. (a) LU distribution from USGS (left), MODIS (center) and NCU data (right) at 3-km resolution, (b) enlarge to encompass the area of northern Taiwan.

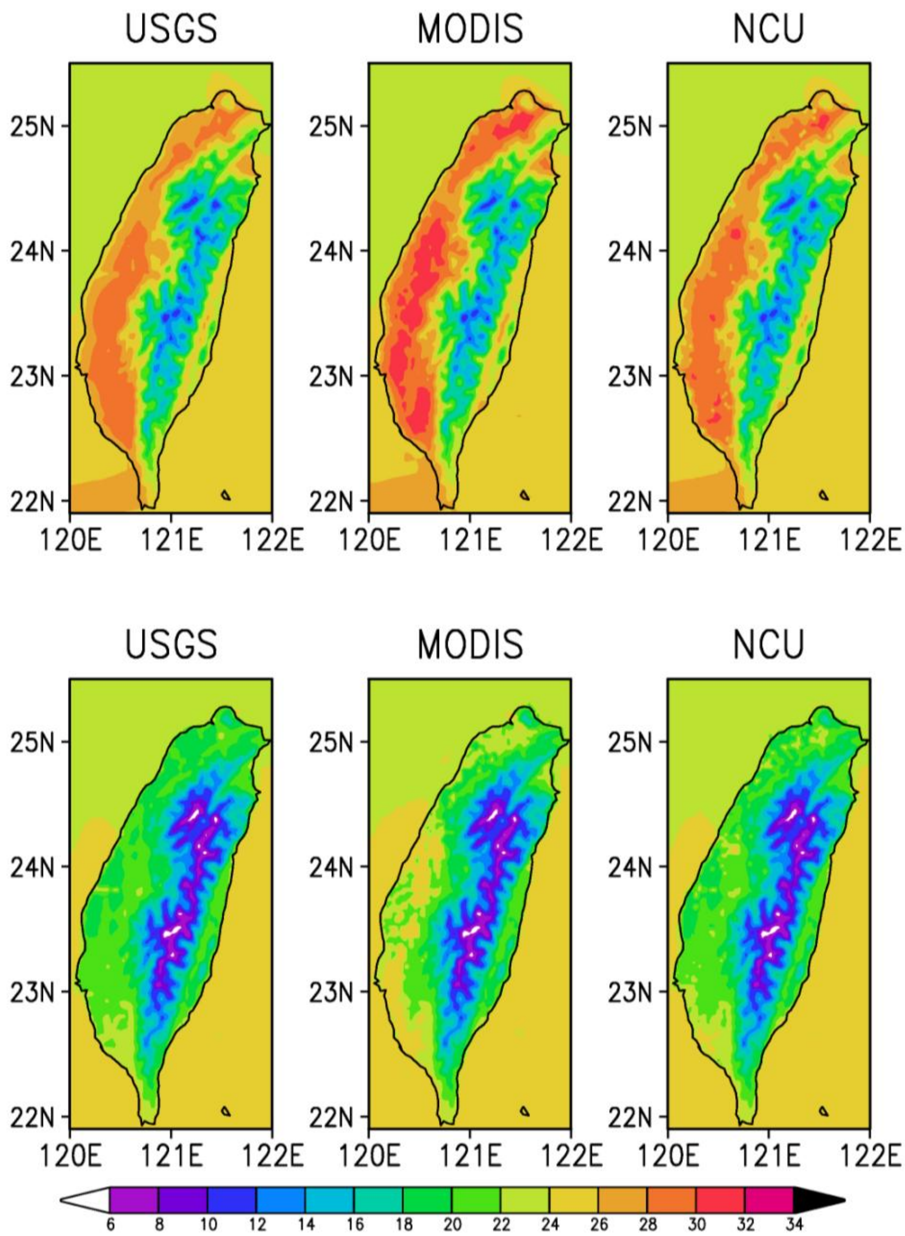

Figure 3. Comparison of 2-m temperature (^{0}C) averaged from hour 1000 to 1600 LST on 9 May (upper panels) and from hour 2200 LST on 9 May to the 0400 LST on 10 May (lower panels) obtained from simulations using USGS (left), MODIS (middle) and NCU (right) LU data.

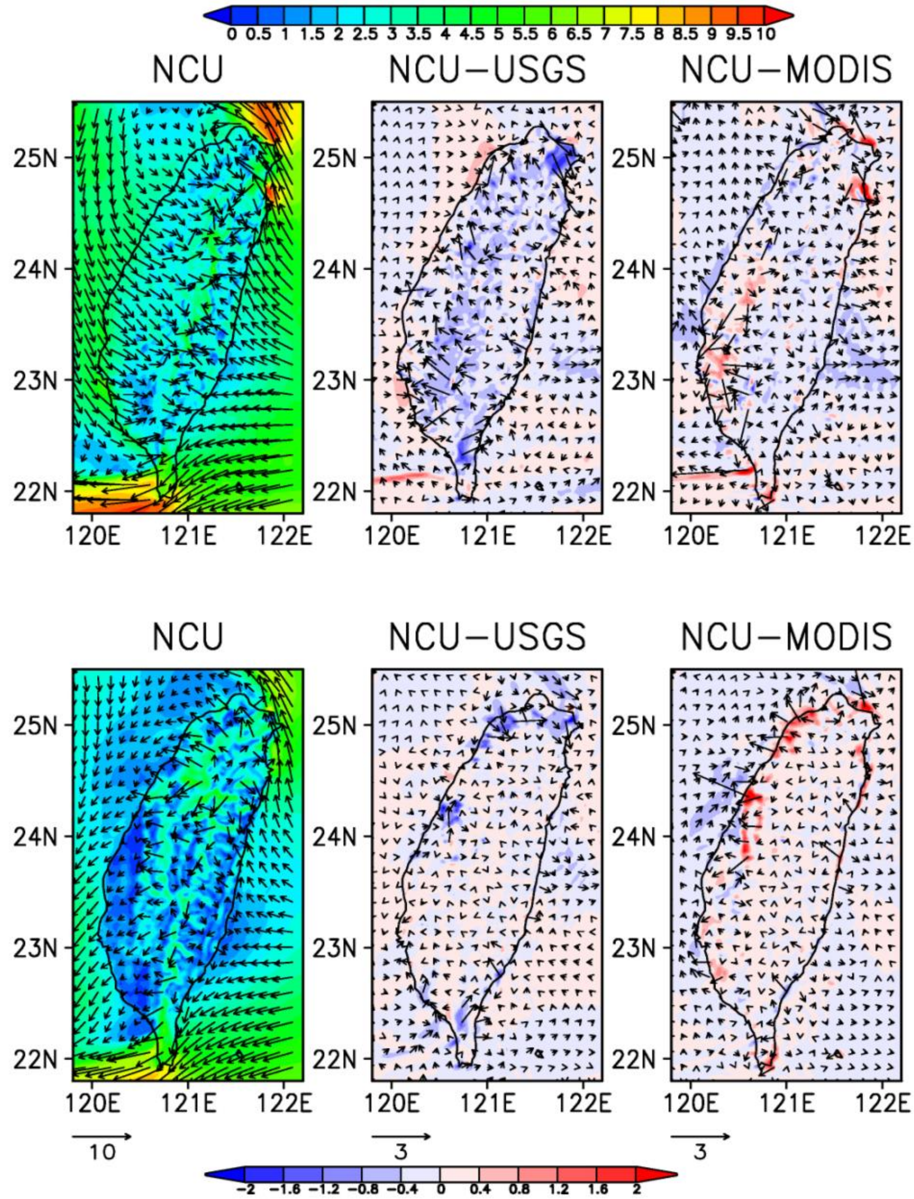

Figure 4. Comparison of surface wind fields (m s^{-1}) averaged from hour 1000 to 1600 LST on 9 May (upper panels) and from hour 2200 LST on 9 May to the 0400 LST on 10 May (lower panels). Leftmost plot is from WRF-NCU and color bar is shown in the top. Center plot is the difference with WRF-USGS subtracted from WRF-NCU. Rightmost plot is the difference with WRF-MODIS subtracted from WRF-NCU. For the difference plot, the color bar is shown in the bottom.

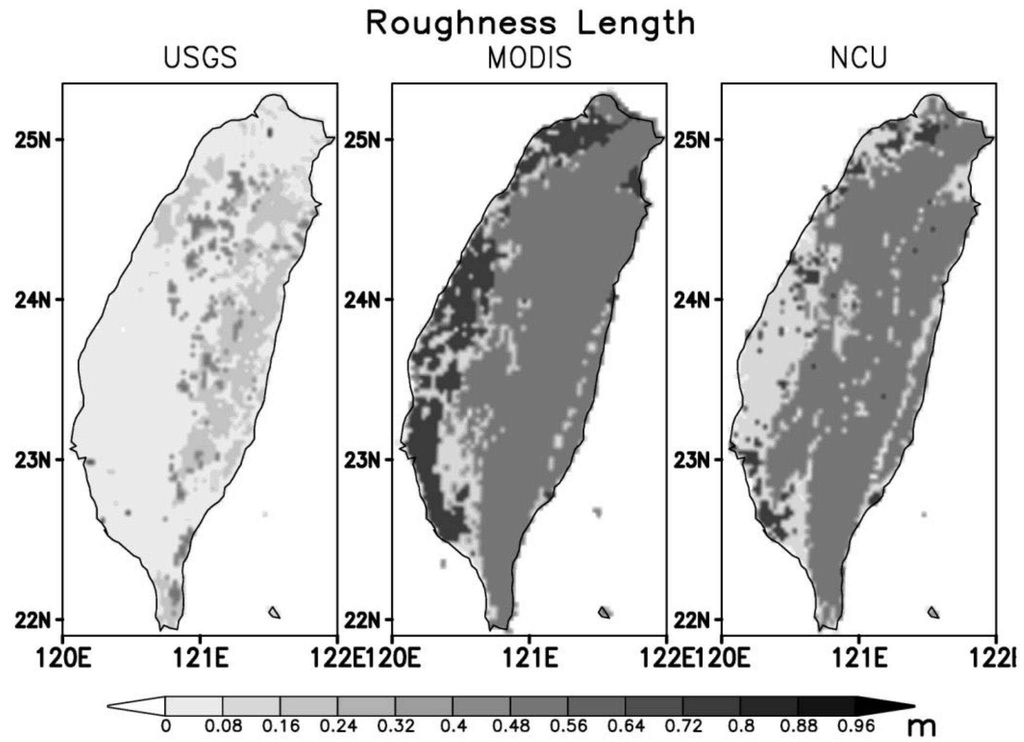

Figure 5. Distribution of roughness length utilized for WRF-USGS (left), WRF-MODIS (center), and WRF-NCU (right) simulations.

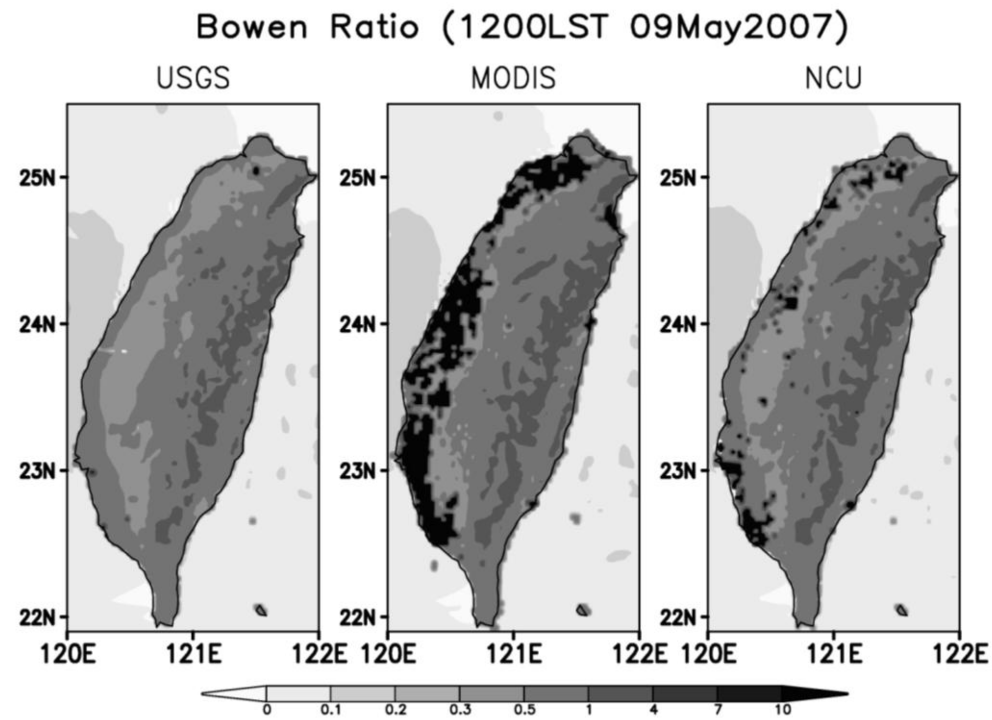

Figure 6. Bowen ratio distribution at 1200 LST on 9 May 2007 from WRF-USGS (left), WRF-MODIS (center), and WRF-NCU (right) simulations.

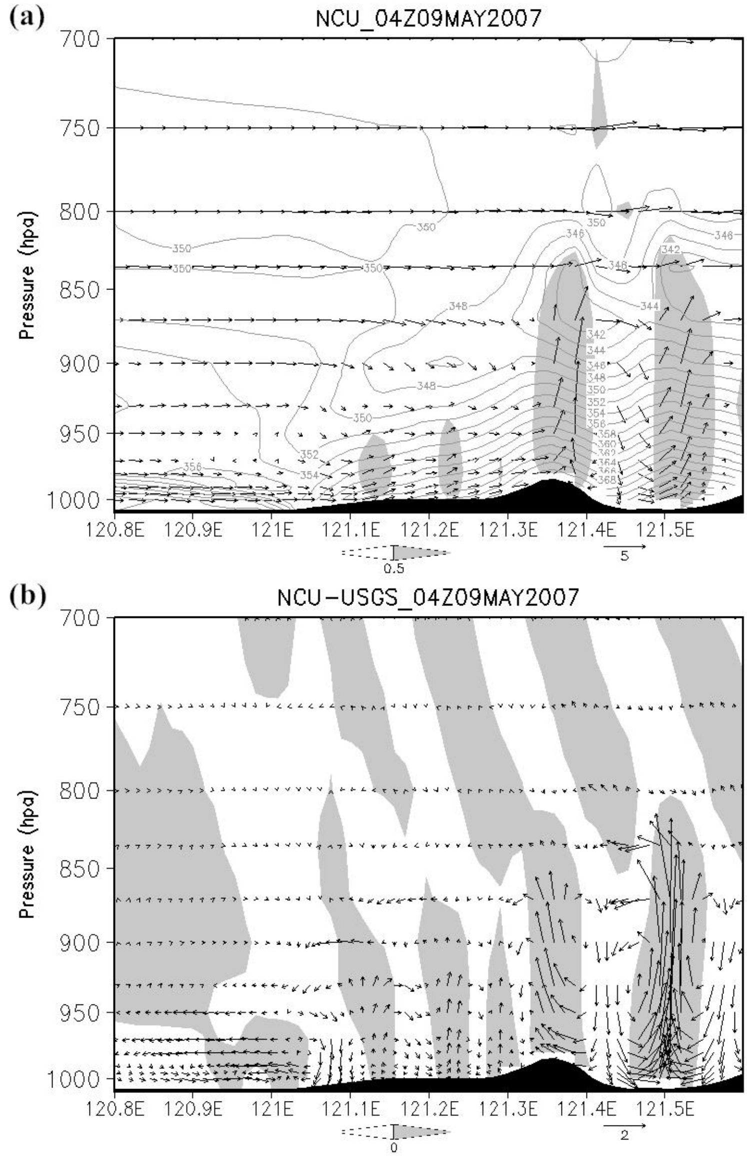

Figure 7. Vertical cross-sectional analysis at 1200 LST on 9 May 2007 from (a) WRF-NCU simulation. Shaded color is for vertical wind speed greater than 0.5 cm s^{-1}. Contour line is for equivalent potential temperature. Wind arrows represent the wind vectors of the $\tilde{u}$ and $\tilde{w}$ wind components (m s^{-1}) ($\tilde{u}$: wind vector along the cross-section line, $\tilde{w}$: 10 times of the vertical wind speed). (b) is difference plot with WRF-USGS subtracted from WRF-NCU. The shaded color is for the difference of vertical wind speed greater than 0 cm s^{-1}.

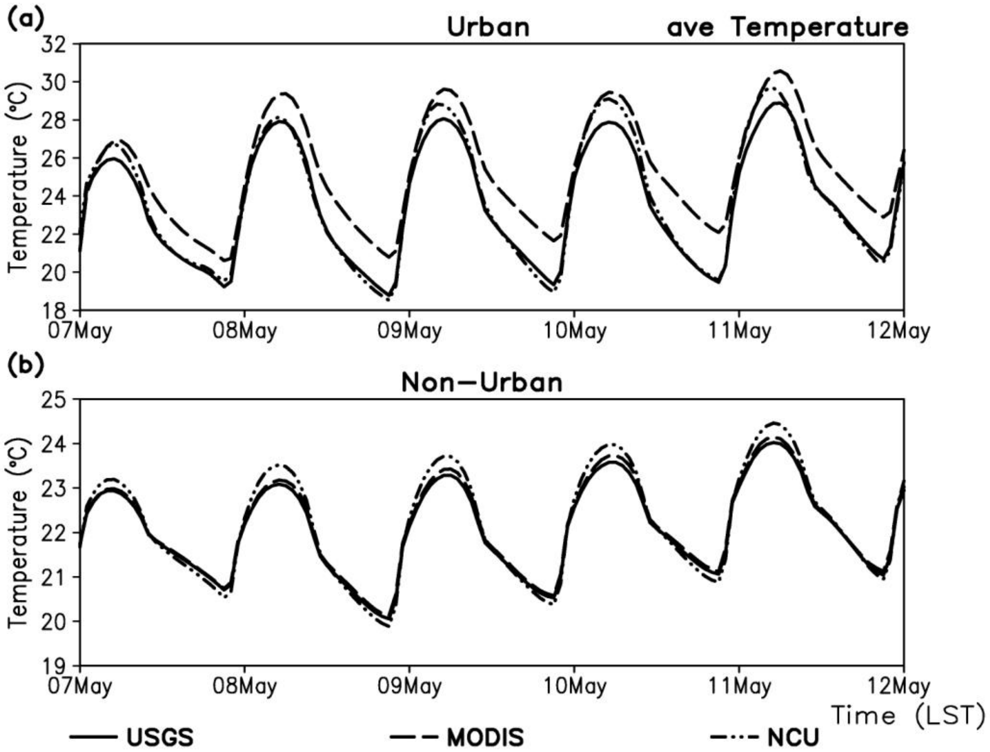

Figure 8. Time series comparison of the temperature from WRF simulations averaged over space for (a) urban areas and (b) non-urban areas.

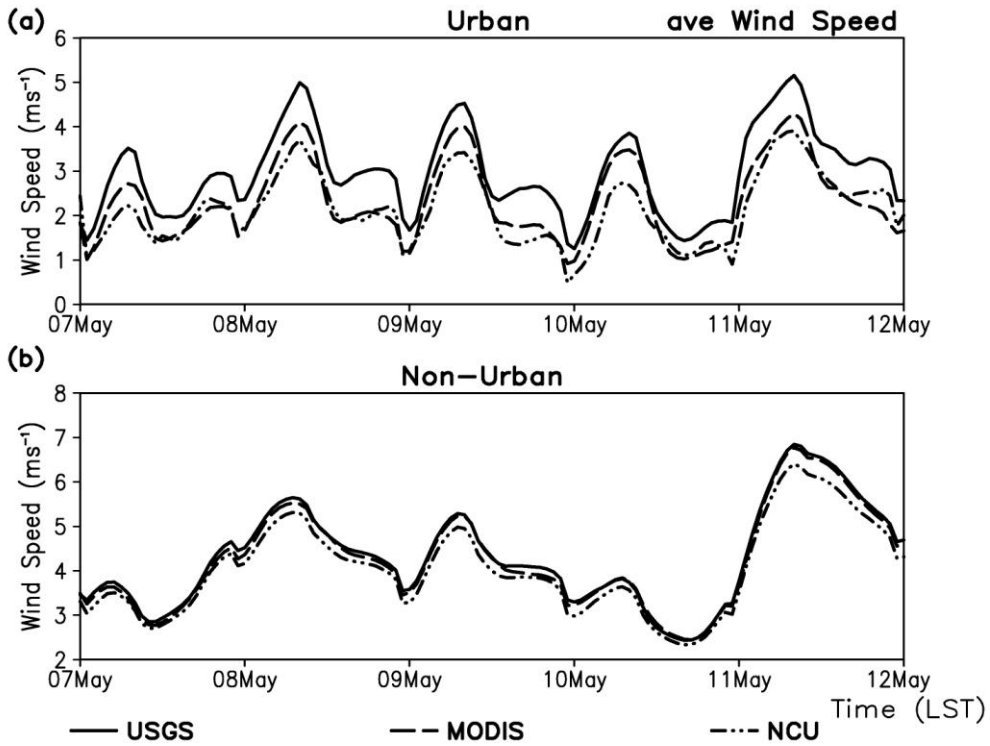

Figure 9. Similar to Figure 8 but for wind speed.

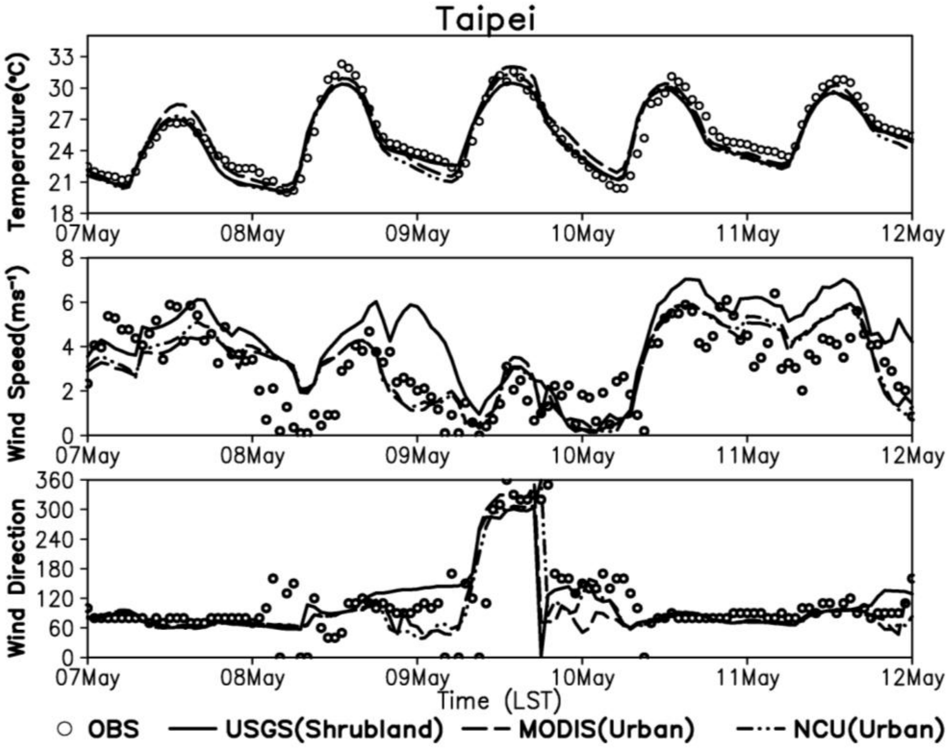

Figure 10. Time-series comparison of 2-m temperature (top), wind speed (middle) and wind direction (degree) (bottom) at Taipei station.

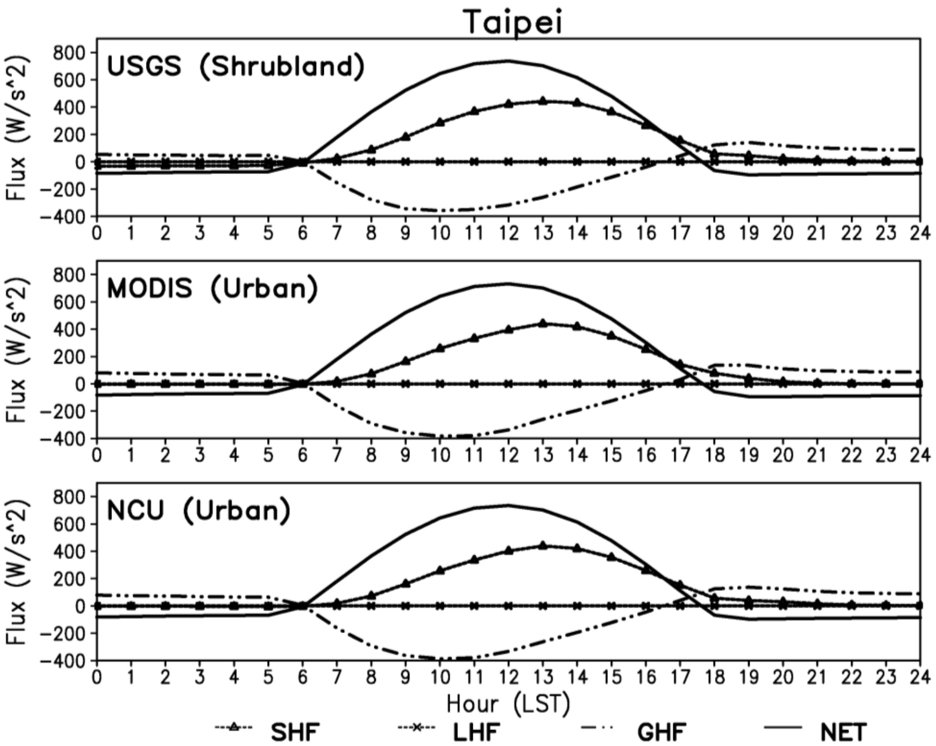

Figure 11. Comparison of simulated sensible heat flux (SHF), latent heat flux (LHF), ground heat flux (GHF) and net radiation (NET) at Taipei site from WRF-USGS (top), WRF-MODIS (middle) and WRF-NCU (bottom) simulations.

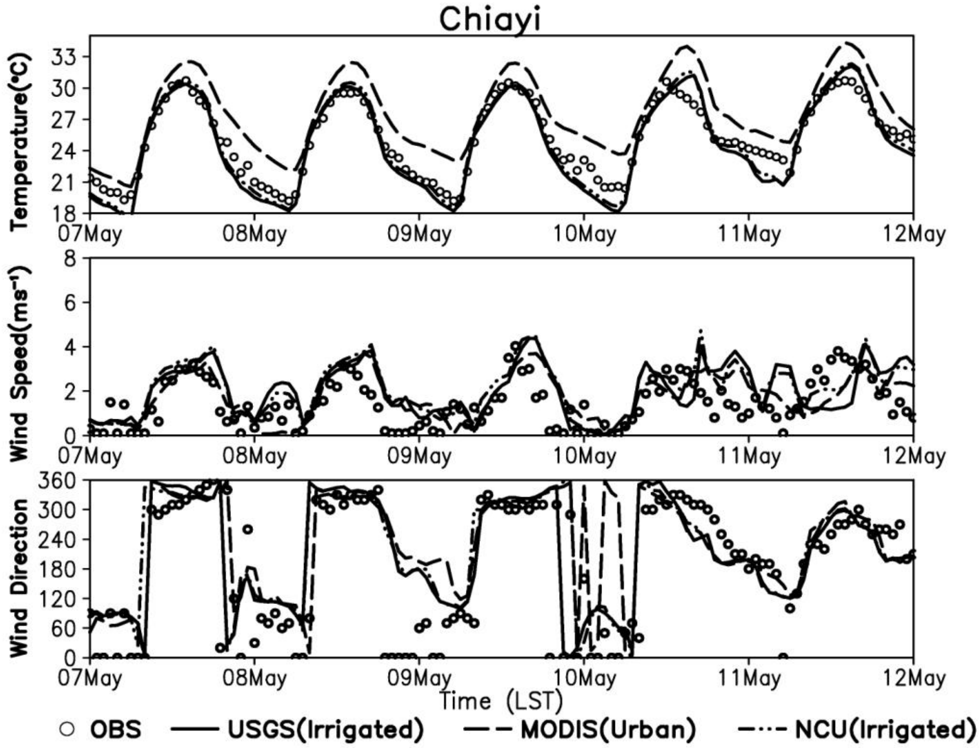

Figure 12. Time-series comparison of 2-m temperature (top), wind speed (middle) and wind direction (degree) (bottom) at Chiayi station.

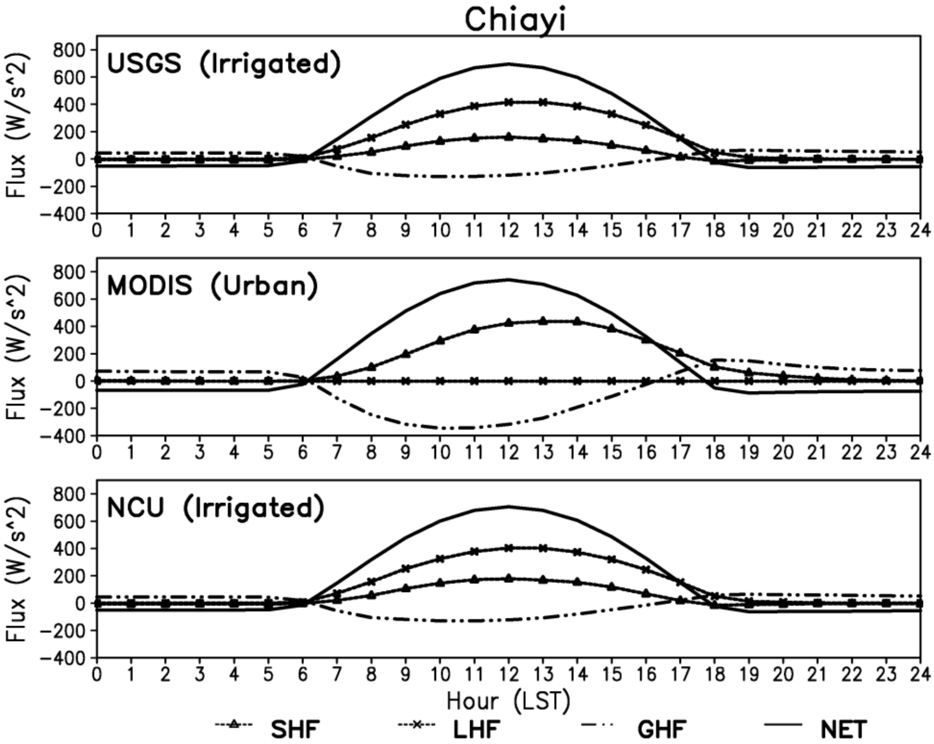

Figure 13. Comparison of simulated sensible heat flux (SHF), latent heat flux (LHF), ground heat flux (GHF) and net radiation (NET) at Chiayi site from WRF-USGS (top), WRF-MODIS (middle) and WRF-NCU (bottom) simulations.

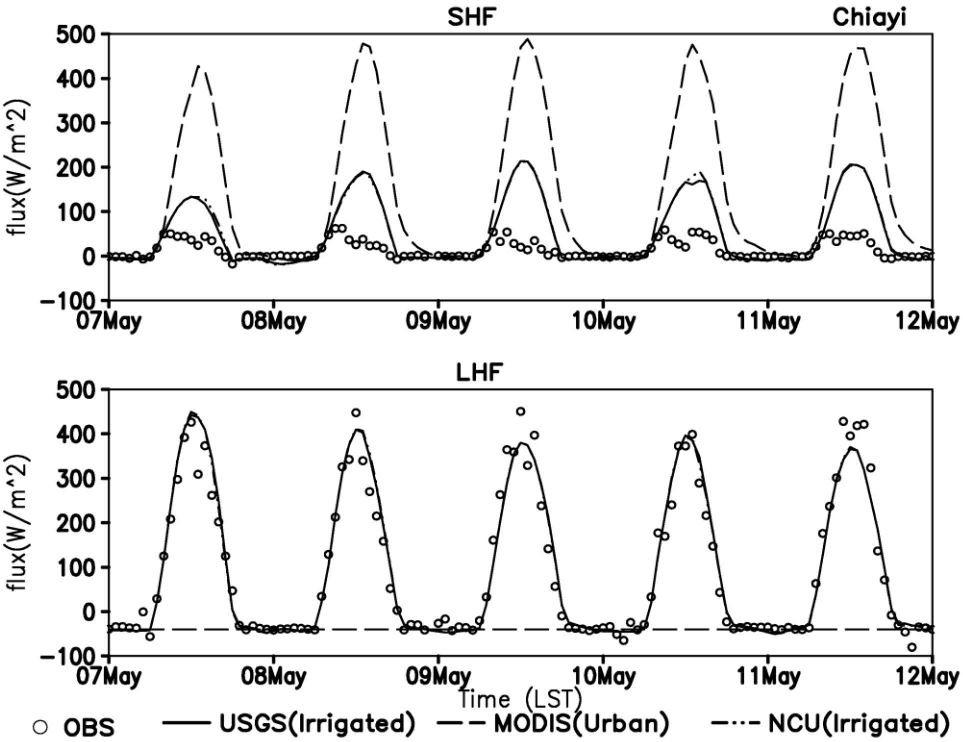

Figure 14. Comparison of the SHF (top) and LHF (bottom) near the Chiayi station.

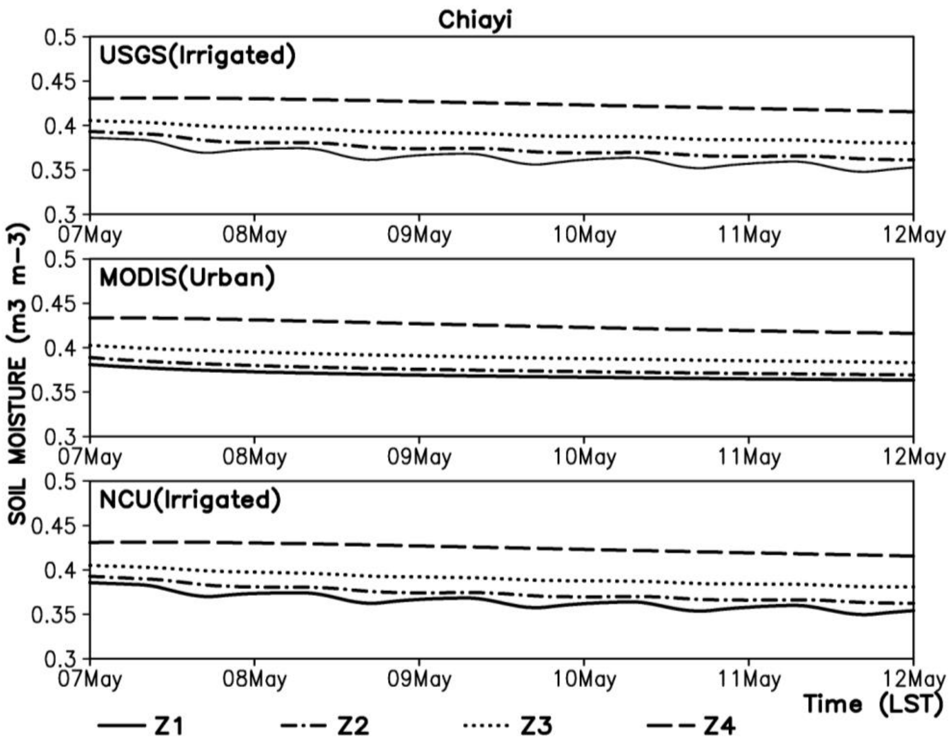

Figure 15. Comparison of the simulated soil moisture at Chiayi station from WRF simulations using USGS (top), MODIS (middle) and NCU (bottom) LU data at different soil layers. Z1, Z2, Z3 and Z4 represent thickness of each soil layer and are 0.1, 0.3, 0.6, and 1.0 m respectively from the ground surface to the bottom.

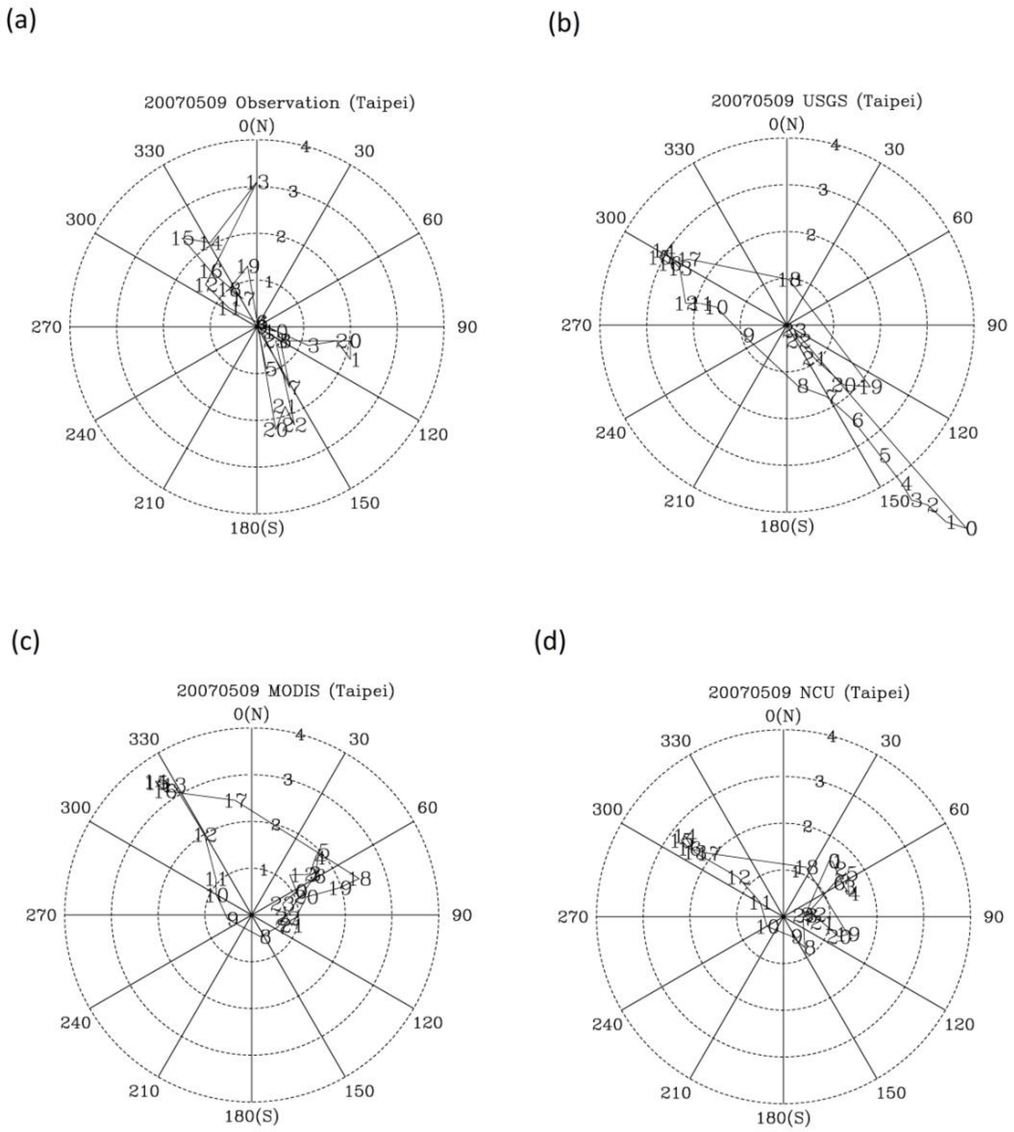

Figure 16. Hodograph comparison at Taipei site on May 9 2007 from (a) observation, (b) WRF-USGS, (c) WRF-MODIS and (d) WRF-NCU. The arrows pointing from the center to the location of number identifier (0~23) represents where the wind comes at the corresponding hour. The distance between the center and the location of number identifier indicates the wind speed (m s^{-1})

Table 1. Land use mapping from NCU to USGS classifications.

NCU	USGS
water body	water body
building	urban
sea	water body
road	urban
riverbed	water
fallow land	dry/irrigated cropland
	dry cropland
grassland	grassland
cropland	dry/irrigated cropland
	irrigated land
forest	mixed forest
no data	the closest type
unidentified	the closest type

Table 2. Percentages of each LU distribution class by area over the land surface of Taiwan (blank for zero distribution).

	USGS	MODIS	NCU
Urban	0.158	16.895	5.113
Dry cropland	8.171		3.057
Irrigated cropland	56.458		15.156
Mixed dry/Irrigated		13.073	1.502
Cropland/Grassland	1.292		0.395
Cropland/Woodland	2.794	1.45	1.529
Grassland	1.133	0.659	5.166
Shrub land	1.871	0.264	0.026
Mixed Shrub/Grassland		0.132	0.712
Savanna	2.003	0.158	
Deciduous Broadleaf	1.898		
Deciduous Needleleaf			
Evergreen Broadleaf	2.609	42.462	
Evergreen Needleleaf	2.478	4.823	0.554
Mixed Forest	18.608	18.872	64.839
Water Bodies		0.712	1.95
Herbaceous Wetland		0.026	
Barren Vegetated	0.501	0.264	
Wooded Tundra	0.026		

Table 3. RMSE comparison of temperature (T, unit: ^{0}C) and wind speed (WS, unit: m s^{-1}) at Taipei and Chiayi sites. The best score is in bold.

	USGS		MODIS		NCU	
RMSE	T	WS	T	WS	T	WS
Taipei	1.08	3.03	1.06	**1.34**	**0.99**	1.32
Chiayi	1.25	1.29	2.63	**0.97**	**1.14**	1.18

Table 4. Bias and RMSE comparison of temperature (^{0}C) and wind speed ($m\ s^{-1}$) for all observed surface sites in Taiwan.

	USGS	MODIS	NCU
temperature (bias)	-0.53	0.357	-0.133
wind speed (bias)	1.145	0.520	0.628
temperature (RMSE)	1.924	1.969	1.856
wind speed (RMSE)	2.215	1.758	1.7946

Short-Range (0–12 h) PQPFs from Time-Lagged Multimodel Ensembles Using LAPS

HUI-LING CHANG

Central Weather Bureau, Taipei, and Department of Atmospheric Sciences, National Central University, Jhong-Li, Taiwan

HUILING YUAN

School of Atmospheric Sciences, and Key Laboratory of Mesoscale Severe Weather, Ministry of Education, Nanjing University, Nanjing, Jiangsu, China, and NOAA/Earth System Research Laboratory, Boulder, Colorado

PAY-LIAM LIN

Department of Atmospheric Sciences, National Central University, Jhong-Li, Taiwan

(Manuscript received 3 April 2011, in final form 30 November 2011)

ABSTRACT

This study pioneers the development of short-range (0–12 h) probabilistic quantitative precipitation forecasts (PQPFs) in Taiwan and aims to produce the PQPFs from time-lagged multimodel ensembles using the Local Analysis and Prediction System (LAPS). By doing so, the critical uncertainties in prediction processes can be captured and conveyed to the users. Since LAPS adopts diabatic data assimilation, it is utilized to mitigate the ‘‘spinup’’ problem and produce more accurate precipitation forecasts during the early prediction stage (0–6 h).

The LAPS ensemble prediction system (EPS) has a good spread–skill relationship and good discriminating ability. Therefore, though it is obviously wet biased, the forecast biases can be corrected to improve the skill of PQPFs through a linear regression (LR) calibration procedure. Sensitivity experiments for two important factors affecting calibration results are also conducted: the experiments on different training samples and the experiments on the accuracy of observation data. The first point reveals that the calibration results vary with training samples. Based on the statistical viewpoint, there should be enough samples for an effective calibration. Nevertheless, adopting more training samples does not necessarily produce better calibration results. It is essential to adopt training samples with similar forecast biases as validation samples to achieve better calibration results. The second factor indicates that as a result of the inconsistency of observation data accuracy in the sea and land areas, only separate calibration for these two areas can ensure better calibration results of the PQPFs.

1. Introduction

Taiwan is noted for its distinctive geographic environment. Various weather systems such as spring rainfall, mei-yu fronts, typhoons, and afternoon thunderstorms constantly occur throughout the year. Among all weather systems, mei-yu fronts and typhoons accompanied by heavy rainfall often cause disasters and economic loss to Taiwan. Therefore, the academic research and governmental organizations emphasize the importance of quantitative precipitation forecasts (QPFs), especially on the short-range (0–12 h) QPFs of severe meso- and convective-scale weather systems, as they could have the most direct impact on people’s property and safety.

One of the primary difficulties in short-range QPFs is the spinup problem (Heckley 1985; Donner 1988), because the processes of condensation and latent heat release are not easily predicted by traditional models. The fundamental causes include the following: 1) the distribution of humidity and convergence fields of the atmosphere cannot be fully resolved by the observations, and 2) most models adopt adiabatic initializations, leading to a situation that the hydrometeors’ information cannot be provided by initial fields and should be driven gradually by the microphysical processes of mesoscale models

Corresponding author address: Huiling Yuan, School of Atmospheric Sciences, Nanjing University, 22 Hankou Rd., Nanjing, Jiangsu 210093, China.
E-mail: yuanhl@nju.edu.cn

DOI: 10.1175/MWR-D-11-00085.1

(Mohanty et al. 1986). Therefore, accurate precipitation forecasts are not easily obtained during the early stage of model integration and the ability of short-range QPFs is seriously affected for mesoscale models.

Early research indicates that if diabatic information could be provided by initial fields, the performance of numerical models during the early stage of model integration would be largely improved, and the ability of short-range QPFs for mesoscale models would be enhanced. Krishnamurti et al. (1991) and Harms et al. (1993) retrieved the vertical distribution of moisture and latent heat by using observed rainfall rates and then introduced them into the initial fields to enrich the diabatic information of numerical models. This showed that the spinup time was reduced and the precipitation forecasts during the early stage of model integration were improved.

The Local Analysis and Prediction System (LAPS) used in this research can mitigate the spinup problem because the diabatic effect has been included during the atmospheric analysis and initialization processes. Therefore, more accurate precipitation forecasts can be obtained during the early stage of a forecast period (Jian et al. 2003). This forecast system was developed by the Central Weather Bureau (CWB) in partnership with the National Oceanic and Atmospheric Administration/Earth System Research Laboratory/Global Systems Division (NOAA/ESRL/GSD), for the purpose of improving the capability of short-range QPFs for severe weather systems.

At present, major forecast centers pay more and more attention to advanced data assimilation schemes. The three-dimensional variational data assimilation (3DVAR) technique has been widely used in operational centers, and several centers [e.g., the European Centre for Medium-Range Weather Forecasts (ECMWF), France, United Kingdom, Japan, and Canada] have switched to 4DVAR. The ensemble Kalman filter (EnKF) is another data assimilation method, which is relatively new and has been tested in some operational developments. Though LAPS does not adopt similar advanced schemes, it does really have stable and good performance of short-range precipitation forecasts from long-term verifications in the past 6 years at CWB. Refer to section 2 for a more detailed description of LAPS.

In addition to improving data assimilation in the numerical weather prediction (NWP) system, in recent years, increasing attention has been paid to ensemble prediction system (EPS) to reduce the forecast biases, especially in short-range QPFs. Rather than the deterministic viewpoint in traditional NWP models, there are various uncertainties in all steps of the NWP system, including observation, first-guess, data assimilation, and prediction processes. The chaos theory states that a small change in the initial conditions can drastically change the long-term behavior of a system through interactions. EPS uses perturbed initial states or considers the physics as stochastic processes, which reflects the chaotic nature in the atmosphere. Averaging the ensemble forecasts from slightly perturbed initial conditions can filter out some unpredictable components of the forecast, and the spread among the forecasts can provide some guidance on the reliability of the forecasts (Toth and Kalnay 1993). This is a fundamental transition and revolutionary change in the NWP development.

The major question of EPS is how to generate ensemble perturbations that reflect the real initial uncertainty (Toth and Kalnay 1993). Two operational ensemble perturbation methods include the breeding of growing modes (BGM) method at the National Centers for Environmental Prediction (NCEP), which contains fast-growing modes corresponding to the evolving atmosphere, and the singular vector method which involves the linear tangent model at the ECMWF.

The early development of EPS focuses on capturing the critical uncertainties in an ensemble system with the final goal of achieving a single best forecast (e.g., adopting the ensemble weighting). For example, several studies investigated ensemble precipitation forecasts in the Taiwan area (Chien et al. 2003; Chien and Jou 2004; Yang et al. 2004) using the fifth-generation Pennsylvania State University–National Center for Atmospheric Research (NCAR) Mesoscale Model (MM5; Grell et al. 1995). They discussed different weighting methods to improve the skill of the ensemble QPFs, including the weighted averaging method, multiple linear regression technique, and the probability matching approach. In some ensemble designs, the ensemble mean was not the best forecast (e.g., Chien et al. 2003), while in other studies the precipitation forecast from the ensemble mean was superior to that of any single member (e.g., Chien et al. 2005). Chien et al. 2005 show that the best skill scores were obtained when the ensemble configuration included three uncertainty sources: initial fields, cumulus parameterizations, and microphysical schemes. Of all the three uncertainty sources, the most advantageous method for ensemble precipitation forecasts was to vary initial fields, followed by varying cumulus parameterizations and microphysical schemes.

As with other recent EPSs, the development of the LAPS EPS emphasized on not only capturing the critical uncertainties, but also conveying the uncertainties to the forecasters and end users, which will help the users further understand the possibility and reliability of forecasts. Some sensitivity experiments were conducted in this study to identify the critical uncertainties in EPS and the time-lagged multimodel ensemble was created. To convey the uncertainties in the prediction process to the users, PQPFs were developed (see section 3).

Early research indicates that calibration is a critical procedure to correct forecast biases and enhance forecast skill in a biased forecast system (Mass 2003). Calibration methods of PQPFs include model output statistics (MOS; Glahn and Lowry 1972; Vislocky and Fritsch 1997), the artificial neural network technique (ANN; Mullen and Buizza 2004; Yuan et al. 2007a), and the linear regression method (LR; Lu et al. 2007; Yuan et al. 2008) to name a few. Calibration results are deeply affected by insufficient numbers (Atger 2003) and interdependence of the samples (Eckel and Walters 1998). In addition, using the long-term training samples with similar climatology characteristics could effectively improve bias correction (e.g., calibration was conducted using the training samples classified by topography or climatology; Yuan et al. 2008). In this study, the verification results showed that the LAPS ensemble was apparently wet biased. Therefore, the LR method (Yuan et al. 2008) was used to correct forecast biases (see section 4).

This study focuses on the short-range PQPFs of typhoons or tropical cyclones (TC) using the time-lagged multimodel ensembles. Since predictability usually decreases in subsynoptic and mesoscale systems, it is more difficult to develop an effective short-range EPS, in particular the TC ensembles (e.g., Cheung 2001). An additional difficulty is the different error characteristics for the tropics, which is mainly the result of the strong convection in the area and the air–sea interaction. In general, skill improvement in forecasting TC motion is quite promising when the uncertainties in the large-scale steering flow can be simulated by the perturbations, while the ensembles for TC intensity are being developed, in part because intensification is not yet fully understood.

The ensemble forecasts of TC precipitation using the LAPS EPS are examined in this study. This report is organized as follows: LAPS and verified observation data are introduced in section 2. The design of the LAPS EPS and the PQPF products are presented in section 3. Sections 4 and 5 describe the calibration methodology of PQPFs and the verification results of PQPFs before and after the LR calibration, respectively. The sensitivity experiments on calibration, including the training samples and accuracy of observation data, are presented in section 6. A summary and future works are given in the last section.

2. Model and data

a. Short-range forecast system LAPS

LAPS has three main components: the observation data ingestion, diabatic data assimilation, and mesoscale model forecast (Fig. 1). The ingested data include model forecasts (used as the background field), surface observations, soundings, Aeronautical Radio Incorporated, Communications, Addressing and Retrieval System (ACARS), Doppler radar data (including reflectivity and radial velocity fields from Wu–Fen–Shan, Ken–Ting, Hua–Lian, and Chi–Gu radars; Fig. 2), satellite IR and visible (VIS) data [from the geostationary multifunctional transport satellite (MTSAT)], and satellite-derived wind fields provided by the University of Wisconsin Cooperative Institute for Meteorological Studies (UW-CIMSS).

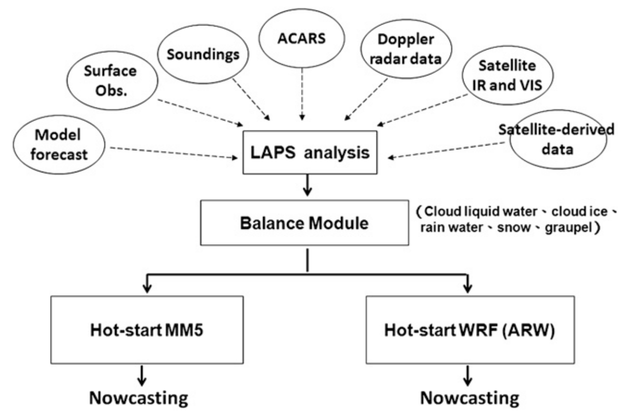

FIG. 1. Schematic diagram of short-range forecast system LAPS.

After data ingestion, LAPS performs diabatic data assimilation, including wind analysis (Albers 1995), surface analysis, temperature analysis, cloud analysis (Albers et al. 1996), moisture analysis (Birkenheuer 1999), and a dynamical balance module. In the procedure of wind, surface pressure, and temperature analysis, LAPS adopts a two-pass successive correction method that can retrieve resolvable information from conventional observations.

Cloud analysis is the key procedure to hot-start mesoscale models, and its products could provide the initial fields with diabatic information, such as cloud liquid water, cloud ice, and vertical motions in the cloud-covered area. Therefore, the spinup problem could be mitigated, more accurate precipitation forecasts could be obtained during the early stage of model integration, and the ability of short-range precipitation forecasts could be largely improved. The moisture analysis is achieved by using the satellite data via a variational scheme.

After completing the atmospheric analysis procedures, the dynamical balance module (Jian and Mcginley 2005) is a crucial component to initialize a mesoscale model diabatically, since it ensures that the momentum and mass fields are consistent with the cloud-derived vertical motions. This module is based on a variational formulation, and the adjustment is done by minimizing a functional containing two constraints. The first constraint is

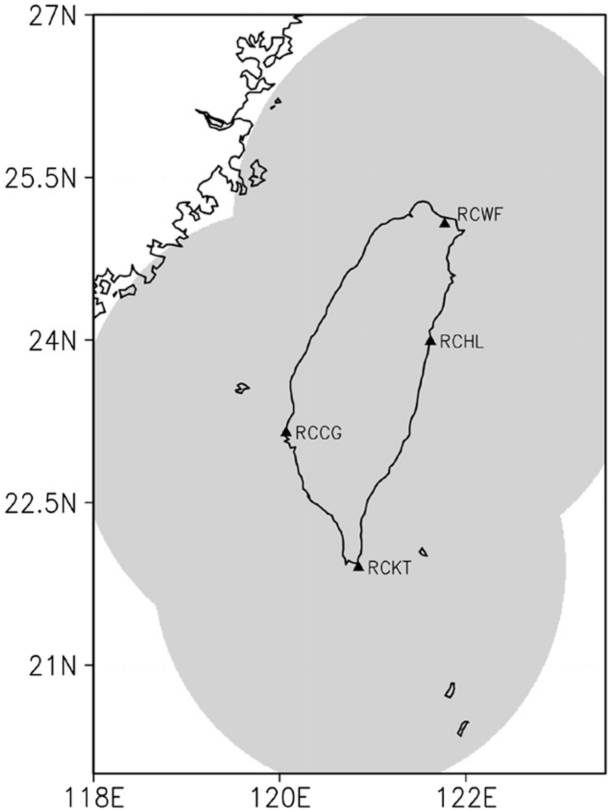

FIG. 2. QPESUMS domain. The radar coverage is indicated by the shaded area, and the four radar sites are indicated by closed triangles, including Wu–Fen–Shan (RCWF), Ken–Ting (RCKT), Hua–Lian (RCHL), and Chi–Gu (RCCG) radars.

mass continuity equation (strong constraint), which forces mass continuity everywhere in the domain. Therefore, the horizontal winds are adjusted to balance with cloud-derived vertical motions to reduce the model shock in the first few time steps. The second constraint (weak constraint) is to reduce the Eulerian time tendencies of the horizontal motion components (u and v), which couple the mass to momentum fields. The net effect is an instant spinup or precipitation. At the final step of the LAPS forecast system, better initial fields from the LAPS data assimilation system are provided to conduct numerical forecasts and produce nowcasting products.

The scheme of TC bogussing was used in this study for short-range PQPFs of TCs. Since the structure of TCs contained in the background is relatively broad and weak, the LAPS analyzed vortex is also too weak as there is not enough observation data over sea areas to support the analysis of typhoon structure. For this reason, a vortex at a location confirmed by the observations (satellite, radar, etc.) is inserted into the background field before data ingestion in LAPS, by using the NCAR–Air Force Weather Agency (AFWA) typhoon bogussing scheme

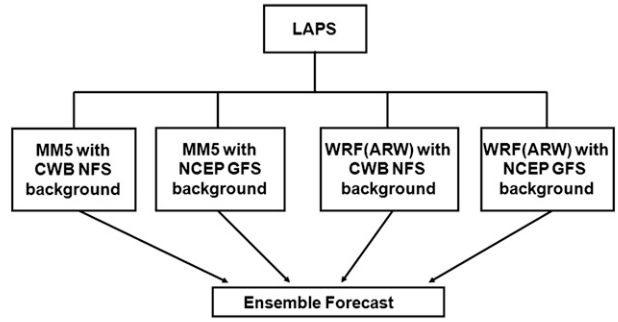

FIG. 3. Schematic diagram of LAPS ensemble system.

(Davis and Low-Nam 2001). Therefore, the track errors of typhoons are usually small for 0–6-h short-range forecasts.

The sea surface temperature data are provided by NCEP. The initial atmospheric fields come from the LAPS analyses. In LAPS, the background fields in the LAPS analysis and lateral boundary conditions are from the same sources, including the model forecasts of 1) the nonhydrostatic forecast system (NFS) at CWB, with 15-km horizontal resolution, and 2) the Global Forecast System (GFS) at NCEP, with 0.5° horizontal resolution. There are two mesoscale numerical models associated with LAPS, including the MM5 model and the Weather Research and Forecasting (WRF) model with the Advanced Research WRF (WRF-ARW) dynamic core. Therefore, totally four different forecast models (Fig. 3) are used by LAPS, including 1) LAPS-MM5: NFS (refers to LAPS-MM5 model with the background field from CWB NFS, and similar for other notations), 2) LAPS-MM5: GFS, 3) LAPS-WRF-ARW: NFS, and 4) LAPS-WRF-ARW: GFS.

Both the MM5 and WRF-ARW models have been widely implemented by international operational and research centers. They are nonhydrostatic mesoscale models, which use the terrain-following vertical coordinate, and possess flexible and multiple nesting capability. The LAPS domain has 141 by 151 grid points (left column of Fig. 5) with 9-km horizontal resolution

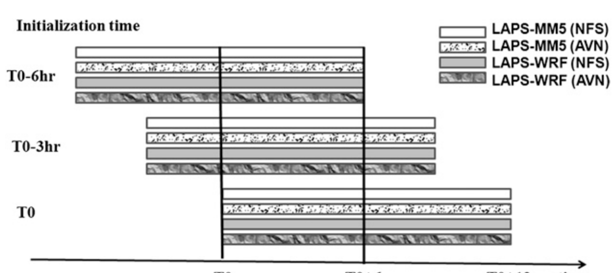

FIG. 4. Schematic diagram of LAPS time-lagged multimodel ensemble.

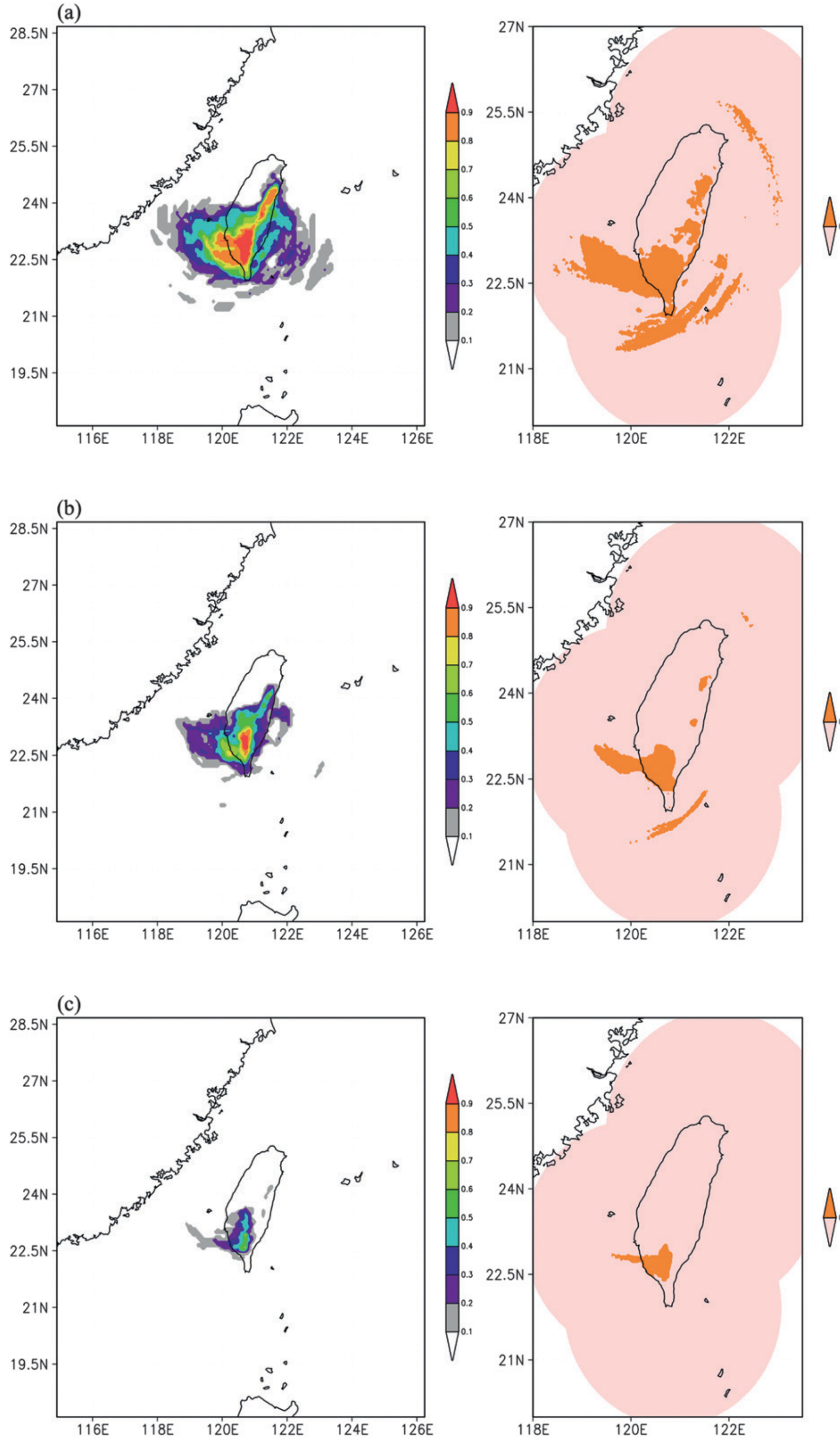

FIG. 5. Distribution of (left) LAPS 0–6-h PQPFs and (right) QPESUMS precipitation (used as truth) probabilities at thresholds (a) 50, (b) 100, and (c) 200 mm $(6\ h)^{-1}$ ending at 1200 UTC 19 Sep 2010. (right) The orange shaded area denotes pixels where QPESUMS precipitation estimations exceed the indicated threshold, and pink shaded area indicates QPESUMS radar coverage.

TABLE 1. Typhoon cases in 2008 and 2009.

	Event: No. of validation times	Start–end
2008	Kalmaegi: 11 (TY 1)	0900 UTC 16 Jul–1500 UTC 18 Jul
	Fung-wong: 24 (TY 2)	0300 UTC 26 Jul–1200 UTC 29 Jul
	Sinlaku: 27 (TY 3)	0000 UTC 11 Sep–1200 UTC 15 Sep
	Hagupit: 11 (TY 4)	0000 UTC 22 Sep–0600 UTC 23 Sep
	Jangmi: 17 (TY 5)	1800 UTC 27 Sep–1800 UTC 29 Sep
	Tot: 5 typhoons 90 6-h PQPFs	
2009	Linfa: 12 (TY 6)	0600 UTC 20 Jun–0300 UTC 22 Jun
	Molave: 7 (TY 7)	0000 UTC 17 Jul–1800 UTC 17 Jul
	Morakot: 39 (TY 8)	1800 UTC 5 Aug–0200 UTC 10 Aug
	Tot: 3 typhoons 58 6-h PQPFs	

and 30 sigma levels vertically with 100 hPa at the vertical top level. For microphysical parameterization, the Schultz scheme (Schultz 1995) is used in the MM5 model and the WRF Single-Moment 5-Class Microphysics scheme (WSM5) in the WRF-ARW model. For planetary boundary layer process parameterizations, the MRF scheme is used in the MM5 model and Yonsei University (YSU) scheme is used in the WRF-ARW model. Cumulus parameterization schemes are deactivated, which is acceptable for orographically forced precipitation in the typhoon cases with 9-km horizontal resolution.

b. *Observation data for forecast verification*

Regarding the observation data needed for precipitation verification, since the conventional automatic rainfall stations are located over the land areas in Taiwan and the land area is only a small part of the LAPS domain, the verification results cannot represent the performance of the LAPS precipitation forecasts as a whole. Therefore, the radar-estimated rainfall data from the quantitative precipitation estimation (QPE) and Segregation Using Multiple Sensors (QPESUMS; Gourley et al. 2001), a system which was developed by CWB and the Water Resources Agency (WRA) in Taiwan cooperating with the National Severe Storm Laboratory (NSSL) in the United States, were used as observation data (i.e., ground truth). The QPESUMS uses the radar data (Fig. 2), covering the island of Taiwan and its nearby sea areas with 1.25-km horizontal resolution. Note that the precipitation estimation in land in Taiwan is calibrated with rainfall observations from rain gauges, but is not calibrated over the sea areas.

3. LAPS ensemble configuration and PQPF products

a. *Time-lagged multimodel ensemble configuration*

Expanded from the single model LAPS-MM5: NFS, we developed the LAPS EPS in order to capture more uncertainties. However, limited by computer resources and real-time operation, critical uncertainty factors such as microphysical parameterizations, background fields, and mesoscale models must be traded off. In the sensitivity experiments, we chose two typhoon and four mei-yu front cases, and performed simulations using five microphysical parameterizations from WRF-ARW (the Lin et al. scheme, the WSM three-class simple ice scheme, the WSM five-class scheme, the Ferrier microphysics scheme, and the WSM six-class graupel scheme), two different background fields (GFS from NCEP and NFS from CWB), and two mesoscale models (MM5 and WRF-ARW). For the 0–6- or 0–12-h QPFs of LAPS, there are only marginal differences when using different microphysical schemes, while different background fields or mesoscale models cause significant differences and become more important uncertainty factors than microphysical parameterizations. As a result, four members with different backgrounds or mesoscale models were chosen as the basis of the LAPS EPS (see section 2; Fig. 3).

TABLE 2. Summary of the difference of statistical samples in the sensitivity experiments.

Expt	Description
SMP-T	Statistical samples were adopted from all radar coverage area within the QPESUMS domain (including sea and land areas), before LR calibration. This experiment was used as a reference one in this study.
SMP-T(LR)	Statistical samples were the same as in the experiment SMP-T, but after LR calibration. The statistical samples were divided into two groups (cases in 2008 and 2009, respectively) when performing the cross-validation procedure.
SMP-T8S(LR)	As in the experiment SMP-T(LR), but the statistical samples were divided into eight groups (eight different typhoon cases in 2008 and 2009) when performing the cross-validation procedure.
SMP-L	As in the experiment SMP-T, but the statistical samples were only adopted from the land area within the QPESUMS domain.
SMP-L(LR)	As in the experiment SMP-T(LR), but the statistical samples were only adopted from the land area within the QPESUMS domain.

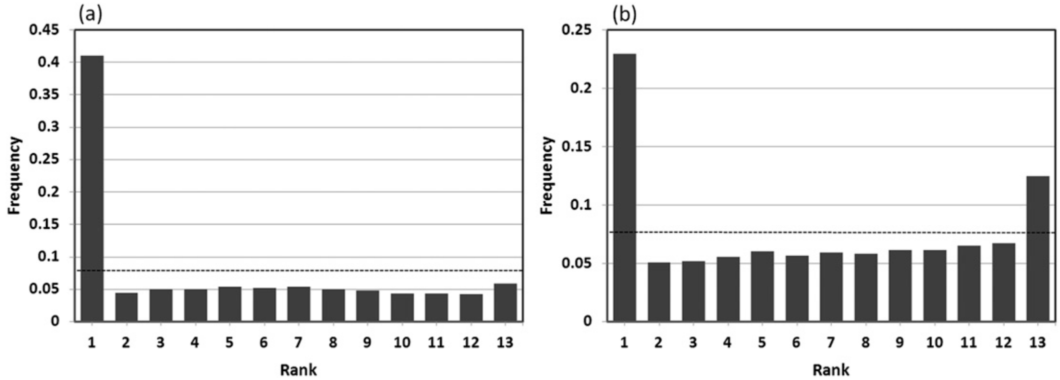

FIG. 6. Rank histograms for LAPS 0–6-h QPFs from the experiments (a) SMP-T and (b) SMP-L. The horizontal dashed line denotes the frequency for a uniform rank distribution.

In addition, time-lagged configurations were adopted to increase the ensemble members by using previous forecasts without additional computational cost. The advantage of time-lagged multimodel ensemble forecasts against simple multimodel ensemble forecasts is discussed in section 5e. The LAPS time-lagged multimodel ensemble (Fig. 4) uses multimodel forecasts initialized at different times to construct ensemble members for the same verification period. The LAPS EPS has four models, and each model is initialized once every 3 h with the forecast length of 12 h. Thus, for the 0–6-h ensemble precipitation forecasts, 3 time-lagged members (the 0–6, 3–9, and 6–12-h QPFs) are available for each model and 4 models in total build up the EPS of 12 members.

In brief, a time-lagged multimodel ensemble system was designed using different background fields, mesoscale models, and initialization times, so as to capture more important uncertainties in the LAPS EPS.

b. PQPF products

The advantage of ensemble PQPFs lies in that the probabilities are determined by the actual data distribution from ensemble members and display the possibility of precipitation over a certain threshold. Therefore, this plays an important part in the development of EPS. In other words, the ultimate goal of ensemble forecasts is to provide more possibility and probability information to the end users instead of a single best forecast. The limitation of PQPFs is that we cannot take all uncertainties into account because of the limited ensemble members.

The PQPFs were created based upon the precipitation forecasts from 12 members of the LAPS time-lagged multimodel ensemble system at different thresholds. For example, at the threshold of 10 mm (6 h)$^{-1}$, if 9 of the 12 members predict 6-h accumulated precipitation over 10 mm, then the precipitation probability is 75% ($9/12 = 0.75$). Figure 5 shows the PQPF products and corresponding observed probabilities of Typhoon Fanapi, which was the most powerful typhoon to hit Taiwan in 2010 and caused a flash flood over areas of southern Taiwan on 19 September 2010. If the estimated rainfall from the QPESUMS is less than the selected threshold, the observed precipitation probability is zero; otherwise, it is one. At the threshold of 100 mm (6 h)$^{-1}$, the LAPS PQPFs show the precipitation probabilities in southern Taiwan are above 90%. There are still 9 of 12 models predicting 6-h accumulated precipitation over 200 mm. These large probabilities imply a high possibility of heavy precipitation.

4. Calibration methodology

In short, calibration is bias correction. In this study, we adopted the LR method (Yuan et al. 2008) to calibrate PQPFs. Before calibration, a series of thresholds [0.25, 0.5, 1.0, 1.5, 2.5, 3.5, 5.0, 7.5, 10.0, 12.5, 15.0, 20.0, 30.0, 40.0, 50.0, and 60.0 mm (6 h)$^{-1}$] were selected based on the distribution of 6-h accumulated precipitation from all of the typhoon cases in 2008. Note that calibration was conducted separately for each selected threshold, including the training and validation processes. During the training process, each record of training samples consisted of one observed precipitation probability $P(x, t)$ and the closet seven ensemble precipitation probabilities $f_i(x, t)$ centered at the selected calibration threshold, which were used to represent the critical part of the probability distribution function (PDF) for the calibration threshold. The LR relationship was obtained by minimizing the errors between the forecasted precipitation probabilities and the observed ones. Then during the validation process another set of data (i.e., validation samples) were applied to the derived LR relationship to obtain the calibrated precipitation probabilities for later verifications.

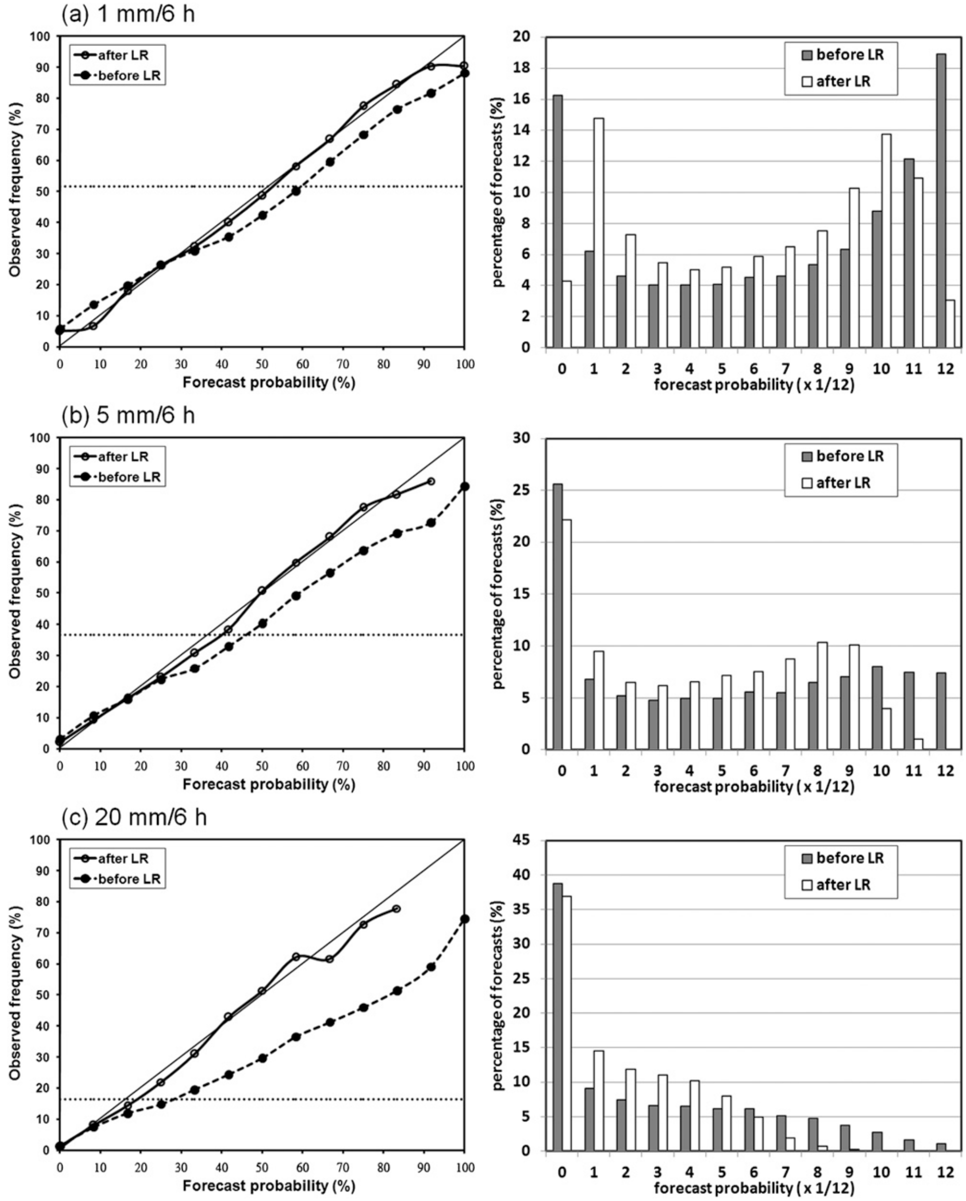

FIG. 7. (left) Reliability diagrams for LAPS 0–6-h PQPFs at thresholds (a) 1, (b) 5, and (c) 20 mm $(6\ \mathrm{h})^{-1}$. Reliability curves from the experiments SMP-T (before LR calibration, dashed line with solid dots) and SMP-T(LR) (after LR calibration, solid line with hollow circles) are shown. The horizontal dashed line indicates the sample climatology frequency. (right) Histograms indicate the corresponding sample ratio (%) of each forecast probability subrange for the experiments SMP-T (before LR, gray) and SMP-T(LR) (after LR, blank).

Because of insufficient statistical samples (eight typhoon cases in 2008 and 2009, Table 1), the calibration was performed via a cross-validation procedure, with the purpose of increasing validation samples to consolidate the representativeness of statistical verification results. For example, in the experiment SMP-T (LR) (Table 2), the five typhoon cases in 2008 were used as the training samples to calibrate the three typhoon cases in 2009, and in turn the 2009 cases were used as the training samples.

After the calibration for all selected thresholds, a checking step was needed to ensure that the distribution of probabilities at each grid point would be monotonic (i.e., the probabilities at lower thresholds were not smaller than those at higher thresholds because the precipitation events reaching higher thresholds implies the events

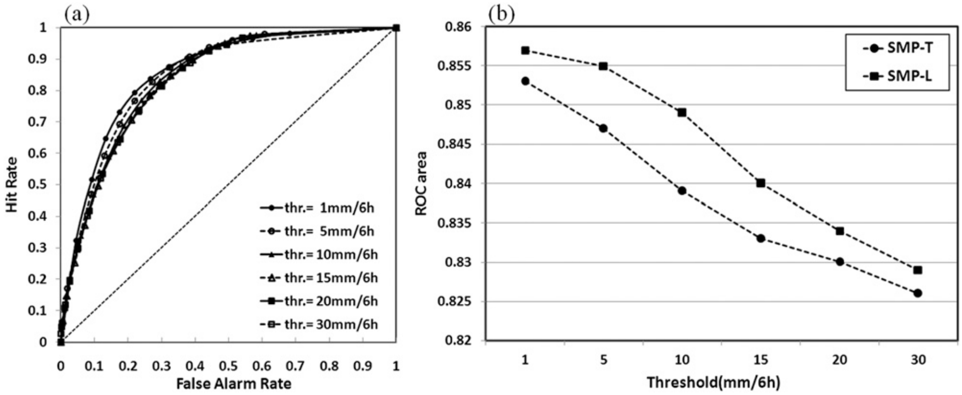

FIG. 8. (a) ROC curves from the experiment SMP-T and (b) the area under the ROC from the experiments SMP-T (line with circles) and SMP-L (line with squares) for LAPS 0–6-h PQPFs at different thresholds [1, 5, 10, 15, 20, and 30 mm (6 h)$^{-1}$].

reaching lower thresholds). Precipitation probabilities with correct monotonic distribution were the final calibrated precipitation probabilities.

The LR method is expressed as the LR equation:

$$P(x,t) = a + \sum_{i=1}^{M} b_i f_i(x,t), \tag{1}$$

where $M = 7, f_i(x, t), i = 1, 2, \ldots, 7$ are the seven ordinal input probabilities (i.e., seven ordinal ensemble precipitation probabilities centered at the calibration threshold described earlier), $P(x, t)$ is the corresponding observed precipitation probability, and a is a constant interpreted as error residual. The coefficients a and b_i are estimated by minimizing the errors between the observed probabilities and the derived ones $[a + \sum_{i=1}^{M} b_i f_i(x,t)]$ in the LR equation using N training samples. The regression coefficients are derived by using the least squares method:

$$\min \sum_{j=1}^{N} \left\{ P(x,t) - \left[a + \sum_{i=1}^{M} b_i f_i(x,t) \right] \right\}^2. \tag{2}$$

By applying the ensemble precipitation probabilities $f_i(x, t)$ from validation samples into the LR in Eq. (1) after obtaining the regression coefficients a and b_i, new forecasted precipitation probabilities $P(x, t)$ (i.e., calibrated probabilities) are obtained. For negative values (or >1), new probabilities are reset to 0 (or 1).

5. Verification and results

Some verification methods were used to evaluate the forecast bias, the discriminating ability, the skill of PQPFs, the spread–skill relationship, as well as the advantage of a time-lagged multimodel EPS against simple multimodel EPSs. Regarding the experiments in this study, please refer to Tables 2 and 3 for a detailed description.

a. Forecast bias

The rank histogram (RH; Hamill 2001), also known as a Talagrand diagram, can be used to evaluate whether or not the ensemble spread of the forecast adequately represents the true variability of the observations. The reference experiment SMP-T (Fig. 6a) from eight typhoon cases in 2008 and 2009 shows an ‘‘L’’ shape of RH distribution, which indicates that the LAPS EPS has significant wet biases.

The reliability diagram (Hsu and Murphy 1986; Hamill 1997) can be used to determine how well the forecast probabilities of an event correspond to their observed frequencies. Reliability is reflected by the proximity of the reliability curve (Fig. 7) to the diagonal line, which depicts a perfect forecast. The closer the reliability curve to the diagonal line, the smaller the probabilistic forecast bias and the higher the reliability. Except for the slightly dry bias in lower forecast probabilities at smaller thresholds [below 5 mm (6 h)$^{-1}$] from the experiment SMP-T (before calibration; Fig. 7), all reliability curves indicate wet biases (i.e., the reliability curve lies below the diagonal line), and the higher the threshold, the more significant the wet bias. The wet bias is apparently corrected after the LR calibration [SMP-T(LR)].

The corresponding histogram (Fig. 7) shows the sample ratio in each forecast probability bin. Regarding the higher thresholds [$>$20 mm (6 h)$^{-1}$], the sample ratios in high forecast probability bins were small, which indicates that the consistency of the forecasts of 12 ensemble members was worse when predicting heavy rainfall; and the wet biases were corrected by adjusting the higher probabilities (less reliable) to the lower ones (the highest calibrated probabilities were 83.37%). In general, the dry and wet biases were corrected by adjusting the lowest and highest probabilities to the mid-range ones via the calibration procedure.

b. Discriminating ability

The relative operating characteristic (ROC; Mason and Graham 1999; Jolliffe and Stephenson 2003; Hamill and Juras 2006; Wilks 2006) curve plots the hit rates versus the false alarm rates using a set of increasing probabilities as warning thresholds (i.e., precipitation event is regarded as occurring when the forecast probability exceeds this warning threshold). The area under the ROC curve (i.e., ROC area) measures the ability of the forecast to discriminate between events and non-events and it ranges from 0 to 1 (perfect score). A forecast with skillful discriminating ability has the ROC area greater than 0.5. The ROC curves (Fig. 8a) and the ROC areas (>0.825; Fig. 8b) from the experiment SMP-T indicate good discriminating ability, which slightly decrease with increasing threshold. Unlike reliability diagrams, the ROC is conditioned on the observations and is not sensitive to the forecast bias. Therefore, a biased forecast may still have good discriminating ability and possibly be improved through calibration, such as the LAPS PQPFs for typhoons (Fig. 8).

c. Forecast skill

The Brier skill score (BSS; Wilks 2006) measures the relative improvement of the probabilistic forecast over a reference forecast in terms of selected thresholds. Sample climatology was used as the reference forecast in this study. The BSS ranges from minus infinity to 1. The positive BSS indicates skillful forecasts with the perfect value of 1. The PQPFs (Fig. 9) from the experiment SMP-T (before calibration) are skillful when compared to climatology at the thresholds below 30 mm (6 h)$^{-1}$. The BSS at each threshold increases significantly after calibration [i.e., SMP-T vs SMP-T (LR) or SMP-T8S (LR)], especially for higher thresholds.

Similar to the BSS, the rank probability skill score (RPSS; Wilks 2006) measures relative improvement of the probabilistic forecast over climatology for a multi-category probabilistic forecast. The RPSS ranges from minus infinity to 1 (perfect), and the positive RPSS indicates a skillful forecast. The spatial distribution of the RPSS from the experiment SMP-T (Fig. 10a) shows that the PQPFs are more skillful over the northeastern island of Taiwan, high mountain areas, and the northeastern sea areas, but less skillful over the eastern sea areas along the coast line and the western sea areas. The black sector area with an angle of 15° in the northwestern direction of Taiwan (Figs. 10a,b) results from the lack of observation data because the radar beams from the Wu–Fen–Shan [Weather Surveillance Radar-1988 Doppler (WSR-88D)] radar site are blocked by the Chi–Shin Mountains. The black line's area (about an angle of 30° with the tangential direction of the eastern coast line of Taiwan), lack of observation data, arises from the blockage of building on radar beams from the Hua–Lian radar site.

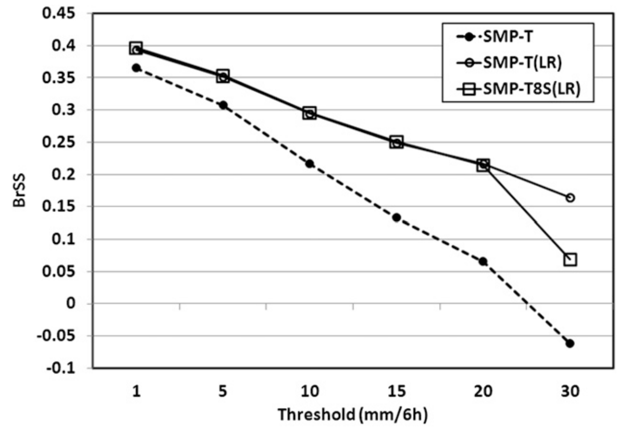

FIG. 9. Brier skill scores at different thresholds for LAPS 0–6-h PQPFs from the experiments SMP-T (dashed line with solid dots), SMP-T (LR) (solid line with hollow circles), and SMP-T8S (LR) (solid line with hollow squares).

The Brier score (BS; Wilks 2006) is used to calculate the magnitude of the probabilistic forecast errors and can be partitioned into three terms: reliability, resolution, and uncertainty (Murphy 1973):

$$\mathrm{BS} = \frac{1}{N}\sum_{j=1}^{N}(P_j - O_j)^2 = \underbrace{\left[\frac{1}{N}\sum_{i=1}^{K} n_i(P_i - \overline{O}_i)^2\right]}_{\text{(reliability)}} - \underbrace{\left[\frac{1}{N}\sum_{i=1}^{K} n_i(\overline{O}_i - O_{\mathrm{avg}})^2\right]}_{\text{(resolution)}} + \underbrace{[O_{\mathrm{avg}}(1 - O_{\mathrm{avg}})]}_{\text{(uncertainty)}}, \qquad (3)$$

where N is the number of verifying samples; $K-1$ is the number of forecast probability subranges (K equals 13 in this study); n_i, P_i, and $\overline{O}_i$ are the number of verifying subsamples, the median value of the forecast probabilities, and the conditional observed frequency at forecast probability subrange i, respectively; and O_{avg} is the sample climatology frequency. The reliability term, which has negative orientation (smaller scores is better), stands for

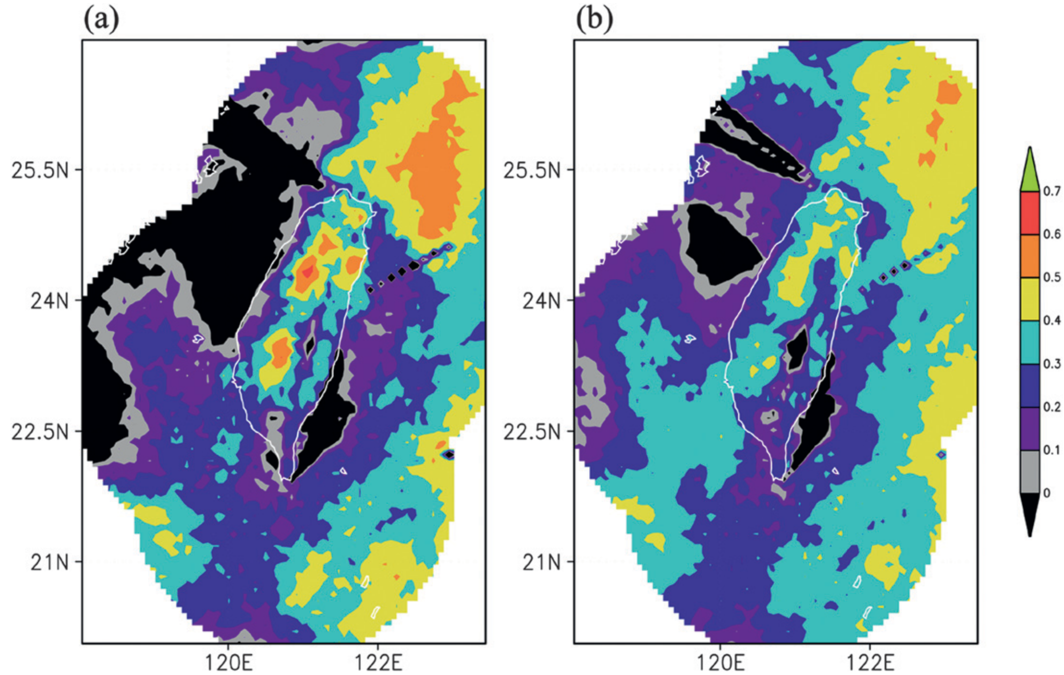

FIG. 10. The spatial distribution of the ranked probabilistic skill score for LAPS 0–6-h PQPFs from the experiments (a) SMP-T (before LR calibration) and (b) SMP-T (LR) (after LR calibration) using four thresholds [1, 5, 10, and 20 mm (6 h)$^{-1}$] to define five categories.

the conditional forecast bias, and the resolution term (positive orientation) represents the forecast ability to discriminate occurrence–nonoccurrence of the events from climatology. The uncertainty term represents for the variability of the observations and will not be altered during the calibration process. For sample climatology, the BSS can be expressed as

$$\mathrm{BSS} = 1 - \frac{\mathrm{BS}}{\mathrm{BS}_{\mathrm{ref}}} = \frac{\text{resolution} - \text{reliability}}{\text{uncertainty}}. \quad (4)$$

Figure 11 shows that at various thresholds the increases of the BSS values (Fig. 9) after calibration [SMP-T(LR) or SMP-T8S(LR)] are achieved by decreasing the reliability term via the calibration procedure, while the resolution term is almost the same after calibration [only slightly decreased in the experiment SMP-T8S (LR) at the threshold of 30 mm (6 h)$^{-1}$]. This calibration result is pretty positive, because sometimes the reduction of the reliability term may be achieved at the cost of the decrease of the resolution term.

d. Spread–skill relationship in the LAPS EPS

In general, an ideal EPS will be expected to have the same size of ensemble spread (SPRD) as their forecast error at the same lead time in order to represent full forecast uncertainty (Kalnay and Dalcher 1987; Whitaker and Loughe 1998; Zhu 2005; Buizza et al. 2005). The SPRD and root-mean-square error (RMSE) of ensemble mean forecasts (Fig. 12) are highly correlated in the LAPS EPS. Except for TY 3, the correlations are all higher than 0.92 with a good regression (high coefficient of determination). In addition, the LAPS EPS is slightly overdispersive for each typhoon case [i.e., the SPRD is slightly larger than the RMSE (almost all data points are located below the diagonal)]. Similarly, the scatterplot

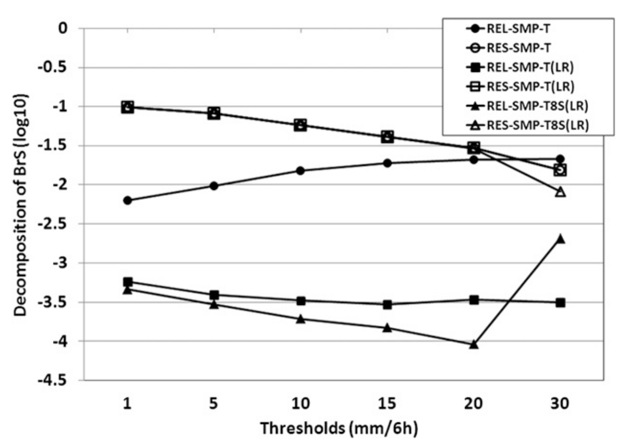

FIG. 11. Decomposition of the Brier score for LAPS 0–6-h PQPFs from the experiments SMP-T (dashed line with circle symbols), SMP-T(LR) (solid line with square symbols), and SMP-T8S(LR) (solid line with triangle symbols). Solid symbols: reliability terms. Hollow symbols: resolution terms.

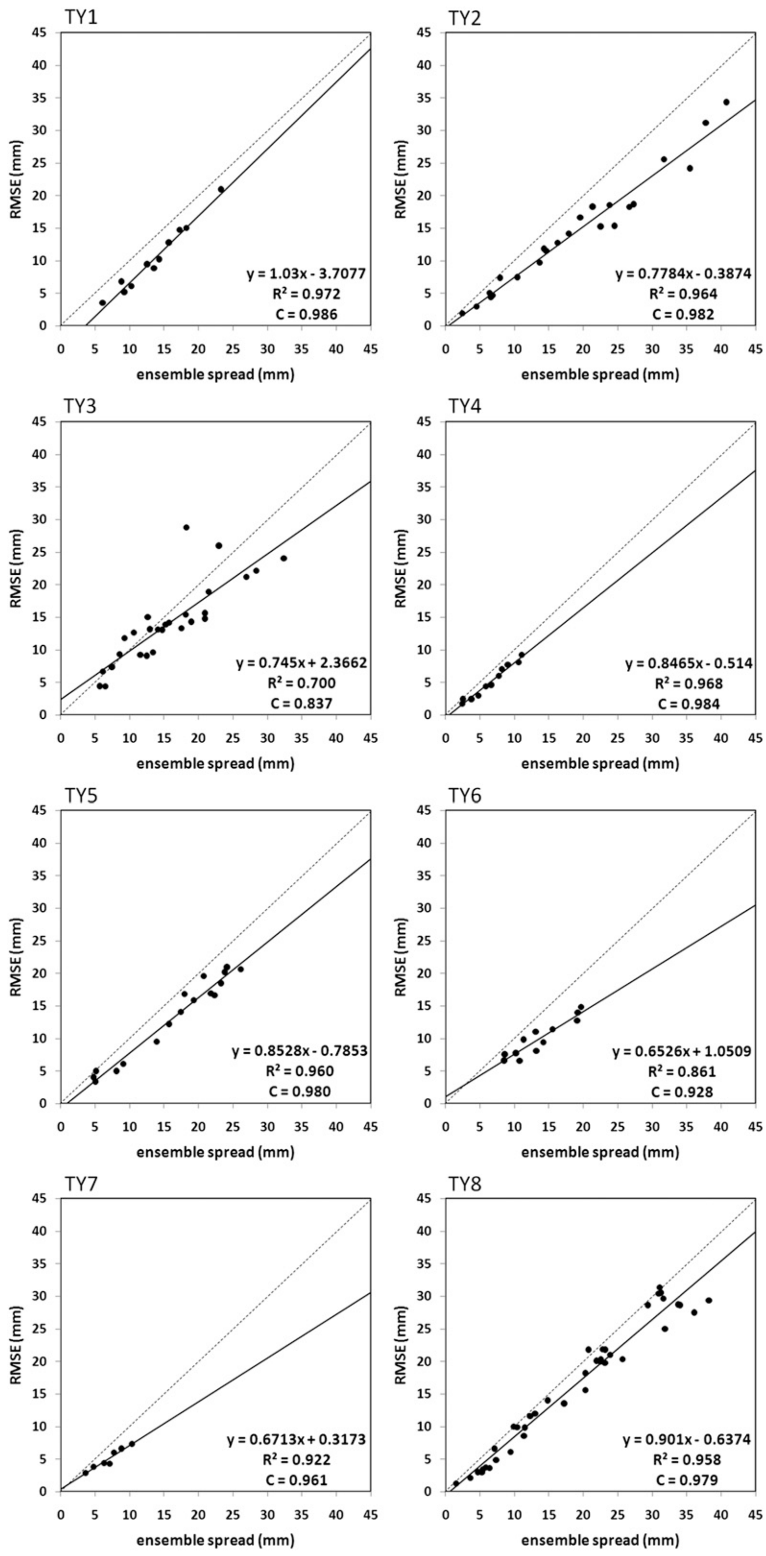

FIG. 12. Scatterplots of the RMSE against the ensemble spread (SPRD) for eight typhoon cases (TY 1–TY 8) from the experiment SMP-T. Each point in the scatterplot comes from one 0–6-h QPF (i.e., RMSE and SPRD are averaged over the QPESUMS domain). The linear regression line, correlation coefficient (C), and the coefficient of determination (R^2) are shown.

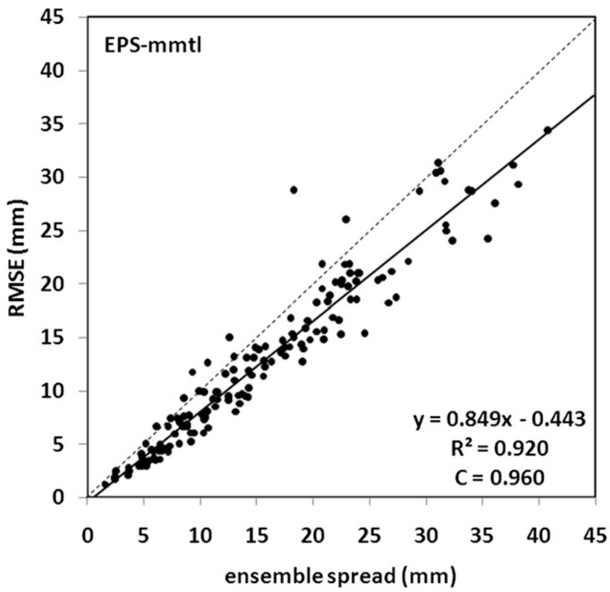

FIG. 13. As in Fig. 12., but for all typhoon cases (TY 1–TY 8) in one plot.

for all typhoon cases (Fig. 13) indicates a high correlation between SPRD and RMSE and slight overdispersion, which becomes more obvious with increasing SPRD.

Table 4 is a contingency table of SPRD and RMSE for 0–6-h ensemble QPFs in the experiment SMP-T. The entries in the table are the joint probability of obtaining the SPRD and RMSE values in the indicated quartiles. If there is no relationship between SPRD and RMSE (i.e., the correlation is zero), all entries in the table will be 0.0625 (=1/16). If there is a perfect linear relationship (i.e., the correlation is unity), all the diagonal entries will be 0.25 and the off-diagonal ones will be zero. The diagonal entries in the table are much higher than 0.0625 and even up to 0.2225. In addition, the contingency table forms a tridiagonal matrix, which indicates that a good spread–skill relationship exists in the LAPS EPS and the SPRD can be used as a predictor of skill, especially when it is extreme (very large or very small).

The scatterplots of EPS-mmtl (Fig. 14a, see Tables 2 and 3 for different samples and ensemble configurations) show that the correlation coefficient in the experiment SMP-T is higher than that in SMP-L. In the experiment SMP-T, TY 4, and TY 7 are the more predictable cases, followed by TY 1 and TY 6. TY 3, TY 5, TY 2, and TY 8 are the less predictable ones. The BSS of eight typhoon cases for the experiment SMP-T (Fig. 15) shows that TY 4 and TY 7 (the more predictable cases) have the highest BSS, followed by TY 1 and TY 6, and then TY 3, TY 5, TY 2, and TY 8 (the less predictable cases). Again, this indicates that small-spread ensemble forecasts have higher skill than large-spread forecasts in the LAPS EPS.

e. Advantage of a time-lagged configuration

One reason to adopt the time-lagged ensemble technique to the short-range forecasting is because a short-range forecast generally possesses a relatively strong dependency on the initial conditions. The forecast errors in the very short range may be strongly correlated to the uncertainties in the initial analysis (Lu et al. 2007). The time-lagged ensembles can be interpreted as the forecasts obtained from a set of perturbed initial conditions (Van den Dool and Rukhovets 1994). In this study, the advantage of time-lagged multimodel ensemble forecasts is compared with simple multimodel ones.

Figure 16 indicates that EPS-mmtl has the highest BSS values among the four different configurations (EPS-mmtl, EPS-m06h, EPS-m09h, and EPS-m12h in Table 3) at all thresholds in the experiment SMP-L (Fig. 16b) and at the thresholds below 15 mm (6 h)$^{-1}$ in the experiment SMP-T (Fig. 16a). Figure 17 shows the relative RMSE (RRMSE) and spatial correlation coefficient of 6-h QPFs of 12 members and 4 ensembles, and EPS-mmtl has the lowest RRMSE and the highest correlation coefficient in both SMP-T and SMP-L.

Regarding the spread–skill relationship (Fig. 14), all three EPSs without time-lagged configuration (EPS-m06h, EPS-m09h, and EPS-m12h) are underdispersive (i.e., the SPRD is smaller than the RMSE) in both SMP-T and SMP-L. Such underdispersion becomes more significant with increasing SPRD, and more severe for shorter-range ensembles (EPS-m06h) and the land samples (SMP-L vs SMP-T). As a time-lagged configuration (EPS-mmtl) is adopted, slight overdispersion exhibits in the experiment SMP-T, and underdispersion is mitigated in the experiment SMP-L but still exists for larger SPRD (>6 mm, shown in the linear regression line), which is consistent with the smaller spread in the rank histogram (Fig. 6b). A time-lagged configuration, which is much more important for the less predictable cases (i.e., larger SPRD) and for the forecasts in the land, can mitigate the underdispersion to better represent the forecast uncertainty (SPRD comparable to RMSE).

6. Sensitivity experiments

In this section, two sets of sensitivity experiments (Table 2) were carried out, including 1) the experiments on different training samples to understand the influence of different training samples over the calibration results, and 2) the experiments on the accuracy of observation data to understand how the inconsistency of observation data accuracy from the sea and land areas will influence the calibration results. In fact, the QPESUMS QPEs, used as the ground truth, have been calibrated

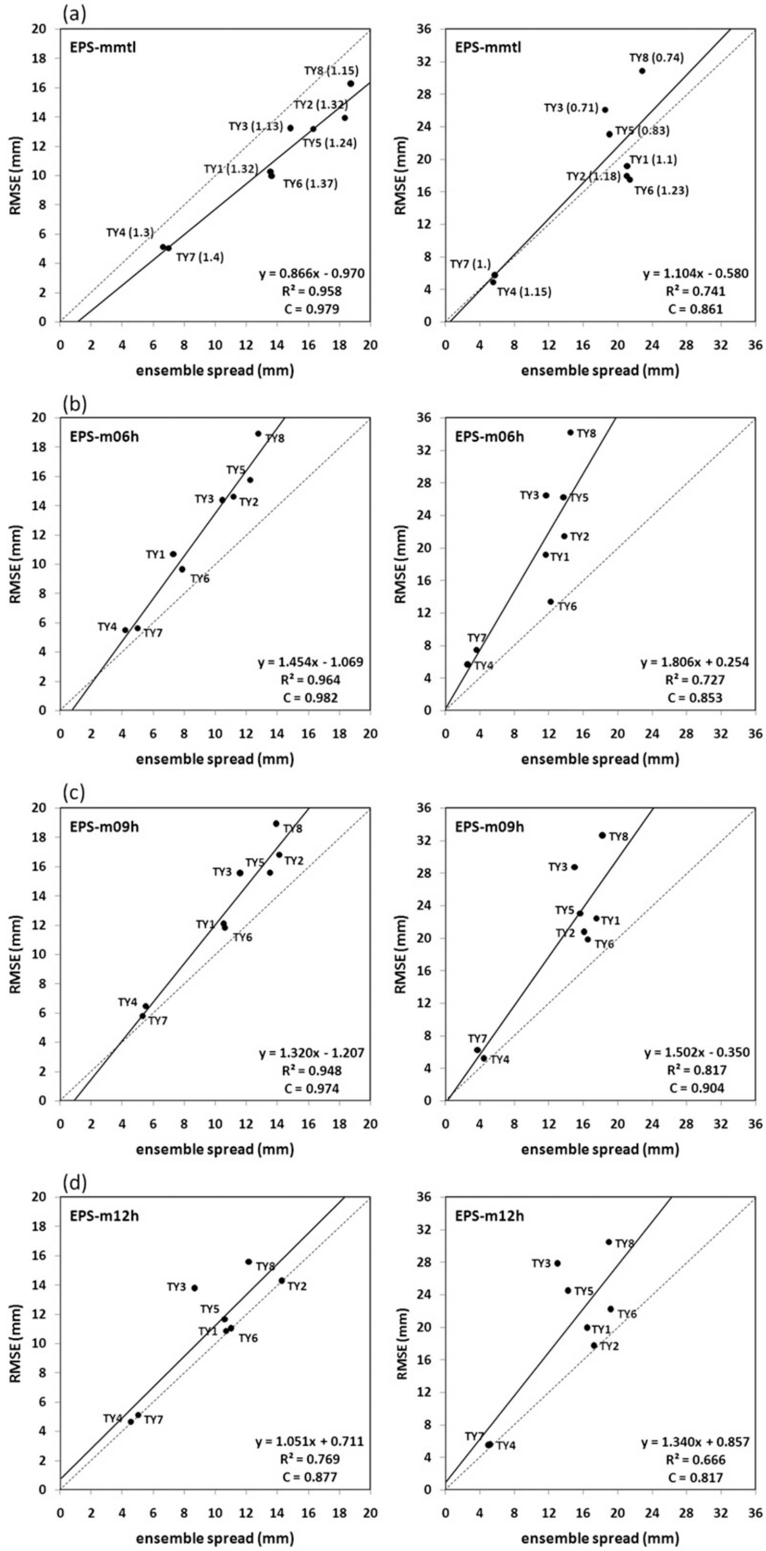

FIG. 14. As in Fig. 13., but for the four different ensemble configurations (a) EPS-mmtl, (b) EPS-m06h, (c) EPS-m09h, and (d) EPS-m12h, respectively. The results of (left) experiment SMP-T and (right) experiment SMP-L. Each point in the scatterplot comes from one typhoon case. The ratio of SPRD over RMSE is also indicated on the plot of EPS-mmtl.

TABLE 3. Summary of models and ensemble prediction systems.

Model 1	LAPS-MM5(NFS) 0–6-h QPFs	Model 7	LAPS-WRF(NFS) 0–6-h QPFs
Model 2	LAPS-MM5(NFS) 3–9-h QPFs	Model 8	LAPS-WRF(NFS) 3–9-h QPFs
Model 3	LAPS-MM5(NFS) 6–12-h QPFs	Model 9	LAPS-WRF(NFS) 6–12-h QPFs
Model 4	LAPS-MM5(AVN) 0–6-h QPFs	Model 10	LAPS-WRF(AVN) 0–6-h QPFs
Model 5	LAPS-MM5(AVN) 3–9-h QPFs	Model 11	LAPS-WRF(AVN) 3–9-h QPFs
Model 6	LAPS-MM5(AVN) 6–12-h QPFs	Model 12	LAPS-WRF(AVN) 6–12-h QPFs
EPS-mmtl	A 12-member ensemble prediction system with models 1–12		
EPS-m06h	A 4-member ensemble prediction system with models 1, 4, 7, and 10		
EPS-m09h	A 4-member ensemble prediction system with models 2, 5, 8, and 11		
EPS-m12h	A 4-member ensemble prediction system with models 3, 6, 9, and 12		

with the observed precipitation from rain gauges in the land areas, while they have no calibration in the sea areas. In a few cases, there was clear discontinuity in QPESUMS QPEs along the costal line of Taiwan.

a. Experiments on different training samples

The difference between the two calibration experiments SMP-T(LR) and SMP-T8S(LR) lies in that the reference experiment SMP-T adopts different training samples during the LR calibration process. All statistical samples in the experiment SMP-T(LR) were divided into two groups when performing the cross-validation procedure, typhoon cases in 2008 (TY 1–TY 5) and 2009 (TY 6–TY 8), respectively, where one of these two groups was used as the training samples to calibrate the other (the validation samples). The experiment SMP-T8S(LR) puts all statistical samples into eight groups, eight different typhoon cases (TY 1–TY 8) in 2008 and 2009, where seven groups were used as the training samples to calibrate the remaining one. In other words, each typhoon case serves as the validation samples in turn. All the calibration results shown in this study have combined all validation samples in one set of figures.

At various thresholds, the LR calibration [SMP-T(LR) or SMP-T8S(LR)] can increase the BSS over the experiment SMP-T (Fig. 9) and shows the improved skill of PQPFs. In addition, the improvement grows with increasing threshold. Only at 30 mm (6 h)$^{-1}$ threshold, the BSS of SMP-T(LR) is much higher than that of SMP-T8S(LR). At other thresholds lower than 30 mm (6 h)$^{-1}$, the resolution values (Fig. 11) vary slightly among these three experiments [SMP-T, SMP-T(LR), and SMP-T8S(LR)], while the reliability values of SMP-T8S(LR) decrease slightly more than those of SMP-T(LR). However, at the threshold of 30 mm (6 h)$^{-1}$, the reliability value of SMP-T8S(LR) decreases far less than that of SMP-T(LR). In addition, the resolution value of SMP-T8S(LR) decreases after the LR calibration, which means that the forecast ability to discriminate the extreme precipitation events from climatology has been lost during the calibration process.

Figure 18 indicates that eight typhoon cases do not show a very good precipitation similarity at 30 mm (6 h)$^{-1}$ threshold in the reliability. In other words, some inconsistency exists among the forecast biases of these eight typhoon cases. Therefore, although the experiment SMP-T8S(LR) used far more training samples than the experiment SMP-T(LR), it does not necessarily produce a better calibration result. Indeed, the calibration principle is constructed based on the consistent (or very similar) distribution of the forecast biases between the training and validation samples.

This sensitivity experiment shows that the calibration results vary with the training samples, and adopting more training samples does not necessarily produce better calibration results. It is essential to apply data with similar forecast biases as the training samples to achieve better calibration results. In the future, the similar typhoon types should be considered to establish various LR relationships based on different typhoon classifications. In addition, individual calibration for the areas with different precipitation characteristics (Yuan et al.

TABLE 4. Contingency table of ensemble spread (SPRD) and RMSE for LAPS 0–6-h ensemble QPFs in experiment SMP-T using the configuration of EPS-mmtl. The entries in the table are the joint probability of obtaining the SPRD and RMSE values in the indicated quartiles.

(Joint probability)		SPRD quartiles 0%–25%	25%–50%	50%–75%	75%–100%
RMSE quartiles	0%–25%	0.2225	0. 0275	0	0
	25%–50%	0.0275	0.1950	0. 0275	0
	50%–75%	0	0. 0275	0.1850	0. 0275
	75%–100%	0	0	0. 0275	0.2225

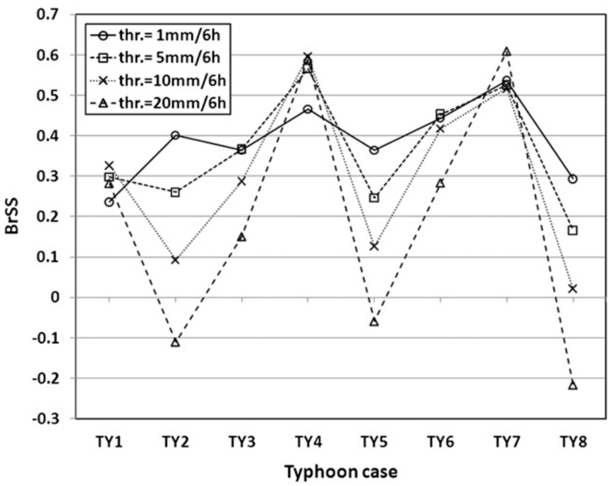

FIG. 15. Brier skill scores of eight typhoon cases (TY 1–TY 8) for experiment SMP-T at different thresholds [1, 5, 10, and 20 mm $(6\ \mathrm{h})^{-1}$].

2007b) would also be the direction for further research and study.

b. *Experiments on the accuracy of observation data*

The forecast skill highly depends on verification/observation data, especially precipitation analyses over the mountainous areas (Yuan et al. 2005). In this study, there are two designed experiments using statistical samples from different radar coverage: the samples of the experiments SMP-T and SMP-T(LR) are adopted from all radar coverage (including the sea and land areas) within the QPESUMS domain, while those of the experiments SMP-L and SMP-L(LR) are only from the land areas in Taiwan, accounting for 9.4% of all samples. Thus, the performance of the experiment SMP-T is almost dominated by the ocean samples.

The RH from the experiment SMP-T (Fig. 6a) shows that the LAPS forecasts for typhoon cases have significant wet biases. The experiment SMP-L (Fig. 6b) shows too small LAPS ensemble spread in the land areas, with about 35% of samples whose observations are outside the extremes of the ensemble forecasts, about 23% (12%) of samples with the observations ranked the lowest (highest). The RH solely from the ocean samples is very similar to that from the experiment SMP-T since more than 90% of samples in the experiment SMP-T come from the sea areas.

Similar to the experiments SMP-T and SMP-T(LR) (Fig. 7), the reliability diagrams (Fig. 19) of SMP-L and SMP-L(LR) show mixed biases at each threshold. Dry (wet) biases come mainly from the samples with lower (higher) forecast probabilities. The higher the threshold, the smaller the sample percentage with higher forecast probabilities. In addition, the experiments SMP-T and SMP-L (Figs. 7 and 19) show that the wet biases become more evident with increasing threshold, and the severe wet biases in SMP-T result mainly from the ocean samples. This overestimation tendency for heavy precipitation may be caused by deactivation of cumulus parameterization in LAPS with 9-km horizontal resolution during the warm rain processes. Generally speaking, both experiments achieve the bias correction by adjusting the extreme forecast probabilities to the medium ones. Note that the samples with higher forecast probabilities are viewed as unreliable at higher thresholds [above 10 mm $(6\ \mathrm{h})^{-1}$, not shown] in the experiment SMP-T (Fig. 7), and thus they are removed after calibration [SMP-T(LR)]. Since the experiment SMP-L (Fig. 19) does not have obvious biases before calibration, the LR calibration only makes a minimal bias correction. This indicates that the LAPS EPS have better discrimination capabilities in the land areas.

The ROC area (Fig. 8b) indicates that at each threshold, the experiment SMP-L has better resolution than the experiment SMP-T (i.e., a better ability to discriminate between precipitation occurrence and nonoccurrence). In

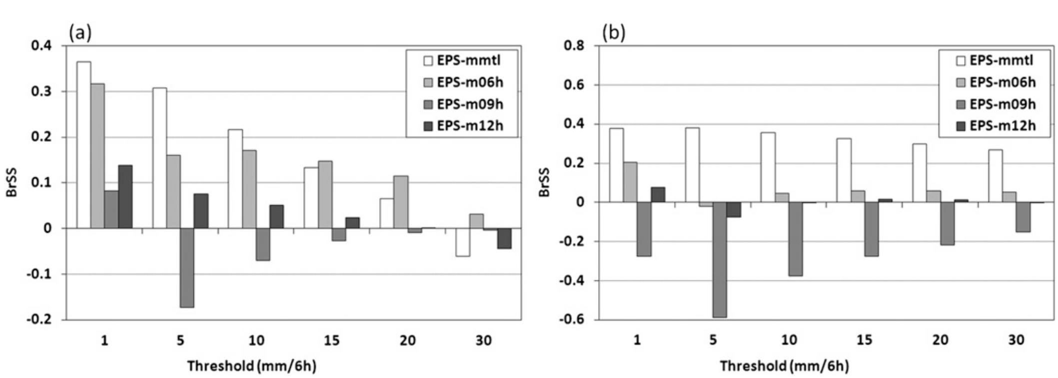

FIG. 16. Brier skill scores at different thresholds for four different ensemble configurations (EPS-mmtl, EPS-m06h, EPS-m09h, and EPS-m12h) for the experiments (a) SMP-T and (b) SMP-L.

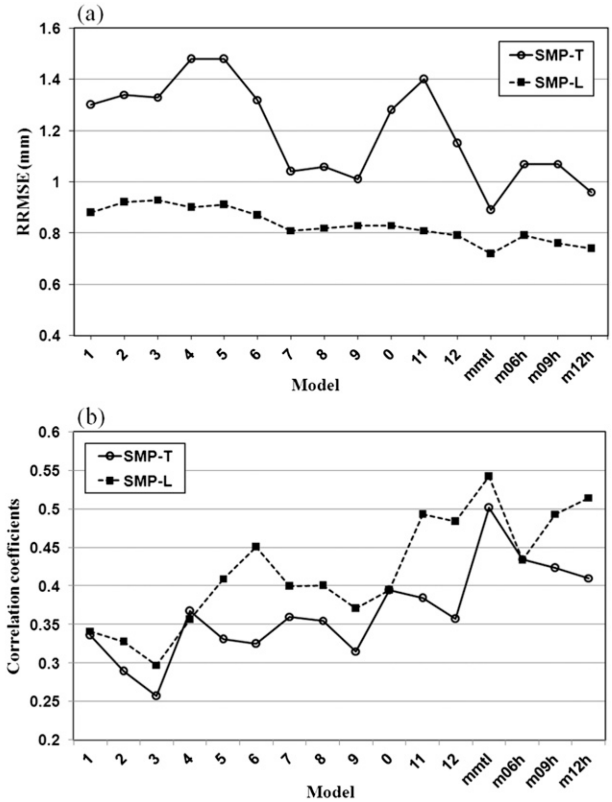

FIG. 17. (a) The RRMSE and (b) the correlation coefficient of 6-h accumulated precipitation forecasts of 12 members and four ensemble configurations (EPS-mmtl, EPS-m06h, EPS-m09h, and EPS-m12h) in Table 3 from the experiments SMP-T (line with circles) and SMP-L (line with squares).

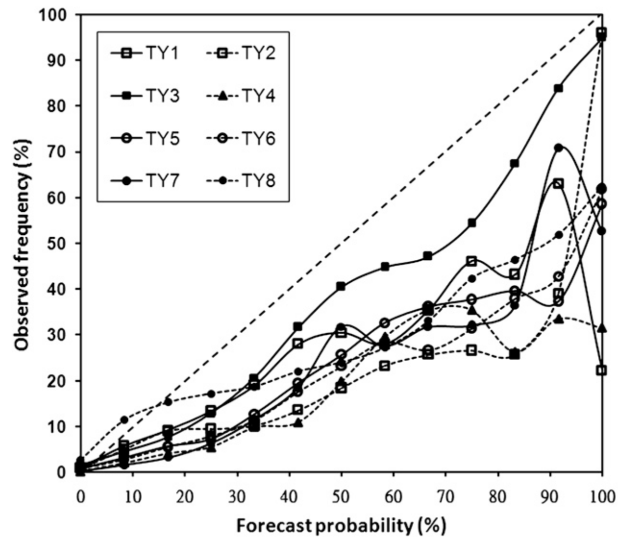

FIG. 18. Reliability diagram for LAPS 0–6-h PQPFs at the threshold of 30 mm (6 h)$^{-1}$. Reliability curves from TY 1 to TY 8 are shown.

addition, the potential usefulness of both the experiments SMP-T and SMP-L slightly reduces with increasing threshold.

Figure 17 reveals that almost every ensemble member has lower RRMSE and higher spatial correlation coefficients in the experiment SMP-L than that in SMP-T (i.e., the performance of QPFs is better in the land areas). In addition, the performance of the ensemble mean in EPS-mmtl excels that of individual ensemble members.

Compared with the experiments SMP-T and SMP-T(LR), the experiments SMP-L and SMP-L(LR) have higher BSS values (Fig. 20). In addition, the BSS values reduce with increasing threshold, and the experiment SMP-T is unskillful when compared to climatology at the threshold of 30 mm (6 h)$^{-1}$. And the forecast skill is improved after calibration at various thresholds [SMP-T(LR) vs SMP-T; SMP-L(LR) vs SMP-L]. Except for the threshold of 1 mm (6 h)$^{-1}$, the BSS values of the experiment SMP-L are even higher than those of the experiment SMP-T(LR) at all thresholds, and the gap widens with increasing threshold.

The spatial distributions of the RPSS (Fig. 10) from the experiments SMP-T and SMP-T(LR) show that the skill of PQPFs was improved at most areas (the southwestern, northwestern, eastern, and southeastern sea areas of Taiwan) after calibration. However, the RPSS values in the northeastern oceanic and mountainous areas of Taiwan apparently decrease after calibration. This could be associated with the poor quality of the QPESUMS QPEs used as the observation data in the sea areas. Because of the inconsistency of the observation data accuracy between the sea and land areas and more abundant ocean samples than the land ones (about 9 times), the RPSS values therefore, in some land areas, obviously fall after calibration (i.e., the probabilistic forecast skill in most sea areas is improved at the cost of those in a few land areas during the calibration process). Compared with the experiment SMP-L (not shown), the RPSS values in the experiment SMP-L(LR) became slightly higher in most coastal areas, with only a minimal reduction in very small parts of mountainous areas.

In summary, there are severe wet biases in the LAPS EPS in the sea areas. Therefore, the performance of precipitation forecasts in the experiment SMP-L (land samples) excels that in the experiment SMP-T (mainly dominated by ocean samples). For typhoon cases, the precipitation in the land areas affected by orographic lifting may be easier to be predicted accurately, in comparison with the forecasts of typhoon rainbands in the sea areas. In addition, the relatively inferior forecast performance in the sea areas probably results from the underestimation of the QPESUMS QPEs. Currently,

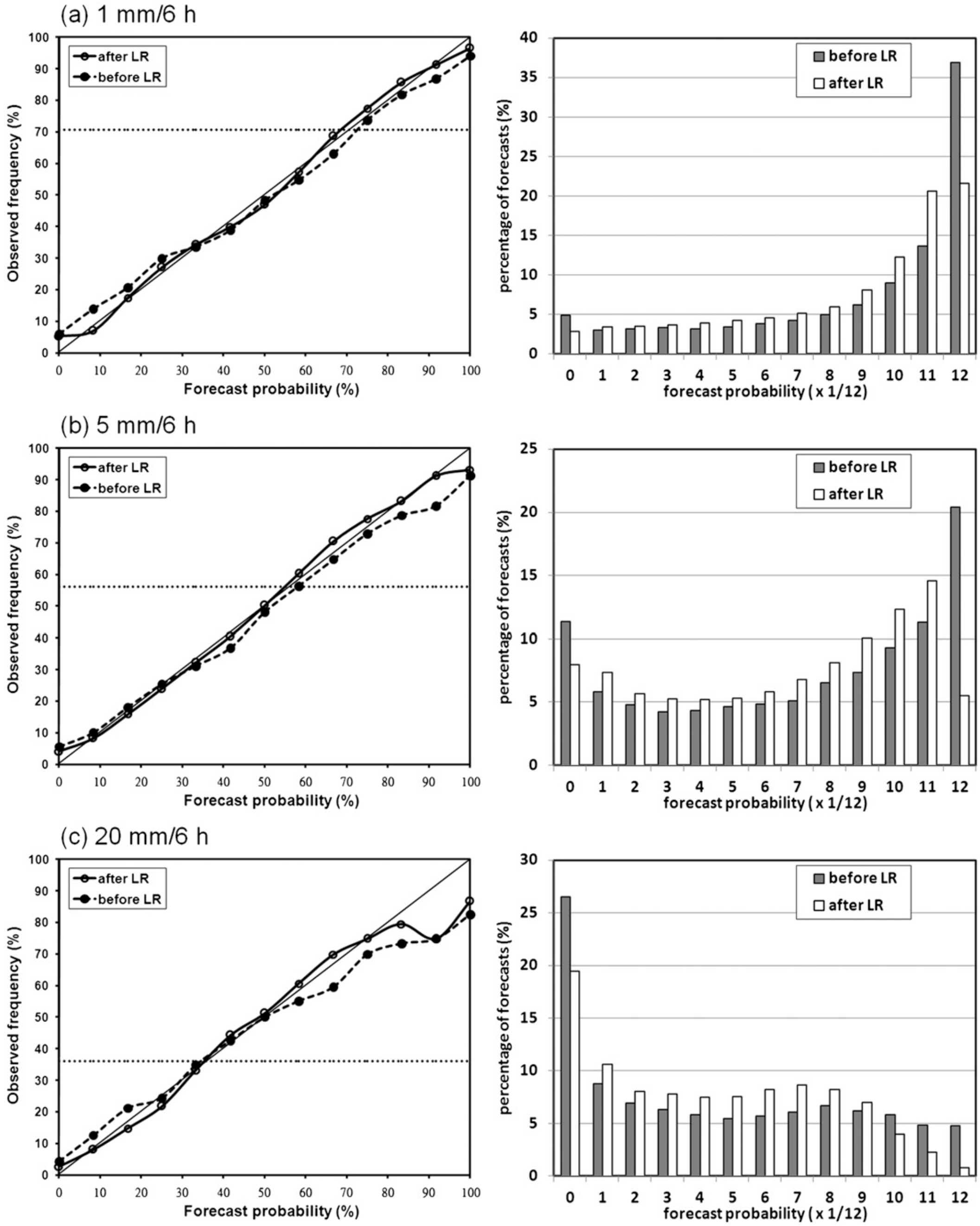

FIG. 19. As in Fig. 7, but from the experiments SMP-L (before LR calibration) and SMP-L (LR) (after LR calibration).

the QPESUMS applies the same Z–R relationship for various weather systems and geographic areas, while previous verifications revealed that the QPEs derived from this Z–R relationship showed a feature of underestimation in the land areas. In the sea areas far from radars, the likelihood of underestimated QPEs is rather high due to higher radar beams. It is not easy to verify these two inferences because of the lack of precipitation observations in the sea areas. To conclude, individual calibration for the sea and land areas is needed to obtain better calibrated PQPFs.

7. Summary and future work

This study pioneers the development of short-range PQPFs in Taiwan. It aims mainly to provide more valuable

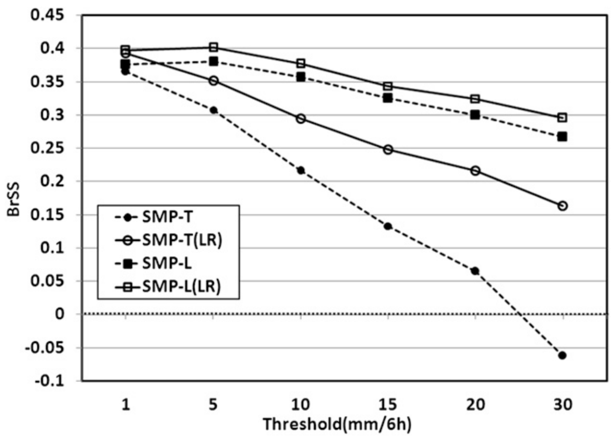

FIG. 20. Brier skill scores at different thresholds for LAPS 0–6-h PQPFs from the experiments SMP-T (dashed line with solid dots), SMP-T(LR) (solid line with hollow circles), SMP-L (dashed line with solid squares), and SMP-L(LR) (solid line with hollow squares).

0–12-h forecast products for severe weather systems seriously affecting general livelihood. Because the data assimilation procedure of LAPS can provide the initial fields of mesoscale models with diabatic information, it can effectively mitigate the major problem of short-range QPFs—the spinup problem during the early stage of model integration. Therefore, this study applies LAPS as a basic tool to develop the PQPFs from time-lagged multimodel ensembles in order to capture the critical uncertainties, and to convey the uncertainties in prediction processes to the forecasters and end users.

Based on the sensitivity experiments, for the 0–6- or 6–12-h QPFs of LAPS, background field and mesoscale model are more critical uncertainty factors compared to microphysical parameterizations. Therefore, we built a multimodel EPS by using different background fields and mesoscale models in order to enlarge the ensemble spread. In addition, we also adopted the time-lagged configuration to increase the ensemble members using previous forecasts without additional computational cost. A time-lagged configuration can make the LAPS EPS have better forecast performance and skill–spread relationship, especially for the less predictable typhoon cases and over the land areas. The PQPF products can actually provide the users with the reliability of precipitation forecasts and the possibility for precipitation exceeding a certain threshold, and can serve as the reference for policy decision makers to deal with disaster prevention and relief.

Because the verification results show significant wet biases in the LAPS EPS for typhoon cases, this study applies the LR method to calibrate the PQPFs. The cross-validation results based on eight typhoon cases in 2008 and 2009 indicate that forecast biases can be corrected via the calibration procedure to improve the skill of PQPFs.

In addition, this study carries out sensitivity experiments on two factors affecting the calibration results, including the training sample size and the accuracy of observation data. The LR calibration results vary with the training samples, and adopting more training samples does not guarantee better calibration results. In fact, the eight typhoon cases did not show a very good precipitation similarity in terms of the reliability and forecast biases (Fig. 18). Therefore, more training samples could cause the poor calibration performance [SMP-T8S(LR) vs SMP-T(LR)]. Most important, the calibration principle is constructed based on the consistent (or very similar) distribution of the forecast biases between the training and validation samples.

In the future, with more collected typhoon cases, the distributions of precipitation forecast biases can be analyzed for different typhoon paths, moving speeds, or precipitation intensities. Then various LR relationships can be established and applied to different distributions of forecast biases in the typhoon cases, thus to produce better calibration results.

The inconsistency of observation data accuracy from the sea and land areas influences the calibration results. This is due to the fact that the QPEs of QPESUMS (used as the ground truth) have been calibrated with the observed precipitation in the land areas, while they have no calibration in the sea areas, which results in slightly worse accuracy. The verifications of PQPFs show that the forecast skill of experiment SMP-T (including ocean and land samples) is improved (such as higher BSS values) after calibration. However, because of the inconsistency of the observation data accuracy in the sea and land areas and more abundant ocean samples (about 9 times of land samples), the bias correction of most sea samples is achieved at the sacrifice of the bias correction of some land samples in the experiment SMP-T(LR). Hence, separate calibration for the sea and land areas may ensure better calibration results of PQPFs.

However, the result was not very positive using the LR method to calibrate the PQPFs for mei-yu front cases. The reason is that the phenomenon of the pattern shift often exists in the LAPS forecasts for mei-yu front cases, which results in incorrect correspondence between the observation and forecast precipitation systems and would seriously affect the calibration results. In the future, the pattern shift needs to be corrected for mei-yu front cases before calibration of PQPFs. In addition, forecast biases in the LAPS EPS vary with distinctive geographic environment in Taiwan, thus performing individual calibration of PQPFs for different regional areas should be considered.

Acknowledgments. The NOAA/ESRL/GSD has supported the technology transfer of the PQPF calibration technique (Yuan et al. 2008) and the LAPS system. Thanks to Drs. Fanthune Moeng, John A. McGinley, and Yuanfu Xie, and Steve Albersat NOAA/ESRL/GSD for facilitating the collaboration and CWB of Taiwan for supporting this project. Thanks to Ms. Annie Reiser at NOAA/ESRL for editing this manuscript and Dr. Chien-Ben Chou at CWB for helpful discussions. We also thank two anonymous reviewers for their valuable comments. The second author (H. Yuan) received the support from Natural Science Foundation of China (41175087), the R&D Special Fund for Public Welfare Industry (Meteorology) (GYHY201206005), Scientific Research Foundation for Introduced Talent, Nanjing University (020722631003), and the Priority Academic Program Development of Jiangsu Higher Education Institutions.

REFERENCES

Albers, S., 1995: The LAPS wind analysis. *Wea. Forecasting,* **10,** 342–352.

——, J. McGinley, D. Birkenheuer, and J. Smart, 1996: The Local Analysis and Prediction System (LAPS): Analyses of clouds, precipitation, and temperature. *Wea. Forecasting,* **11,** 273–287.

Atger, F., 2003: Spatial and interannual variability of the reliability of ensemble-based probabilistic forecasts: Consequences for calibration. *Mon. Wea. Rev.,* **131,** 1509–1523.

Birkenheuer, D., 1999: The effect of using digital satellite imagery in the LAPS moisture analysis. *Wea. Forecasting,* **14,** 782–788.

Buizza, R., P. L. Houtekamer, Z. Toth, G. Pellerin, M. Wei, and Y. Zhu, 2005: A comparison of the ECMWF, MSC, and NCEP global ensemble prediction systems. *Mon. Wea. Rev.,* **133,** 1076–1097.

Cheung, K. K. W., 2001: A review of ensemble forecasting techniques with a focus on tropical cyclone forecasting. *Meteor. Appl.,* **8,** 315–332.

Chien, F.-C., and B. J.-D. Jou, 2004: MM5 ensemble mean precipitation forecasts in the Taiwan area for three early summer convective (mei-yu) seasons. *Wea. Forecasting,* **19,** 735–750.

——, Y.-C. Shao, B. J.-D. Jou, P.-L. Lin, M.-J. Yang, J.-S. Hong, J.-H. Teng, and H.-C. Lin, 2003: Precipitation verification of the MM5 ensemble forecast (in Chinese with an English abstract). *Atmos. Sci.,* **31,** 77–94.

——, Y.-C. Liu, B. J.-D. Jou, P.-L. Lin, J.-S. Hong, and L.-F. Hsiao, 2005: MM5 ensemble rainfall forecasts during the 2003 Mei-yu season (in Chinese with an English abstract). *Atmos. Sci.,* **33,** 255–275.

Davis, C. A., and S. Low-Nam, 2001: The NCAR-AFWA tropical cyclone bogussing scheme. Air Force Weather Agency (AFWA) Rep., 13 pp. [Available online at http://www.mmm.ucar.edu/mm5/mm5v3/tc-report.pdf.]

Donner, L. J., 1988: An initialization for cumulus convection in numerical weather prediction models. *Mon. Wea. Rev.,* **116,** 377–385.

Eckel, F. A., and M. K. Walters, 1998: Calibrated probabilistic quantitative precipitation forecasts based on the MRF ensemble. *Wea. Forecasting,* **13,** 1132–1147.

Glahn, H. R., and D. A. Lowry, 1972: The use of model output statistics (MOS) in objective weather forecasting. *J. Appl. Meteor.,* **11,** 1203–1211.

Gourley, J. J., J. Zhang, R. A. Maddox, C. M. Calvert, and K. W. Howard, 2001: A real-time precipitation monitoring algorithm—Quantitative Precipitation Estimation Using Multiple Sensors (QPE-SUMS). Preprints, *Symp. on Precipitation Extremes: Prediction, Impacts, and Responses,* Albuquerque, NM, Amer. Meteor. Soc., 57–60.

Grell, G., J. Dudhia, and D. Stauffer, 1995: A description of the fifth-generation Penn State/NCAR Mesoscale Model (MM5). NCAR Tech. Note NCAR/TN-398+STR, 138 pp.

Hamill, T. M., 1997: Reliability diagrams for multicategory probabilistic forecasts. *Wea. Forecasting,* **12,** 736–741.

——, 2001: Interpretation of rank histograms for verifying ensemble forecasts. *Mon. Wea. Rev.,* **129,** 550–560.

——, and J. Juras, 2006: Measuring forecast skill: Is it real skill or is it the varying climatology? *Quart. J. Roy. Meteor. Soc.,* **132,** 2905–2923.

Harms, D. E., R. V. Madala, S. Raman, and K. D. Sashegyi, 1993: Diabatic initialization tests using the Naval Research Laboratory limited-area numerical weather prediction model. *Mon. Wea. Rev.,* **121,** 3184–3190.

Heckley, W. A., 1985: Systematic errors of the ECMWF operational forecasting model in tropical regions. *Quart. J. Roy. Meteor. Soc.,* **111,** 709–738.

Hsu, W.-R., and A. H. Murphy, 1986: The attributes diagram: A geometrical framework for assessing the quality of probability forecasts. *Int. J. Forecasting,* **2,** 285–293.

Jian, G.-J., and J. McGinley, 2005: Evaluation of a short-range forecast system on quantitative precipitation forecasts associated with tropical cyclones of 2003 near Taiwan. *J. Meteor. Soc. Japan,* **83,** 657–681.

——, S.-L. Shieh, and J. McGinley, 2003: Precipitation associated with Typhoon Sinlaku (2002) in Taiwan area using the LAPS diabatic initialization for MM5. *TAO,* **14,** 1–28.

Jolliffe, I. T., and D. B. Stephenson, 2003: *Forecast Verification: A Practitioner's Guide in Atmospheric Science.* Wiley, 254 pp.

Kalnay, E., and A. Dalcher, 1987: Forecasting forecast skill. *Mon. Wea. Rev.,* **115,** 349–356.

Krishnamurti, T. N., J. Xue, H. S. Bedi, K. Ingles, and D. Oosterhof, 1991: Physical initialization for numerical weather prediction over the tropics. *Tellus,* **43AB,** 53–81.

Lu, C., H. Yuan, B. Schwartz, and S. Benjamin, 2007: Short-range forecast using time-lagged ensembles. *Wea. Forecasting,* **22,** 580–595.

Mason, S. J., and N. E. Graham, 1999: Conditional probabilities, relative operating characteristics, and relative operating levels. *Wea. Forecasting,* **14,** 713–725.

Mass, C. F., 2003: IFPS and the future of the National Weather Service. *Wea. Forecasting,* **18,** 75–79.

Mohanty, U. C., A. Kasahara, and R. Errico, 1986: The impact of diabatic heating on the initialization of a global forecast model. *J. Meteor. Soc. Japan,* **64,** 805–817.

Mullen, S. L., and R. Buizza, 2004: Calibration of probabilistic precipitation forecasts from the ECMWF EPS by an artificial neural network. Preprints, *17th Conf. on Probability and Statistics in the Atmospheric Sciences*, Seattle, WA, Amer. Meteor. Soc., J5.6.

Murphy, A. H., 1973: A new vector partition of the probability score. *J. Appl. Meteor.,* **12,** 595–600.

Schultz, P., 1995: An explicit cloud physics parameterization for operational numerical weather prediction. *Mon. Wea. Rev.,* **123,** 3331–3343.

Toth, Z., and E. Kalnay, 1993: Ensemble forecasting at NMC: The generation of perturbations. *Bull. Amer. Meteor. Soc.,* **74,** 2317–2330.

Van den Dool, H. M., and L. Rukhovets, 1994: On the weights for an ensemble-averaged 6–10-day forecast. *Wea. Forecasting,* **9,** 457–465.

Vislocky, R. L., and J. M. Fritsch, 1997: Performance of an advanced MOS system in the 1996–97 national collegiate weather forecasting conference. *Bull. Amer. Meteor. Soc.,* **78,** 2851–2857.

Whitaker, J. S., and A. F. Loughe, 1998: The relationship between ensemble spread and ensemble mean skill. *Mon. Wea. Rev.,* **126,** 3292–3302.

Wilks, D. S., 2006: *Statistical Methods in the Atmospheric Sciences.* 2nd ed. Academic Press, 627 pp.

Yang, M.-J., B. J.-D. Jou, S.-C. Wang, J.-S. Hong, P.-L. Lin, J.-H. Teng, and H.-C. Lin, 2004: Ensemble prediction of rainfall during the 2000–2002 Mei-Yu seasons: Evaluation over the Taiwan area. *J. Geophys. Res.,* **109,** D18203, doi:10.1029/2003JD004368.

Yuan, H., S. L. Mullen, X. Gao, S. Sorooshian, J. Du, and H. H. Juang, 2005: Verification of probabilistic quantitative precipitation forecasts over the southwest United States during winter 2002/03 by the RSM ensemble system. *Mon. Wea. Rev.,* **133,** 279–294.

——, X. Gao, S. L. Mullen, S. Sorooshian, J. Du, and H. H. Juang, 2007a: Calibration of probabilistic quantitative precipitation forecasts with an artificial neural network. *Wea. Forecasting,* **22,** 1287–1303.

——, S. L. Mullen, X. Gao, S. Sorooshian, J. Du, and H. H. Juang, 2007b: Short-range probabilistic Quantitative Precipitation Forecasts over the southwest United States by the RSM ensemble system. *Mon. Wea. Rev.,* **135,** 1685–1698.

——, J. A. McGinley, P. J. Schultz, C. J. Anderson, and C. Lu, 2008: Short-range precipitation forecasts from time-lagged multimodel ensembles during the HMT-West-2006 campaign. *J. Hydrometeor.,* **9,** 477–491.

Zhu, Y., 2005: Ensemble forecast: A new approach to uncertainty and predictability. *Adv. Atmos. Sci.,* **22** (6), 781–788.

JOURNAL OF GEOPHYSICAL RESEARCH, VOL. 117, A10318, doi:10.1029/2012JA017700, 2012

Assimilation of FORMOSAT-3/COSMIC electron density profiles into a coupled thermosphere/ionosphere model using ensemble Kalman filtering

I. T. Lee,[1,2] T. Matsuo,[3,4] A. D. Richmond,[2] J. Y. Liu,[1,5] W. Wang,[2] C. H. Lin,[6] J. L. Anderson,[7] and M. Q. Chen[1]

Received 8 March 2012; revised 14 August 2012; accepted 17 September 2012; published 13 October 2012.

[1] This paper presents our effort to assimilate FORMOSAT-3/COSMIC (F3/C) GPS Occultation Experiment (GOX) observations into the National Center for Atmospheric Research (NCAR) Thermosphere Ionosphere Electrodynamics General Circulation Model (TIE-GCM) by means of ensemble Kalman filtering (EnKF). The F3/C electron density profiles (EDPs) uniformly distributed around the globe which provide an excellent opportunity to monitor the ionospheric electron density structure. The NCAR TIE-GCM simulates the Earth's thermosphere and ionosphere by using self-consistent solutions for the coupled nonlinear equations of hydrodynamics, neutral and ion chemistry, and electrodynamics. The F3/C EDP are combined with the TIE-GCM simulations by EnKF algorithms implemented in the NCAR Data Assimilation Research Testbed (DART) open-source community facility to compute the expected value of electron density, which is 'the best' estimate of the current ionospheric state. Assimilation analyses obtained with real F3/C electron density profiles are compared with independent ground-based observations as well as the F3/C profiles themselves. The comparison shows the improvement of the primary ionospheric parameters, such as NmF2 and hmF2. Nevertheless, some unrealistic signatures appearing in the results and high rejection rates of observations due to the applied outlier threshold and quality control are found in the assimilation experiments. This paper further discusses the limitations of the model and the impact of ensemble member creation approaches on the assimilation results, and proposes possible methods to avoid these problems for future work.

Citation: Lee, I. T., T. Matsuo, A. D. Richmond, J. Y. Liu, W. Wang, C. H. Lin, J. L. Anderson, and M. Q. Chen (2012), Assimilation of FORMOSAT-3/COSMIC electron density profiles into a coupled thermosphere/ionosphere model using ensemble Kalman filtering, *J. Geophys. Res.*, *117*, A10318, doi:10.1029/2012JA017700.

1. Introduction

[2] The ionospheric electron density distribution can affect human activities and systems, such as navigation and HF communication systems. To monitor the state of the ionosphere, so-called ionospheric weather, solely by observations is difficult due to lack of observations with sufficient spatial and temporal resolutions. Modeling the ionospheric weather is complex, since it varies with longitude, latitude, altitude, local time (LT), season, solar activity, and the geomagnetic condition. The ionospheric variability results from changes in internal and external drivers, such as neutral wind circulation, solar radiation, solar wind and interplanetary magnetic field interaction with the magnetosphere, and from the dynamical and nonlinear response of the thermosphere and ionosphere to these changes. Most empirical and physics-based theoretical/numerical models can simulate many climatological features of the ionosphere, but fail to reproduce the ionospheric weather due to lack of reliable estimations of the ionospheric drivers [*Scherliess et al.*, 2006]. In addition, recent studies point out that the ionospheric drivers that are crucial to the specification of the ionospheric weather involve not only solar radiation and high-latitude electric fields and particle precipitation but also the thermospheric composition, temperature, and winds [*Datta-Barua et al.*, 2009; *Scherliess et al.*, 2009].

[1]Institute of Space Science, National Central University, Chung-Li, Taiwan.
[2]High Altitude Observatory, National Center for Atmospheric Research, Boulder, Colorado, USA.
[3]Cooperative Institute for Research in Environmental Sciences, University of Colorado Boulder, Colorado, USA.
[4]Space Weather Prediction Center, National Oceanic and Atmospheric Administration, Boulder, Colorado, USA.
[5]National Space Organization, Hsinchu, Taiwan.
[6]Department of Earth Science, National Cheng Kung University, Tainan, Taiwan.
[7]Institute for Mathematics Applied to Geosciences, National Center for Atmospheric Research, Boulder, Colorado, USA.

Corresponding author: J. Y. Liu, Institute of Space Science, National Central University, Chung-Li 32054, Taiwan. (jyliu@jupiter.ss.ncu.edu.tw)

0148-0227/12/2012JA017700

[3] A powerful technique to reproduce the ionospheric weather is data assimilation that combines physics-based simulations of the ionosphere with observations. Many data assimilation models of the ionosphere have been developed in the past decade, based on either empirical or physics-based models and different types of ionospheric measurements [*Howe et al.*, 1998; *Pi et al.*, 2003; *Bust et al.*, 2004; *Hajj et al.*, 2004; *Scherliess et al.*, 2004, 2006; *Schunk et al.*, 2004; *Mandrake et al.*, 2005; *Fuller-Rowell et al.*, 2006; *Komjathy et al.*, 2010; *Matsuo and Araujo-Pradere*, 2011]. They mainly assimilated ground-based observations with limited global coverage, and were thus not able to represent the global electron density distribution with high accuracy. As the global navigation satellite system evolves, total electron content (TEC) and radio occultation observations become increasingly available over the entire globe.

[4] This paper presents preliminary results from the first use of ensemble Kalman filtering (EnKF) to assimilate FORMOSAT-3/COSMIC (F3/C) electron density profiles (EDPs) into the National Center for Atmospheric Research (NCAR) Thermosphere-Ionosphere-Electrodynamics General Circulation Model (TIE-GCM). The F3/C provides three-dimensional (3D) ionospheric electron densities over the entire globe to cover areas without sufficient other observations, such as in the oceans, deserts, and polar regions. Unlike an ordinary Kalman filter, the EnKF allows for the use of a fully nonlinear forecast model without any modification. Furthermore, the forecast model error covariance is represented by the sample covariance calculated from an ensemble of model forecasts, and therefore the space- and time-dependent description of the forecast model error covariance is attained with a moderate computational cost. In addition, in this assimilation system, both the state of the thermosphere and ionosphere can be estimated by using the EnKF. The main objective of this paper is to demonstrate that an improvement in global ionospheric electron density specification is achieved by assimilating the F3/C observations into the TIE-GCM. The results of the assimilation are validated with independent ionosonde measurements.

2. Assimilation System

[5] The EnKF assimilation system is constructed with the NCAR TIE-GCM and the Data Assimilation Research Testbed (DART) [*Anderson et al.*, 2009]. Detailed descriptions of this EnKF system can be found in T. Matsuo et al. (Thermospheric mass density specification using an ensemble Kalman filter, submitted to *Journal of Geophysical Research*, 2012).

[6] The NCAR TIE-GCM is a 3D, time-dependent, physics-based model of the earth's coupled thermosphere and ionosphere. The TIE-GCM uses a finite differencing technique to obtain a self-consistent solution for the thermospheric and ionospheric dynamics, the associated dynamo electric field and currents, and the electrodynamic feedback on neutral and plasma motions and thermodynamics [*Roble et al.*, 1988; *Richmond et al.*, 1992]. The TIE-GCM calculates the global distribution of neutral wind circulation, temperature, electrodynamics, and compositional structure of the upper atmosphere and ionosphere. The standard horizontal grid resolution of the model is $5^\circ \times 5^\circ$ in longitude and latitude. There are 29 pressure surfaces at half-scale-height intervals extending from 97 km to about 700 km (depending on the solar activity). At the upper boundary, the vertical O^+ flux and electron heat flux are specified, which approximates the plasma mass and heat exchange between the plasmasphere and the ionosphere.

[7] The EnKF is proposed as a Monte-Carlo approximation of a Kalman filter [*Evensen*, 1994]. It allows the use of a fully nonlinear dynamical model such as the TIEGCM as a forecast model, and uses the sample statistics from an ensemble of model forecasts to compute the impact of observations on the state variables [e.g., *Evensen*, 2009]. The ensemble of model simulations essentially emulates the evolution of the probability distribution. The posterior refers to the posterior probability distribution obtained after assimilation of observations, and the prior means that probability distribution prior to assimilation. Because the EnKF is a recursive filter (i.e., a type of filter which re-uses its output as an input), the state of each posterior ensemble member is integrated forward by the TIEGCM over the course of one assimilation cycle to yield the prior ensemble for the next assimilation time. Specifically, the mean of the posterior ensemble serves as an assimilation analysis, and is equivalent to the assimilation analysis obtained according to the conventional Kalman filter analysis equation [*Daley*, 1991; *Evensen*, 2009]. Because the sample covariance is computed from a smaller ensemble than what is required for the size of covariance associated with models like the TIEGCM, it is important to control spurious correlations by limiting the correlation length with a localization function. This procedure is called covariance localization [*Houtekamer and Mitchell*, 2006], and is usually applied during the regression step used to transform and localize the innovations back into the state-space.

[8] The DART is an open-source community software for ensemble data assimilation developed and maintained by the Data Assimilation Research Section at NCAR [*Anderson et al.*, 2009]. By using DART's carefully engineered ensemble data assimilation algorithms and diagnostic tools, state-of-the-art data assimilation systems can be implemented for different geophysical models with great ease. The DART includes a variety of algorithms for computing the updated observation ensemble including the perturbed observation ensemble Kalman filter [*Burgers et al.*, 1998] and the ensemble adjustment Kalman filter [*Anderson*, 2001].

[9] *Matsuo and Araujo-Pradere* [2011] presented successful observing system simulation experiments for ionosonde observations using the same assimilation system used in this study. They concluded that by self-consistently treating the coupling of the ionosphere and thermosphere both in the forecast and update steps of Kalman filtering, the thermospheric states can indeed be estimated from ionospheric observations, in turn improving the overall ionospheric specification. Hence, the electron density, the main dynamical variables of the thermosphere (neutral temperature and winds), and the major-constituent compositions (atomic and molecular oxygen mass mixing ratios) are included as part of the EnKF state vector in this study. (Note the sum of mixing ratios of major species (O, O_2, and N_2) is set to 1 in the TIE-GCM.) To ensure that assimilation analyses of these variables always remain within physically meaning ranges, the minimum electron density is set equal to $10^3/\mathrm{cm}^3$, and the O and O_2 mixing ratios are bound

between zero and one. When assimilation updates end up outside these bounds, the maximum and/or minimum values are used instead of the updated values for assimilation analyses.

[10] The F3/C mission consists of six micro-satellites that were launched on 15 April 2006 and reached their mission orbit of 800 km around December 2007. The main payload on board the F3/C satellites is the GPS Occultation Experiment, which provides global observations of the ionosphere to reconstruct the 3D electron density structure up to 800 km altitude. This data set makes it possible to study global ionospheric features at various altitudes in both hemispheres. The measurements have been used for operational numerical weather prediction, climate/reanalysis studies and ionospheric physics. The F3/C EDP is retrieved from GPS radio-occultation (RO) data along the GPS-LEO (low earth orbit) radio links near the raypath tangent points. Recent studies show that ionospheric electron densities derived from the RO sounding around and above the F_2 peak are reasonably accurate, whereas those below the F region should be used with great caution because of the assumption of spherical symmetry used in the Abel inversion [*Lei et al.*, 2007; *Kelley et al.*, 2009; *Liu et al.*, 2010; *Yue et al.*, 2010]. Therefore, the F3/C EDP observation error applied in this study is assumed to be the sum of a 10% instrumentation error and the estimated Abel inversion error percentage [*Liu et al.*, 2010; *Yue et al.*, 2010].

[11] An observational forward operator which maps the model state variables to the observed parameters is needed. The TIE-GCM simulates the 3D electron density at grid location in pressure coordinates, and the F3/C EDP provides electron density profiles at irregular longitude and latitude locations. To simplify the forward operator computation and avoid the complication of missing model values above its upper boundary, the F3/C EDP is chosen for this new assimilation system development, instead of the line-of-sight integrated electron densities. The assimilation window is 1 h, which means that the F3/C EDPs occurring within 30 min of the assimilation time are assimilated. On average, there are approximately 85 profiles collected globally every hour, and used in each assimilation step. The F3/C EDP is retrieved from F3/C radio occultation and published by the COSMIC Data Analysis and Archive Center (CDAAC) at the University Corporation for Atmospheric Research (UCAR). In this study, all EDPs are sampled between 160 and 450 km with a 10 km resolution and have quality control criteria applied to avoid assimilating obviously bad data, such as negative densities.

3. Ensemble Members Generating Strategy

[12] The thermosphere-ionosphere system is strongly controlled by external forcing, and therefore ensemble members are generated by perturbing the input forcing parameters of the TIE-GCM. In the filtering experiments presented in this paper, 90 ensemble members are generated via centered Gaussian distributions of three primary model input parameters: the solar 10.7 cm radio flux (F10.7, used as a proxy for solar EUV radiation) and auroral hemispheric power and cross-tail potential drop that control high-latitude energy and momentum input to the model. The hemispheric power and cross-tail potential are assumed to be correlated with each other, but correlation of F10.7 with the hemispheric power and cross-tail potential is not considered. The mean values of the Gaussian distributions come from corresponding observations of the F10.7 and the three-hour planetary K index (Kp) published on the NOAA National Geophysical Data Center webpage, where Kp is used to estimate the hemispheric power and cross-tail potential [*Boyle et al.*, 1997; *Zhang and Paxton*, 2008]. The widths of the distributions are specified by a 14-day standard deviation of F10.7 and ± 0.5 unit of Kp. The values are 5×10^{-22} W/m^{2}Hz for F10.7, 2 GW for the hemispheric power, and 10 kV for the cross-tail potential.

[13] Our early numerical tests, however, showed that the ensemble members generated by perturbing these three model input parameters, although spanning a great range of electron number densities, did not yield sufficiently diverse profile shapes/altitude distributions to fully cover the observations variability. In order to increase the range of ionospheric F region peak heights (hmF2) and give sufficiently diverse profile shapes/altitude distributions, the vertical $E \times B$ plasma drift is also varied. The vertical drifts have a Gaussian-like distribution when we perturb the three forcing parameters. Nevertheless, the spread due to the parameters alone is not enough to give an adequate diversity of profile shapes. Therefore, ensemble members are divided into three groups with default, higher, and lower global vertical $E \times B$ plasma drift multiplying factors, which are 1.0, 1.5, and 0.5, respectively, to either raise or lower hmF2 and diversify the profile shapes.

[14] The forcing parameters assigned to each ensemble member are held unchanged over the assimilation time step. The spin-up time for each ensemble member is 10 h. In addition, the topside ionospheric electron density predicted by the original TIE-GCM is often higher than that from the nighttime F3/C observations, and this gross model bias resulted in a poor performance of filtering. The default nighttime vertical O^+ flux at the top boundary of the TIE-GCM is -2.0×10^8/cm^{2}s at most locations, with some latitudinal and solar zenith angle dependence. To improve the performance of filtering it has been reduced to one-fourth of this default value, and this change has led to better nighttime results.

[15] Those 90 ensemble members are used to provide the necessary information on the variability of the thermosphere and ionosphere, and to calculate the sample covariance matrix to describe the correction and variance of the model forecast error.

4. Result and Interpretation

[16] The assimilation experiment is conducted for 12–13 April 2008 under geomagnetic quiet conditions. The observed F10.7 and Kp are averaged in this two days period. The corresponding values of F10.7, hemispheric power, and cross-tail potential are 69.0×10^{-22} W/m^{2}Hz, 27.0 GW and 48.2 kV, respectively, which are used as the centered values for Gaussian distributions to generate initial ensemble members. In the EnKF framework, the probability distribution of ensemble members is assumed to be Gaussian. Therefore, the ensemble mean is used to represent the expected value of the probability distribution. The covariance localization function used in this study is given by the *Gaspari and Cohn* [1999] function with a half-width of about 10 degrees (about

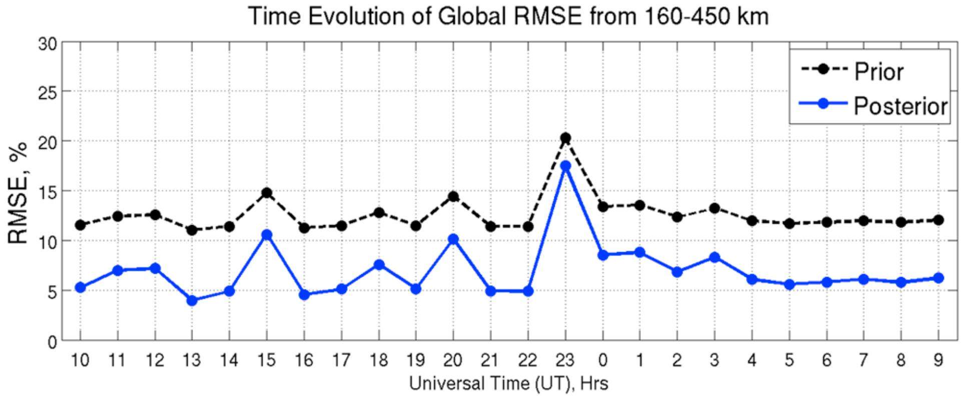

Figure 1. Global root-mean square percentage error of the prior/posterior against the F3/C observations from 160 to 450 km altitude. The black dashed and blue lines indicate the prior and posterior, respectively.

1,100 km) in the horizontal and 200 km in the vertical. The assimilation results are compared with the stand-alone TIE-GCM without any observations assimilated under the same conditions and in the same time period.

[17] To assess this newly developed assimilation system, the root-mean square errors (RMSE) at the profile locations for each assimilation cycle are estimated between 160 and 450 km. The RMSE percentage of the electron density is calculated from the difference between the model simulated and F3/C observed electron density values, divided by the F3/C value. Figure 1 shows the globally averaged electron density RMSE percentage variation with the universal time (UT) from 10:00 UT on 12 April to 09:00 UT on 13 April 2008. The RMSE percentage became large around 15:00, 20:00, and 23:00 UT, but it generally decreased after the assimilation of F3/C EDPs. The overall decrease was about 5%. This assessment demonstrates that the EnKF assimilation system can adjust the electron density from the TIE-GCM toward the F3/C observations.

[18] Figure 2 displays control (ensemble mean value without assimilation) and posterior (ensemble mean value after assimilation) F region peak densities (NmF2) from 10:00 UT on 12 April to 09:00 UT on 13 April. The irregular structures associated with the F3/C EDP locations are the results of adjustment, especially pronounced in the equatorial ionization anomaly (EIA) region and the midlatitude region in the Southern Hemisphere in the 11:00, 12:00, 14:00, 19:00, and 08:00 UT maps. Slight enhancements of the NmF2 appear during the evening period over the geomagnetic equator in the 19:00, 20:00, 22:00, 03:00, 04:00, 06:00, 08:00, and 09:00 UT maps.

[19] Figure 3 illustrates the control and posterior electron densities in latitude and height along the −75°E longitude from 05:00 LT on 12 April to 04:00 LT on 13 April. At most times, the electron density distribution shows adjustments in altitude and magnitude near the F3/C EDP locations. This demonstrates that assimilating F3/C EDP into the TIE-GCM alters not only the peak density but also the peak height of the F region, related to the altitudinal information provided by the F3/C EDP. In addition, the EIA features become more prominent in the Northern Hemisphere except for the 11:00, 15:00 and 19:00 LT slices. Moreover, the two EIA crest shifts closer to the geomagnetic equator from the 11:00 LT slice, and acquires a sharper poleward edge in the Southern Hemisphere for the 14:00 and 15:00 slices. The electron density is enhanced above 250 km over the geomagnetic equator for the 22:00, 23:00 and 01:00 LT slices, as also seen in Figure 2 for the 03:00, 04:00 and 06:00 UT maps at certain longitudes.

5. Validation

[20] To further validate the assimilation results with independent observations, we use ionospheric NmF2 and hmF2 obtained from ionosondes located at the Jicamarca (JIC, −12.0°N, −76.8°E) in Peru, at the Donghwa station (TWN, 22.4°N, 120.5°E) in Taiwan, and at the Gakona station (GAK, 62.4°N, −145.0°E) in Alaska, corresponding to the magnetic equatorial region, EIA region, and high-latitude region, respectively. Figure 4 illustrates hmF2 and NmF2 comparisons for the control and posterior results at JIC from 04/12 06:00 LT to 04/13 18:00 LT. A radio occultation event does not regularly occur within the one hour assimilation cycle and within the localization window at any given location, so there are only 26 out of 37 h when an F3/C EDP is nearby the validation station and affects the posterior electron density. The RMSE percentage is calculated from the difference between the model hmF2 and NmF2 and ionosonde observations, divided by ionosonde observations for that assimilation cycle. This parameter is used to determine whether assimilation led to improvement in electron density specification. The average RMSE percentage of the control and posterior are 16.4% and 12.9% for hmF2, and 29.7% and 26.2% for NmF2 during this period. It shows that about 43% (16/37) of the time the posterior model state agrees better with observations for both hmF2 and NmF2 at JIC. Only about 11% of the time (4/37), neither hmF2 nor NmF2 is improved for this particular period. Nevertheless, when we consider only times when an F3/C EDP is nearby the validation station, assimilation of F3/C EDP leads to a better agreement of hmF2 and NmF2 with observations for about 81% (21/26) and 54% (14/26) of the assimilation cycles, respectively.

[21] Figure 5 shows another comparison as in Figure 4 at TWN from 04/12 18:00 to 04/13 23:00 LT. There are only 18 out of 30 h when an F3/C radio occultation event occurs nearby the station. The average RMSE percentage for the control and posterior are 13% and 14% for hmF2, and 43%

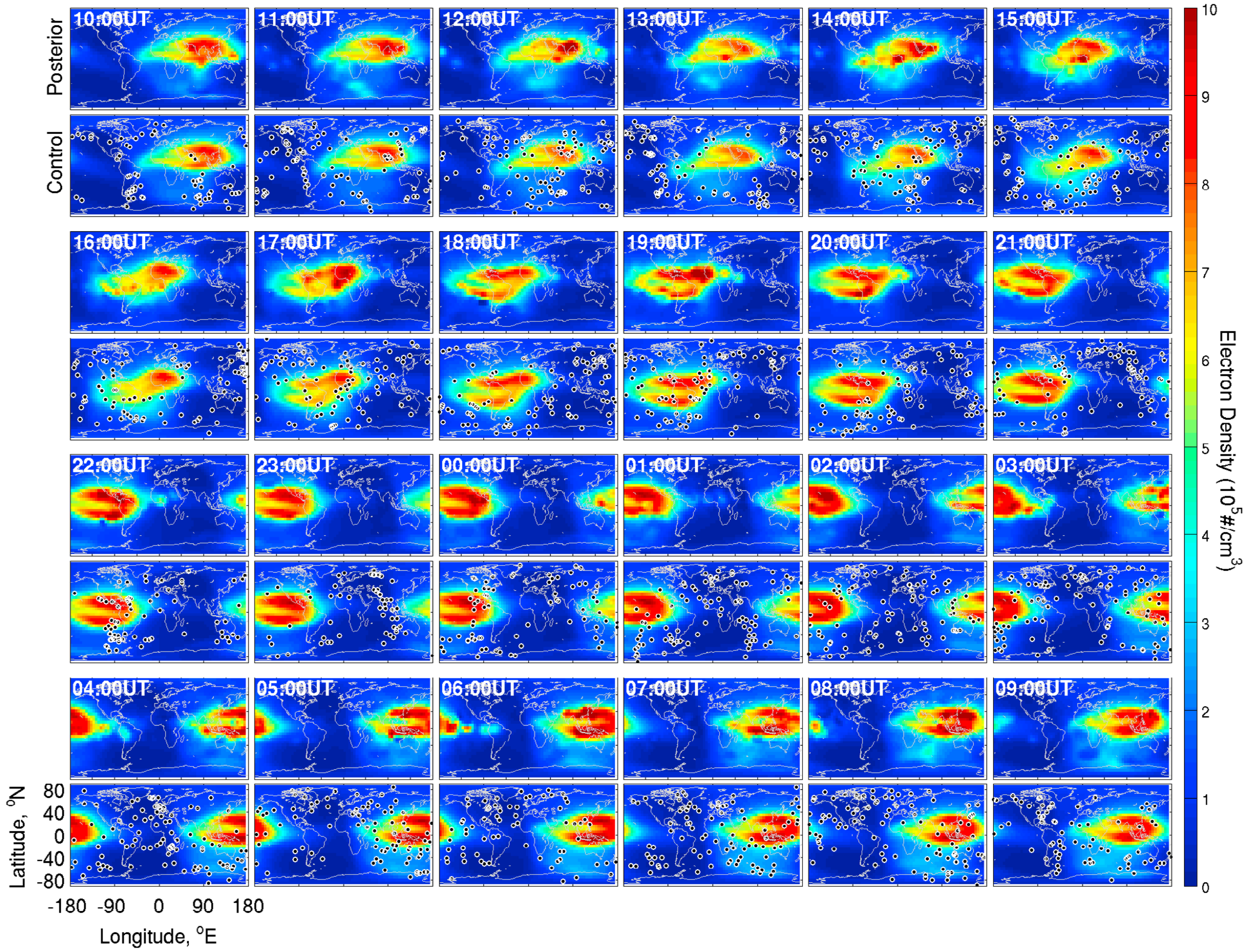

Figure 2. Global NmF2 maps from 2008/04/12 06:00 UT to 2008/04/13 04:00 UT before and after assimilating the FORMOSAT-3/COSMIC electron density profiles. The upper and lower row of each panel displays the posterior and control, respectively. The black dots indicate the observation locations.

and 37% for NmF2. The results at TWN are consistent with the JIC results, and only about 10% of the time (3/30), neither hmF2 nor NmF2 is improved for this particular period. Moreover, the assimilation of F3/C EDPs yields better agreement of hmF2 and NmF2 with observations for about 55% (10/18) and 72% (13/18) of the assimilation cycles, respectively.

[22] Figure 6 shows the high-latitude comparison at GAK from 04/12 05:00 to 04/13 13:00 LT. There are only 18 out of 33 h when an F3/C radio occultation event occurs nearby the station. The results at GAK are qualitatively consistent with previous results, and only 10% of the time (2/20), neither hmF2 nor NmF2 is improved for this particular period. Assimilation of F3/C EDPs yields better agreement of hmF2 and NmF2 with observations for about 82% (9/11) and 72% (8/11) of the assimilation cycles, respectively. However, the improvements are relatively small. The average percentage RMSE for the control and posterior are both about 18% for hmF2 and NmF2, with only a slightly smaller reduction in percentage RMSE for the posterior. The validation results suggest that assimilating the F3/C EDPs can improve the agreement between the modeled electron densities and observations not only at the magnetic equator and EIA region, but also at high latitudes.

[23] In general, the validation results show that the overall improvement of hmF2 (67% = 58/89) and NmF2 (62% = 54/89) is attained at most of the assimilation cycles with a low percentage of degradation (10% = 9/87). Once again, this confirms that our assimilation experiments with F3/C EDP are working reliably. Note that the improvement of hmF2 (72% = 40/55) is more obvious than that of NmF2 (63% = 35/55) by assimilating F3/C EDPs.

6. Discussion

[24] Assimilation of F3/C EDP into the TIE-GCM improves the accuracy of modeled global electron density and decreases the RMSE especially at, but not limited to, the profile locations. After assimilating F3/C EDPs into the NCAR TIE-GCM, the global NmF2 maps reveal hemispheric asymmetry of the EIA crests, higher electron densities at midlatitude, and density enhancement over the magnetic equator. The TIE-GCM simulations predict that the two EIA crests have roughly the same peak densities around the March

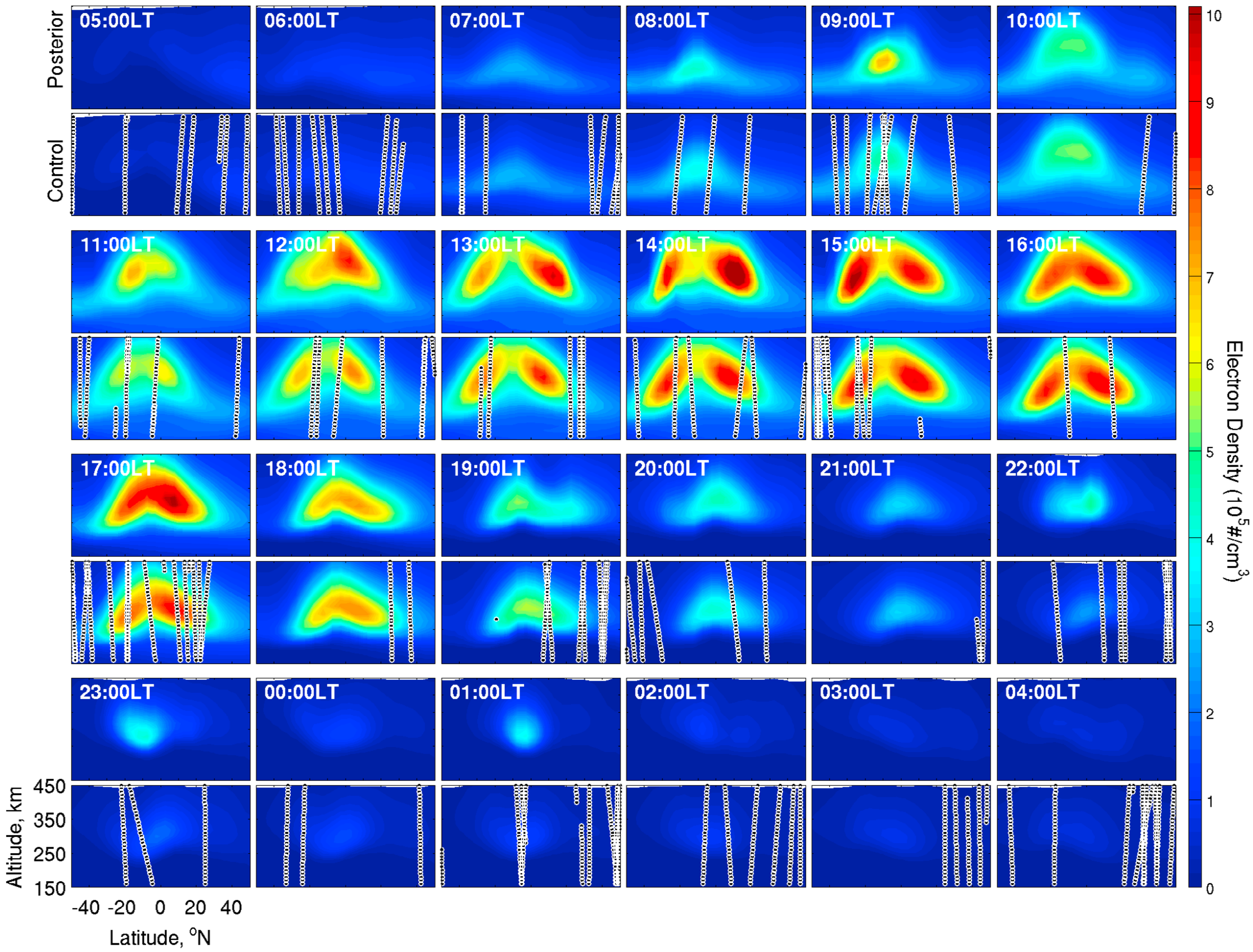

Figure 3. Latitude/height slices along −75°E from 2008/04/12 05:00 UT (10:00 LT) to 2008/04/13 04:00 UT (23:00 LT) before and after assimilating the FORMOSAT-3/COSMIC electron density profiles. The upper and lower row of each panel displays the posterior and control, respectively. The black dots indicate the observation profiles located between −60 and −90°E longitude within 30 min of a given assimilation time.

equinox. However, the electron density in the Northern Hemisphere becomes higher than in the Southern Hemisphere when the F3/C observations are assimilated. The validation result for TWN also shows an increase of NmF2 over the TIE-GCM control run, improving the agreement with the ionosonde observations. At solstice, asymmetry of the EIA may result from a trans-equatorial neutral wind blowing from the summer hemisphere to the winter hemisphere. This causes upward motion of the plasma in the summer hemisphere and downward motion in the winter hemisphere [*Lei et al.*, 2007]. Hemispheric asymmetry of neutral composition can also contribute to EIA asymmetry. The assimilation results suggest that either the thermospheric circulation or the composition in the TIE-GCM, or both, need to be modified to be able to represent the EIA asymmetry shown by the F3/C assimilation at equinox. The density enhancement over the magnetic equator is also seen in the Jicamarca ionosonde measurements (shown in Figure 4), which further validates the assimilation system. The higher electron density at midlatitude and the density enhancement over the magnetic equator after the assimilation of F3/C EDPs also suggest that additional adjustments to TIE-GCM might be needed.

[25] Figure 3 shows how the assimilation of F3/C EDPs shifts the two EIA crests closer to the geomagnetic equator for the 11:00 LT and also reverses the hemispheric asymmetry of the EIA. The closer EIA crests suggest that the magnitude of the E × B fountain effect predicted by the model could be too strong. On the other hand, some features, such as the reversal of the hemispheric asymmetry of the EIA and the disappearance of the density enhancement over just one assimilation cycle, are likely to be artifacts due to the fact that E3/C EDP comes and goes for a given location. This is because an assimilation adjustment is sustained only over a short period and fairly rapidly relaxes toward climatology with a time scale on the order of one hour, due to the natural relaxation time of the ionosphere due to ion diffusion and loss. *Jee et al.* [2007] replaced electron and O^+ densities as initial conditions of the Thermosphere Ionosphere Nested Grid model [*Wang et al.*, 1999] and ran with the same forcing parameters, showing that the *e*-folding decay time of the initialization lasts only about 1∼4 h around the F_2 peak

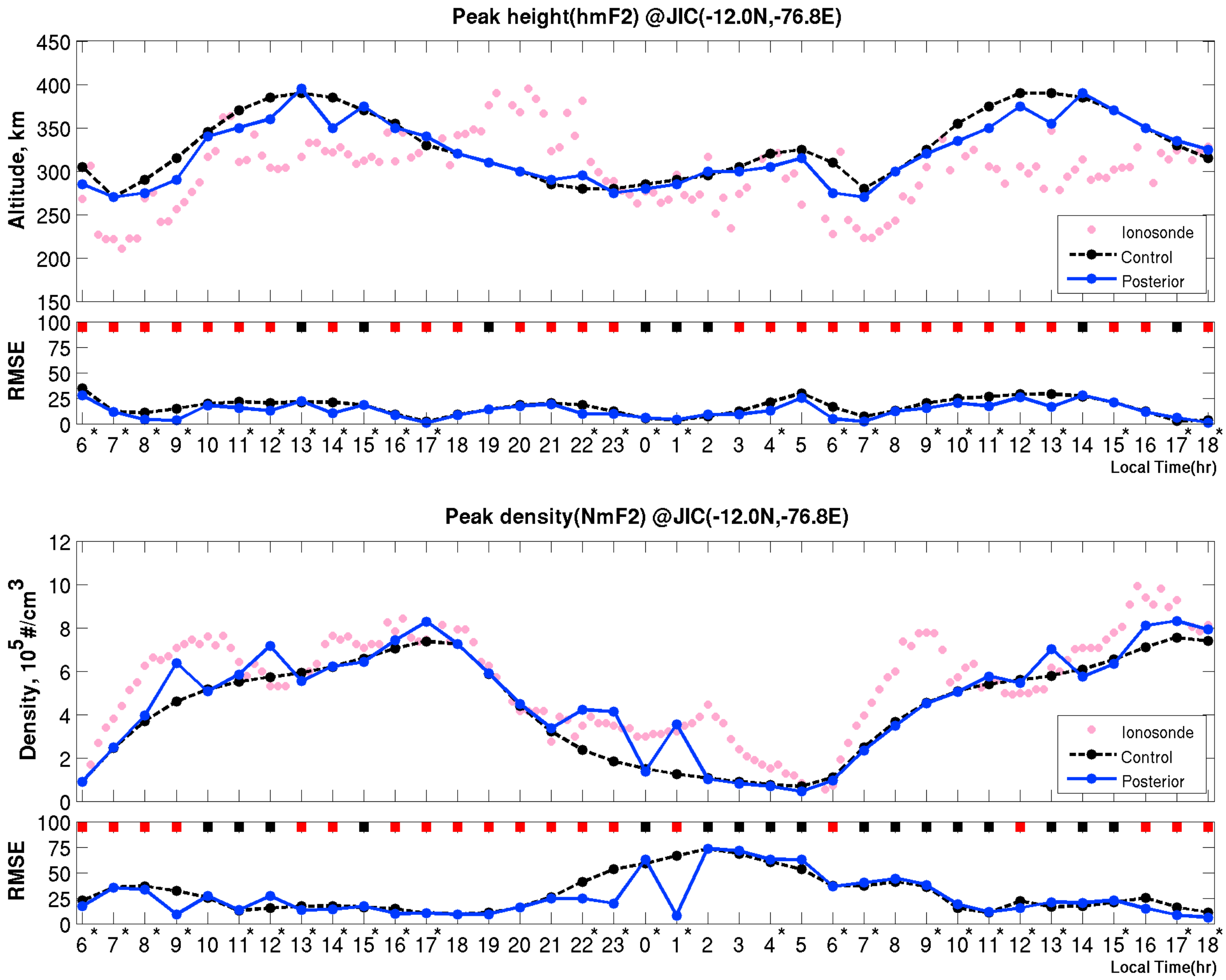

Figure 4. Comparison of assimilation analysis results over the Jicamarca station in Peru to ionosonde observations. The pink dots indicate the raw ionosonde measurements. The dashed black and solid blue lines are the control and posterior, respectively. The red/black colored boxes stand for improvement/failure as determined by the RMSE percentages. On the time scale, an hour with an asterisk is used to represent that F3/C observations were sufficiently close in space and time to station to directly affect the posterior value at the assimilating cycle.

and less than 1 h below the F_2 peak. In our experiments, the posterior electron density also approximately relaxes back toward the climatology of the TIEGCM over the course of one assimilation cycle (one hour) and remains unchanged when no observations are available.

[26] Furthermore, we expect ionospheric drivers such as thermospheric winds and low-latitude E $\times$ B drift to affect this relaxation time scale. Some studies have shown that these drivers can be inferred from electron density observations and made consistent with the electron density distribution. For example, recent studies have developed algorithms to estimate the neutral wind based on the relationship between the neutral wind and the electron density distribution [*Luan and Solomon*, 2008; *Datta-Barua et al.*, 2009]. Moreover, *Pi et al.* [2003] and *Scherliess et al.* [2009] demonstrated that by using an assimilation model to estimate the low-latitude E $\times$ B drift or neutral wind one can improve electron density specification. In our experiments, the thermospheric winds and compositions are adjusted by assimilation of electron density profiles, but this did not result in a significant extension of the relaxation time scale. It is partly due to the fact the spin-up time of ensemble members in our experiments is only 10 h and the coupled thermosphere-ionosphere system has not yet reached a steady state completely, as suggested by follow-up experiments with a longer spin-up time. In future studies, the relationship of relaxation time scale to the forcing estimation and the spin-up time needs to be addressed further.

[27] The validation of the assimilation results with ionosonde observations indicates that the RMSE percentage of NmF2 is reduced more significantly than that of hmF2. This is partly due to the inadequate vertical resolution of the TIE-GCM in comparison with the F3/C EDP. The vertical coordinate in the TIE-GCM is $\ln(p_0/p)$, where p is pressure and p_0 is a reference pressure. The model vertical resolution (half scale height) with respect to geometric height is smaller at lower altitudes (2.5–10.0 km, below 150 km) and larger at higher altitudes (10.0–25.0 km, above 150 km). Although

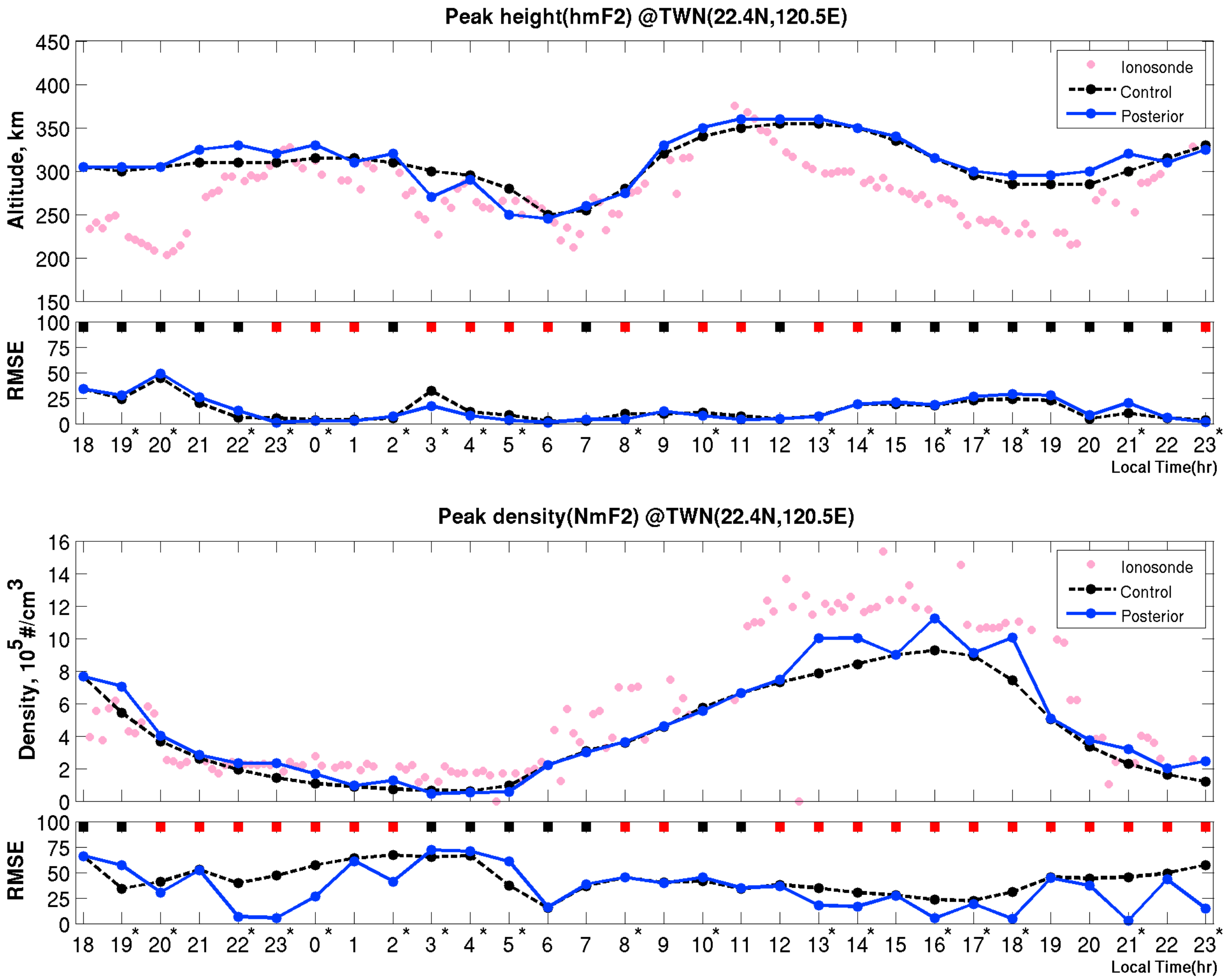

Figure 5. Similar to the Figure 4. Comparison of assimilation analysis results over the Donghwa station in Taiwan to ionosonde observations.

the posterior ensemble has been adjusted by assimilating the F3/C EDP with 10 km resolution, the adjustment of hmF2 is not accurately resolved after converting the height back to the model pressure level.

[28] It is important to mention that about 35% of the F3/C observations are rejected by the quality control (QC) and outlier threshold (OT) criteria we successively impose during the assimilation process. For an individual EDP, only those data at particular heights that do not meet the acceptance criteria are rejected, while the remainder of the data for that EDP is retained. An example shown in Figure 7 illustrates the rejection criteria for a poorly assimilated EDP. Below 200 km altitude, the F3/C EDP goes negative, which is unphysical and fails to pass the quality control. Only positive observations are used for assimilation, and so the negative observations are rejected. In addition, the consistency between the prior state and an observation can be assessed using the prior ensemble standard deviation and the observation error, in order to identify outliers. In this study, the outlier threshold is set to four times the standard deviation of the prior ensemble members plus four times the observation error. For example, in Figure 7 four ensemble standard deviations (one-sided length of the black bar) does

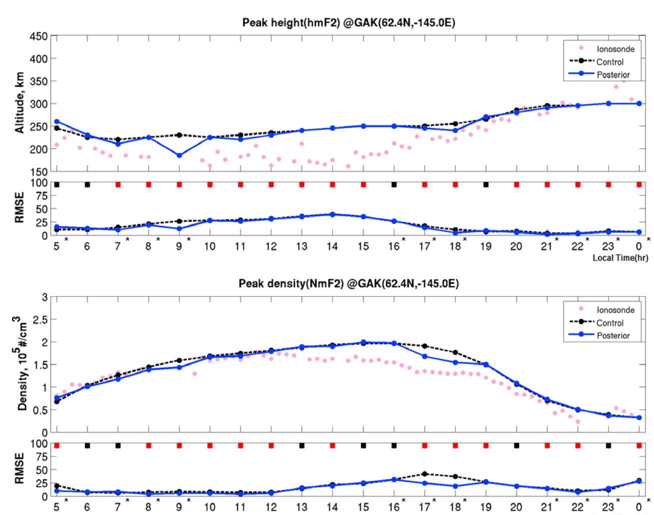

Figure 6. Similar to the Figure 4. Comparison of assimilation analysis results over the Gakona station in Alaska to ionosonde observations.

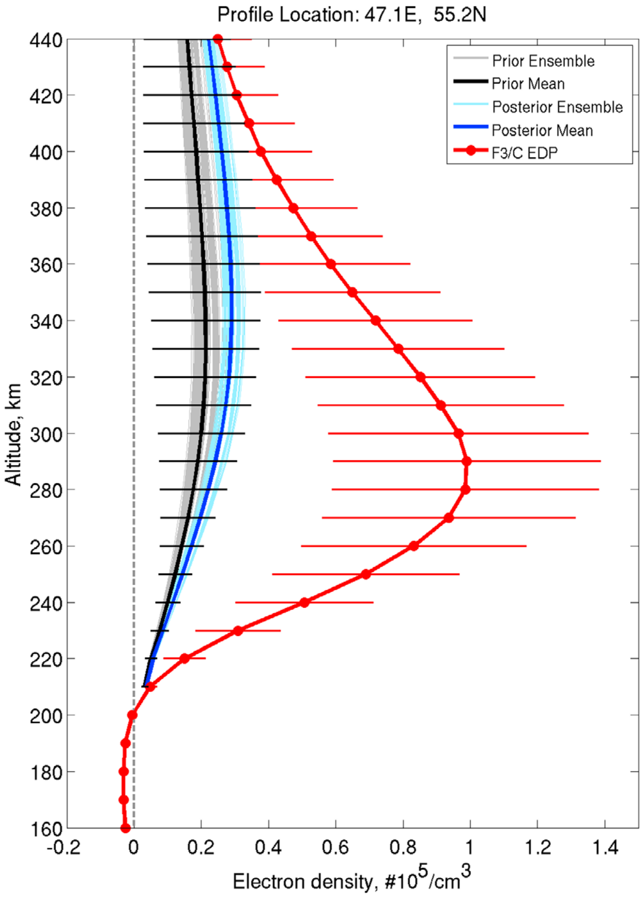

Figure 7. Example of conditions giving rise to rejected observations due to surpassing the outlier threshold (210–350 km) or failing quality control due to negative densities (160–200 km). The horizontal black and red lines are used to indicate ±4 times the standard deviation of prior ensemble members and ±4 times the observation error, respectively.

not overlap four times the observation error (one-sided length of the red bar) between 210 and 350 km, indicating a large model-observation inconsistency. Therefore, the observations at these particular altitudes are rejected due to this outlier threshold criterion. For this profile, only values at 360 km and above are retained for assimilation. Thus, the result is a posterior distribution closer to the prior than to the observations.

[29] Figure 8 demonstrates the percentage of rejection due to either outlier threshold or quality control, and total rejection is shown as a function of local time and altitude. The average rejection rate is about 35%, mainly due to the outlier threshold. The rejection rate due to the quality control is less than 7%. It increases sharply around midnight (00:00–01:00 LT), which is mostly caused by the negative value problem of the F3/C EDP at lower altitudes. This implies that the F3/C EDP is almost useless at lower altitudes, and suggests that improvement might be achieved by assimilating the F3/C line-of-sight integrated electron content (radio occultation total electron content or ROTEC) instead of Abel-inverted vertical profiles. However, the TIE-GCM provides no electron density values above its upper boundary, where parts of the raypaths between the F3/C and GPS satellites lie. It is therefore not possible to carry out a complete forward modeling of the ROTEC from the TIE-GCM output alone. Hence, improved retrieval methods are desired to increase the utility of profiles in the data assimilation system in the future. The rejection rate due to the outlier threshold reveals a clear day/night contrast, and it is generally higher during the nighttime period than in the daytime period. Worth noting here is that the observations are rejected mostly at lower altitudes during the daytime period but at higher altitudes during the nighttime period. This suggests that there exists a large inconsistency between the TIE-GCM and the F3/C observations at these particular altitudes and local times, for reasons that are not fully understood. The OT rejection is found to be an important part of the data assimilation process, as it improves the agreement of the posterior EDPs with the independent ionosonde data.

[30] In the EnKF algorithm, if ensemble members have insufficient spread to cover the range of observations, the model will be given more weight than it should be given, which results in an inappropriate posterior state estimation. In this study, the ensemble members are generated simply by perturbing the F10.7, the hemispheric power, the cross-tail potential, and the vertical drift velocity. The solar EUV radiation (parameterized by F10.7) affects the daytime ionization rate and thus strongly affects the electron densities in the ionosphere. The hemisphere power and the cross-tail potential are used to control auroral precipitation and the convection electric field at higher latitudes, which affect the global thermosphere neutral wind and composition and electrodynamics and, consequently, the global ionospheric electron density. The vertical drift velocity influences the plasma motion and changes the peak height of the *F* region. Nevertheless, these ensemble members are still not adequate to cover the full range of ionospheric conditions observed by the F/3C. More work is needed to select other physical parameters in the model to perturb and to test them to reduce systematic model-observation inconsistencies and thereby the rejection rate of observations.

7. Conclusion

[31] In this paper, for the first time F3/C electron density profiles are successfully assimilated into the NCAR TIE-GCM by using a recently developed ensemble Kalman filter data assimilation system. The assimilation experiments have been conducted under geomagnetic quiet conditions. The reduced RMSE percentage shows that assimilating the F3/C EDPs brings the NCAR TIE-GCM electron densities closer to both the assimilated and independent observations.

[32] The validation of the assimilation results has been carried out by comparing with independent measurements of NmF2 and hmF2 by the JIC, TWN, and GAK ionosondes in the magnetic equatorial, EIA, and high-latitude regions. This comparison demonstrates that the posterior NmF2 and hmF2 obtained by assimilating the F3/C EDP into the TIE-GCM agree better with observations than those from the default TIE-GCM simulations. The ionosonde observations confirm interesting features such as the hemispheric asymmetry of the EIA, and the equatorial density enhancement, which appear to be real ionospheric signatures.

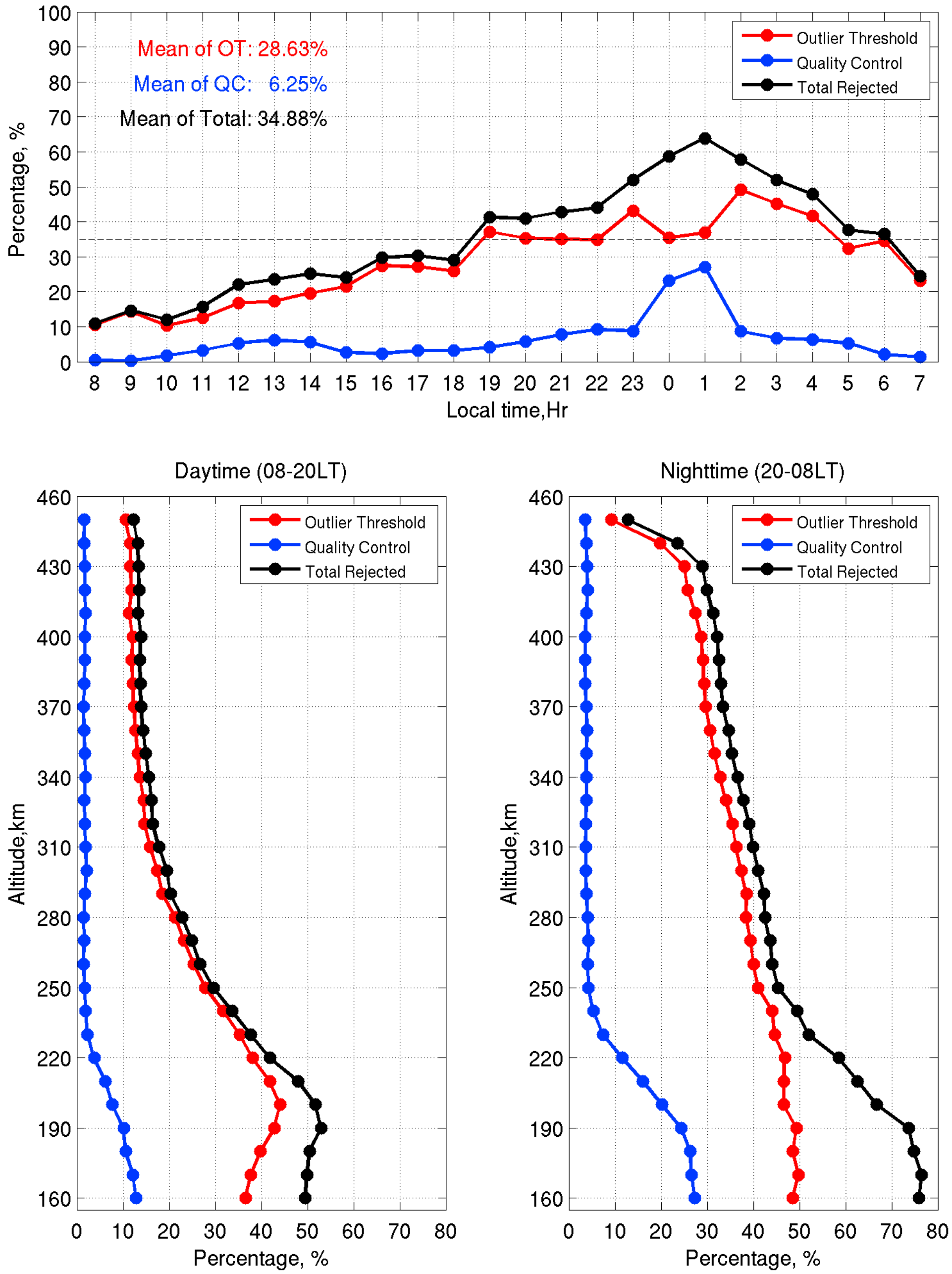

Figure 8. Percentages of rejected observations resulting from the outlier threshold (OT) and quality control (QC) criteria applied to the observations.

[33] To reduce the high rejection rate of observations during nighttime and at lower altitudes that results from the outlier threshold criterion, better ensemble member generation and model bias correction strategies are needed to fully cover the observations, and to improve the consistency between the TIE-GCM simulations and the F3/C observations. In addition to perturbing the solar F10.7 index, the hemispheric power, and the cross-tail potential, other forcing parameters such as tides, O^+ flux at the top boundary of the model and plasma drift velocity should be considered in future work.

[34] Furthermore, the use of the EnKF in this study only estimated the thermosphere and ionosphere states, such as the electron density, the neutral temperature and winds, and the atomic and molecular oxygen mixing ratios by assimilating the F3/C observations. We did not attempt to estimate any forcing parameters such as the solar F10.7 index, the hemispheric power, the cross-tail potential, and the plasma drift. The forcing parameters assigned to each ensemble member are held unchanged over the entire duration of assimilation experiment. However, it would be desirable to estimate them, for instance, by including them as part of the EnKF state vector (Matsuo et al., submitted manuscript, 2012), since the thermosphere-ionosphere system is strongly controlled by external drivers.

[35] **Acknowledgments.** ITL is supported by a Newkirk Fellowship from the High Altitude Observatory of the National Center for Atmospheric Research. The National Center for Atmospheric Research is sponsored by the National Science Foundation. TM is supported by the Air Force Office of Scientific Research Multidisciplinary University Research Initiative award FA9550-07-1-0565. This work is supported in part by National Sciences Council (NSC) grants, NSC 98-2111-M-008-008-MY3 and National Space Organization grants, NSPO-S-101014. This work is also supported in part by the Center for Integrated Space Weather Modeling (CISM), which is funded by the STC Program of the National Science Foundation under Agreement ATM-0120950, and NASA grants NNX10AQ59G and NNX09AN57G. The authors wish to thank the reviewers for their useful comments.

[36] Robert Lysak thanks two anonymous reviewers for their assistance in evaluating this manuscript.

References

Anderson, J. L. (2001), An ensemble adjustment Kalman filter for data assimilation, *Mon. Weather Rev.*, *129*, 2884–2903, doi:10.1175/1520-0493(2001)129<2884:AEAKFF>2.0.CO;2.

Anderson, J. L., T. Hoar, K. Raeder, H. Liu, N. Collins, R. Torn, and A. F. Arellano (2009), The Data Assimilation Research Testbed: A community data assimilation facility, *Bull. Am. Meteorol. Soc.*, *90*, 1283–1296, doi:10.1175/2009BAMS2618.1.

Boyle, C. B., P. H. Reiff, and M. R. Hairston (1997), Empirical polar cap potentials, *J. Geophys. Res.*, *102*(A1), 111–125, doi:10.1029/96JA01742.

Burgers, G., P. J. van Leeuwen, and G. Evensen (1998), Analysis scheme in the ensemble Kalman filter, *Mon. Weather Rev.*, *126*, 1719–1724, doi:10.1175/1520-0493(1998)126<1719:ASITEK>2.0.CO;2.

Bust, G. S., T. W. Garner, and T. L. Gaussiran II (2004), Ionospheric Data Assimilation Three-Dimensional (IDA3D): A global, multisensor, electron density specification algorithm, *J. Geophys. Res.*, *109*, A11312, doi:10.1029/2003JA010234.

Daley, R. (1991), *Atmospheric Data Analysis*, Cambridge Univ. Press, New York.

Datta-Barua, S., G. S. Bust, G. Crowley, and N. Curtis (2009), Neutral wind estimation from 4-D ionospheric electron density images, *J. Geophys. Res.*, *114*, A06317, doi:10.1029/2008JA014004.

Evensen, G., (1994) Sequential data assimilation with a nonlinear quasi-geostrophic model using Monte Carlo methods to forecast error statistics, *J. Geophys. Res.*, *99*, 10,143–10,162.

Evensen, G. (2009), *Data Assimilation: The Ensemble Kalman Filter*, 330 pp., Springer, Berlin.

Fuller-Rowell, T. J., E. A. Araujo-Pradere, C. Minter, M. Codrescu, P. Spencer, D. Robertson, and A. R. Jacobson (2006), US-TEC: A new data assimilation product from the Space Environment Center characterizing the ionospheric total electron content using real-time GPS data, *Radio Sci.*, *41*, RS6003, doi:10.1029/2005RS003393.

Gaspari, G., and S. Cohn (1999), Construction of correlation functions in two and three dimensions, *Q. J. R. Meteorol. Soc.*, *125*(554), 723–757, ISSN:1477-870X.

Hajj, G. A., B. D. Wilson, C. Wang, X. Pi, and I. G. Rosen (2004), Data assimilation of ground GPS total electron content into a physics-based ionospheric model by use of the Kalman filter, *Radio Sci.*, *39*, RS1S05, doi:10.1029/2002RS002859.

Houtekamer, P. L., and H. L. Mitchell (2006), Ensemble Kalman filtering, *Q. J. R. Meteorol. Soc.*, *131*(613), 3269–3289, doi:10.1256/qj.05.135.

Howe, B. M., K. Runciman, and J. A. Secan (1998), Tomography of the ionosphere: Four-dimensional simulations, *Radio Sci.*, *33*, 109–128, doi:10.1029/97RS02615.

Jee, G., A. G. Burns, W. Wang, S. C. Solomon, R. W. Schunk, L. Scherliess, D. C. Thompson, J. J. Sojka, and L. Zhu (2007), Duration of an ionospheric data assimilation initialization of a coupled thermosphere-ionosphere model, *Space Weather*, *5*, S01004, doi:10.1029/2006SW000250.

Kelley, M. C., V. K. Wong, N. Aponte, C. Coker, A. J. Mannucci, and A. Komjathy (2009), Comparison of COSMIC occultation-based electron density profiles and TIP observations with Arecibo incoherent scatter radar data, *Radio Sci.*, *44*, RS4011, doi:10.1029/2008RS004087.

Komjathy, A., B. Wilson, X. Pi, V. Akopian, M. Dumett, B. Iijima, O. Verkhoglyadova, and A. J. Mannucci (2010), JPL/USC GAIM: On the impact of using COSMIC and ground-based GPS measurements to estimate ionospheric parameters, *J. Geophys. Res.*, *115*, A02307, doi:10.1029/2009JA014420.

Lei, J., et al. (2007), Comparison of COSMIC ionospheric measurements with ground-based observations and model predictions: Preliminary results, *J. Geophys. Res.*, *112*, A07308, doi:10.1029/2006JA012240.

Liu, J. Y., C. Y. Lin, C. H. Lin, H. F. Tsai, S. C. Solomon, Y. Y. Sun, I. T. Lee, W. S. Schreiner, and Y. H. Kuo (2010), Artificial plasma cave in the low-latitude ionosphere results from the radio occultation inversion of the FORMOSAT-3/COSMIC, *J. Geophys. Res.*, *115*, A07319, doi:10.1029/2009JA015079.

Luan, X., and S. C. Solomon (2008), Meridional winds derived from COSMIC radio occultation measurements, *J. Geophys. Res.*, *113*, A08302, doi:10.1029/2008JA013089.

Mandrake, L., B. Wilson, C. Wang, G. Hajj, A. Mannucci, and X. Pi (2005), A performance evaluation of the operational Jet Propulsion Laboratory/University of Southern California Global Assimilation Ionospheric Model (JPL/USC GAIM), *J. Geophys. Res.*, *110*, A12306, doi:10.1029/2005JA011170.

Matsuo, T., and E. A. Araujo-Pradere (2011), Role of thermosphere-ionosphere coupling in a global ionospheric specification, *Radio Sci.*, *46*, RS0D23, doi:10.1029/2010RS004576.

Pi, X., C. Wang, G. A. Hajj, G. Rosen, B. D. Wilson, and G. J. Bailey (2003), Estimation of $E \times B$ drift using a global assimilative ionospheric model: An observation system simulation experiment, *J. Geophys. Res.*, *108*(A2), 1075, doi:10.1029/2001JA009235.

Richmond, A. D., E. C. Ridley, and R. G. Roble (1992), A thermosphere/ionosphere general circulation model with coupled electrodynamics, *Geophys. Res. Lett.*, *19*, 601–604, doi:10.1029/92GL00401.

Roble, R. G., E. C. Ridley, A. D. Richmond, and R. E. Dickinson (1988), A coupled thermosphere/ionosphere general circulation model, *Geophys. Res. Lett.*, *15*, 1325–1328, doi:10.1029/GL015i012p01325.

Scherliess, L., R. W. Schunk, J. J. Sojka, and D. C. Thompson (2004), Development of a physics-based reduced state Kalman filter for the ionosphere, *Radio Sci.*, *39*, RS1S04, doi:10.1029/2002RS002797.

Scherliess, L., R. W. Schunk, J. J. Sojka, D. C. Thompson, and L. Zhu (2006), Utah State University global assimilation of ionospheric measurements Gauss-Markov Kalman filter model of the ionosphere: Model description and validation, *J. Geophys. Res.*, *111*, A11315, doi:10.1029/2006JA011712.

Scherliess, L., D. C. Thompson, and R. W. Schunk (2009), Ionospheric dynamics and drivers obtained from a physics-based data assimilation model, *Radio Sci.*, *44*, RS0A32, doi:10.1029/2008RS004068.

Schunk, R. W., et al. (2004), Global assimilation of ionospheric measurements (GAIM), *Radio Sci.*, *39*, RS1S02, doi:10.1029/2002RS002794.

Wang, W., T. L. Killeen, A. G. Burns, and R. G. Roble (1999), A high resolution, three-dimensional, time dependent, nested grid model of the coupled thermosphere-ionosphere, *J. Atmos. Sol. Terr. Phys.*, *61*, 385–397, doi:10.1016/S1364-6826(98)00079-0.

Yue, X., W. S. Schreiner, J. Lei, S. V. Sokolovskiy, C. Rocken, D. C. Hunt, and Y.-H. Kuo (2010), Error analysis of Abel retrieved electron density profiles from radio occultation measurements, *Ann. Geophys.*, *28*, 217–222, doi:10.5194/angeo-28-217-2010.

Zhang, Y., and L. J. Paxton (2008), An empirical Kp-dependent global auroral model based on TIMED/GUVI FUV data, *J. Atmos. Sol. Terr. Phys.*, *70*, 1231–1242, doi:10.1016/j.jastp.2008.03.008.

Assimilation of FORMOSAT-3/COSMIC electron density profiles into a coupled thermosphere/ionosphere model using ensemble Kalman filtering

I. T. Lee,[1,2] T. Matsuo,[3,4] A. D. Richmond,[2] J. Y. Liu,[1,5] W. Wang,[2] C. H. Lin,[6] J. L. Anderson,[7] and M. Q. Chen[1]

Received 8 March 2012; revised 14 August 2012; accepted 17 September 2012; published 13 October 2012.

[1] This paper presents our effort to assimilate FORMOSAT-3/COSMIC (F3/C) GPS Occultation Experiment (GOX) observations into the National Center for Atmospheric Research (NCAR) Thermosphere Ionosphere Electrodynamics General Circulation Model (TIE-GCM) by means of ensemble Kalman filtering (EnKF). The F3/C electron density profiles (EDPs) uniformly distributed around the globe which provide an excellent opportunity to monitor the ionospheric electron density structure. The NCAR TIE-GCM simulates the Earth's thermosphere and ionosphere by using self-consistent solutions for the coupled nonlinear equations of hydrodynamics, neutral and ion chemistry, and electrodynamics. The F3/C EDP are combined with the TIE-GCM simulations by EnKF algorithms implemented in the NCAR Data Assimilation Research Testbed (DART) open-source community facility to compute the expected value of electron density, which is 'the best' estimate of the current ionospheric state. Assimilation analyses obtained with real F3/C electron density profiles are compared with independent ground-based observations as well as the F3/C profiles themselves. The comparison shows the improvement of the primary ionospheric parameters, such as NmF2 and hmF2. Nevertheless, some unrealistic signatures appearing in the results and high rejection rates of observations due to the applied outlier threshold and quality control are found in the assimilation experiments. This paper further discusses the limitations of the model and the impact of ensemble member creation approaches on the assimilation results, and proposes possible methods to avoid these problems for future work.

Citation: Lee, I. T., T. Matsuo, A. D. Richmond, J. Y. Liu, W. Wang, C. H. Lin, J. L. Anderson, and M. Q. Chen (2012), Assimilation of FORMOSAT-3/COSMIC electron density profiles into a coupled thermosphere/ionosphere model using ensemble Kalman filtering, *J. Geophys. Res.*, *117*, A10318, doi:10.1029/2012JA017700.

1. Introduction

[2] The ionospheric electron density distribution can affect human activities and systems, such as navigation and HF communication systems. To monitor the state of the ionosphere, so-called ionospheric weather, solely by observations is difficult due to lack of observations with sufficient spatial and temporal resolutions. Modeling the ionospheric weather is complex, since it varies with longitude, latitude, altitude, local time (LT), season, solar activity, and the geomagnetic condition. The ionospheric variability results from changes in internal and external drivers, such as neutral wind circulation, solar radiation, solar wind and interplanetary magnetic field interaction with the magnetosphere, and from the dynamical and nonlinear response of the thermosphere and ionosphere to these changes. Most empirical and physics-based theoretical/numerical models can simulate many climatological features of the ionosphere, but fail to reproduce the ionospheric weather due to lack of reliable estimations of the ionospheric drivers [*Scherliess et al.*, 2006]. In addition, recent studies point out that the ionospheric drivers that are crucial to the specification of the ionospheric weather involve not only solar radiation and high-latitude electric fields and particle precipitation but also the thermospheric composition, temperature, and winds [*Datta-Barua et al.*, 2009; *Scherliess et al.*, 2009].

[1]Institute of Space Science, National Central University, Chung-Li, Taiwan.
[2]High Altitude Observatory, National Center for Atmospheric Research, Boulder, Colorado, USA.
[3]Cooperative Institute for Research in Environmental Sciences, University of Colorado Boulder, Colorado, USA.
[4]Space Weather Prediction Center, National Oceanic and Atmospheric Administration, Boulder, Colorado, USA.
[5]National Space Organization, Hsinchu, Taiwan.
[6]Department of Earth Science, National Cheng Kung University, Tainan, Taiwan.
[7]Institute for Mathematics Applied to Geosciences, National Center for Atmospheric Research, Boulder, Colorado, USA.

Corresponding author: J. Y. Liu, Institute of Space Science, National Central University, Chung-Li 32054, Taiwan. (jyliu@jupiter.ss.ncu.edu.tw)

0148-0227/12/2012JA017700

[3] A powerful technique to reproduce the ionospheric weather is data assimilation that combines physics-based simulations of the ionosphere with observations. Many data assimilation models of the ionosphere have been developed in the past decade, based on either empirical or physics-based models and different types of ionospheric measurements [*Howe et al.*, 1998; *Pi et al.*, 2003; *Bust et al.*, 2004; *Hajj et al.*, 2004; *Scherliess et al.*, 2004, 2006; *Schunk et al.*, 2004; *Mandrake et al.*, 2005; *Fuller-Rowell et al.*, 2006; *Komjathy et al.*, 2010; *Matsuo and Araujo-Pradere*, 2011]. They mainly assimilated ground-based observations with limited global coverage, and were thus not able to represent the global electron density distribution with high accuracy. As the global navigation satellite system evolves, total electron content (TEC) and radio occultation observations become increasingly available over the entire globe.

[4] This paper presents preliminary results from the first use of ensemble Kalman filtering (EnKF) to assimilate FORMOSAT-3/COSMIC (F3/C) electron density profiles (EDPs) into the National Center for Atmospheric Research (NCAR) Thermosphere-Ionosphere-Electrodynamics General Circulation Model (TIE-GCM). The F3/C provides three-dimensional (3D) ionospheric electron densities over the entire globe to cover areas without sufficient other observations, such as in the oceans, deserts, and polar regions. Unlike an ordinary Kalman filter, the EnKF allows for the use of a fully nonlinear forecast model without any modification. Furthermore, the forecast model error covariance is represented by the sample covariance calculated from an ensemble of model forecasts, and therefore the space- and time-dependent description of the forecast model error covariance is attained with a moderate computational cost. In addition, in this assimilation system, both the state of the thermosphere and ionosphere can be estimated by using the EnKF. The main objective of this paper is to demonstrate that an improvement in global ionospheric electron density specification is achieved by assimilating the F3/C observations into the TIE-GCM. The results of the assimilation are validated with independent ionosonde measurements.

2. Assimilation System

[5] The EnKF assimilation system is constructed with the NCAR TIE-GCM and the Data Assimilation Research Testbed (DART) [*Anderson et al.*, 2009]. Detailed descriptions of this EnKF system can be found in T. Matsuo et al. (Thermospheric mass density specification using an ensemble Kalman filter, submitted to *Journal of Geophysical Research*, 2012).

[6] The NCAR TIE-GCM is a 3D, time-dependent, physics-based model of the earth's coupled thermosphere and ionosphere. The TIE-GCM uses a finite differencing technique to obtain a self-consistent solution for the thermospheric and ionospheric dynamics, the associated dynamo electric field and currents, and the electrodynamic feedback on neutral and plasma motions and thermodynamics [*Roble et al.*, 1988; *Richmond et al.*, 1992]. The TIE-GCM calculates the global distribution of neutral wind circulation, temperature, electrodynamics, and compositional structure of the upper atmosphere and ionosphere. The standard horizontal grid resolution of the model is $5^\circ \times 5^\circ$ in longitude and latitude. There are 29 pressure surfaces at half-scale-height intervals extending from 97 km to about 700 km (depending on the solar activity). At the upper boundary, the vertical O^+ flux and electron heat flux are specified, which approximates the plasma mass and heat exchange between the plasmasphere and the ionosphere.

[7] The EnKF is proposed as a Monte-Carlo approximation of a Kalman filter [*Evensen*, 1994]. It allows the use of a fully nonlinear dynamical model such as the TIEGCM as a forecast model, and uses the sample statistics from an ensemble of model forecasts to compute the impact of observations on the state variables [e.g., *Evensen*, 2009]. The ensemble of model simulations essentially emulates the evolution of the probability distribution. The posterior refers to the posterior probability distribution obtained after assimilation of observations, and the prior means that probability distribution prior to assimilation. Because the EnKF is a recursive filter (i.e., a type of filter which re-uses its output as an input), the state of each posterior ensemble member is integrated forward by the TIEGCM over the course of one assimilation cycle to yield the prior ensemble for the next assimilation time. Specifically, the mean of the posterior ensemble serves as an assimilation analysis, and is equivalent to the assimilation analysis obtained according to the conventional Kalman filter analysis equation [*Daley*, 1991; *Evensen*, 2009]. Because the sample covariance is computed from a smaller ensemble than what is required for the size of covariance associated with models like the TIEGCM, it is important to control spurious correlations by limiting the correlation length with a localization function. This procedure is called covariance localization [*Houtekamer and Mitchell*, 2006], and is usually applied during the regression step used to transform and localize the innovations back into the state-space.

[8] The DART is an open-source community software for ensemble data assimilation developed and maintained by the Data Assimilation Research Section at NCAR [*Anderson et al.*, 2009]. By using DART's carefully engineered ensemble data assimilation algorithms and diagnostic tools, state-of-the-art data assimilation systems can be implemented for different geophysical models with great ease. The DART includes a variety of algorithms for computing the updated observation ensemble including the perturbed observation ensemble Kalman filter [*Burgers et al.*, 1998] and the ensemble adjustment Kalman filter [*Anderson*, 2001].

[9] *Matsuo and Araujo-Pradere* [2011] presented successful observing system simulation experiments for ionosonde observations using the same assimilation system used in this study. They concluded that by self-consistently treating the coupling of the ionosphere and thermosphere both in the forecast and update steps of Kalman filtering, the thermospheric states can indeed be estimated from ionospheric observations, in turn improving the overall ionospheric specification. Hence, the electron density, the main dynamical variables of the thermosphere (neutral temperature and winds), and the major-constituent compositions (atomic and molecular oxygen mass mixing ratios) are included as part of the EnKF state vector in this study. (Note the sum of mixing ratios of major species (O, O_2, and N_2) is set to 1 in the TIE-GCM.) To ensure that assimilation analyses of these variables always remain within physically meaning ranges, the minimum electron density is set equal to $10^3/cm^3$, and the O and O_2 mixing ratios are bound

between zero and one. When assimilation updates end up outside these bounds, the maximum and/or minimum values are used instead of the updated values for assimilation analyses.

[10] The F3/C mission consists of six micro-satellites that were launched on 15 April 2006 and reached their mission orbit of 800 km around December 2007. The main payload on board the F3/C satellites is the GPS Occultation Experiment, which provides global observations of the ionosphere to reconstruct the 3D electron density structure up to 800 km altitude. This data set makes it possible to study global ionospheric features at various altitudes in both hemispheres. The measurements have been used for operational numerical weather prediction, climate/reanalysis studies and ionospheric physics. The F3/C EDP is retrieved from GPS radio-occultation (RO) data along the GPS-LEO (low earth orbit) radio links near the raypath tangent points. Recent studies show that ionospheric electron densities derived from the RO sounding around and above the F_2 peak are reasonably accurate, whereas those below the F region should be used with great caution because of the assumption of spherical symmetry used in the Abel inversion [*Lei et al.*, 2007; *Kelley et al.*, 2009; *Liu et al.*, 2010; *Yue et al.*, 2010]. Therefore, the F3/C EDP observation error applied in this study is assumed to be the sum of a 10% instrumentation error and the estimated Abel inversion error percentage [*Liu et al.*, 2010; *Yue et al.*, 2010].

[11] An observational forward operator which maps the model state variables to the observed parameters is needed. The TIE-GCM simulates the 3D electron density at grid location in pressure coordinates, and the F3/C EDP provides electron density profiles at irregular longitude and latitude locations. To simplify the forward operator computation and avoid the complication of missing model values above its upper boundary, the F3/C EDP is chosen for this new assimilation system development, instead of the line-of-sight integrated electron densities. The assimilation window is 1 h, which means that the F3/C EDPs occurring within 30 min of the assimilation time are assimilated. On average, there are approximately 85 profiles collected globally every hour, and used in each assimilation step. The F3/C EDP is retrieved from F3/C radio occultation and published by the COSMIC Data Analysis and Archive Center (CDAAC) at the University Corporation for Atmospheric Research (UCAR). In this study, all EDPs are sampled between 160 and 450 km with a 10 km resolution and have quality control criteria applied to avoid assimilating obviously bad data, such as negative densities.

3. Ensemble Members Generating Strategy

[12] The thermosphere-ionosphere system is strongly controlled by external forcing, and therefore ensemble members are generated by perturbing the input forcing parameters of the TIE-GCM. In the filtering experiments presented in this paper, 90 ensemble members are generated via centered Gaussian distributions of three primary model input parameters: the solar 10.7 cm radio flux (F10.7, used as a proxy for solar EUV radiation) and auroral hemispheric power and cross-tail potential drop that control high-latitude energy and momentum input to the model. The hemispheric power and cross-tail potential are assumed to be correlated with each other, but correlation of F10.7 with the hemispheric power and cross-tail potential is not considered. The mean values of the Gaussian distributions come from corresponding observations of the F10.7 and the three-hour planetary K index (Kp) published on the NOAA National Geophysical Data Center webpage, where Kp is used to estimate the hemispheric power and cross-tail potential [*Boyle et al.*, 1997; *Zhang and Paxton*, 2008]. The widths of the distributions are specified by a 14-day standard deviation of F10.7 and ± 0.5 unit of Kp. The values are 5×10^{-22} W/m^{2}Hz for F10.7, 2 GW for the hemispheric power, and 10 kV for the cross-tail potential.

[13] Our early numerical tests, however, showed that the ensemble members generated by perturbing these three model input parameters, although spanning a great range of electron number densities, did not yield sufficiently diverse profile shapes/altitude distributions to fully cover the observations variability. In order to increase the range of ionospheric F region peak heights (hmF2) and give sufficiently diverse profile shapes/altitude distributions, the vertical $E \times B$ plasma drift is also varied. The vertical drifts have a Gaussian-like distribution when we perturb the three forcing parameters. Nevertheless, the spread due to the parameters alone is not enough to give an adequate diversity of profile shapes. Therefore, ensemble members are divided into three groups with default, higher, and lower global vertical $E \times B$ plasma drift multiplying factors, which are 1.0, 1.5, and 0.5, respectively, to either raise or lower hmF2 and diversify the profile shapes.

[14] The forcing parameters assigned to each ensemble member are held unchanged over the assimilation time step. The spin-up time for each ensemble member is 10 h. In addition, the topside ionospheric electron density predicted by the original TIE-GCM is often higher than that from the nighttime F3/C observations, and this gross model bias resulted in a poor performance of filtering. The default nighttime vertical O^+ flux at the top boundary of the TIE-GCM is -2.0×10^8/cm^{2}s at most locations, with some latitudinal and solar zenith angle dependence. To improve the performance of filtering it has been reduced to one-fourth of this default value, and this change has led to better nighttime results.

[15] Those 90 ensemble members are used to provide the necessary information on the variability of the thermosphere and ionosphere, and to calculate the sample covariance matrix to describe the correction and variance of the model forecast error.

4. Result and Interpretation

[16] The assimilation experiment is conducted for 12–13 April 2008 under geomagnetic quiet conditions. The observed F10.7 and Kp are averaged in this two days period. The corresponding values of F10.7, hemispheric power, and cross-tail potential are 69.0×10^{-22} W/m^{2}Hz, 27.0 GW and 48.2 kV, respectively, which are used as the centered values for Gaussian distributions to generate initial ensemble members. In the EnKF framework, the probability distribution of ensemble members is assumed to be Gaussian. Therefore, the ensemble mean is used to represent the expected value of the probability distribution. The covariance localization function used in this study is given by the *Gaspari and Cohn* [1999] function with a half-width of about 10 degrees (about

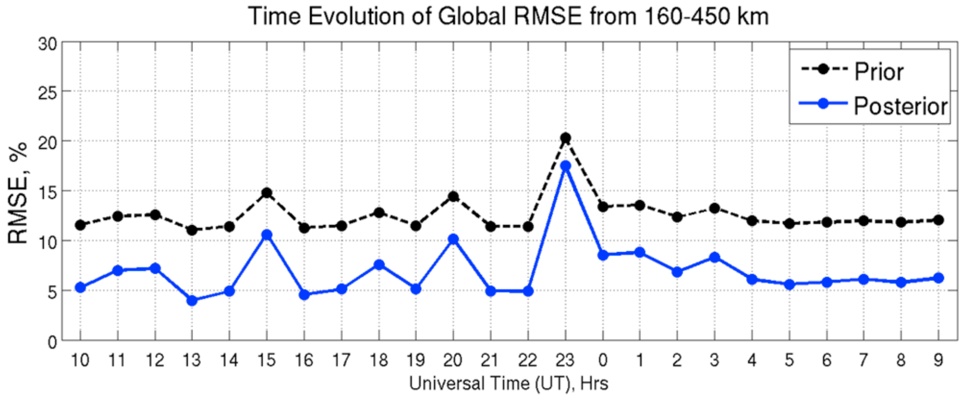

Figure 1. Global root-mean square percentage error of the prior/posterior against the F3/C observations from 160 to 450 km altitude. The black dashed and blue lines indicate the prior and posterior, respectively.

1,100 km) in the horizontal and 200 km in the vertical. The assimilation results are compared with the stand-alone TIE-GCM without any observations assimilated under the same conditions and in the same time period.

[17] To assess this newly developed assimilation system, the root-mean square errors (RMSE) at the profile locations for each assimilation cycle are estimated between 160 and 450 km. The RMSE percentage of the electron density is calculated from the difference between the model simulated and F3/C observed electron density values, divided by the F3/C value. Figure 1 shows the globally averaged electron density RMSE percentage variation with the universal time (UT) from 10:00 UT on 12 April to 09:00 UT on 13 April 2008. The RMSE percentage became large around 15:00, 20:00, and 23:00 UT, but it generally decreased after the assimilation of F3/C EDPs. The overall decrease was about 5%. This assessment demonstrates that the EnKF assimilation system can adjust the electron density from the TIE-GCM toward the F3/C observations.

[18] Figure 2 displays control (ensemble mean value without assimilation) and posterior (ensemble mean value after assimilation) F region peak densities (NmF2) from 10:00 UT on 12 April to 09:00 UT on 13 April. The irregular structures associated with the F3/C EDP locations are the results of adjustment, especially pronounced in the equatorial ionization anomaly (EIA) region and the midlatitude region in the Southern Hemisphere in the 11:00, 12:00, 14:00, 19:00, and 08:00 UT maps. Slight enhancements of the NmF2 appear during the evening period over the geomagnetic equator in the 19:00, 20:00, 22:00, 03:00, 04:00, 06:00, 08:00, and 09:00 UT maps.

[19] Figure 3 illustrates the control and posterior electron densities in latitude and height along the −75°E longitude from 05:00 LT on 12 April to 04:00 LT on 13 April. At most times, the electron density distribution shows adjustments in altitude and magnitude near the F3/C EDP locations. This demonstrates that assimilating F3/C EDP into the TIE-GCM alters not only the peak density but also the peak height of the F region, related to the altitudinal information provided by the F3/C EDP. In addition, the EIA features become more prominent in the Northern Hemisphere except for the 11:00, 15:00 and 19:00 LT slices. Moreover, the two EIA crest shifts closer to the geomagnetic equator from the 11:00 LT slice, and acquires a sharper poleward edge in the Southern Hemisphere for the 14:00 and 15:00 slices. The electron density is enhanced above 250 km over the geomagnetic equator for the 22:00, 23:00 and 01:00 LT slices, as also seen in Figure 2 for the 03:00, 04:00 and 06:00 UT maps at certain longitudes.

5. Validation

[20] To further validate the assimilation results with independent observations, we use ionospheric NmF2 and hmF2 obtained from ionosondes located at the Jicamarca (JIC, −12.0°N, −76.8°E) in Peru, at the Donghwa station (TWN, 22.4°N, 120.5°E) in Taiwan, and at the Gakona station (GAK, 62.4°N, −145.0°E) in Alaska, corresponding to the magnetic equatorial region, EIA region, and high-latitude region, respectively. Figure 4 illustrates hmF2 and NmF2 comparisons for the control and posterior results at JIC from 04/12 06:00 LT to 04/13 18:00 LT. A radio occultation event does not regularly occur within the one hour assimilation cycle and within the localization window at any given location, so there are only 26 out of 37 h when an F3/C EDP is nearby the validation station and affects the posterior electron density. The RMSE percentage is calculated from the difference between the model hmF2 and NmF2 and ionosonde observations, divided by ionosonde observations for that assimilation cycle. This parameter is used to determine whether assimilation led to improvement in electron density specification. The average RMSE percentage of the control and posterior are 16.4% and 12.9% for hmF2, and 29.7% and 26.2% for NmF2 during this period. It shows that about 43% (16/37) of the time the posterior model state agrees better with observations for both hmF2 and NmF2 at JIC. Only about 11% of the time (4/37), neither hmF2 nor NmF2 is improved for this particular period. Nevertheless, when we consider only times when an F3/C EDP is nearby the validation station, assimilation of F3/C EDP leads to a better agreement of hmF2 and NmF2 with observations for about 81% (21/26) and 54% (14/26) of the assimilation cycles, respectively.

[21] Figure 5 shows another comparison as in Figure 4 at TWN from 04/12 18:00 to 04/13 23:00 LT. There are only 18 out of 30 h when an F3/C radio occultation event occurs nearby the station. The average RMSE percentage for the control and posterior are 13% and 14% for hmF2, and 43%

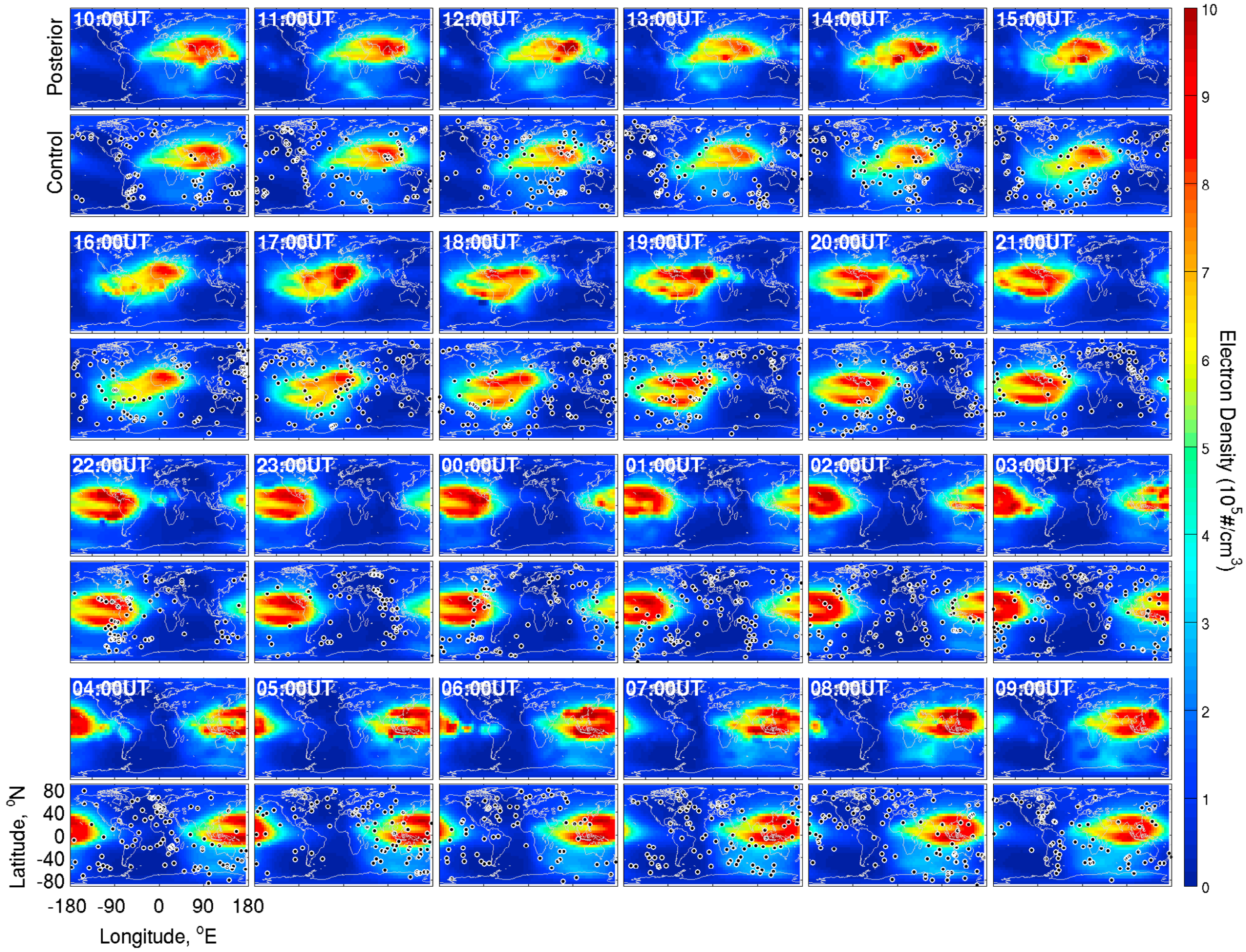

Figure 2. Global NmF2 maps from 2008/04/12 06:00 UT to 2008/04/13 04:00 UT before and after assimilating the FORMOSAT-3/COSMIC electron density profiles. The upper and lower row of each panel displays the posterior and control, respectively. The black dots indicate the observation locations.

and 37% for NmF2. The results at TWN are consistent with the JIC results, and only about 10% of the time (3/30), neither hmF2 nor NmF2 is improved for this particular period. Moreover, the assimilation of F3/C EDPs yields better agreement of hmF2 and NmF2 with observations for about 55% (10/18) and 72% (13/18) of the assimilation cycles, respectively.

[22] Figure 6 shows the high-latitude comparison at GAK from 04/12 05:00 to 04/13 13:00 LT. There are only 18 out of 33 h when an F3/C radio occultation event occurs nearby the station. The results at GAK are qualitatively consistent with previous results, and only 10% of the time (2/20), neither hmF2 nor NmF2 is improved for this particular period. Assimilation of F3/C EDPs yields better agreement of hmF2 and NmF2 with observations for about 82% (9/11) and 72% (8/11) of the assimilation cycles, respectively. However, the improvements are relatively small. The average percentage RMSE for the control and posterior are both about 18% for hmF2 and NmF2, with only a slightly smaller reduction in percentage RMSE for the posterior. The validation results suggest that assimilating the F3/C EDPs can improve the agreement between the modeled electron densities and observations not only at the magnetic equator and EIA region, but also at high latitudes.

[23] In general, the validation results show that the overall improvement of hmF2 (67% = 58/89) and NmF2 (62% = 54/89) is attained at most of the assimilation cycles with a low percentage of degradation (10% = 9/87). Once again, this confirms that our assimilation experiments with F3/C EDP are working reliably. Note that the improvement of hmF2 (72% = 40/55) is more obvious than that of NmF2 (63% = 35/55) by assimilating F3/C EDPs.

6. Discussion

[24] Assimilation of F3/C EDP into the TIE-GCM improves the accuracy of modeled global electron density and decreases the RMSE especially at, but not limited to, the profile locations. After assimilating F3/C EDPs into the NCAR TIE-GCM, the global NmF2 maps reveal hemispheric asymmetry of the EIA crests, higher electron densities at midlatitude, and density enhancement over the magnetic equator. The TIE-GCM simulations predict that the two EIA crests have roughly the same peak densities around the March

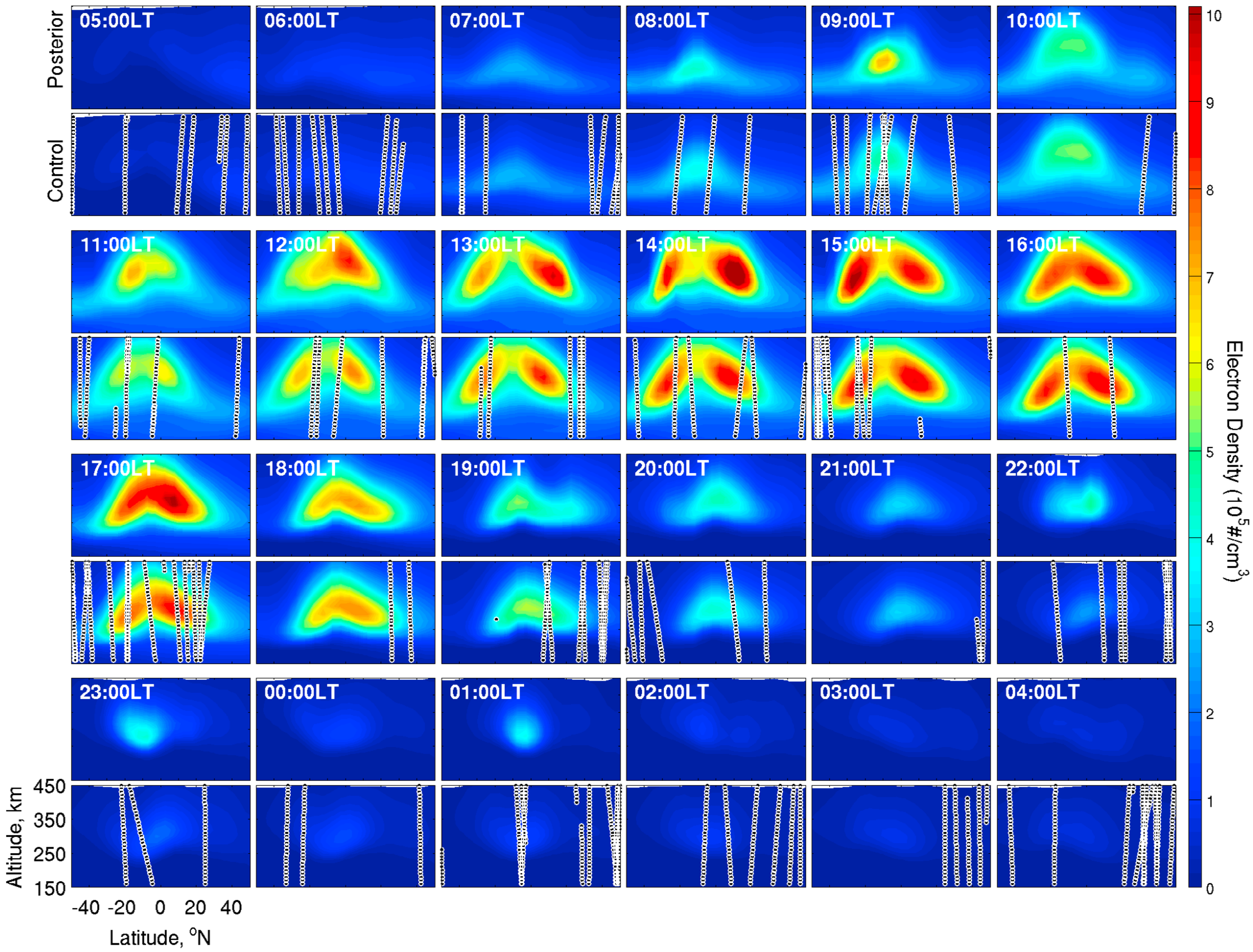

Figure 3. Latitude/height slices along −75°E from 2008/04/12 05:00 UT (10:00 LT) to 2008/04/13 04:00 UT (23:00 LT) before and after assimilating the FORMOSAT-3/COSMIC electron density profiles. The upper and lower row of each panel displays the posterior and control, respectively. The black dots indicate the observation profiles located between −60 and −90°E longitude within 30 min of a given assimilation time.

equinox. However, the electron density in the Northern Hemisphere becomes higher than in the Southern Hemisphere when the F3/C observations are assimilated. The validation result for TWN also shows an increase of NmF2 over the TIE-GCM control run, improving the agreement with the ionosonde observations. At solstice, asymmetry of the EIA may result from a trans-equatorial neutral wind blowing from the summer hemisphere to the winter hemisphere. This causes upward motion of the plasma in the summer hemisphere and downward motion in the winter hemisphere [*Lei et al.*, 2007]. Hemispheric asymmetry of neutral composition can also contribute to EIA asymmetry. The assimilation results suggest that either the thermospheric circulation or the composition in the TIE-GCM, or both, need to be modified to be able to represent the EIA asymmetry shown by the F3/C assimilation at equinox. The density enhancement over the magnetic equator is also seen in the Jicamarca ionosonde measurements (shown in Figure 4), which further validates the assimilation system. The higher electron density at midlatitude and the density enhancement over the magnetic equator after the assimilation of F3/C EDPs also suggest that additional adjustments to TIE-GCM might be needed.

[25] Figure 3 shows how the assimilation of F3/C EDPs shifts the two EIA crests closer to the geomagnetic equator for the 11:00 LT and also reverses the hemispheric asymmetry of the EIA. The closer EIA crests suggest that the magnitude of the E × B fountain effect predicted by the model could be too strong. On the other hand, some features, such as the reversal of the hemispheric asymmetry of the EIA and the disappearance of the density enhancement over just one assimilation cycle, are likely to be artifacts due to the fact that E3/C EDP comes and goes for a given location. This is because an assimilation adjustment is sustained only over a short period and fairly rapidly relaxes toward climatology with a time scale on the order of one hour, due to the natural relaxation time of the ionosphere due to ion diffusion and loss. *Jee et al.* [2007] replaced electron and O^+ densities as initial conditions of the Thermosphere Ionosphere Nested Grid model [*Wang et al.*, 1999] and ran with the same forcing parameters, showing that the *e*-folding decay time of the initialization lasts only about 1∼4 h around the F_2 peak

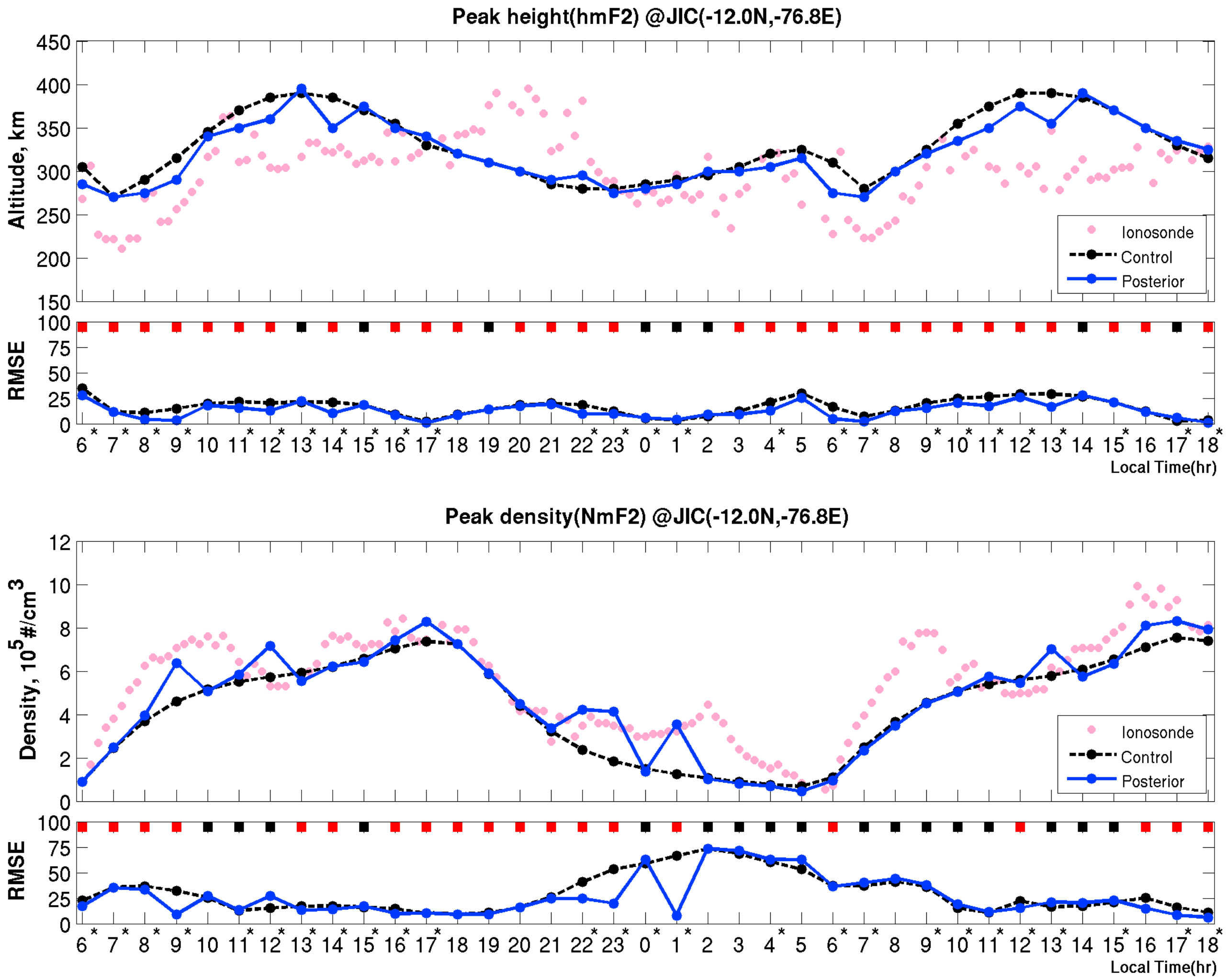

Figure 4. Comparison of assimilation analysis results over the Jicamarca station in Peru to ionosonde observations. The pink dots indicate the raw ionosonde measurements. The dashed black and solid blue lines are the control and posterior, respectively. The red/black colored boxes stand for improvement/failure as determined by the RMSE percentages. On the time scale, an hour with an asterisk is used to represent that F3/C observations were sufficiently close in space and time to station to directly affect the posterior value at the assimilating cycle.

and less than 1 h below the F_2 peak. In our experiments, the posterior electron density also approximately relaxes back toward the climatology of the TIEGCM over the course of one assimilation cycle (one hour) and remains unchanged when no observations are available.

[26] Furthermore, we expect ionospheric drivers such as thermospheric winds and low-latitude E $\times$ B drift to affect this relaxation time scale. Some studies have shown that these drivers can be inferred from electron density observations and made consistent with the electron density distribution. For example, recent studies have developed algorithms to estimate the neutral wind based on the relationship between the neutral wind and the electron density distribution [*Luan and Solomon*, 2008; *Datta-Barua et al.*, 2009]. Moreover, *Pi et al.* [2003] and *Scherliess et al.* [2009] demonstrated that by using an assimilation model to estimate the low-latitude E $\times$ B drift or neutral wind one can improve electron density specification. In our experiments, the thermospheric winds and compositions are adjusted by assimilation of electron density profiles, but this did not result in a significant extension of the relaxation time scale. It is partly due to the fact the spin-up time of ensemble members in our experiments is only 10 h and the coupled thermosphere-ionosphere system has not yet reached a steady state completely, as suggested by follow-up experiments with a longer spin-up time. In future studies, the relationship of relaxation time scale to the forcing estimation and the spin-up time needs to be addressed further.

[27] The validation of the assimilation results with ionosonde observations indicates that the RMSE percentage of NmF2 is reduced more significantly than that of hmF2. This is partly due to the inadequate vertical resolution of the TIE-GCM in comparison with the F3/C EDP. The vertical coordinate in the TIE-GCM is $\ln(p_0/p)$, where p is pressure and p_0 is a reference pressure. The model vertical resolution (half scale height) with respect to geometric height is smaller at lower altitudes (2.5–10.0 km, below 150 km) and larger at higher altitudes (10.0–25.0 km, above 150 km). Although

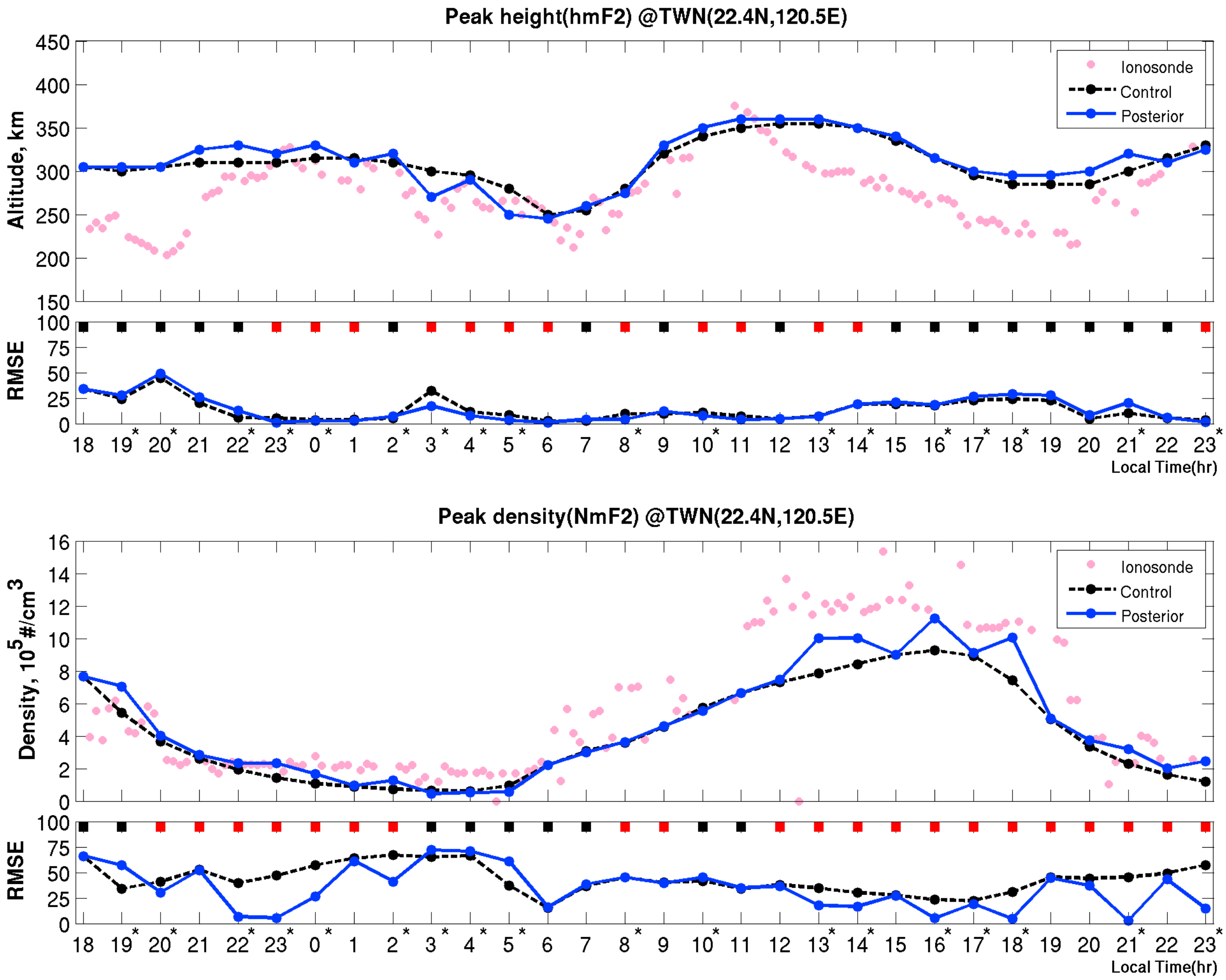

Figure 5. Similar to the Figure 4. Comparison of assimilation analysis results over the Donghwa station in Taiwan to ionosonde observations.

the posterior ensemble has been adjusted by assimilating the F3/C EDP with 10 km resolution, the adjustment of hmF2 is not accurately resolved after converting the height back to the model pressure level.

[28] It is important to mention that about 35% of the F3/C observations are rejected by the quality control (QC) and outlier threshold (OT) criteria we successively impose during the assimilation process. For an individual EDP, only those data at particular heights that do not meet the acceptance criteria are rejected, while the remainder of the data for that EDP is retained. An example shown in Figure 7 illustrates the rejection criteria for a poorly assimilated EDP. Below 200 km altitude, the F3/C EDP goes negative, which is unphysical and fails to pass the quality control. Only positive observations are used for assimilation, and so the negative observations are rejected. In addition, the consistency between the prior state and an observation can be assessed using the prior ensemble standard deviation and the observation error, in order to identify outliers. In this study, the outlier threshold is set to four times the standard deviation of the prior ensemble members plus four times the observation error. For example, in Figure 7 four ensemble standard deviations (one-sided length of the black bar) does

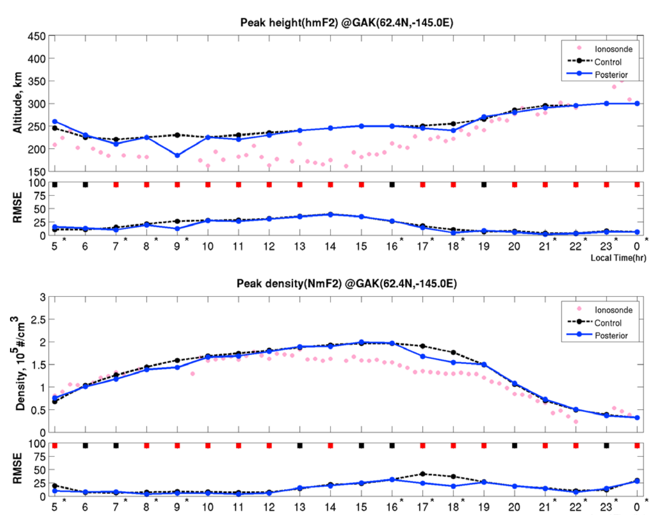

Figure 6. Similar to the Figure 4. Comparison of assimilation analysis results over the Gakona station in Alaska to ionosonde observations.

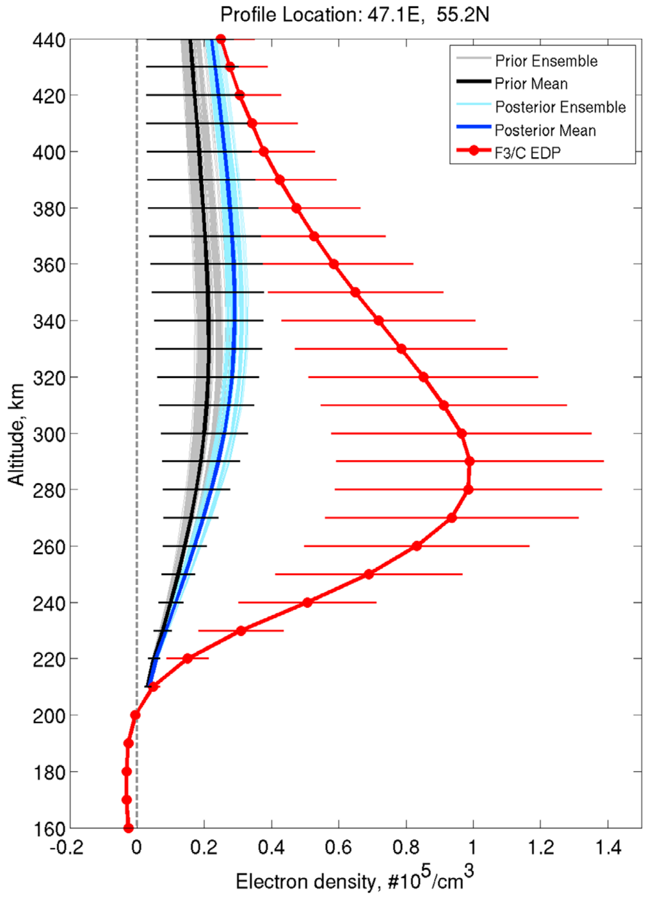

Figure 7. Example of conditions giving rise to rejected observations due to surpassing the outlier threshold (210–350 km) or failing quality control due to negative densities (160–200 km). The horizontal black and red lines are used to indicate ±4 times the standard deviation of prior ensemble members and ±4 times the observation error, respectively.

not overlap four times the observation error (one-sided length of the red bar) between 210 and 350 km, indicating a large model-observation inconsistency. Therefore, the observations at these particular altitudes are rejected due to this outlier threshold criterion. For this profile, only values at 360 km and above are retained for assimilation. Thus, the result is a posterior distribution closer to the prior than to the observations.

[29] Figure 8 demonstrates the percentage of rejection due to either outlier threshold or quality control, and total rejection is shown as a function of local time and altitude. The average rejection rate is about 35%, mainly due to the outlier threshold. The rejection rate due to the quality control is less than 7%. It increases sharply around midnight (00:00–01:00 LT), which is mostly caused by the negative value problem of the F3/C EDP at lower altitudes. This implies that the F3/C EDP is almost useless at lower altitudes, and suggests that improvement might be achieved by assimilating the F3/C line-of-sight integrated electron content (radio occultation total electron content or ROTEC) instead of Abel-inverted vertical profiles. However, the TIE-GCM provides no electron density values above its upper boundary, where parts of the raypaths between the F3/C and GPS satellites lie. It is therefore not possible to carry out a complete forward modeling of the ROTEC from the TIE-GCM output alone. Hence, improved retrieval methods are desired to increase the utility of profiles in the data assimilation system in the future. The rejection rate due to the outlier threshold reveals a clear day/night contrast, and it is generally higher during the nighttime period than in the daytime period. Worth noting here is that the observations are rejected mostly at lower altitudes during the daytime period but at higher altitudes during the nighttime period. This suggests that there exists a large inconsistency between the TIE-GCM and the F3/C observations at these particular altitudes and local times, for reasons that are not fully understood. The OT rejection is found to be an important part of the data assimilation process, as it improves the agreement of the posterior EDPs with the independent ionosonde data.

[30] In the EnKF algorithm, if ensemble members have insufficient spread to cover the range of observations, the model will be given more weight than it should be given, which results in an inappropriate posterior state estimation. In this study, the ensemble members are generated simply by perturbing the F10.7, the hemispheric power, the cross-tail potential, and the vertical drift velocity. The solar EUV radiation (parameterized by F10.7) affects the daytime ionization rate and thus strongly affects the electron densities in the ionosphere. The hemisphere power and the cross-tail potential are used to control auroral precipitation and the convection electric field at higher latitudes, which affect the global thermosphere neutral wind and composition and electrodynamics and, consequently, the global ionospheric electron density. The vertical drift velocity influences the plasma motion and changes the peak height of the *F* region. Nevertheless, these ensemble members are still not adequate to cover the full range of ionospheric conditions observed by the F/3C. More work is needed to select other physical parameters in the model to perturb and to test them to reduce systematic model-observation inconsistencies and thereby the rejection rate of observations.

7. Conclusion

[31] In this paper, for the first time F3/C electron density profiles are successfully assimilated into the NCAR TIE-GCM by using a recently developed ensemble Kalman filter data assimilation system. The assimilation experiments have been conducted under geomagnetic quiet conditions. The reduced RMSE percentage shows that assimilating the F3/C EDPs brings the NCAR TIE-GCM electron densities closer to both the assimilated and independent observations.

[32] The validation of the assimilation results has been carried out by comparing with independent measurements of NmF2 and hmF2 by the JIC, TWN, and GAK ionosondes in the magnetic equatorial, EIA, and high-latitude regions. This comparison demonstrates that the posterior NmF2 and hmF2 obtained by assimilating the F3/C EDP into the TIE-GCM agree better with observations than those from the default TIE-GCM simulations. The ionosonde observations confirm interesting features such as the hemispheric asymmetry of the EIA, and the equatorial density enhancement, which appear to be real ionospheric signatures.

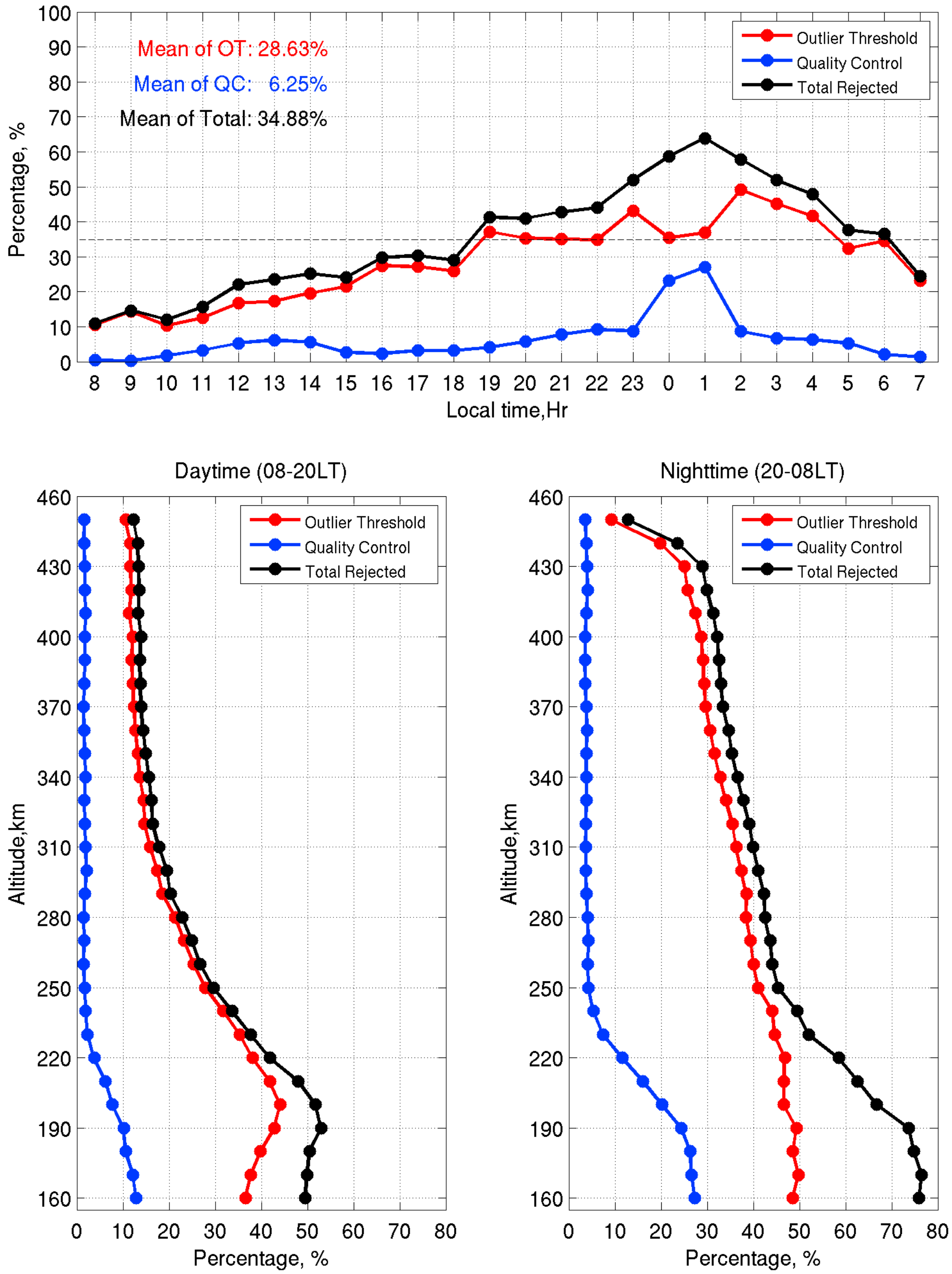

Figure 8. Percentages of rejected observations resulting from the outlier threshold (OT) and quality control (QC) criteria applied to the observations.

[33] To reduce the high rejection rate of observations during nighttime and at lower altitudes that results from the outlier threshold criterion, better ensemble member generation and model bias correction strategies are needed to fully cover the observations, and to improve the consistency between the TIE-GCM simulations and the F3/C observations. In addition to perturbing the solar F10.7 index, the hemispheric power, and the cross-tail potential, other forcing parameters such as tides, O^+ flux at the top boundary of the model and plasma drift velocity should be considered in future work.

[34] Furthermore, the use of the EnKF in this study only estimated the thermosphere and ionosphere states, such as the electron density, the neutral temperature and winds, and the atomic and molecular oxygen mixing ratios by assimilating the F3/C observations. We did not attempt to estimate any forcing parameters such as the solar F10.7 index, the hemispheric power, the cross-tail potential, and the plasma drift. The forcing parameters assigned to each ensemble member are held unchanged over the entire duration of assimilation experiment. However, it would be desirable to estimate them, for instance, by including them as part of the EnKF state vector (Matsuo et al., submitted manuscript, 2012), since the thermosphere-ionosphere system is strongly controlled by external drivers.

[35] **Acknowledgments.** ITL is supported by a Newkirk Fellowship from the High Altitude Observatory of the National Center for Atmospheric Research. The National Center for Atmospheric Research is sponsored by the National Science Foundation. TM is supported by the Air Force Office of Scientific Research Multidisciplinary University Research Initiative award FA9550-07-1-0565. This work is supported in part by National Sciences Council (NSC) grants, NSC 98-2111-M-008-008-MY3 and National Space Organization grants, NSPO-S-101014. This work is also supported in part by the Center for Integrated Space Weather Modeling (CISM), which is funded by the STC Program of the National Science Foundation under Agreement ATM-0120950, and NASA grants NNX10AQ59G and NNX09AN57G. The authors wish to thank the reviewers for their useful comments.

[36] Robert Lysak thanks two anonymous reviewers for their assistance in evaluating this manuscript.

References

Anderson, J. L. (2001), An ensemble adjustment Kalman filter for data assimilation, *Mon. Weather Rev.*, *129*, 2884–2903, doi:10.1175/1520-0493(2001)129<2884:AEAKFF>2.0.CO;2.

Anderson, J. L., T. Hoar, K. Raeder, H. Liu, N. Collins, R. Torn, and A. F. Arellano (2009), The Data Assimilation Research Testbed: A community data assimilation facility, *Bull. Am. Meteorol. Soc.*, *90*, 1283–1296, doi:10.1175/2009BAMS2618.1.

Boyle, C. B., P. H. Reiff, and M. R. Hairston (1997), Empirical polar cap potentials, *J. Geophys. Res.*, *102*(A1), 111–125, doi:10.1029/96JA01742.

Burgers, G., P. J. van Leeuwen, and G. Evensen (1998), Analysis scheme in the ensemble Kalman filter, *Mon. Weather Rev.*, *126*, 1719–1724, doi:10.1175/1520-0493(1998)126<1719:ASITEK>2.0.CO;2.

Bust, G. S., T. W. Garner, and T. L. Gaussiran II (2004), Ionospheric Data Assimilation Three-Dimensional (IDA3D): A global, multisensor, electron density specification algorithm, *J. Geophys. Res.*, *109*, A11312, doi:10.1029/2003JA010234.

Daley, R. (1991), *Atmospheric Data Analysis*, Cambridge Univ. Press, New York.

Datta-Barua, S., G. S. Bust, G. Crowley, and N. Curtis (2009), Neutral wind estimation from 4-D ionospheric electron density images, *J. Geophys. Res.*, *114*, A06317, doi:10.1029/2008JA014004.

Evensen, G., (1994) Sequential data assimilation with a nonlinear quasi-geostrophic model using Monte Carlo methods to forecast error statistics, *J. Geophys. Res.*, *99*, 10,143–10,162.

Evensen, G. (2009), *Data Assimilation: The Ensemble Kalman Filter*, 330 pp., Springer, Berlin.

Fuller-Rowell, T. J., E. A. Araujo-Pradere, C. Minter, M. Codrescu, P. Spencer, D. Robertson, and A. R. Jacobson (2006), US-TEC: A new data assimilation product from the Space Environment Center characterizing the ionospheric total electron content using real-time GPS data, *Radio Sci.*, *41*, RS6003, doi:10.1029/2005RS003393.

Gaspari, G., and S. Cohn (1999), Construction of correlation functions in two and three dimensions, *Q. J. R. Meteorol. Soc.*, *125*(554), 723–757, ISSN:1477-870X.

Hajj, G. A., B. D. Wilson, C. Wang, X. Pi, and I. G. Rosen (2004), Data assimilation of ground GPS total electron content into a physics-based ionospheric model by use of the Kalman filter, *Radio Sci.*, *39*, RS1S05, doi:10.1029/2002RS002859.

Houtekamer, P. L., and H. L. Mitchell (2006), Ensemble Kalman filtering, *Q. J. R. Meteorol. Soc.*, *131*(613), 3269–3289, doi:10.1256/qj.05.135.

Howe, B. M., K. Runciman, and J. A. Secan (1998), Tomography of the ionosphere: Four-dimensional simulations, *Radio Sci.*, *33*, 109–128, doi:10.1029/97RS02615.

Jee, G., A. G. Burns, W. Wang, S. C. Solomon, R. W. Schunk, L. Scherliess, D. C. Thompson, J. J. Sojka, and L. Zhu (2007), Duration of an ionospheric data assimilation initialization of a coupled thermosphere-ionosphere model, *Space Weather*, *5*, S01004, doi:10.1029/2006SW000250.

Kelley, M. C., V. K. Wong, N. Aponte, C. Coker, A. J. Mannucci, and A. Komjathy (2009), Comparison of COSMIC occultation-based electron density profiles and TIP observations with Arecibo incoherent scatter radar data, *Radio Sci.*, *44*, RS4011, doi:10.1029/2008RS004087.

Komjathy, A., B. Wilson, X. Pi, V. Akopian, M. Dumett, B. Iijima, O. Verkhoglyadova, and A. J. Mannucci (2010), JPL/USC GAIM: On the impact of using COSMIC and ground-based GPS measurements to estimate ionospheric parameters, *J. Geophys. Res.*, *115*, A02307, doi:10.1029/2009JA014420.

Lei, J., et al. (2007), Comparison of COSMIC ionospheric measurements with ground-based observations and model predictions: Preliminary results, *J. Geophys. Res.*, *112*, A07308, doi:10.1029/2006JA012240.

Liu, J. Y., C. Y. Lin, C. H. Lin, H. F. Tsai, S. C. Solomon, Y. Y. Sun, I. T. Lee, W. S. Schreiner, and Y. H. Kuo (2010), Artificial plasma cave in the low-latitude ionosphere results from the radio occultation inversion of the FORMOSAT-3/COSMIC, *J. Geophys. Res.*, *115*, A07319, doi:10.1029/2009JA015079.

Luan, X., and S. C. Solomon (2008), Meridional winds derived from COSMIC radio occultation measurements, *J. Geophys. Res.*, *113*, A08302, doi:10.1029/2008JA013089.

Mandrake, L., B. Wilson, C. Wang, G. Hajj, A. Mannucci, and X. Pi (2005), A performance evaluation of the operational Jet Propulsion Laboratory/University of Southern California Global Assimilation Ionospheric Model (JPL/USC GAIM), *J. Geophys. Res.*, *110*, A12306, doi:10.1029/2005JA011170.

Matsuo, T., and E. A. Araujo-Pradere (2011), Role of thermosphere-ionosphere coupling in a global ionospheric specification, *Radio Sci.*, *46*, RS0D23, doi:10.1029/2010RS004576.

Pi, X., C. Wang, G. A. Hajj, G. Rosen, B. D. Wilson, and G. J. Bailey (2003), Estimation of $E \times B$ drift using a global assimilative ionospheric model: An observation system simulation experiment, *J. Geophys. Res.*, *108*(A2), 1075, doi:10.1029/2001JA009235.

Richmond, A. D., E. C. Ridley, and R. G. Roble (1992), A thermosphere/ionosphere general circulation model with coupled electrodynamics, *Geophys. Res. Lett.*, *19*, 601–604, doi:10.1029/92GL00401.

Roble, R. G., E. C. Ridley, A. D. Richmond, and R. E. Dickinson (1988), A coupled thermosphere/ionosphere general circulation model, *Geophys. Res. Lett.*, *15*, 1325–1328, doi:10.1029/GL015i012p01325.

Scherliess, L., R. W. Schunk, J. J. Sojka, and D. C. Thompson (2004), Development of a physics-based reduced state Kalman filter for the ionosphere, *Radio Sci.*, *39*, RS1S04, doi:10.1029/2002RS002797.

Scherliess, L., R. W. Schunk, J. J. Sojka, D. C. Thompson, and L. Zhu (2006), Utah State University global assimilation of ionospheric measurements Gauss-Markov Kalman filter model of the ionosphere: Model description and validation, *J. Geophys. Res.*, *111*, A11315, doi:10.1029/2006JA011712.

Scherliess, L., D. C. Thompson, and R. W. Schunk (2009), Ionospheric dynamics and drivers obtained from a physics-based data assimilation model, *Radio Sci.*, *44*, RS0A32, doi:10.1029/2008RS004068.

Schunk, R. W., et al. (2004), Global assimilation of ionospheric measurements (GAIM), *Radio Sci.*, *39*, RS1S02, doi:10.1029/2002RS002794.

Wang, W., T. L. Killeen, A. G. Burns, and R. G. Roble (1999), A high resolution, three-dimensional, time dependent, nested grid model of the coupled thermosphere-ionosphere, *J. Atmos. Sol. Terr. Phys.*, *61*, 385–397, doi:10.1016/S1364-6826(98)00079-0.

Yue, X., W. S. Schreiner, J. Lei, S. V. Sokolovskiy, C. Rocken, D. C. Hunt, and Y.-H. Kuo (2010), Error analysis of Abel retrieved electron density profiles from radio occultation measurements, *Ann. Geophys.*, *28*, 217–222, doi:10.5194/angeo-28-217-2010.

Zhang, Y., and L. J. Paxton (2008), An empirical Kp-dependent global auroral model based on TIMED/GUVI FUV data, *J. Atmos. Sol. Terr. Phys.*, *70*, 1231–1242, doi:10.1016/j.jastp.2008.03.008.

Planetary and Space Science 60 (2012) 363–369

Contents lists available at SciVerse ScienceDirect

Planetary and Space Science

journal homepage: www.elsevier.com/locate/pss

On relation between mid-latitude ionospheric ionization and quasi-trapped energetic electrons during 15 December 2006 magnetic storm

A.V. Suvorova [a,b,*], L.-C. Tsai [a], A.V. Dmitriev [c,a]

[a] Center for Space and Remote Sensing Research, National Central University, Jhongli, Taiwan
[b] Skobeltsyn Institute of Nuclear Physics Moscow State University, Moscow, Russia
[c] Institute of Space Science, National Central University, Jhongli, Taiwan

ARTICLE INFO

Article history:
Received 4 July 2011
Received in revised form
14 October 2011
Accepted 7 November 2011
Available online 18 November 2011

Keywords:
Ionospheric storms
Radiation belts
Magnetic storms

ABSTRACT

We report simultaneous observations of intense fluxes of quasi-trapped energetic electrons and substantial enhancements of ionospheric electron concentration (EC) at low and middle latitudes over the Pacific region during the geomagnetic storm on 15 December 2006. Electrons with energy of tens of keV were measured at altitude of ~800–900 km by POES and DMSP satellites. Experimental data from COSMIC/FS3 satellites and global network of ground-based GPS receivers were used to determine height profiles of EC and vertical total EC, respectively. A good spatial and temporal correlation between the electron fluxes and EC enhancements was found. This fact allows us to suggest that the quasi-trapped energetic electrons can be an important source of ionospheric ionization at middle latitudes during magnetic storms.

1. Introduction

Storm-time dynamics of total electron content (TEC), the integral with height of the ionospheric electron density profile, was studied comprehensively from auroral to equatorial latitudes for many decades (e.g. Mendillo, 2006). Nowadays, numerous studies concern with an unresolved problem of TEC enhancements, so-called positive ionospheric storms (e.g. Balan et al., 2010; Mendillo et al., 2010; Wei et al., 2011). Complex mechanism of thermosphere–ionosphere system response to a geomagnetic storm involves a number of different agents such as disturbance electric fields, changes in neutral winds system and neutral chemical composition, gravity waves and diffusion. However, it is very difficult to pick out the agents forming the positive ionospheric storms.

Because of its high conductivity, the ionosphere responds quickly to variations of electric field due to such effects as magnetospheric convection, ionospheric dynamo-disturbance and various kinds of wave disturbances (e.g. Biktash, 2004). Balan et al. (2011) discuss an importance of thermospheric storms developing simultaneously with ionospheric ones. Relative role of prompt penetrating (under-shielded) electric field (PPEF) and equatorward neutral winds as two sources of positive ionospheric storms at low and middle latitudes is intensively discussed in literature (Lei et al., 2008; Pedatella et al., 2009; Balan et al., 2010; Mendillo et al., 2010). Possible errors in the models are attributed to under-representation of conditions at lower altitudes, variability of the neutral wind and/or coupling with auroral sources.

Recent studies and models of the ionospheric disturbances observed during a strong geomagnetic storm on 14–15 December 2006 have revealed that the PPEF and equatorward neutral winds alone can not explain a long-lasting intense positive ionospheric storm occurred over the Pacific sector during maximum and recovery phase of the magnetic storm (Lei et al., 2008; Pedatella et al., 2009). Lei et al. (2008) showed that the CMIT model simulations were able to capture the positive storm effect at equatorial ionization anomaly (EIA) crest regions during 00–03 UT on December 15. On the other hand, the authors pointed out that the model was unable to reproduce the positive effects observed for several hours after 03 UT. In addition, the CMIT simulation predicted a depletion of plasma densities over the low-latitude region at 00–03 UT on 15 December that is inconsistent with the observations. Pedatella et al. (2009) reported that during this time the height of F-layer peak increased by greater than 100 km. It was assumed that the TEC increases, observed in the topside ionosphere/plasmasphere at middle to high latitudes, might be explained by the effects of particle precipitation. However, experimental evidence of this assumption was not reported.

Here we analyze fluxes of energetic electrons observed by low-altitude (heights ~800 to 900 km) satellites of POES and DMSP fleets during magnetic storm on 15 December 2006. We

* Corresponding author at: Center for Space and Remote Sensing Research, National Central University, Jhongli, Taiwan. Tel.: +886 3 4227151 57651.
E-mail address: suvorova_alla@yahoo.com (A.V. Suvorova).

0032-0633/$ - see front matter © 2011 Elsevier Ltd. All rights reserved.
doi:10.1016/j.pss.2011.11.001

demonstrate a good correlation of the mid-latitude ionospheric ionization enhancements observed over the Pacific region with the intense fluxes of quasi-trapped energetic electrons.

2. Positive ionospheric storm

A geomagnetic storm started at about 14 UT on 14 December 2006, when a CME-driven interplanetary shock (IS) affected the Earth's magnetosphere. The storm initial phase was lasting until ~2330 UT. After that the CME-related main phase of severe geomagnetic storm began. The storm maximum with $Dst \sim -150$ nT and Kp~8+ was observed after midnight of 15 December. The recovery phase started at ~08 UT on 15 December. The storm main and recovery phases were accompanied by a long-lasting (from 00 to 14 UT) and widely expanded (from 12 to 24 LT) strong positive ionospheric storm with the ionization enhanced up to 50 TECU ($1\text{TECU}=10^{12}$ electrons/cm^2) over the Pacific and American regions (from 120° to 300° longitude) (Lei et al., 2008; Pedatella et al., 2009).

One of the very important factors in the study of storm-time disturbances is a consistent choice of quiet-time period. Previous studies of this event used moderately disturbed day on December 13 as a day of "quiet conditions". We use a day on December 3 when the solar and geomagnetic activity was very quiet. This choice allows revealing prominent positive ionospheric storms on the initial, main and recovery phases of the geomagnetic storm. Fig. 1 demonstrates the development of strong enhancement of vertical TEC (VTEC) at 00–06 UT on 15 December. Global ionospheric maps (GIM) of VTEC are provided every 2 h by a world-wide network of ground-based GPS receivers. The residual VTEC (dVTEC) was calculated as a difference between the disturbed and quiet days.

The positive storms in VTEC tend to occur in the postnoon and dusk sectors above Pacific and American region. We can distinguish two branches of the VTEC enhancements at low (~10° to 20° deg) and middle (~30° to 40°) latitudes. The low-latitude positive storm is oriented strictly along the geomagnetic equator at geomagnetic latitudes of ~15°. This storm is mostly pronounced and can be explained in the frame of a continuous complex effect of daytime eastward PPEF and equatorward neutral wind (Balan et al., 2010). The positive storm at middle latitudes persists within first 6 h and then diminishes fast after ~06 UT. It seems that the maximum of mid-latitude storm is slightly moving pole-ward from ~30° to 40° of geomagnetic latitude. There is no clear explanation of this positive storm.

Vertical profiles of electron concentration (EC) were measured in COSMIC/FS3 space-borne experiment. The EC is expressed as a number of electrons per cubic centimeter (cc). Six satellites of the COSMIC/FS3 mission produce a sounding of the ionosphere on the base of radio occultation (RO) technique, which makes use of radio signals transmitted by the GPS satellites (Hajj et al., 2000). Usually over 2500 soundings per day provide EC height profiles over ocean and land. A 3-D EC distribution is deduced through

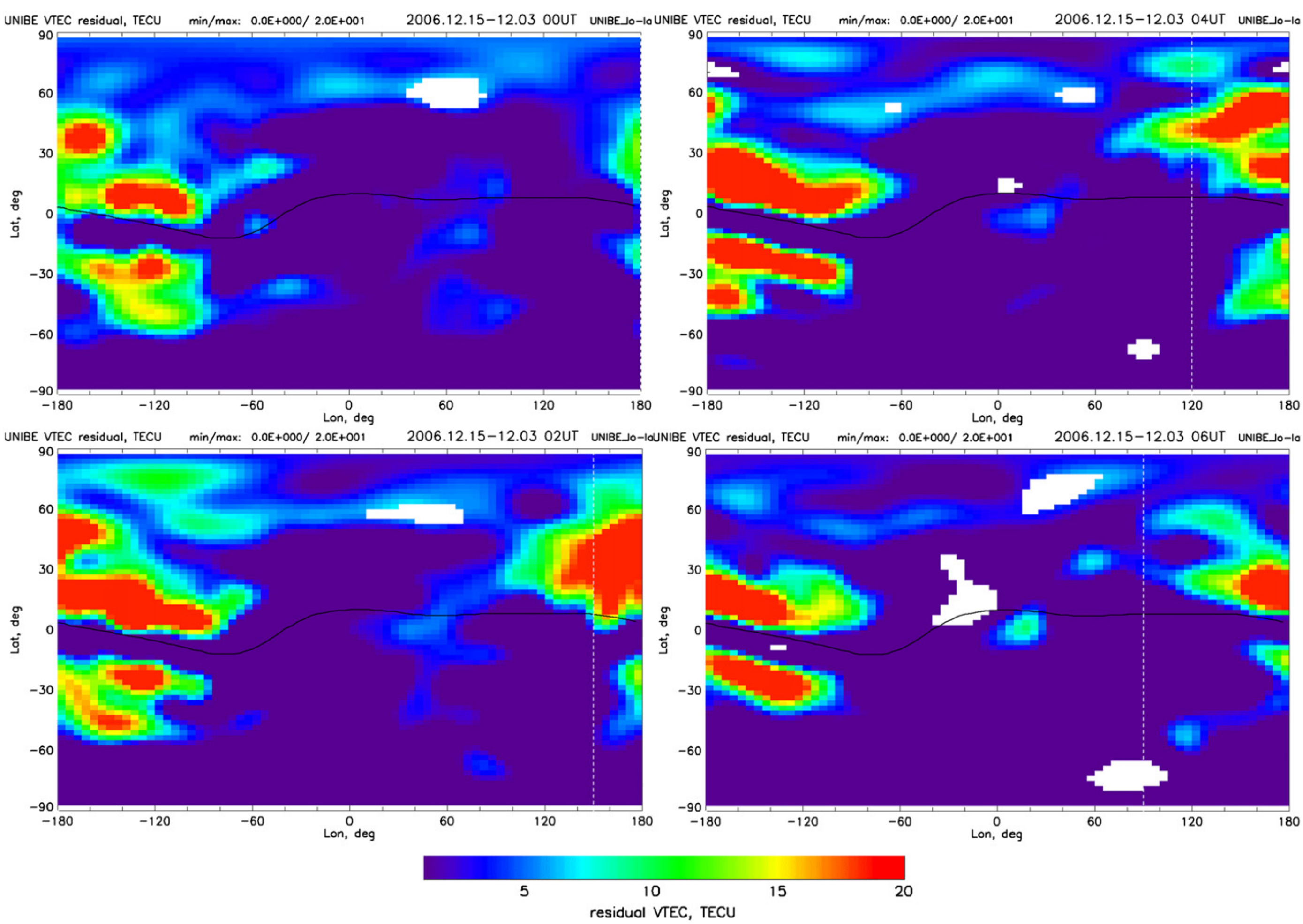

Fig. 1. Global ionospheric maps of residual vertical total electron content (dVTEC) between the quiet day on December 3 and disturbed day on 15 December 2006 at 00–06 UT. Geomagnetic equator is indicated by black curve. Local noon is depicted by vertical white dashed line. Strong positive ionospheric storms are visible as large red spots.

relaxation using red-black smoothing on numerous EC height profiles. This 3-D EC image is used as an initial guess to start the iterative Multiplicative Algebraic Reconstruction Technique (MART) algorithm, and 3-D tomography of the EC is then produced around the whole globe with a time step of 2 h and spatial grid of 5° in longitude, 1° in latitude and 5 km in height (Tsai et al., 2006).

Fig. 2a represents a geographic map of residual total electron content (TEC) at 04–06 UT on 15 December 2006. The TEC is calculated as a height integral of EC provided by the COSMIC/FS3 3-D ionospheric tomography in the range of altitudes below 830 km. Similarly to the GIM dVTEC, the residual TEC is derived by subtraction of the storm-time TEC on 15 December 2006 from the quiet-day TEC on 3 December and expressed in TECU. Comparing Figs. 1 and 2a, one can see a good agreement between the spatial distribution of GIM dVTEC and residual TEC obtained at 04 to 06 UT on 15 December 2006. Note that the magnitudes of residual TEC are slightly smaller than those of GIM dVTEC, probably because the TEC calculation is limited by the height of 830 km.

Fig. 2b shows a meridional cut of EC obtained from COSMIC/FS3 3-D ionospheric tomography at 04 to 06 UT on 15 December

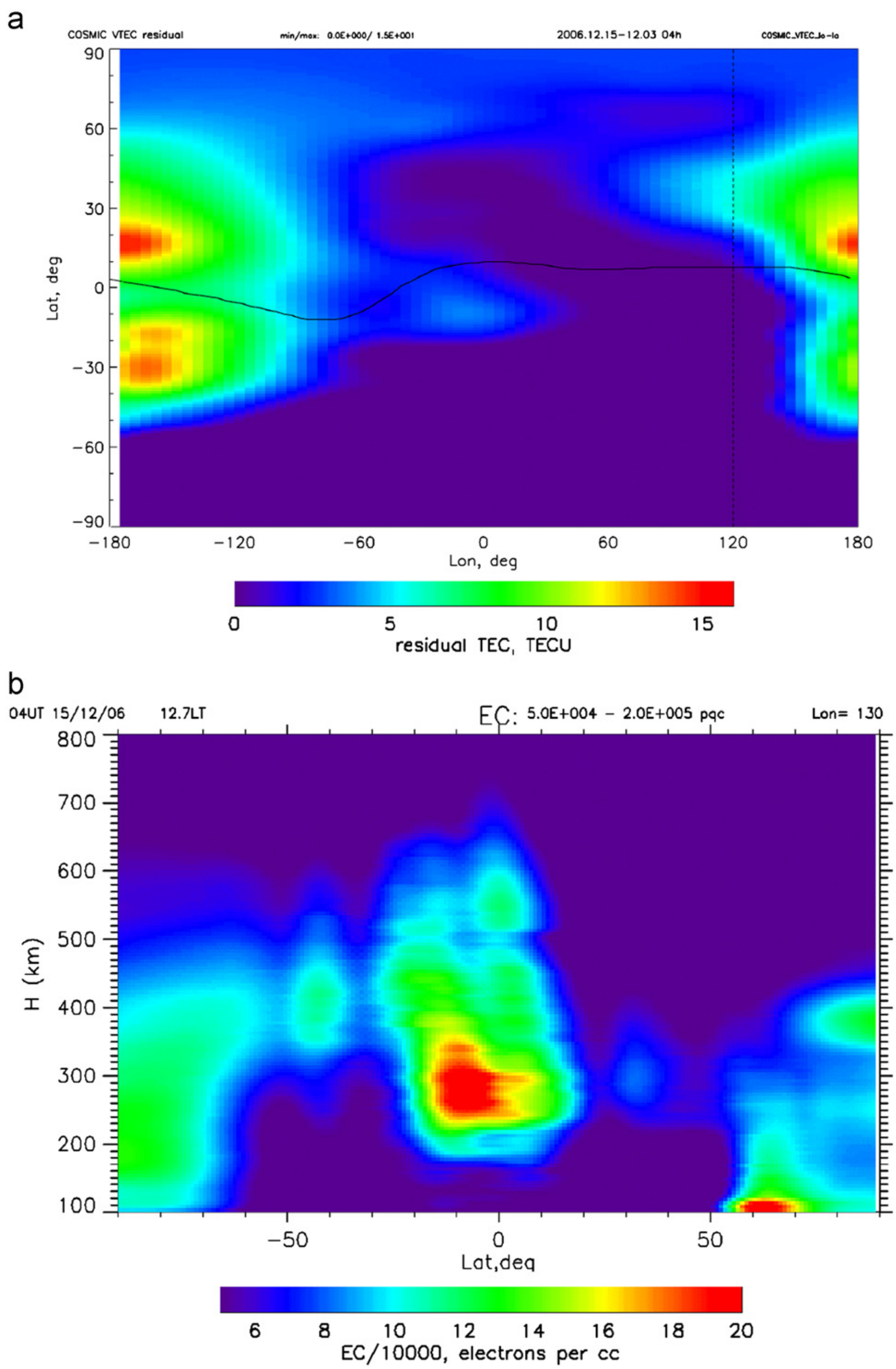

Fig. 2. COSMIC/FS3 3-D tomography of electron concentration (EC) at 04–06 UT on 15 December 2006: (a) geographic map of residual total electron content (TEC) obtained by subtraction of the quiet-day TEC on December 3; (b) meridional cut of EC in the range of longitudes from 130° to 135°. Geomagnetic equator is indicated by the black curve. Local noon is depicted by the vertical black dashed line.

in longitudinal range of 130° to 135°, which is covered well by the measurements. One can see a prominent low-latitude (−20° to 20°) enhancement of EC peaked at 250–300 km. The EC also increases at middle latitudes of ~30°–40° in both southern and northern hemispheres. In the southern hemisphere, the maximum of mid-latitude enhancement is located at height of ~400 km.

It is important to point out that the EC enhancements expand significantly to higher altitudes (up to 600 km and above). Note that similar pattern is revealed at other longitudes above the Pacific region during whole of the main phase and maximum of the geomagnetic storm from 00 to 06 UT. Elevation of the EC to higher altitudes in the equatorial region proves the presence of strong dawn-dusk electric field operating together with the equatorward neutral winds from the higher latitudes (Balan et al., 2010). At middle latitudes, the presence of elevated and widely expanded EC enhancement might indicate to the operation of a magnetospheric mechanism of charged particle contribution to redundant ionization of the mid-latitude ionosphere.

3. Quasi-trapped electrons

Fig. 3 demonstrates geographic distribution of >30 keV electron fluxes observed during magnetically quiet interval and during magnetic storm on 14–15 December 2006. The electrons are measured at altitude of 800 km by a fleet of 5 POES satellites (Huston and Pfitzer, 1998; Evans and Greer, 2004). During magnetic quiet (Fig. 3a), the vast majority of electron population at low altitudes is trapped in the inner radiation belt (IRB). Because of tilted

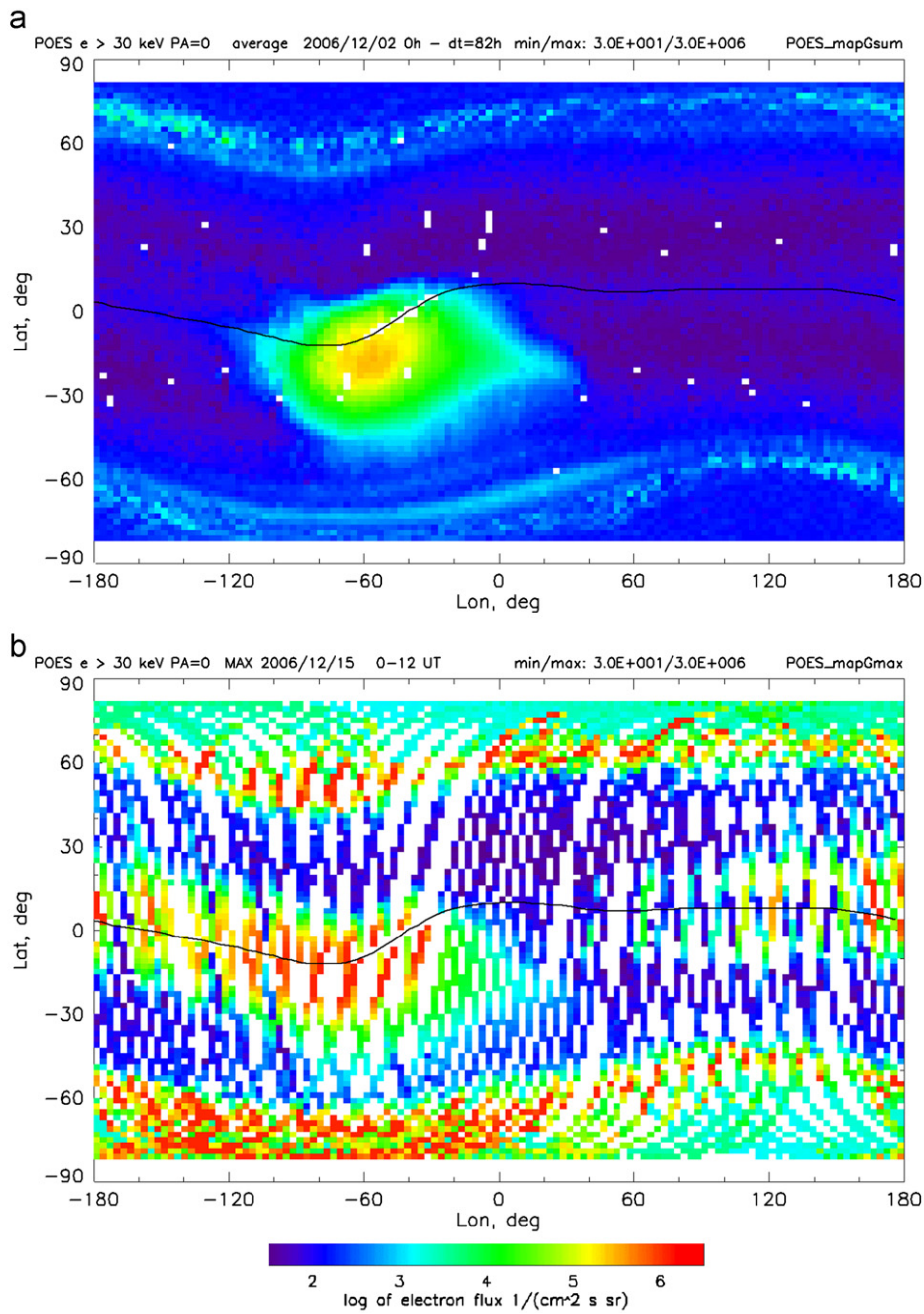

Fig. 3. Geographic distribution of >30 keV electron fluxes detected by a fleet of 5 POES satellites at ~800 km altitude: (a) during magnetic quiet period on 2–4 December, 2006 and (b) during magnetic storm at 00–12 UT on 15 December 2006. Geomagnetic equator is indicated by the black curve.

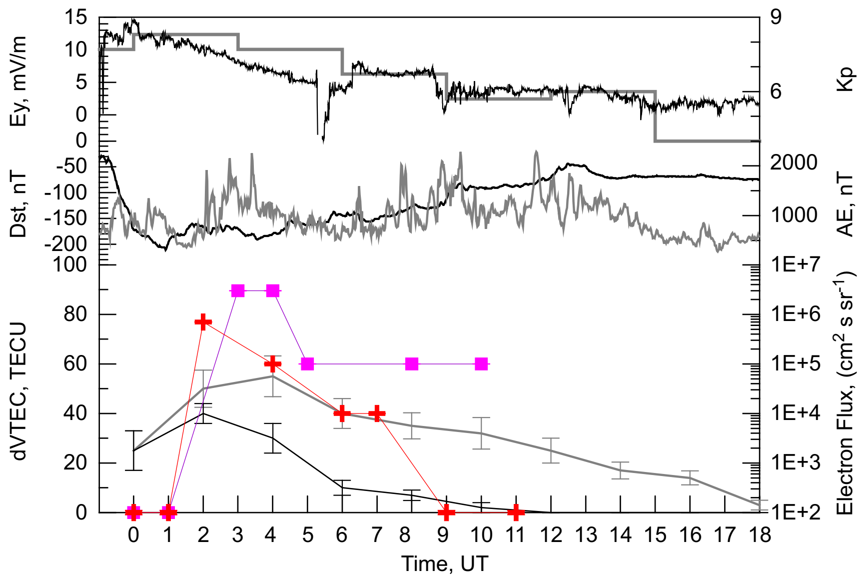

Fig. 4. Variation of the interplanetary electric field *Ey*, geomagnetic indices, fluxes of >30 keV magnetospheric electrons and ionospheric residual VTEC (dVTEC) during magnetic storm from 00 to 18 UT on 15 December (from top to bottom): *Kp*-index (gray) and *Ey* (black); *Dst* (black) and *AE* (gray) indices; electron fluxes at $\sim 120^{\circ}$ longitude (red), at $\sim 180^{\circ}$ (violet), maximum values of dVTEC at middle (black) and low (gray) latitudes (For interpretation of the references to color in this figure legend, the reader is referred to the web version of this article.).

and shifted geomagnetic dipole, the lower edge of IRB sinks to the ionospheric altitudes in the region of South Atlantic Anomaly (SAA) located in the range of longitudes from -120° to 0° and latitudes from -50° to 10°. The fluxes of energetic electrons in the quiet-time SAA are moderate ($<10^5\ \mathrm{cm^{-2}\,s^{-1}\,sr^{-1}}$).

During magnetic storms, the electrons precipitate intensively in a wide longitudinal range from the outer and inner radiation belts to high and to middle latitudes, respectively. As one can see in Fig. 3b, the storm-time fluxes of >30 keV electrons at low and middle latitudes enhance by more than 5 orders of magnitude and exceed 10^6 particles per $\mathrm{cm^2\,s\,sr}$ that might be interpreted as "equatorial aurora". We have to point out that very intense electron fluxes are observed in the forbidden range of drift shells above the Pacific region. Particles, which penetrate in this region are quasi-trapped, because they cannot close the circle of azimuthal drift path around the Earth, but they are inevitably lost in the SAA region. These quasi-trapped particles can produce an additional ionization of the ionosphere, especially at high altitudes where the recombination rate is very low because of very rarefied atmosphere.

Fig. 4 demonstrates temporal dynamics of the quasi-trapped electron fluxes and the strength of ionospheric storms together with variations of geomagnetic indices and interplanetary electric field. We compare maxima of electron fluxes (Fig. 3b) with maxima of dVTEC (Fig. 1). One can clearly see that the intense particle fluxes and positive ionospheric storms appear during maximum of the geomagnetic storm, which is accompanied by very large interplanetary electric field *Ey* of $\sim$5–10 mV/m and strong auroral activity with AE varying from 1000–2000 nT. The electron fluxes are more intense at longitudes of $\sim 180^{\circ}$ than those at longitudes of $\sim 120^{\circ}$. The intense fluxes of quasi-trapped electrons coexist and correlate with the positive ionospheric storm observed at middle latitudes. The low-latitude storm has much longer duration and its maximum occurs later.

4. Discussion and summary

We have demonstrated that the storm-time ionospheric disturbances on 15 December 2006 exhibit two positive storms occurred at low and middle latitudes. The low-latitude positive storm in the IEA crest regions can result from continuous effects of long-lasting daytime eastward PPEF and equatorward neutral wind (Balan et al., 2010). Pedatella et al. (2009) mentioned a positive ionospheric storm observed during that time in the southern hemisphere at geographic latitudes near 50°S above Pacific. This storm was explained by effects of soft particle precipitation associated with an equatorward movement of the poleward boundary of the trough region. However, the origin of positive ionospheric storm at latitudes of $\sim 30^{\circ}$ to 40° is still unclear.

Here we consider the fluxes of quasi-trapped electrons at low latitudes as a possible source of the mid-latitude ionospheric storm. Using POES data on electron fluxes in energy ranges >30 keV, >100 keV and >300 keV, we find that the integral fluxes of electrons with pitch angles about 90° have very steep spectrum, which can be fitted by a power low $F(>E,\ \mathrm{keV}) = 4.7\times10^{13}\,E^{-4.8}\ (\mathrm{cm^2\,s\,sr})^{-1}$. Note that POES also measures fluxes of electrons in the loss cone (pitch angles about 0°). Those fluxes are several-orders weaker than quasi-trapped ones.

From the spectrum, we calculate the electron integral energy flux of $\mathrm{JE} \sim 1.8\times10^{12}\ \mathrm{eV/(cm^2\,s)}$. Using DMSP data on soft electrons in energy range below 30 keV, we find local enhancements of >1keV electrons with integral energy fluxes up to $\mathrm{JE} \sim 10^{12}\ \mathrm{eV/(cm^2\,s)}$. Hence, the total integral energy flux of electrons can be estimated to be $\sim 2.8\times10^{12}\ \mathrm{eV/(cm^2\,s)}$ that is equivalent to $4.5\times10^{-3}\ \mathrm{W\,m^{-2}}$. Note that this energy flux is comparable to that produced by X-class strong solar flares, which ionospheric impact can achieve $\sim$20 TECU (e.g. Tsurutani et al., 2005). In the ionosphere, enriched by oxygen with first ionization potential of 13.6 eV, this integral energy flux produces 2.1×10^{11} ion-electron pairs per $\mathrm{cm^2\,s}$. In the topside ionosphere, the recombination rate of electrons decreases fast with atmospheric density and can be estimated to be $\sim 10^{-2}\ \mathrm{s^{-1}}$. Hence, the total electron content produced by the quasi-trapped electrons can be estimated to be $\sim 2.1\times10^{13}\ \mathrm{cm^{-2}}$, i.e. $\sim$20 TECU.

Further, we have to estimate the spatial region where the electrons lose their energy in ionization of the atmospheric atoms. A precipitating electron with energy of $\sim$30 keV and zero pitch angle is able to reach altitudes of $\sim$90 km (e.g. Dmitriev et al., 2010). However, from POES observations we find that a vast majority of the electrons is quasi-trapped and has pitch angles close to 90°. Such electrons are bouncing along the magnetic field lines about top points (of the field line). This bouncing motion is very fast and has a period of a portion of second.

Because of asymmetrical orientation of the geomagnetic dipole, the height of top points varies with longitude. Fig. 5 shows longitudinal variation of the height of drift shells (L-shells) calculated for the geomagnetic equator using IGRF model of epoch 2005. Participating in a gradient drift, energetic electrons move eastward along the drift shells. One can see that the L-shells are descending starting from the region of Indochina at longitudes of ~120°. In this region, the height of ~900 km corresponds to the $L \sim 1.05$. Above the Pacific region, the altitude of top points for bouncing electron decreases with increasing longitude. The drift shells reach minimal heights in the SAA region, where practically all the particles quasi-trapped at $L < 1.1$ are lost. At altitudes of 1000 km and below, the period of the azimuthal drift for 30 keV electrons is ~20 h (Lyons and Williams, 1984). Hence, the electrons with large pitch angles can make many thousands of bounces before they are lost in the SAA region.

Taking into account the specific ionization of electrons (the energy loss per unit distance) and standard vertical profile of the upper atmosphere (e.g. Dmitriev et al., 2008), we can calculate the number of bounces between the top point at 800 km and mirror points at height Hmin until the ~30 keV electron has lost whole of the energy in ionization. By this way, we find that for Hmin below 600 km, the ~30 keV electrons lost whole energy within ~2 h. During this time, the electrons pass eastward no more than ~30° in longitudes, because of very slow azimuthal drift. Hence, the quasi-trapped electrons, observed westward from the longitude of −150°, have a quite high chance to lose whole of their energy in ionization of the ionosphere. Because of arched magnetic field configuration, this ionization is released in the region of geomagnetic latitudes above ~20°. It is important to note that the charged particle spend most of the time in vicinity of the mirror point. Hence, the quasi-trapped electrons lose most of energy rather at low to middle latitudes than at the equator. That corresponds well to the spatial location of mid-latitude positive ionospheric storm.

Another important issue is conditions required for the downward transport of electrons from the IRB to the heights below 1000 km. The well-know mechanism is a radial diffusion across the drift shells. However, in the strong magnetic field at low altitudes this diffusion is very slow that results in very weak fluxes of energetic electrons at the forbidden drift shells at low latitudes. In contrast, geomagnetic storms are accompanied by a very strong penetrated electric field of dawn–dusk direction. In the nightside, this electric field is pointed westward that results in fast (a few hours) $E \times B$ drift of particles across the magnetic field lines toward the Earth. Then the electrons drift eastward through the morning sector toward noon.

We can summarize that during magnetic storm, the energetic electrons (~30 keV) drift fast radially from the IRB to the ionospheric altitudes in the nightside sector. Drifting azimuthally eastward, the quasi-trapped electrons lose the energy in ionization of the atmospheric gases and, thus, produce abundant ionization of the mid-latitude ionosphere.

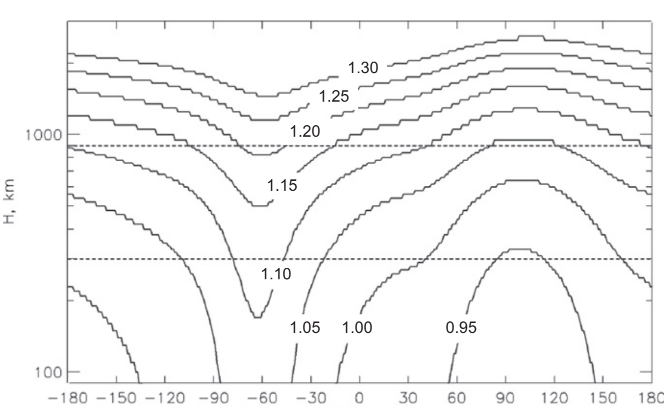

Fig. 5. Longitudinal variation of the height of various drift shells at geomagnetic equator calculated from IGRF model for epoch of 2005. Quasi-trapped energetic electrons drift eastward along the drift shells and pass the highest (lowest) heights in the Indochina (SAA) region. Horizontal dashed lines indicate the heights of 300 km and 900 km.

Acknowledgments

The authors thank a team of NOAA's Polar Orbiting Environmental Satellites for providing experimental data about energetic particles and Kyoto World Data Center for Geomagnetism (http://wdc.kugi.kyoto-u.ac.jp/index.html) for providing the Dst, Kp and AE geomagnetic indices. The Global Ionosphere Maps/VTEC Data from European Data Center was obtained through ftp://ftp.unibe.ch/aiub/CODE/. The ACE solar wind data were provided by N. Ness and D.J. McComas through the CDAWeb website. We acknowledge Dr. Patrick Newell for help with providing DMSP data. The DMSP particle detectors were designed by Dave Hardy of AFRL, and data obtained from JHU/APL. This work was supported by grant NSC 99-2811-M-008-093 and Ministry of Education under the Aim for Top University program at NCU of Taiwan #985603-20.

References

Biktash, L., 2004. Role of the magnetospheric and ionospheric currents in generation of the equatorial scintillations during geomagnetic storms. Annales Geophysicae 22, 3195–3202.

Balan, N., Shiokawa, K., Otsuka, Y., Kikuchi, T., Vijaya Lekshmi, D., Kawamura, S., Yamamoto, M., Bailey, G.J., 2010. A physical mechanism of positive ionospheric storms at low latitudes and midlatitudes. Journal of Geophysical Research 115, A02304. doi:10.1029/2009JA014515.

Balan, N., Yamamoto, M., Liu, J.Y., Otsuka, Y., Liu, H., Luhr, H., 2011. New aspects of thermospheric and ionospheric storms revealed by CHAMP. Journal of Geophysical Research 116, A07305. doi:10.1029/2010JA016399.

Dmitriev, A.V., Tsai, L.-C., Yeh, H.-C., Chang, C.-C., 2008. COSMIC/FORMOSAT-3 tomography of SEP ionization in the polar cap. Geophysical Research Letters 35, L22108. doi:10.1029/2008GL036146.

Dmitriev, A.V., Jayachandran, P.T., Tsai, L.-C., 2010. Elliptical model of cutoff boundaries for the solar energetic particles measured by POES satellites in December 2006. Journal of Geophysical Research 115, A12244. doi:10.1029/2010JA015380.

Evans, D.S., Greer, M.S., Polar Orbiting Environmental Satellite Space Environment Monitor: 2. Instrument Descriptions and Archive Data Documentation, Technical Memorandum version 1.4, NOAA Space Environment Laboratory, Boulder, CO, USA, 2004.

Hajj, G.A., Lee, L.C., Pi, X., Romans, L.J., Schreiner, W.S., Straus, P.R., Wang, C., 2000. COSMIC GPS ionospheric sensing and space weather. Terrestrial Atmospheric and Oceanic Sciences 11 (1), 235–272.

Huston, S.L., Pfitzer, K.A., 1998. Space Environment Effects: Low-Altitude Trapped Radiation Model, NASA/CR-1998-208593. Marshall Space Flight Center, Huntsville, AL, USA.

Lyons, L.R., Williams, D.J., 1984. Quantitative Aspects of Magnetospheric Physics. D. Reidel Pub. Co., Dordrecht Boston.

Lei, J., Burns, A.G., Tsugawa, T., Wang, W., Solomon, S.C., Wiltberger, M., 2008. Observations and simulations of quasiperiodic ionospheric oscillations and large-scale traveling ionospheric disturbances during the December 2006 geomagnetic storm. Journal of Geophysical Research 113, A06310. doi:10.1029/2008JA013090.

Mendillo, M., 2006. Storms in the ionosphere: Patterns and processes for total electron content. Reviews of Geophysics 44, RG4001. doi:10.1029/2005RG000193.

Mendillo, M., Wroten, J., Roble, R., Rishbeth, H., 2010. The equatorial and low-latitude ionosphere within the context of global modeling. Journal of Atmospheric and Solar-Terrestrial Physics 72, 358–368. doi:10.1016/j.jastp.2009.03.026.

Pedatella, N.M., Lei, J., Larson, K.M., Forbes, J.M., 2009. Observations of the ionospheric response to the 15 December 2006 geomagnetic storm: long-duration positive storm effect. Journal of Geophysical Research 114, A12313. doi:10.1029/2009JA014568.

Tsai, L.-C., Tsai, W.H., Chou, J.Y., Liu, C.H., 2006. Ionospheric tomography of the reference GPS/MET experiment through the IRI model. Terrestrial Atmospheric and Oceanic Sciences 17, 263–276.

Tsurutani, B.T., et al., 2005. The October 28, 2003 extreme EUV solar flare and resultant extreme ionospheric effects: comparison to other Halloween events and the Bastille day event. Geophysical Research Letters 32. doi:10.1029/2004GL021475L03S09. doi:10.1029/2004GL021475.

Wei, Y., Hong, M., Pu, Z., et al., 2011. Responses of the ionospheric electric field to the sheath region of ICME: a case study. Journal of Atmospheric and Solar-Terrestrial Physics 73, 123–129. doi:10.1016/j.jastp.2010.03.004.

Earth Planets Space, **64**, 545–551, 2012

A comparison of a model using the FORMOSAT-3/COSMIC data with the IRI model

Yoshihiro Kakinami[1]*, Jann-Yenq Liu[1,2], and Lung-Chih Tsai[2]

[1]*Institute of Space Science, National Central University, No. 300 Jhongda Rd. Jhongli, Taoyuan 32001, Taiwan*
[2]*Center for Space and Remote Sensing Research, National Central University, No. 300 Jhongda Rd. Jhongli, Taoyuan 32001, Taiwan*

(Received August 18, 2010; Revised January 4, 2011; Accepted October 8, 2011; Online published July 27, 2012)

In this study, an empirical model constructed using data of FORMOSAT3/COSMIC (F3/C) from 29 June, 2006, to 17 October, 2009, retrieves altitude profiles of electron density (N_e). The model derives global N_e profiles from 150 to 590 km altitude as functions of the solar EUV flux, day of year, local time and location under geomagnetically quiet conditions ($K_p < 4$). N_e profiles derived by the model are further compared with those of the International Reference Ionosphere (IRI). Results show that the F_2 peak altitude h_mF_2 and the electron density N_mF_2, as well as the electron density above, derived by the model are lower than those of the IRI model. The F3/C model reproduces observations of F3/C well at 410-km altitude while the IRI model overestimates them. The overestimation of the IRI model becomes large with decrease of EUV flux. It is found that the topside vertical scale height of the F3/C model shows high values not only magnetic dip equator but also middle latitude. The results differ significantly from those of IRI, but agree with those observed by topside sounders, Alouette and ISIS satellites.
Key words: IRI, electron density, topside ionosphere, empirical model, FORMOSAT-3/COSMIC, vertical scale height.

1. Introduction

The International Reference Ionosphere (IRI) has been developed since 1978 (Rawer *et al.*, 1978) and is established as the most standard and reliable ionospheric empirical model. Since a large amount of ionosonde data has been used, IRI derives a relatively accurate electron density (N_e) profile below the F_2 peak. However, the IRI model might still have some shortcomings in the topside ionosphere, because very limited satellite data are included. Bilitza (2004) and Bilitza *et al.* (2006) based on Alouette/ISIS topside sounder observations reported that the IRI model overestimates N_e above the F_2 peak height. Furthermore, Kakinami *et al.* (2008) found an in-situ N_e observation at a 600-km altitude with the Hinotori satellite which differed from the IRI N_e. This shortcoming also results in a difference between the Total Electron Content (TEC) reproduction and real observations, because the TEC is calculated using an integration of the N_e profile. Meanwhile, the IRI model overestimates the TEC in the equatorial region (Bilitza and Williamson, 2000) during high solar activity, while the IRI model overestimates and underestimates the TEC over Taiwan (24°N 120°E) during low and high solar activity, respectively (Kakinami *et al.*, 2009).

Six FORMOSAT-3/COSMIC (F3/C) micro satellites which constituted a global positioning system (GPS) occultation experiment (GOX) payload were launched on 14 April, 2006, and put into a low Earth orbit of 800-km altitude with a 72° inclination. An average of 1800 electron density profiles was obtained in a day globally. Lei *et al.* (2007) reported that N_e profiles measured with F3/C are consistent with N_mF_2 and h_mF_2 obtained with incoherent scatter radars at Millstone Hill and Jicamarca. An N_e profile obtained using GOX has an advantage in its coverage of observations, compared with the peak density and peak altitude of the ionosphere obtained with ground-based observations, because it was able to cover ocean and desert areas, where there are usually no receivers. Taking advantage of this feature, we have constructed an empirical model of the N_e profile measured with F3/C, which reproduces the N_e profile globally. In this paper, we describe the methodology in constructing the model and compare the empirical model based on F3/C observations with the IRI model.

2. Methodology of the Construction of an Empirical Model

The methodology of constructing an empirical model based on F3/C data is described in this section. Henceforth, the empirical model based on N_e profiles obtained by F3/C is referred to as the F3/C model. The F3/C model reproduces N_e as functions of the solar EUV flux, day of year (DOY), local time (LT), altitude and location. A similar methodology has been applied to empirical models of transition height (Marinov *et al.*, 2004; Kutiev and Marinov, 2007), vertical scale height in the top-

*Now at Institute of Seismology and Volcanology, Hokkaido University, Kita 10 Nishi 8, Kita-ku, Sapporo 060-0810, Japan.

doi:10.5047/eps.2011.10.017

side ionosphere (Kutiev *et al.*, 2006) and TEC over Taiwan (Kakinami *et al.*, 2009). Daily EUV (0.1–50 nm) measured by the Solar Heliospheric Observatory (SOHO) (Judge *et al.*, 1998) and posted on the web site of the Space Science Center of the University of Southern California (http://www.usc.edu/dept/space_science/), is used to construct the model. The released EUV fluxes are modified using the Sun-Earth distance because the released daily EUV fluxes are adjusted at 1 AU. Data are not used in the model construction when the EUV exceeds 10^{11} photon/cm^2 sec due to a solar flare. The EUV variation used in the F3/C model, which is excluded the fluctuated day, is shown in Fig. 1. Observed N_{e} profiles are accumulated under geomagnetically quiet conditions ($K_{\mathrm{p}} < 4$) from 29 June, 2006, to 17 October, 2009. Since N_{e} profiles are calculated using the Abel inversion with an assumption of spherical symmetry, the errors mainly appear below 250 km around the equatorial ionization anomaly region (Liu *et al.*, 2010), which leads to a negative value of the N_{e} profile in some cases. Therefore, observed N_{e} profiles showing a negative value are not used in the model construction. At first, the empirical model which has functions of EUV, DOY and LT is constructed in each 3-dimensional bin whose size is 30° in longitude, 18° in latitude and 20 km (40 km) altitude between 150 and 390 (390 and 590) km altitude with steps of 10° in longitude and 6° in latitude. It is assumed that the solar flux variation of $\log_{10}(N_{\mathrm{e}})$ is proportional to the EUV flux, while the DOY and LT variation of $\log_{10}(N_{\mathrm{e}})$ are derived using a combination of trigonometric functions of wavenumbers 1–3 and 1–4, respectively. The modeled functions are calculated for each bin. The functions for F, DOY and LT are defined as follows:

$$f(\mathrm{EUV}) = a_1 + a_2\mathrm{EUV}, \tag{1}$$

$$\begin{aligned} g(\mathrm{DOY}) &= b_1 + \sum_{i=1}^{3}(b_{2i}\cos 2\pi i\cdot\mathrm{DOY} \\ &\qquad + b_{2i+1}\sin 2\pi i\cdot\mathrm{DOY}) \\ &= b_1 g'_1 + \cdots + b_7 g'_7, \end{aligned} \tag{2}$$

$$\begin{aligned} h(\mathrm{LT}) &= c_1 + \sum_{i=1}^{4}\left(c_{2i}\cos\frac{\pi i\cdot\mathrm{LT}}{12} + c_{2i+1}\sin\frac{\pi i\cdot\mathrm{LT}}{12}\right) \\ &= c_1 h'_1 + \cdots + c_9 h'_9, \end{aligned} \tag{3}$$

where a, b, c are coefficients for fitting. DOY is normalized by the length of the year. The function reproducing N_{e} is assumed to be the product of these 3 functions. Then we can obtain:

$$\begin{aligned} \log_{10} N_{\mathrm{e}}(\mathrm{EUV}, \mathrm{DOY}, \mathrm{LT}) &= f(\mathrm{EUV})\cdot g(\mathrm{DOY})\cdot h(\mathrm{LT}) \\ &= \sum_{i,j,k} a_i f'_i \cdot b_j g'_j \cdot c_k h'_k \\ &= \sum_{n=1}^{126}\alpha_n \log_{10} N'_{\mathrm{e}n}, \end{aligned} \tag{4}$$

where $n = (i-1)\times 63 + (j-1)\times 9 + k$, $i = 1, 2$, $j = 1, \ldots, 7$, $k = 1, \ldots, 9$. In order to calculate the coefficients α, more than 126 data are required. The α can be obtained by solving the following normal-equation matrix:

$$\begin{pmatrix} \sum \log_{10} N_{\mathrm{e}}\cdot\log_{10} N'_{\mathrm{e}1} \\ \vdots \\ \sum \log_{10} N_{\mathrm{e}}\cdot\log_{10} N'_{\mathrm{e}126} \end{pmatrix} = \begin{pmatrix} \sum \log_{10} N'_{\mathrm{e}1}\cdot\log_{10} N'_{\mathrm{e}1} & \cdots & \sum \log_{10} N'_{\mathrm{e}1}\cdot\log_{10} N'_{\mathrm{e}126} \\ \vdots & \ddots & \vdots \\ \sum \log_{10} N'_{\mathrm{e}126}\cdot\log_{10} N'_{\mathrm{e}1} & \cdots & \sum \log_{10} N'_{\mathrm{e}126}\cdot\log_{10} N'_{\mathrm{e}126} \end{pmatrix}\begin{pmatrix} \alpha_1 \\ \vdots \\ \alpha_{126} \end{pmatrix}. \tag{5}$$

The α are calculated in each 3-dimensional bin. Finally, the modeled N_{e} is obtained by linearly interpolating between the bins.

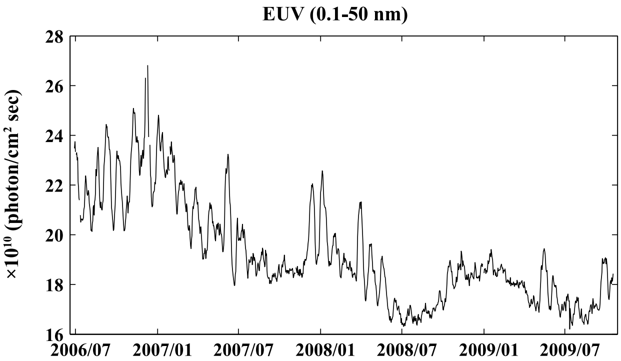

Fig. 1. EUV variation observed with SOHO from 29 June, 2006, to 17 October, 2009. Only data used in the construction of the F3/C model are shown.

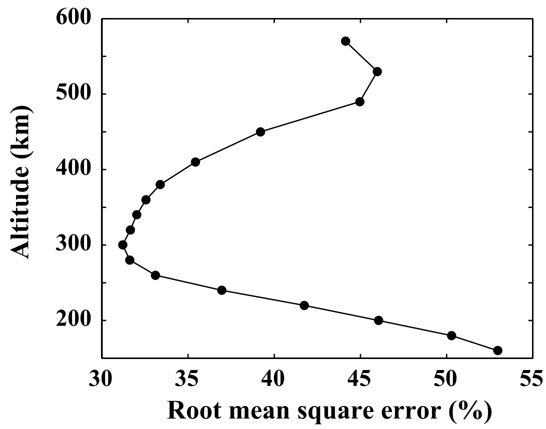

Fig. 2. Variation of root mean square error of the F3/C model with altitude.

3. Results and Discussion

In order to estimate the accuracy of the F3/C model, the root-mean-square error (RMS) is calculated as follows,

$$\mathrm{RMS} = \sqrt{\frac{1}{n}\sum_{i=1}^{n}\{(o_i - m_i)/m_i\}^2}, \tag{6}$$

where n, o_i, m_i, denote the data number, the N_{e} observed with F3/C, and the N_{e} derived by the F3/C model, respectively. RMSs at each altitude level are displayed in Fig. 2. The RMS is over 50% below 200 km while the RMS decreases with increasing altitude, and shows a minimum

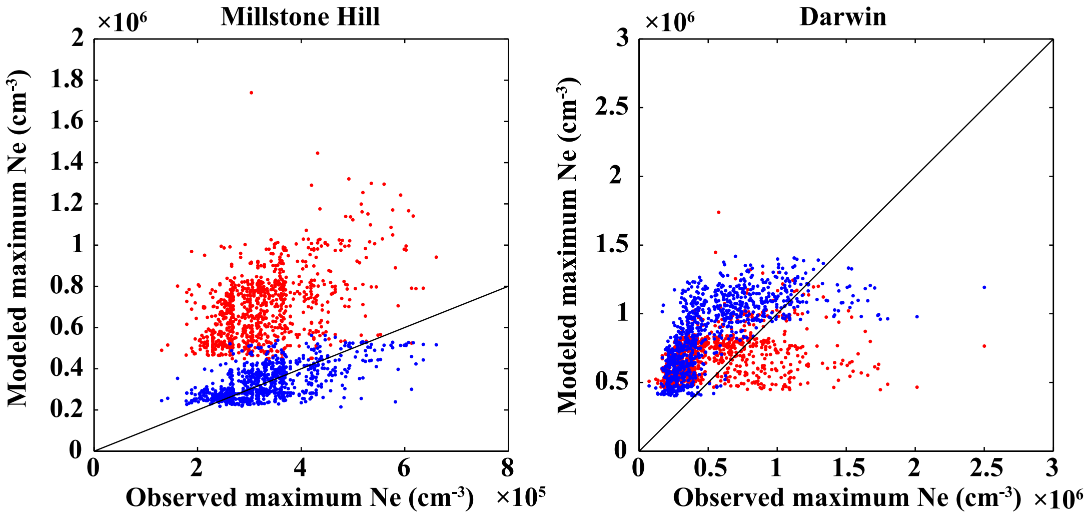

Fig. 3. Comparison of peak electron density derived by the F3/C model and the IRI model with ionosonde observations at 1200 LT at Millstone Hill (left) and Darwin (right) from 29 June, 2006, to 17 October, 2009. Red and blue dots indicate the F3/C and the IRI model results.

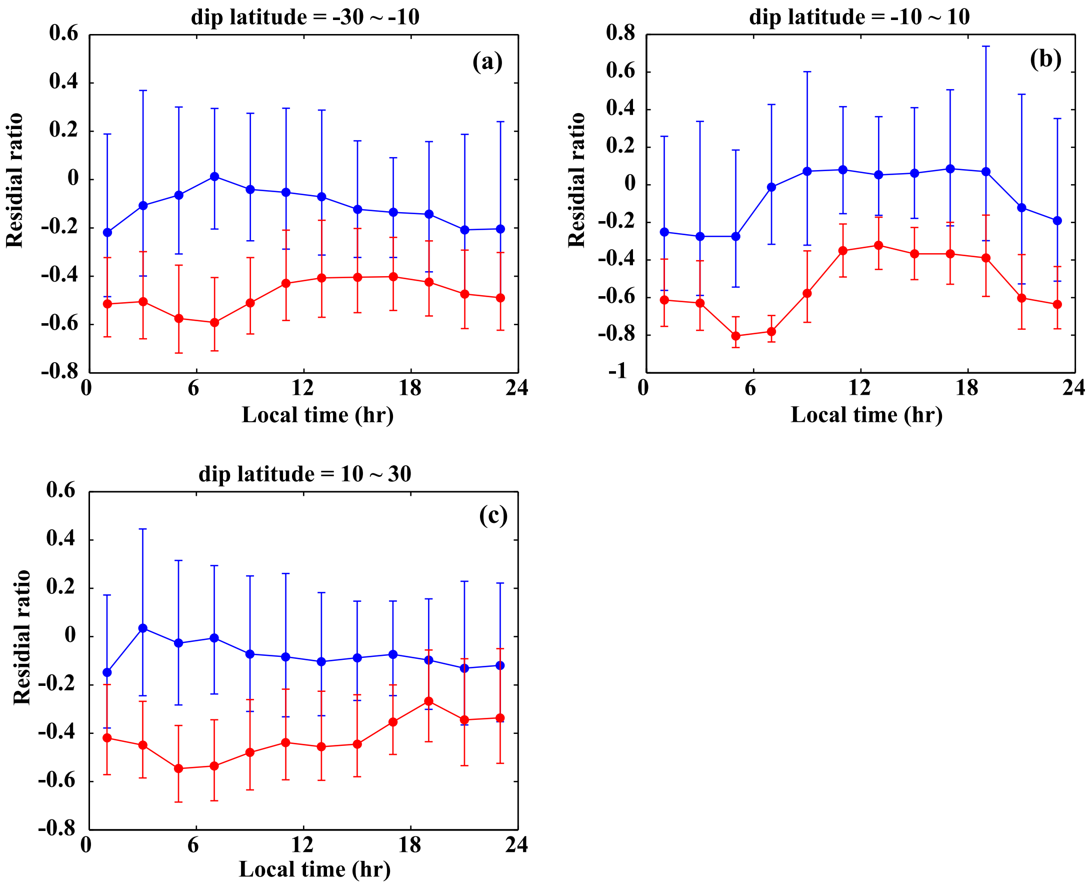

Fig. 4. Local time variation of the residual ratios for the F3/C (blue) and IRI (red) models in (a) dip latitude $= -30 \sim -10$, (b) dip latitude $= -10 \sim 10$ and (c) dip latitude $= 10 \sim 30$. Dots and error bars denote median and quartiles.

value at 300 km. The RMS increases with increasing altitude over 300 km and reaches about 45% around 500 km. Below 250 km, the estimation error of the N_e profile is very large due to the fundamental issue of the Abel inversion (Liu *et al.*, 2010), and the data used in the construction have inherent errors. Such errors might produce a high dispersion and show high RMS. On the other hand, since a similar high variability is seen in the N_e model using the HINOTORI data at 600 km (Kakinami *et al.*, 2008), the dispersion of N_e might be high above 400 km.

The peak N_e calculated with the F3/C model are compared with those measured with ionospondes (Millstone Hill at 71.5°W, 42.6°N and Darwin at 131.0°E, 12.7°S) and IRI2007 with standard options (henceforth, we use the same IRI version) from 29 June, 2006, to 17 October, 2009, under geomagnetically quiet conditions, $K_p < 4$ (Fig. 3). The

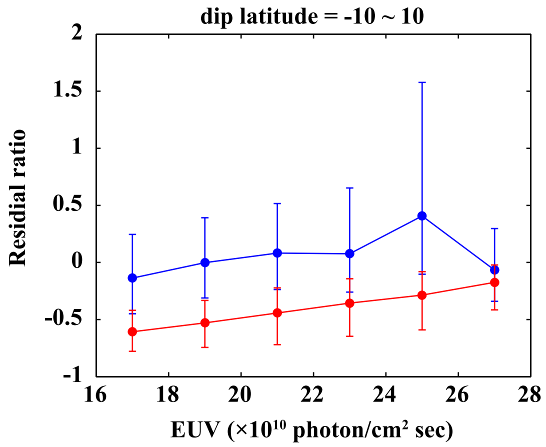

Fig. 5. Solar flux variation of the residual ratios for the F3/C (blue) and IRI models (red) in dip latitude = −10 ∼ 10. Dots and error bars denote median and quartiles.

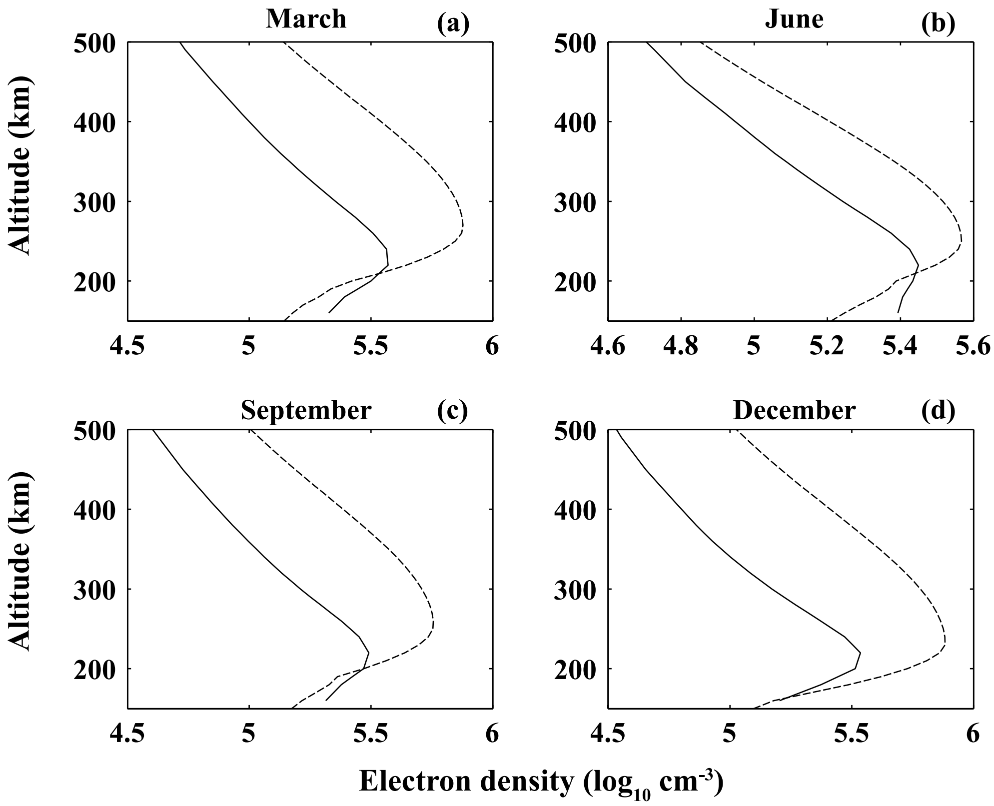

Fig. 6. Electron density profiles derived by the F3/C (solid line) and IRI models (dashed line) at 42.5°N 288.5°E at 1200 LT in March (a), June (b), September (c) and December (d). Intensities of EUV applied to calculations are 1.99, 1.99, 1.84 and 2.20 × 10^{11} photon/cm^2 sec, which are the actual conditions of solar flux in each month of 2007.

results with IRI match the observations at Millstone Hill, while those with the F3/C model overestimate the observations. Meanwhile, both models overestimate at Darwin in many cases. This result indicates that the reproduction of peak density by the IRI also has shortcomings at some locations.

In order to compare the observed N_e using F3/C with the F3/C and IRI model, residual ratios, $(o_i - m_i)/m_i$, where o_i and m_i denote the observed N_e at 410 km and the modeled N_e at 410 km, are calculated. Figure 4 displays the local time variation of the residual ratios for the F3/C and IRI models. Though the F3/C model slightly overestimates the observations by 10–20% during night time in all latitudes, the F3/C model agrees with the observations on the whole. However, the IRI model always overestimates observations by 40–60% at all local times and latitudes. Figure 5 shows the solar flux variation of the residual ratios for the F3/C and IRI models. The F3/C model shows a good agreement with the observations except for EUV $> 24 \times 10^{10}$ photon/cm^2 sec. As shown in Fig. 1, since the data number for EUV $> 24 \times 10^{10}$ photon/cm^2 sec is very small, the reliability of the F3/C model is less than that for EUV $< 24 \times 10^{10}$ photon/cm^2 sec. On the other hand, the IRI model overestimates the observations

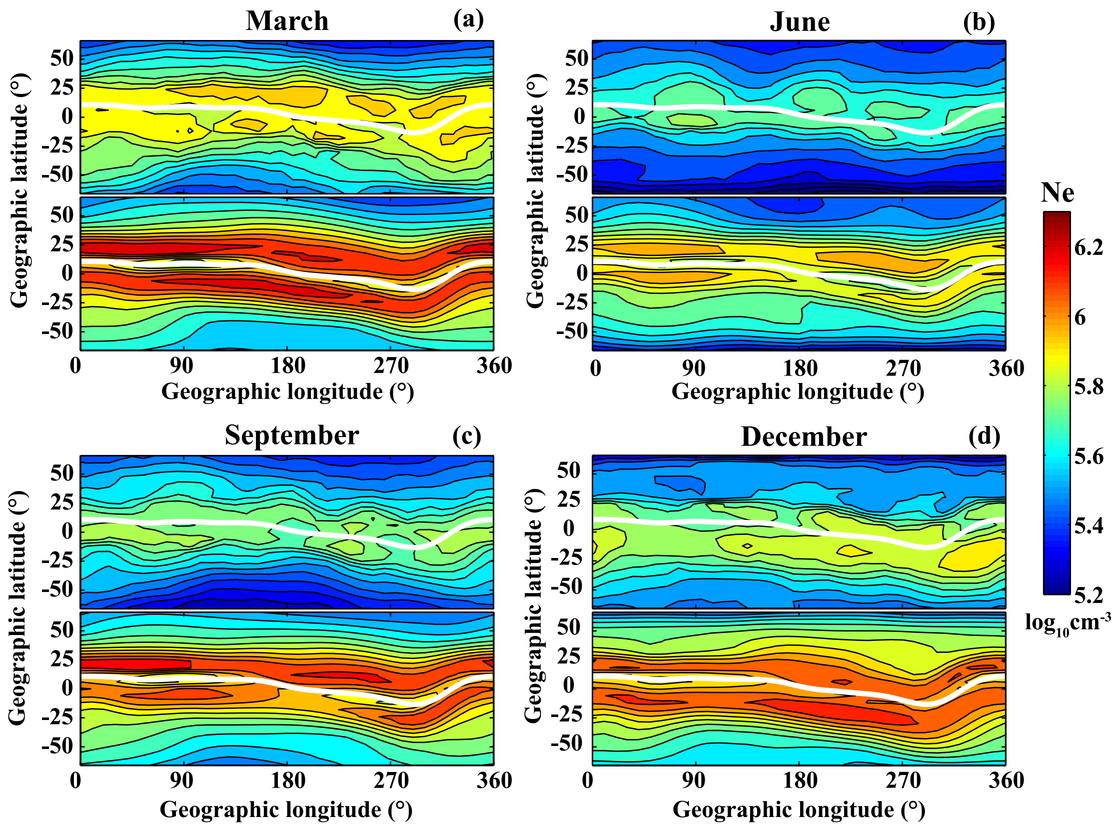

Fig. 7. Peak electron density maps derived by F3/C (top) and IRI model (bottom) at 1200 LT in March (a), June (b), September (c) and December (d). White curves indicate magnetic equator. Intensities of EUV applied to calculations are the same as Fig. 6.

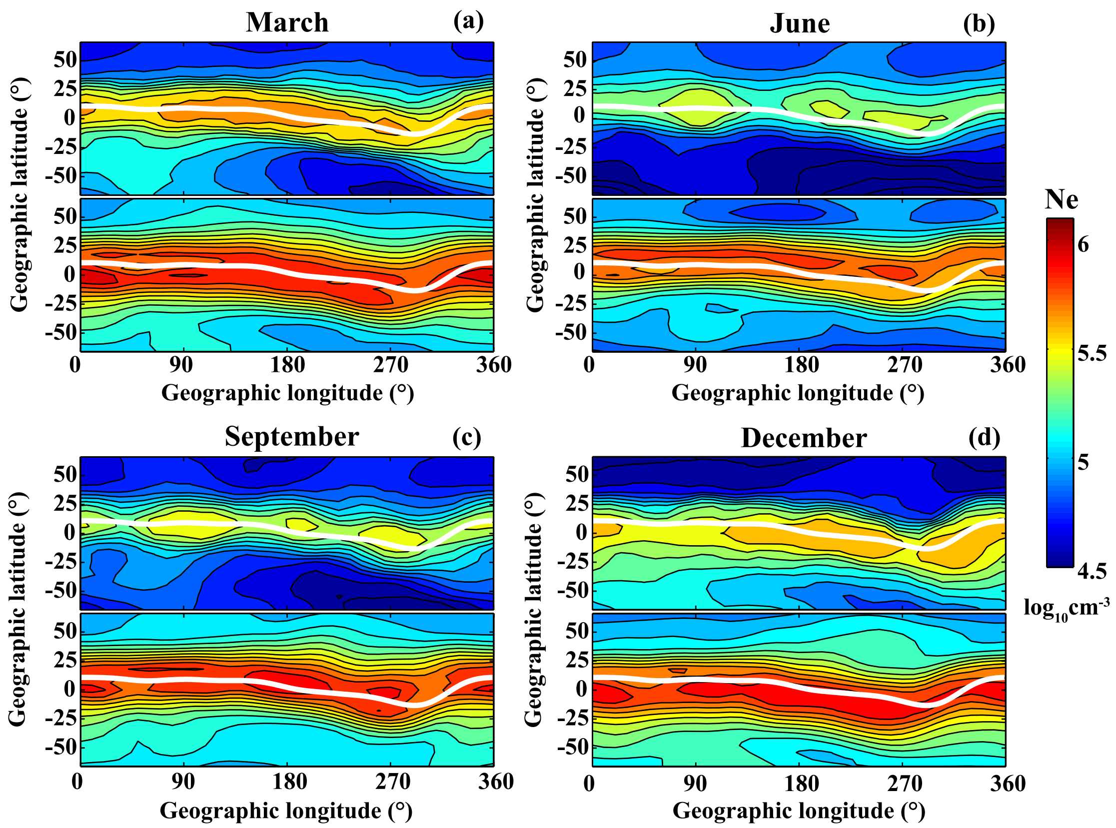

Fig. 8. Electro density maps at 450 km derived by F3/C (top) and IRI model (bottom) at 1200 LT in March (a), June (b), September (c) and December (d). White curves indicate magnetic equator. Intensities of EUV applied to calculations are the same as Fig. 6.

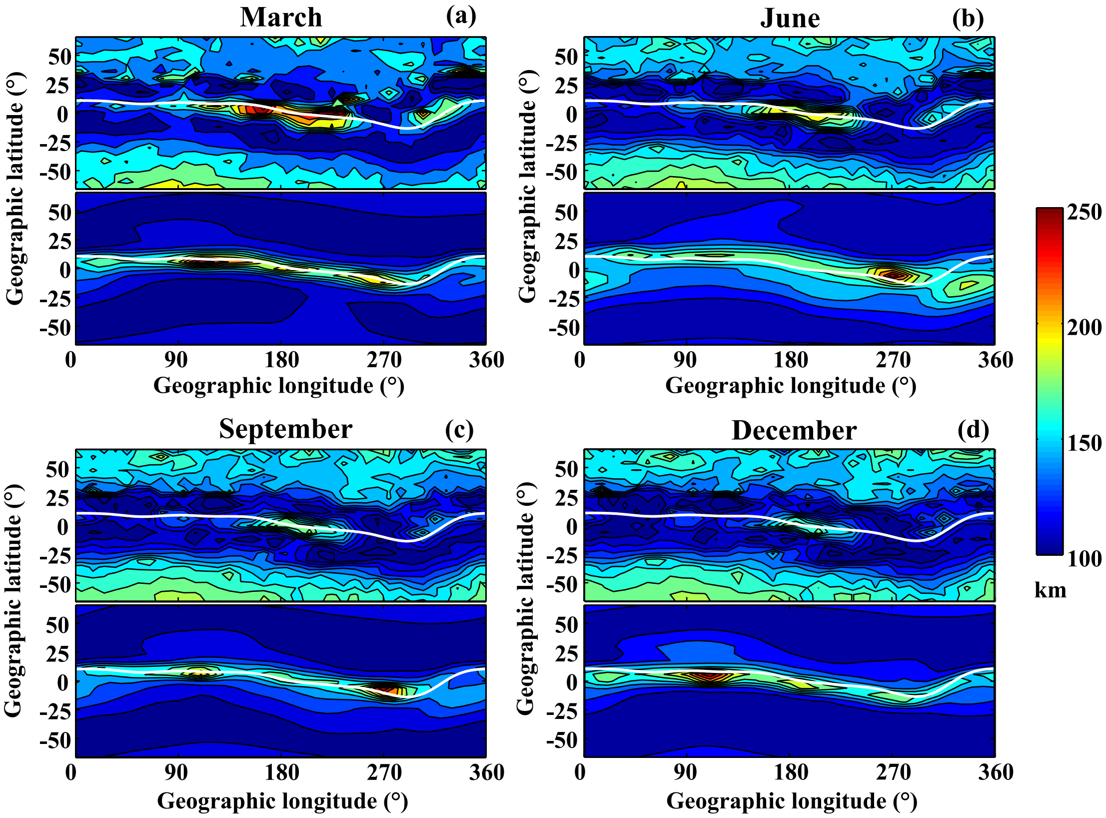

Fig. 9. Vertical scale height at 450 km derived by the F3/C model (top) and IRI model (bottom) at 1200 LT in March (a), June (b), September (c) and December (d). White curves indicate magnetic equator. Intensities of EUV applied in the calculations are the same as Fig. 6.

when EUV is low. The accuracy of the IRI model improves with an increase of EUV. This tendency of the IRI model to solar flux is similar to that of TEC over Taiwan (Kakinami *et al.*, 2009).

The altitude profile of N_e derived by the F3/C and the IRI models above Inamori Hall, Kagoshima University (42.5°N 288.5°E), where the IRI 2009 workshop was held, are shown in Fig. 6. The N_e derived by the IRI model is higher than that of the F3/C model at, and above the peak height in all seasons as shown in Figs. 4 and 5. In addition, the peak altitude h_mF_2 derived by the IRI model is higher than that of the F3/C model in all seasons. The vertical scale height (VSH) of the IRI model, which is defined as $-dh/d(\ln N_e)$ (Kutiev *et al.*, 2006), is slightly lower than that of the F3/C model in June. The N_e derived by IRI is lower than that of the F3/C model in the lower ionosphere in all seasons except December.

Figure 7 shows the seasonal variation of peak N_e (N_mF_2) at 1200 LT derived by the F3/C (top panel) and the IRI (bottom panel) models. The maximum of N_mF_2 is located beside the magnetic equator for both models. N_mF_2 derived by IRI is higher than that of the F3/C model in all seasons. A longitudinal structure of N_mF_2 exists in both models. Small patch-like maxima of N_mF_2 appear in the F3/C model, while wide-longitude-range maxima of N_mF_2 appear in IRI in March (Fig. 7(a)). A four-peak (2-peak) longitudinal structure is detected in the F3/C (IRI) model in June. The IRI model shows a clear 2-peak longitudinal structure in September. On the other hand, the F3/C model displays a 2-peak or more small-scale longitudinal structure in September. A four or three-peak structure appears in both models in December.

The seasonal variation of N_e at 450 km derived by the F3/C and IRI models are shown in Fig. 8. The N_e derived by the IRI model is generally higher than that of the F3/C model around the magnetic equator. In contrast to the N_mF_2 shown in Fig. 7, a large-scale longitudinal structure, which is similarly reported by many scientists (e.g. Sagawa *et al.*, 2005; Immel *et al.*, 2006; Lin *et al.*, 2007; Kakinami *et al.*, 2011), is clearly seen around the magnetic equator in the F3/C model. According to Kakinami *et al.* (2011), the 4-peak structure of N_e at 660 km observed with the DEMETER satellite is the most pronounced in September while a 3-peak structure appears in March and December. Though the IRI model also shows a longitudinal structure, the longitudinal structure retrieved with the F3/C model is more pronounced than that of the IRI and its seasonal variation agrees with previous studies.

Seasonal variations of VSH at 450 km derived by the F3/C and IRI models are shown in Fig. 9. The IRI model shows a maxima of VSH along the magnetic equator with a 10° latitude width while the F3/C model only displays a small maxima of VSH around 140–240°E and 300°E near the magnetic equator. In the F3/C model, maxima of VSH around 140–240°E near the magnetic equator are always significant in all seasons, which show a maximum value in March. However, a maximum of VSH around 300°E is only significant in March. The longitudinal structure seen in the VSH derived by the F3/C model differs from those of N_e at 450 km (Fig. 8). Meanwhile, 3 or 4 maxima of VSH derived by the IRI model appear around the magnetic equator. The location of each peak roughly corresponds to the locations of the maximum of N_e shown in Fig. 8. A significant difference in the VSH between the F3/C and the IRI models appears in the middle latitude. The VSH derived by the IRI model only shows a maximum around the magnetic equator, a sharp drop away from the magnetic equator and is almost constant in low and middle latitudes. Meanwhile, VSH derived by the F3/C model shows maxima (minima) around magnetic equator (beside geomagnetic equator) and increases with increasing latitude in low and middle latitudes. Similar VSH results are observed not only in F3/C data (Liu *et al.*, 2008) but also by the topside sounder onboard the Alouette and ISIS satellites (Kutiev and Marinov, 2007). Especially, VHS derived by the F3/C model higher than 50°S is higher than the magnetic equator in September and December.

4. Summary

We have constructed an empirical model based on N_e profiles observed with F3/C under geomagnetically quiet conditions ($K_p < 4$). The F3/C model derives global N_e profiles between altitudes of 150 and 590 km as functions of the solar EUV flux, day of year, local time and location. The N_e above the F_2 peak, and the F_2 peak altitude, derived by the F3/C model is lower than those derived by the IRI. The F3/C model reproduces a longitudinal structure better than the IRI model. The F3/C model also derives VSH which show good agreement with measurements obtained from topside sounders onboard the Alouette and ISIS satellites. Since the F3/C model has a big advantage of greater data coverage, it helps us to understand a variety of upper ionospheric phenomenon. As a result, the F3/C model contributes an improvement over the IRI model.

Acknowledgments. This work was partially supported by the Earth Observation Research Center, Japan Aerospace Exploration Agency (Y. K.) and the National Science Council project NSC 98-2116-M-008-006-MY3 grant of the National Central University (Y. K. and J. Y. L.).

References

Bilitza, D., A correction for the IRI topside electron density model based on Alouette/ISIS topside sounder data, *Adv. Space Res.*, **33**, 838–843, 2004.

Bilitza, D. and R. Williamson, Towards a better representation of the IRI topside based on ISIS and Alouette data, *Adv. Space Res.*, **25**(1), 149–152, 2000.

Bilitza, D., B. W. Reinsch, S. Radicella, S. Pulinets, T. Gulyaeva, and L. Triskova, Improvements of the international reference ionosphere model for the topside electron density profile, *Radio Sci.*, **41**, RS5S15, doi:10.1029/2005RS003370, 2006.

Immel, T. J., E. Sagawa, S. L. England, S. B. Henderson, M. E. Hagan, S. B. Mende, H. U. Frey, C. M. Swenson, and L. J. Paxton, Control of equatorial ionospheric morphology by atmospheric tides, *Geophys. Res. Lett.*, **33**, L15108, doi:10.1029/2006GL026161, 2006.

Judge, D. L., D. R. McMullin, S. Ogawa, D. Hovestadt, B. Klecker, M. Hilchenbach, L. R. Canfield, R. E. Vest, R. Watts, C. Tarrio, M. Kuhne, and P. Wurz, First solar EUV irradiances obtained from SOHO by the CELIAS/SEM, *Sol. Phys.*, **177**, 161–173, 1998.

Kakinami, Y., S. Watanabe, and K.-I. Oyama, An empirical model of electron density in low latitude at 600 km obtained by Hinotori satellite, *Adv. Space Res.*, **41**, 1494–1498, doi:10.1016/j.asr.2007.09.031, 2008.

Kakinami, Y., C. H. Chen, J. Y. Liu, K.-I. Oyama, W. H. Yang, and S. Abe, Empirical models of Total Electron Content based on functional fitting over Taiwan during geomagnetic quiet condition, *Ann. Geophys.*, **27**, 3321–3333, 2009.

Kakinami, Y., C. H. Lin, J. Y. Liu, M. Kamogawa, S. Watanabe, and M. Parrot, Daytime longitudinal structure of electron density and temperature in the topside ionosphere observed by the Hinotori and DEMETER satellites, *J. Geophys. Res.*, doi:10.1029/2010JA015632, 2011.

Kutiev, I. and P. Marinov, Topside sounder model of scale height and transition height characteristics of the ionosphere, *Adv. Space Res.*, **39**, 759–766, 2007.

Kutiev, I., P. Marinov, and S. Watanabe, Model of topside ionosphere scale height based on topside sounder data, *Adv. Space Res.*, **37**, 943–950, 2006.

Lei, J., S. Syndergaard, A. G. Burns, S. C. Solomon, W. Wang, Z. Zeng, R. G. Roble, Q. Wu, Y.-H. Kuo, J. M. Holt, S.-R. Zhang, D. L. Hysell, F. S. Rodrigues, and C. H. Lin, Comparison of COSMIC ionospheric measurements with ground-based observations and model predictions: Preliminary results, *J. Geophys. Res.*, **112**, A07308, doi:10.1029/2006JA012240, 2007.

Lin, C. H., W. Wang, M. E. Hagan, C. C. Hsiao, T. J. Immel, M. L. Hsu, J. Y. Liu, L. J. Paxton, T. W. Fang, and C. H. Liu, Plausible effect of atmospheric tides on the equatorial ionosphere observed by the FORMOSAT-3/COSMIC: Three-dimensional electron density structures, *Geophys. Res. Lett.*, **34**, L11112, doi:10.1029/2007GL029265, 2007.

Liu, L., M. He, W. Wan, and M.-L. Zhang, Topside ionospheric scale heights retrieved from Constellation Observing System for Meteorology, Ionosphere, and Climate radio occultation measurements, *J. Geophys. Res.*, **113**, A10304, doi:10.1029/2008JA013490, 2008.

Liu, J. Y., C. Y. Lin, C. H. Lin, H. F. Tsai, S. C. Solomon, Y. Y. Sun, I. T. Lee, W. S. Schreiner, and Y. H. Kuo, Artificial plasma cave in the low atitude ionosphere results from the radio occultation inversion of the FORMOSAT–3/COSMIC, *J. Geophys. Res.*, **115**, A07319, doi:10.1029/2009JA015079, 2010.

Marinov, P., I. Kutiev, and S. Watanabe, Empirical model of O+-H+ transition height based on topside sounder data, *Adv. Space Res.*, **34**, 2021–2025, 2004.

Rawer, K., D. Bilitza, and S. Ramakrishnan, Goals and status of international reference ionosphere, *Rev. Geophys.*, **16**, 177–181, 1978.

Sagawa, E., T. J. Immel, H. U. Frey, and S. B. Mende, Longitudinal structure of the equatorial anomaly in the nighttime ionosphere observed by IMAGE/FUV, *J. Geophys. Res.*, **110**, A11302, doi:10.1029/2004JA010848, 2005.

Y. Kakinami (e-mail: kakinami@mail.sci.hokudai.ac.jp), J.-Y. Liu, and L.-C. Tsai

GPS Solut
DOI 10.1007/s10291-012-0282-8

ORIGINAL ARTICLE

Application of the TaiWan Ionospheric Model to single-frequency ionospheric delay corrections for GPS positioning

Ernest Pagaran Macalalad · Lung-Chih Tsai · Joz Wu · Chao-Han Liu

Received: 17 November 2011 / Accepted: 20 July 2012

Abstract The performance of a three-dimensional ionospheric electron density model derived from FormoSat3/COSMIC GPS Radio Occultation measurements, called the TaiWan Ionosphere Model (TWIM), in removing the ionospheric delays in single-frequency pseudorange observations is presented. Positioning results using TWIM have been compared with positioning results using other ionospheric models, such as the Klobuchar (KLOB) and the global ionospheric model (GIM). C/A code pseudoranges have been observed at three International GPS Service reference stations that are representative of mid-latitude (BOR1 and IRKJ) and low-latitude (TWTF) regions of the ionosphere. The observations took place during 27 geomagnetically quiet days from April 2010 to October 2011. We perform separate solutions using the TWIM, KLOB, GIM ionospheric models and carry out a solution applying no ionospheric correction at all. We compute the daily mean horizontal errors (DMEAN) and the daily RMS (DRMS) for these solutions with respect to the published reference station coordinates. It has demonstrated that TEC maps generate using the TWIM exhibit a detailed structure of the ionosphere, particularly at low-latitude region, whereas the Klobuchar and the GIM only provide the basic diurnal and geographic features of the ionosphere. Also, it is shown that even for lower satellite elevations, the TWIM provides better positioning than the Klobuchar and GIM models. Specifically, using TWIM, the difference of the uncorrected solution (no ionospheric correction), and the other solutions, relative to the uncorrected solution, is 45 % for the mean horizontal error (DMEAN) and 42 % for the horizontal root-mean-square error (DRMS). Using Klobuchar and GIM, the percent for DMEAN only reaches to about 12 % and 3 %, while the values for the DRMS are only 12 and 4 %, respectively. In the vertical direction, all models have a percentage of about 99 and 70 % for the mean vertical error (VMEAN) and vertical root-mean-square error (VRMS), respectively. These percentages show the greater impact of TWIM on the ionospheric correction compared to the other models. In at least 40 % of the observed days and across all stations, TWIM has the smallest DMEAN, VMEAN, DRMS, and VRMS daily values. These values reach 100 % at station TWTF. This shows the overall performance of TWIM is better than the Klobuchar and GIM.

Keywords Single-frequency GPS positioning · Ionospheric model · Ionospheric delay

E. P. Macalalad (✉) · L.-C. Tsai
Institute of Space Science, National Central University, Chung-Li, Taiwan, ROC
e-mail: macalalade@gmail.com; 986403601@cc.ncu.edu.tw

L.-C. Tsai · J. Wu
Center for Space and Remote Sensing Research, National Central University, Chung-Li, Taiwan, ROC

C.-H. Liu
Academia Sinica, Taipei, Taiwan, ROC

Introduction

Degradation of the accuracy of the derived coordinates using global positioning system (GPS) can be attributed to the following sources: errors in satellite ephemeris, errors by satellite clocks, atmospheric errors, receiver errors, multipath interference, and position dilution of precision (PDOP) (Spencer et al. 2003). Since 2000, when the selective availability in GPS has been removed, the ionosphere has become the main error source in single-frequency

Published online: 09 August 2012

GPS positioning (Camargo et al. 2000; Ovstedal 2002). This is due to the ability of the ionosphere to impact an incoming radio wave. The behavior of the ionosphere primarily depends on the local time, season, solar activity, viewing direction, location of the receiver, and the earth's magnetic field (Klobuchar 1987; Camargo et al 2000). These can in turn cause different effects to the accuracy of GPS positioning. First-order ionospheric delay can be practically removed in the GPS signals using dual-frequency GPS receivers, which uses both *L1* (1,575.42 MHz) and *L2* (1,227.60 MHz) bands. However, these devices are more expensive and thus are generally not available for most users.

A number of ionospheric models have been developed for single-frequency GPS positioning. One of the first models was developed by Klobuchar (1987). He developed an operational ionospheric model to be broadcast by GPS satellites to provide the user corrections of approximately 50 % RMS of the ionospheric range error (Klobuchar 1987). Ovstedal (2002) used the precise satellite orbits and satellite clock corrections and the global ionospheric model (GIM) supplied by International GPS Service (IGS) in absolute GPS positioning. He was able to demonstrate a sub-meter epoch-to-epoch accuracy in the horizontal and approximately 1-meter accuracy in the vertical. One of the most recent models is called the Multi Instrument Data Analysis System (MIDAS). Developed for regional applications, Allain and Mitchell (2009) used data from dual-frequency receivers distributed across Europe. They compared their results with other models such as Klobuchar and the International Reference Ionosphere (IRI). They showed that using MIDAS, and precise satellite orbit data from IGS, the average position is within 1.5 m while using Klobuchar and IRI, the average position is 4 and 3 m respectively.

We present ionospheric delay correction for single-frequency GPS pseudoranges using a numerical and phenomenological model, called the TaiWan Ionospheric Model (TWIM). Its performance is compared to other ionospheric models such as Klobuchar and GIM. It is hoped that this will provide single-frequency GPS users an alternative ionospheric model that would give higher positioning accuracy than most models used today.

Ionospheric corrections

Given the total electron content (TEC) along the signal path, ionospheric delay (d_{ion}) in the pseudorange can be determined as:

$$d_{\text{ion}} = \frac{40.3\text{TEC}}{f^2} \tag{1}$$

Numerically, one TEC is equivalent to about 16 cm of delay in the *L1* pseudorange. Generally, ionospheric effects usually amount to about 30 m of error in the pseudorange measurements, depending on the elevation angle of the satellite. Moreover, among the errors that contribute to the pseudorange measurements, the ionospheric error is the most variable and difficult to compensate since the ionosphere is very dynamic and ionospheric radio propagation is dependent on the frequency of the radio wave.

In this study, the TWIM, which is a three-dimensional ionospheric electron density (n_e) model, is used to calculate ionospheric delay for GPS single-frequency receivers (Tsai et al 2009). It is a numerical and phenomenological model of global ionospheric electron density that is constructed from monthly weighted and half-hourly radio occultation (RO) measurements from Formosat3/COSMIC GPS. The half-hour vertical n_e profiles are derived from 30-day data set from the day of observation with much weight (Gaussian-shaped weighting function) given to days closer to the day of observation. For example, n_e profiles for day 254 use RO observations from day 224 to 254. Additionally, further interpolation is done within the half-hour profiles. The 30-day data provide enough RO observations to produce global electron density profiles at a 30-min temporal resolution with a 3° spatial resolution.

Each layer (F2, F1, E, or D) is characterized by a Chapman-type function, which is described by its peak electron density ($n_{e\max}$), peak density height (h_m), and scale height H. Thus, these parameters can be used to obtain the electron density n_e at a specific longitude (θ), latitude (λ) and height (h) using the least-squares error fitting of the observed profile to the Chapman functions:

$$n_e(\theta,\lambda,h) = \sum_{i=1}^{n} n_{e\max}(\theta,\lambda) \times \exp\left\{\frac{1}{2}\left[1 - \frac{h-h_m(\theta,\lambda)}{H(\theta,\lambda)} - \exp\left(-\frac{h-h_m(\theta,\lambda)}{H(\theta,\lambda)}\right)\right]\right\} \tag{2}$$

Each i represents a physical layer of F2, F1, E, or D. Surface spherical harmonics are applied to map the derived Chapman layer parameters in geodetic coordinates. Thus, the TWIM is three dimensional. In addition, all of these layers can occur during the daytime. The F1 and D layers decay at night and can be hidden within the other layers, but the F1 and D-layer parameters are still derivable at all times by least-squares error fitting. The TWIM does not account for electron density in the plasmasphere.

It should also be noted that because every electron density estimates by the TWIM uses a 30-day data set, any disturbances in the ionosphere, such as storms, in a given day will be masked by the other non-disturbed days within the 30-day period. Moreover, the Formosat3/COSMIC cannot provide dense enough RO observations to observe disturbed Ne profiles when magnetic storm happens. During these events, the retrieved Ne profiles are removed because the signal-to-noise ratio values are very low. Therefore, such events may not be observed. However, this data set is enough to model the ionosphere during geomagnetically quiet days.

The n_e profiles are used to calculate the point-to-point slant TEC (STEC) between the receiver and each GPS satellite (Tsai et al 2009). These are used to determine the ionospheric delay on the *L1* frequency. The corrections made using TWIM are compared to two of the most commonly used ionosphere models for single-frequency positioning. Both vertical TECs generated by Klobuchar and GIM, which are two-dimensional ionosphere models, are translated to slant delay using elevation-dependent mapping functions.

The atmospheric errors (tropospheric and ionospheric) are highly dependent to elevation angles. Thus, these errors can be minimized by setting elevation masks or cutoff angles. These angles do not allow data coming from satellites at low elevation where they are subject to more biases as compared to higher elevation angles. Moreover, setting an elevation mask can also minimize other elevation-dependent biases, such as multipath effects. In this study, elevation masks are set at 10°.

Method

Single-frequency GPS data are recorded during the most geomagnetically quiet days per month from April 2010 to October 2011—a total of 27 days— by three IGS reference stations (BOR1, IRKJ, and TWTF) at a 2-min sampling interval. Tables 1 and 2 show the details of each station and the geomagnetically quiet days used in this study. These days were chosen since TWIM is a quiet time model.

GPS raw data in RINEX format (ftp://igscb.jpl.nasa.gov/igscb/data/format/rinex211.txt) are used. The RINEX files include the pseudorange and carrier phase observations and the satellite navigation message for each GPS satellite. Satellite positions are calculated using the GPS satellite broadcast ephemeris, that is only the data contained in the RINEX files are used. The receiver positions are calculated using L1 C/A code pseudoranges corrected for satellite clock bias, relativistic clock bias, timing group delay, and tropospheric error. A base solution is carried out in which the ionospheric delay is not applied; this solution is referred to as uncorrected (UNC) solution. Three additional solutions are carried out per epoch and station but now correcting the ionospheric delay using the Klobuchar (KLOB), GIM and TWIM models respectively.

The errors in the horizontal (east and north) and vertical are calculated by differencing the computed position and the known reference position. The horizontal error D is calculated as

$$D = \sqrt{E^2 + N^2} \tag{3}$$

where E and N are the differences in the east and north direction between both solutions. The daily mean and the root-mean square (RMS) values of these differences are calculated per station and labeled as EMEAN, NMEAN, ERMS, and NRMS. To represent the daily horizontal position accuracy, we compute the daily mean of (3) denoted by DMEAN. We also compute the distance RMS, labeled DRMS, which contains 65–69 % probability of observations being within a horizontal circle with radius DRMS and center at the reference position, as (Conley et al. 2006):

$$\mathrm{DRMS} = \sqrt{\mathrm{ERMS}^2 + \mathrm{NRMS}^2} \tag{4}$$

The daily mean error along the vertical (VMEAN) and its RMS error (VRMS) are used to describe the vertical accuracy of each observation. The difference of uncorrected and corrected data, relative to the uncorrected data, is then expressed in percent. This percentage expresses the impact of the ionospheric model and is given by.

$$\%\mathrm{diff} = \frac{\mathrm{UNC} - \mathrm{ION}}{\mathrm{UNC}} \times 100\ \% \tag{5}$$

where UNC is the value obtained using no ionospheric models and ION is value obtained when using an ionospheric model. Eq. (5) is applied to mean and RMS values. Positive percentage shows improvement in the observations while negative percentage pertains to measurements whose errors are worse than the uncorrected data.

Table 1 Details of the three IGS stations used in this study

Code	Location	Longitude	Latitude	Height (m)	Local time (h)
BOR1	Boroweic, Poland	52°16′37″	17°04′24″	124.9	+2
IRKJ	Irkutsk, Russia	52°13′08″	104°18′58″	502.1	+7
TWTF	Taoyuan, Taiwan	24°57′13″	121°09′52″	201.5	+8

Table 2 List of days used in this study with their minimum, maximum 3-h Kp index, and daily total Kp index

Date	DOY	Minimum 3-h Kp index	Maximum 3-h Kp index	Total Kp index
2010 (14 days)				
04/26/2010	116	0	7	23
05/23/2010	143	0	3	7
05/24/2010	144	0	7	20
06/12/2010	163	3	10	33
07/10/2010	191	0	3	17
07/17/2010	198	0	3	20
08/22/2010	234	0	3	17
08/30/2010	242	0	3	13
09/11/2010	254	0	3	10
09/12/2010	255	0	7	20
10/02/2010	275	0	0	0
11/06/2010	310	0	7	20
11/26/2010	330	0	10	20
12/10/2010	344	0	3	10
2011 (13 days)				
01/30/2011	30	0	3	13
02/03/2011	34	0	7	23
03/15/2011	74	0	3	13
04/26/2011	116	0	7	30
05/20/2011	140	0	7	33
06/29/2011	180	0	7	33
07/27/2011	208	0	13	47
08/18/2011	230	0	10	37
08/31/2011	243	0	7	20
09/19/2011	262	0	10	37
09/23/2011	266	0	7	33
10/28/2011	301	0	3	3
10/29/2011	302	0	3	3

Results and discussion

This section demonstrates the performance of TWIM in GPS positioning. The results, which include the total electron content maps, the horizontal and vertical positional errors and RMS values, are compared to the Klobuchar and GIM models at different elevation angles, time, and geographical locations. The percent occurrence of the days that yielded lowest errors for all days of observations is also presented.

Total electron content map

Nine global VTEC maps for Klobuchar, GIM, and TWIM at epochs 0300UT, 0400UT, and 0500UT on August 22, 2010 (DOY 234) are shown in Fig. 1, which is chosen arbitrarily. The test sites are shown in red triangles. The basic diurnal and geographic features of the ionosphere are shown in all nine maps, that is, peak density during day time and in the low-latitude regions while the minimum density is featured during night time and in the mid-latitude regions. We can also observe the westward shift of the peak density area as the time moves forward. The maximum VTEC value shown on the GIM maps is the greatest among the three models while the Klobuchar maps displayed the least peak density that is shifted to higher latitudes. The TWIM, on the other hand, provides a more detailed VTEC maps as compared with the other two models. For example, the well-known equatorial ionization anomaly (EIA) is clearly shown in the TWIM VTEC maps in the daytime sector. Furthermore, the TWIM can provide three-dimensional electron densities while Klobuchar and GIM only provide two-dimensional (longitudinal and latitudinal) VTEC models.

The calculated 24-h ionospheric slant delays in meters using Klobuchar, GIM, and TWIM on DOY 234 for the three test sites are shown in Fig. 2. The white and gray areas indicate local daytime (0600–1800LT) and nighttime (1800–0600LT). The figure clearly shows the typical diurnal variation of ionosphere where electron density is higher during daytime than in night time. Moreover, the mid-latitude stations (BOR1 and IRKJ) produce low ionospheric delay while the low-latitude station (TWTF) provides high ionospheric slant delays during daytime. This corresponds to the high density provided by the EIA. Meanwhile, all stations yield approximately equal ionospheric slant delays during nighttime. Slant delays calculated from the Klobuchar model are consistent for all stations, showing the half cosine-shaped daytime and constant nighttime electron densities. The GIM-derived slant delays, on the other hand, are closer to the TWIM-derived slant delays with the TWIM providing a wider range of values than GIM. However, GIM produce larger ionospheric delay than TWIM. This is because GIM have the largest peak electron density as previously described in Fig. 1.

Figure 3 that shows the horizontal errors D (Eq. 3) and the vertical errors using the three models KLB, GIM, and TWIM for the three stations and epochs 0300UT, 0400UT, and 0500UT for DOY 234. As shown in this figure, the TWIM generally provides the smallest error for the stations in both horizontal and vertical direction. Meanwhile, Klobuchar provide largest error in both horizontal and vertical directions. This indirectly shows that TWIM generally provides a better estimation of the slant TEC around the GPS receivers.

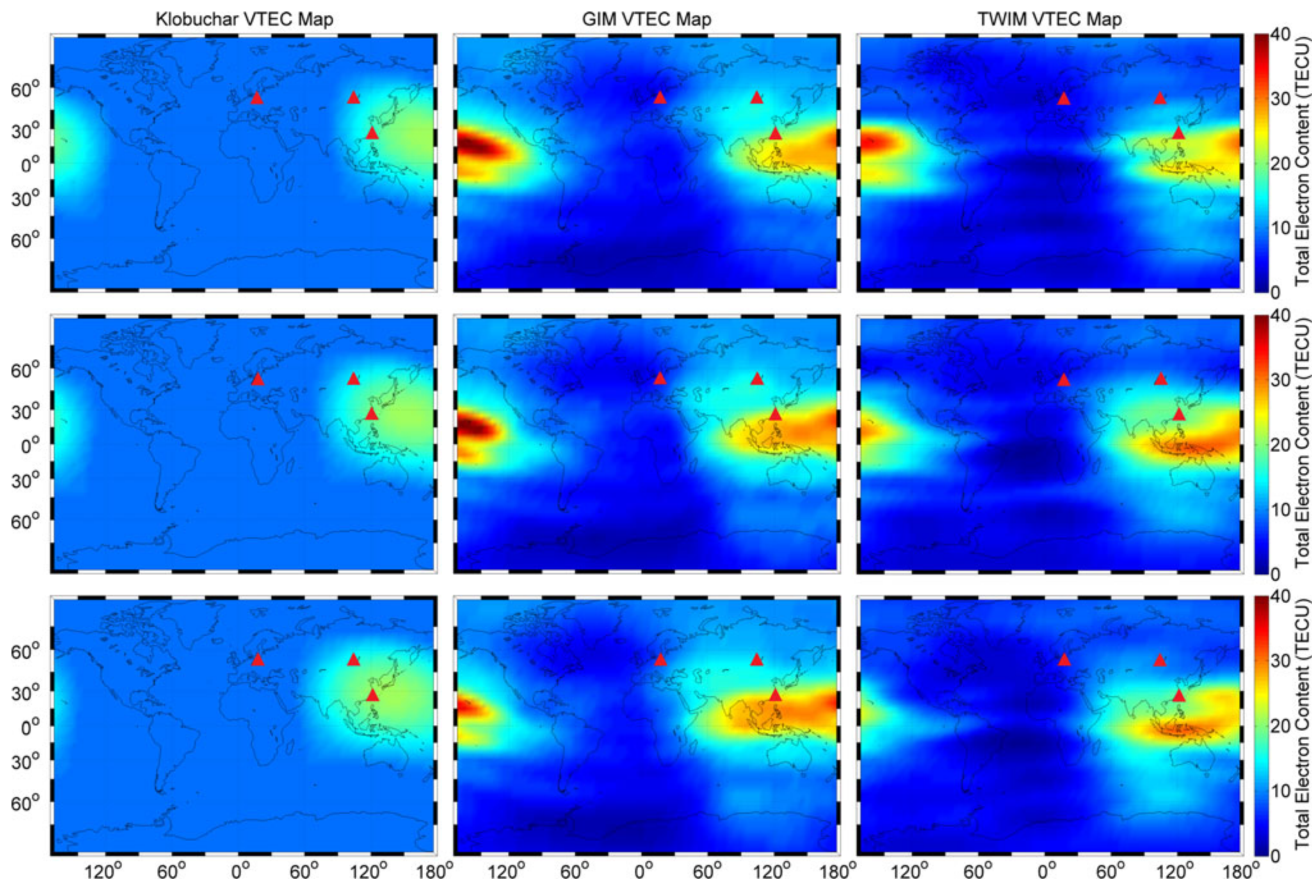

Fig. 1 Global VTEC maps for Klobuchar (*col 1*), GIM (*col 2*), and TWIM (*col 3*) at epochs 0300UT (*top row*), 0400UT (*middle row*), and 0500UT (*bottom row*) for DOY 234

Elevation mask

Different elevation masks have been applied to test which elevation angle will yield better results. The resulting DRMS and VRMS (Eq. 4) at different elevation masks (0°, 5°, 10°, 15°, and 20°) for DOY 234 for different ionospheric models are shown in Fig. 4. The positioning accuracy has improved when low elevation masks (5° and 10°) are applied. However, as the elevation mask is set higher (15° and 20°), the positioning seems to degrade in quality. This is because at larger elevations masks, more satellites are ignored, which will result in larger dilution of precision values and worse positioning quality. It indicates that TWIM performs better than the other models for observations at low elevations and demonstrates the ability of TWIM to provide good electron density profiles. The figure shows that even without applying any elevation masks, TWIM still produces better results than the other models.

Positioning results

Figure 5 shows a sample diurnal variation of the east, north and vertical errors at TWTF station for DOY 234. The effect of the ionosphere in GPS positioning is clearly shown in the vertical error where errors of uncorrected solutions reach about 15 m in daytime and approach zero in nighttime. Moreover, improvements made by different models in the positioning are most evident in the vertical (height) direction. This is because the ionospheric delays are all directed above the receiver. The ionospheric effect in the horizontal is present in all directions (east–west and north–south). In this case, parts of the errors in one direction, say east, can be canceled by the errors in the opposite direction (west).

The performance of TWIM in the horizontal and vertical directions for the stations for DOY 234 can be stated as follows: TWIM exhibits the smallest mean horizontal error (DMEAN) of 1.05, 0.99, and 1.18 m for stations BOR1,

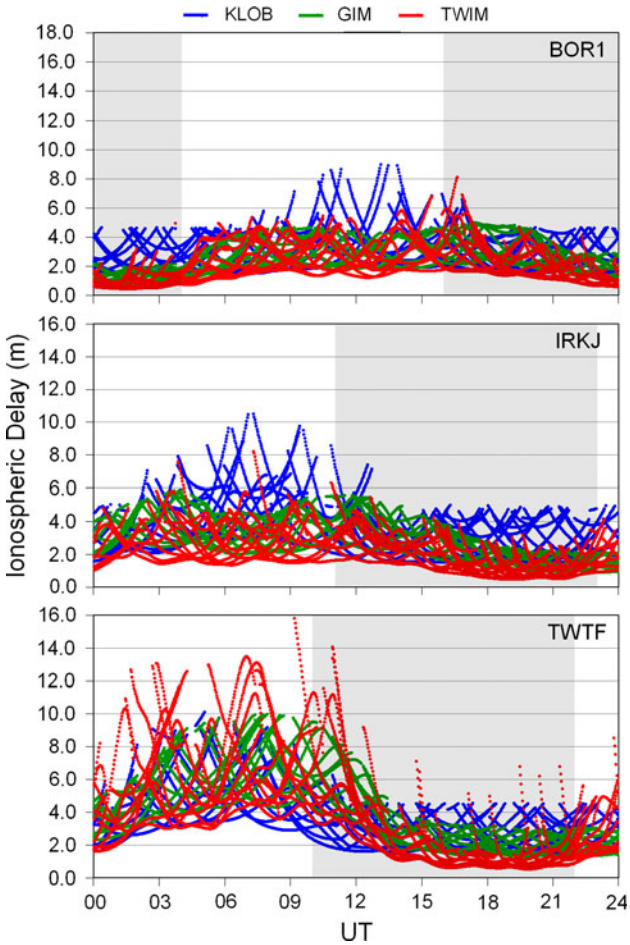

Fig. 2 Slant ionospheric delay calculated by Klobuchar (KLB), GIM, and TWIM for BOR1 IRKJ, and TWTF stations for DOY 234

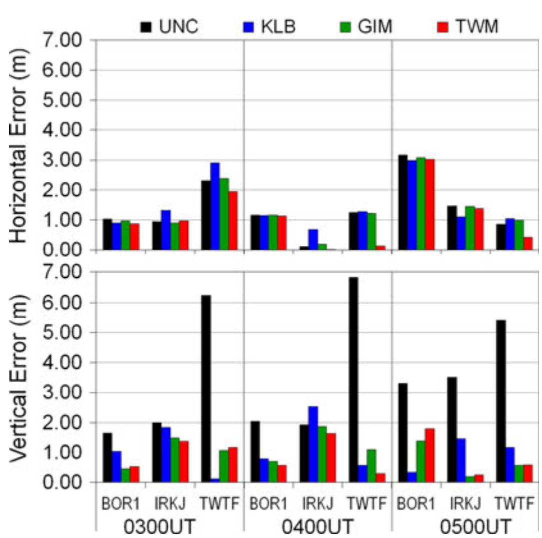

Fig. 3 Horizontal and vertical errors at epochs 0300UT, 0400UT, and 0500UT for DOY 234 for different ionospheric models

IRKJ, and TWTF, corresponding to percentage (Eq. 5) of 10, 9, and 29 %. The DRMS using TWIM is also the smallest among the models with values of 1.28, 1.11, and 1.35 m for the same station sequence, corresponding to percentage of 7, 8, and 33 %. This means that TWTF has exhibited the greatest positioning improvement compared to the other two stations. Regarding the vertical direction, Klobuchar provides the smallest mean vertical error (VMEAN) (−0.15 m) at station BOR1 (95 %), but TWIM has given the best results in stations IRKJ and TWTF at −0.44 m (78 %) and −0.18 m (96 %), respectively. TWIM also provides sub-meter mean vertical errors for all stations. The VRMS are smallest using TWIM with values at 1.65, 1.87, and 2.18 m for stations BOR1, IRKJ, and TWTF, respectively. This corresponds to percentages of 54, 37, and 60 %. For this example, the generally trend of increasing accuracy (based on DRMS and VRMS) is GIM, Klobuchar, and TWIM for station BOR1 while for stations IRKJ and TWTF, the trend is Klobuchar, GIM, and TWIM.

Figure 6 shows DMEAN and VMEAN observed at station TWTF for all days of observations and using all ionospheric models. The DMEAN ranges 1.24–5.67 m using Klobuchar, 1.19–5.96 m using GIM, and 1.08–4.32 m using TWIM. The VMEAN varies from 3.16 to 10.06 m, −1.82 to 1.64 m, −1.43 to 1.60 m, and −3.29 to 1.01 m using Klobuchar, GIM, and TWIM, respectively. Using TWIM, 48 % of the days observed have DMEAN of 1.50 m or less while 70 % of the observed days have VMEAN of 1.00 m or less. Negative VMEAN corresponds to observations below the reference point. The DRMS and VRMS results for all days of observation using all ionospheric models are shown in Fig. 7. The DRMS using Klobuchar, GIM, and TWIM vary from 1.49 to 6.73 m, 1.42 to 7.14 m, and 1.33 to 5.07 m, respectively. Using TWIM, 16 (59 %) of the days have DRMS of 2.0 m or less. The VRMS range from 1.98 to 6.12 using Klobuchar, 1.89 to 6.63 m using GIM, and 1.75 to 6.38 using TWIM. TWIM provides the smallest DMEAN and DRMS for all observations, whereas it provides the smallest VMEAN and VRMS for 11, and 15 days, respectively.

The corresponding percentages of the DMEAN and VMEAN for the difference of uncorrected solution and ionospheric corrected solution at station TWTF for all days of observation are shown in Fig. 8. The values demonstrate the amount of corrections made by each model to the uncorrected solutions. The percentage of DMEAN ranges from 0.56 to 12.33 %, 0.16 to 2.56 %, and 8.70 to 45.07 % using Klobuchar, GIM, and TWIM, respectively. This shows the good performance of TWIM in correcting positioning in the horizontal direction. On the other hand, the percentage of VMEAN using Klobuchar, GIM, and TWIM varies 55.98–99.44 %, 71.74–99.48 %, and 46.71–99.05 %, respectively. Figure 9 shows the percentage of DRMS and

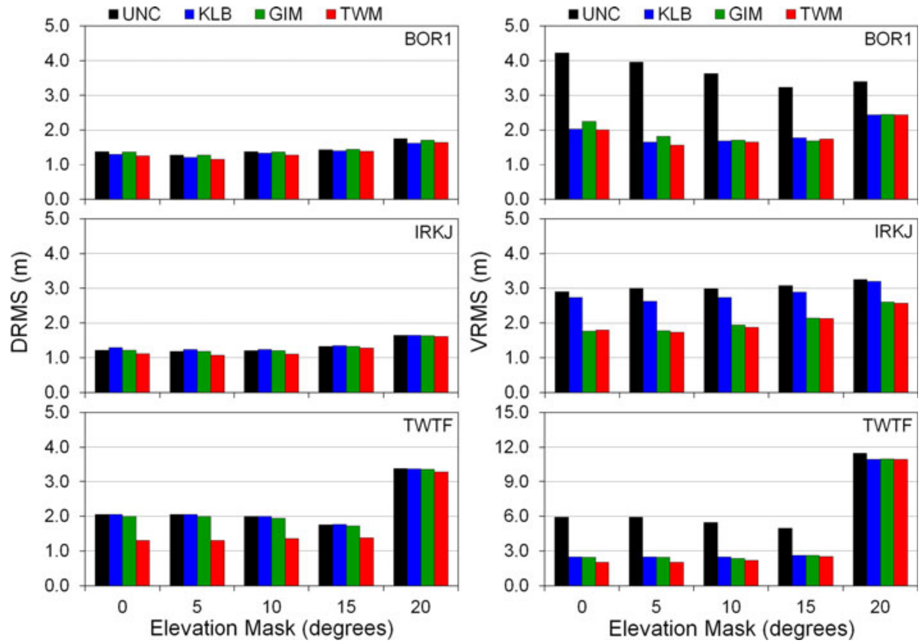

Fig. 4 Summary of DRMS (*col 1*) and VRMS (*col 2*) at different elevation masks (0°, 5°, 10°, 15°, and 20°) for DOY 234 for different ionospheric models at stations BOR1 IRKJ and TWTF

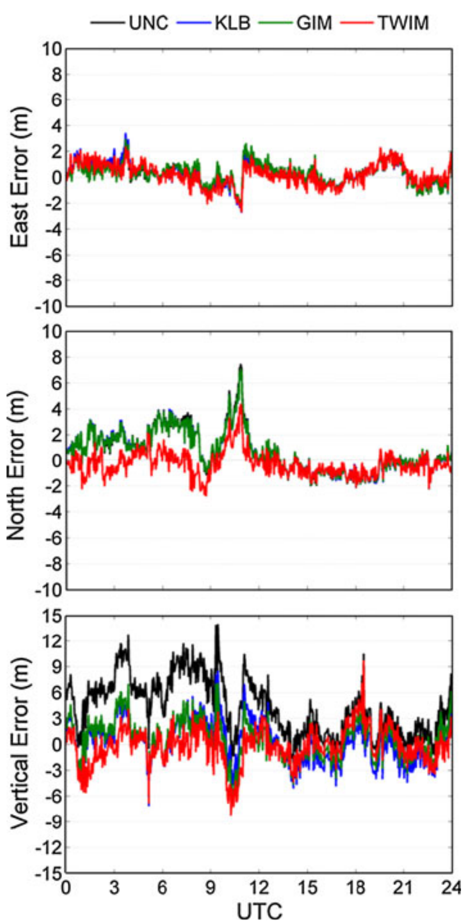

Fig. 5 An example of diurnal variation of east, north and vertical errors at station TWTF for DOY 234 using different models

VRMS for all days of observations at TWTF station. Using Klobuchar, GIM, and TWIM, the percentage of DRMS ranges from 0.14 to 11.89 %, 0.23 to 3.67 %, and 9.21 to 42.32 %, respectively, while the percentage of VRMS varies from 44.95 to 70.72 %, 46.70 to 69.00 %, and 36.17 to 71.54 %, respectively.

The remaining errors that have not been accounted for by the ionospheric delays can be attributed to the uncertainties in the models, both in troposphere and ionosphere. Moreover, errors brought about by the accuracy of the broadcast ephemeris can also be a source of error since the precise ephemeris of the IGS was not used.

Table 3 summarizes the percentage of occurrence of Klobuchar, GIM, and TWIM with the smallest mean horizontal and vertical errors, DRMS, and VRMS for stations BOR1, IRKJ, and TWTF. As mentioned above, all observed days show that TWIM provided the smallest DMEAN and DRMS at station TWTF. Meanwhile, 41 % (11 days) and 56 % (15 days) of the observed days provide the least VMEAN and VRMS, respectively. On the other hand, 26 % (7 days) and 30 % (8 days) of the observed days the Klobuchar model has smallest VMEAN and VRMS, respectively. GIM provides the smallest VMEAN and VRMS in 33 % (9 days) and 15 % (4 days) of the days of observation. Thirteen days or 48 % using TWIM have 2.5 m of VRMS or less. In stations BOR1 and IRKJ, the TWIM also provides the most occurrences of smallest DMEAN, VMEAN, DRMS, and DRMS with at least 50 % occurrence, except for VMEAN at station BOR1.

The performance of TWIM across all stations and all days of observation are generally better than the other

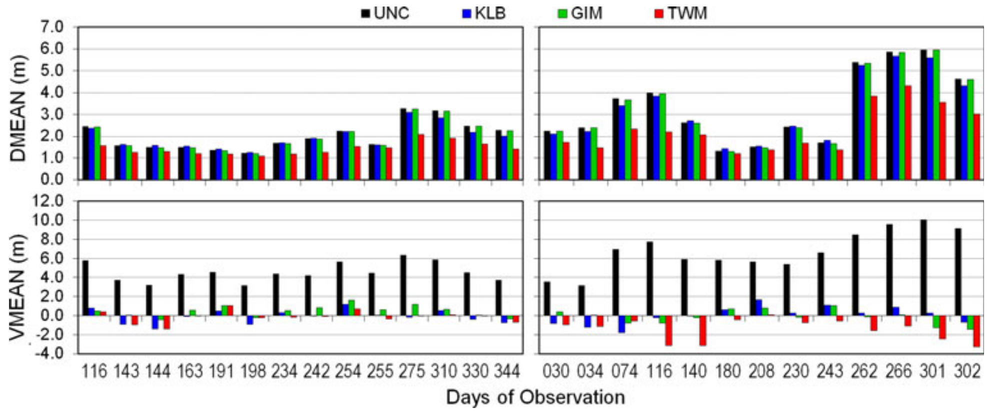

Fig. 6 DMEAN and VMEAN using all ionospheric models observed at station TWTF for all days of observation

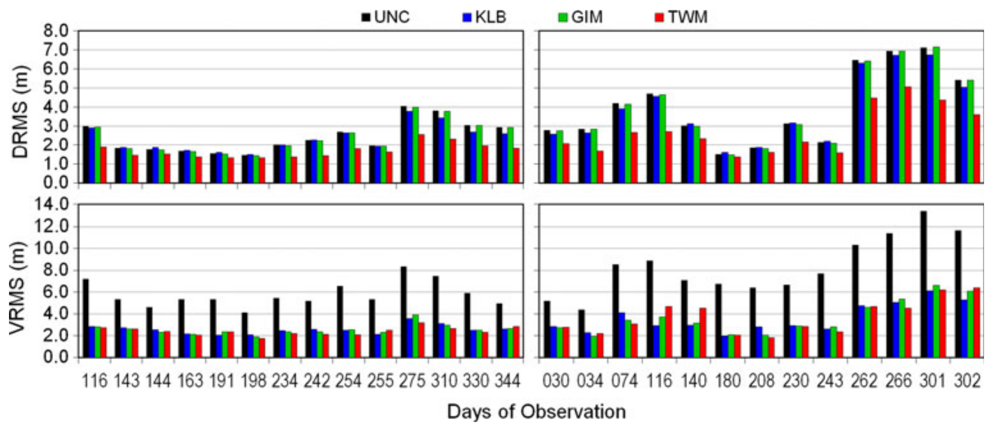

Fig. 7 DRMS and VRMS using all ionospheric models observed at station TWTF for all days of observation

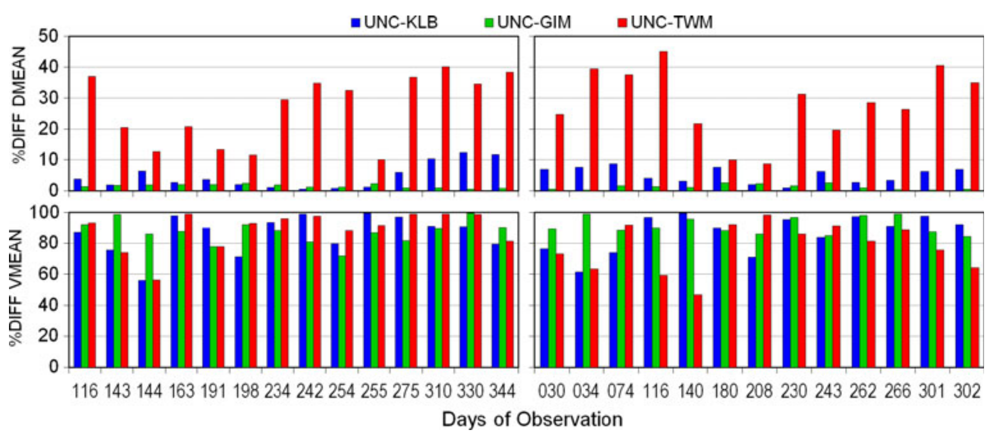

Fig. 8 Percentages of DMEAN and VMEAN for the difference of uncorrected solution and ionospheric corrected solution at station TWTF for all days of observation

models expect for the mean vertical error at BOR1. For all stations, the general order of increasing accuracy (based on the RMS errors) is GIM, Klobuchar, and TWIM in the horizontal while it is Klobuchar, GIM, and TWIM along the vertical. In addition, the TWIM seems to provide a good ionospheric model at low latitude (EIA region) as shown in the results at station TWTF especially in the horizontal. The accuracy of TWIM can also be attributed to the number of occultation use in the modeling as well as the distribution of the occultation points at each region. That is, the denser the occultation points in a specific region the better the estimate of electron density the TWIM will provide. However, such evaluation is beyond the scope of the study.

Conclusions and future work

GPS satellite-receiver slant TEC at three stations (BOR1, IRKJ, and TWTF) were determined for 27 days with geomagnetically quiet conditions during a period of 2 years using the TWIM model and compared with

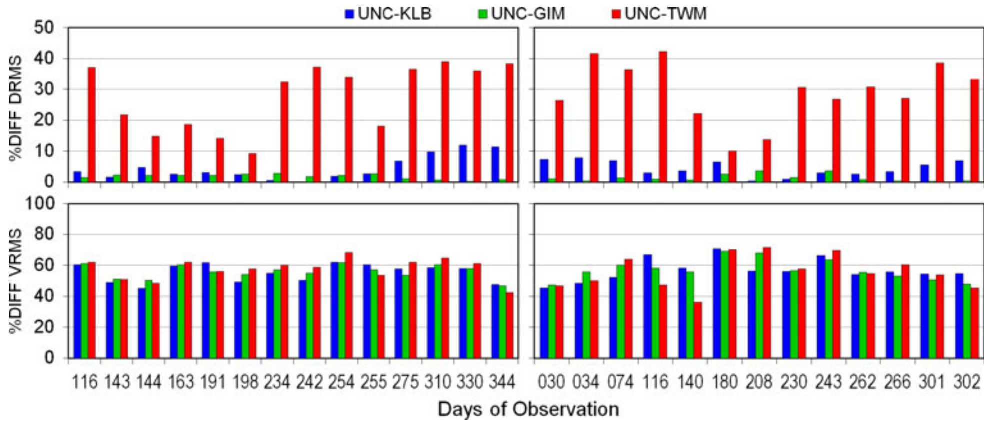

Fig. 9 Percentages of DRMS and VRMS for the difference of uncorrected solution and ionospheric corrected solution at station TWTF for all days of observation

Table 3 Percentage of occurrence of ionospheric model with smallest DMEAN, VMEAN, DRMS, VRMS

Percentage of occurrence	BOR1			IRKJ			TWTF		
	KLB (%)	GIM (%)	TWIM (%)	KLB (%)	GIM (%)	TWIM (%)	KLB (%)	GIM (%)	TWIM (%)
DMEAN	26	0	74	48	0	52	0	0	100
VMEAN	37	33	30	22	19	59	26	33	41
DRMS	26	0	74	22	15	63	0	0	100
VRMS	4	46	50	4	30	67	30	15	56

commonly used models such as Klobuchar and GIM. All models have exhibited typical diurnal characteristics of the ionosphere. However, the TEC maps using TWIM provide a more detailed representation of the current state of the ionosphere as compared to using Klobuchar and GIM ionospheric maps, especially in the low-latitude region, which resulted to better positioning at this region. The TWIM can provide three-dimensional ionospheric electron density values and improve horizontal and vertical positioning significantly compared to Klobuchar and GIM.

Best possible positioning is achieved using a 10° elevation mask. The solutions were able to remove the effect of very low elevation angles but still able to maintain enough satellites to produce good DOPs and positioning results. In addition, the TWIM provides better positioning even for lower elevation masks as compared with the other models. This indicates the high quality of TWIM in producing three-dimensional ionospheric electron density maps over a wider range of satellite elevation.

It is shown that the TWIM is for all days of observation and across all stations generally better than the other models. The average order of increasing accuracy is GIM, Klobuchar, and TWIM along the horizontal, and it is Klobuchar, GIM, and TWIM along the vertical. Judging from the overall result at station TWTF, the TWIM seems to provide good ionospheric model at low latitude (EIA region) particularly in the horizontal.

In the future research, positioning can be improved by using precise GPS orbit information provided by IGS and better tropospheric models. The performance of the TWIM in GPS positioning with respect to the number of occultation points should also be studied. Lastly, the performance of the TWIM in GPS positioning at various geomagnetic and solar activities can be explored in order to establish the applicability of TWIM in different space weather conditions.

References

Allain DJ, Mitchell CN (2009) Ionospheric delay corrections for single-frequency GPS receivers over Europe using tomographic mapping. GPS Sol 13:141–151

Camargo PDO, Monico JFG, Ferreira LDD (2000) Application of ionospheric corrections in the equatorial regions for L1 GPS users. Earth Planets Space 52(1):1083–1089

Conley R, Cosentino R, Hegarty C, Kaplan E, Leva JL, de Haag M, Van Dyke K (2006) Performance of standalone GPS. In: Kaplan ED, Hegarty C (eds) Understanding GPS: principles and applications. Norwood, MA, pp 237–319

Klobuchar JA (1987) Ionospheric time-delay algorithm for single-frequency GPS users. IEEE Trans Aerosp Electron Syst AES 23(3):325–331

Ovstedal O (2002) Absolute positioning with single-frequency GPS receivers. GPS Sol 5(4):33–44

Spencer J, Frizzelle BG, Page PH, Voger JB (2003) Global positioning system: a field guide for the social sciences. Blackwell Publishing Ltd, Oxford

Tsai LC, Liu CH, Hsiao TY, Huang JY (2009) A near real-time phenomenological model of ionospheric electron density based on GPS radio occultation data. Radio Sci 44:RS5002. doi: 10.1029/2009RS004154

Author Biographies

Ernest Pagaran Macalalad is a PhD candidate at the Graduate Institute of Space Science of the National Central University, Taiwan. His current research interests are GPS positioning using the TaiWan Ionosphere Model (TWIM) and ionospheric scintillation studies from beacon stations and GPS radio occultation from FORMOSAT-3/COSMIC.

Lung-Chih Tsai is a professor at the Center for Space and Remote Sensing Research in National Central University, Taiwan. His research focuses on the study of the ionosphere and upper atmosphere: theory and instrument of ionospheric sounders, data processing and analysis to GPS receiver and radio occultation system, satellite beacon receiver, and JASON.

Joz Wu is a professor at the Center for Space and Remote Sensing Research in National Central University, Taiwan. He graduated in 1974 with a Master of Science degree from National Cheng-Kung University in Taiwan. He acquired a Doktor-Ingenieur degree in 1986 from Universität Hannover, Germany. One of his research topics is phase ambiguity resolution used in the global positioning system (GPS).

Chao-Han Liu is an IEEE Fellow and a Distinguished Research fellow at the Institute of Astronomy and Astrophysics in Academia Sinica in Taiwan. He received his Ph.D. in Electrical Engineering from Brown University in 1965. His major research areas are radio science, space communication, and solar-terrestrial physics.

Terr. Atmos. Ocean. Sci., Vol. 23, No. 1, 9-15, February 2012
doi: 10.3319/TAO.2011.08.03.01(T)

Seismo-Traveling Ionospheric Disturbances Triggered by the 12 May 2008 M 8.0 Wenchuan Earthquake

Jann-Yenq Liu[1, 2, 3, *], Yang-Yi Sun[1], Ho-Fang Tsai[4], and Chien-Hung Lin[5]

[1] *Institute of Space Science, National Central University, Jhongli, Taiwan*
[2] *Center for Space and Remote Sensing Research, National Central University, Jhongli, Taiwan*
[3] *National Space Organization, Hsinchu, Taiwan*
[4] *GPS Science and Application Research Center, National Central University, Jhongli, Taiwan*
[5] *Department of Earth Sciences, National Cheng Kung University, Tainan, Taiwan*

Received 17 May 2011, accepted 3 August 2011

ABSTRACT

A network of 6 ground-based GPS receivers in East Asia was employed to study seismo-traveling ionospheric disturbances (STIDs) triggered by an M 8.0 earthquake which occurred at Wenchuan on 12 May 2008. The network detected 5 STIDs on the south side of the epicenter area. A study on the distances of the detected STIDs to the epicenter versus their associated traveling times shows that the horizontal speed is about 600 m s^{-1}. Applying the circle method, we find that the 5 circles intercept at a point right above the epicenter when the horizontal speed of 600 m s^{-1} is given. Global searches of the ray-tracing and the beam-forming techniques confirm that the STIDs are induced by vertical motions in the Earth's surface during the Wenchuan Earthquake.

Key words: STID, GPS, TEC, Wenchuan Earthquake

Citation: Liu, J. Y., Y. Y. Sun, H. F. Tsai, and C. H. Lin, 2012: Seismo-traveling ionospheric disturbances triggered by the 12 May 2008 M 8.0 Wenchuan Earthquake. Terr. Atmos. Ocean. Sci., 23, 9-15, doi: 10.3319/TAO.2011.08.03.01(T)

1. INTRODUCTION

During earthquake occurrences, vertical motion of the Earth's surface creates mechanical disturbances (acoustic gravity waves or AGWs) in the atmosphere, which propagate into the ionosphere and interact with the ionized gas (hereafter, seismo-traveling ionospheric disturbances; STIDs) (Davies 1990). Using ionograms recorded by MF/HF (median/high frequency) ionosondes and frequency shifts probed by HF Doppler sounders, scientists have observed STIDs triggered by strong earthquakes (Davies and Baker 1965; Leonard and Barnes 1965; Row 1967; Yuen et al. 1969; Tanaka et al. 1984; Blanc 1985; Artru et al. 2004; Liu et al. 2006a). Due to limited numbers and/or short distances among stations of ionosonde or Doppler sounding networks, it is rather difficult to study the propagation of STIDs in detail. Liu et al. (2006a) for the first time applied the circle method (Lay and Wallace 1995) on ionograms recorded by 3 ionosonde stations and found the origin and propagation speed of STIDs triggered by the 26 December 2004 M 9.3 Sumatra Earthquake.

Recently, the total electron content (TEC) derived from data recorded by dense ground-based receivers of the global positioning system (GPS) have been employed to examine STIDs such as Rayleigh, gravity, shock, and tsunami waves triggered by earthquakes (Calais and Minster 1995; Afraimovich et al. 2001; Ducic et al. 2003; Artru et al. 2005; Heki and Ping 2005; Astafyeva and Afraimovich 2006; Jung et al. 2006; Liu et al. 2006b; Astafyeva and Heki 2009; Astafyeva et al. 2009; Liu et al. 2010, 2011). Based on Calais and Minster (1995), most scientists find the time-distance relationship between the triggered disturbances and the epicenter to estimate STID speeds. On the other hand, Jung et al. (2006) and Liu et al. (2006b and 2010) employed the beam-forming and/or the ray-tracing methods analyzing GPS TEC observations to locate the origin and compute average propagation speeds of STIDs triggered by the 13 January 2001 M_w 7.6 El Salvador Earthquake, the 26 December 2004 M_w 9.3 Sumatra Earthquake, and the 20 September 1999 M_w 7.6 Chi-Chi Earthquake, respectively.

* *Corresponding author*
E-mail: jyliu@jupiter.ss.ncu.edu.tw

The paper briefly reviews the amplification effect, the ground-based GPS TEC observation, and the exiting methods of STID analyses. In data analyses, we first employ the time-distance relationship (Calais and Minster 1995) estimating the propagation speed, and apply the circle method (Lay and Wallace 1995) locating the source, and finally use the ray-tracing (Lee and Stewart 1981) and beam-forming (Huang et al. 1999) method to simultaneously find the speed, source location, and onset time of STIDs triggered by the 12 May 2008 M_w 8.0 Wenchuan Earthquake.

2. AMPLIFICATION FACTOR AND IONOSPHERIC GPS TEC

Near-surface earthquakes causing large vertical near-field displacement of the Earth's surface excite mechanical disturbances (i.e., AGWs) in the atmosphere, which propagate to the ionosphere where they couple into the ionized gas inducing disturbances by the effects resulting from collision, i.e., STIDs (Blanc 1985). Since atmospheric density decreases almost exponentially with altitude, energy conservation implies that pulse amplitude increases upward as it propagates into the atmosphere and ionosphere. The amplification factor can reach tens to hundreds of thousands at ionospheric heights (Calais and Minster 1995). Both potential and kinetic energy density can be found. Based on the concept of energy conservation, the energy density of STIDs can be expressed as,

$$1/2\ \rho_G v_G^2 = 1/2\ \rho_I v_I^2 \tag{1}$$

where G and I denote the ground and the ionosphere, respectively. Thus, ρ_G and v_G (ρ_I and v_I) stand for the mass density of the atmosphere and maximum oscillation speed on the ground (in the ionosphere), respectively. For a simple harmonic motion, the oscillation speed can be written $v = A\omega$, where A is the oscillation amplitude and ω is the angular frequency. Therefore, Eq. (1) can be given as

$$\rho_G (A_G \omega_G)^2 = \rho_I (A_I \omega_I)^2 \tag{2}$$

It has been known that when an earthquake occurs, the associated vertical motion of the Earth's surface excites AGWs at numerous frequencies in the atmosphere near the Earth's surface. Since the atmosphere acts a low-pass filter, high frequency waves with periods shorter than 1 minute can quickly be damped. By contrast, low frequency waves with periods longer than 5 minutes generally could travel through the atmosphere efficiently and reach the ionosphere. If the wave-wave interaction is small and/or negligible, the angular frequency of the long-period waves remains unchanged, $\omega = \omega_G = \omega_I$, and we find that the oscillation amplitude is inversely proportional to the density, which is written as

$$A_i / A_G = (\rho_G / \rho_I)^{1/2} \tag{3}$$

It is found the density ratio between the ground and the ionosphere in the solar minimum year of 2008 is 10^{10} (Kelly 2009). Therefore, for an ideal case of a plane source, the amplification factor is about 10^5. However, for a real-world case of a point source of an epicenter or a line source of a fault zone, the amplification factor becomes about 10^4.

The GPS consists of more than 24 satellites, distributed over 6 orbits encircling the globe. Recently, geodetic scientists investigated Earth's surface deformation rates using ground-based GPS networks (e.g., see Calais and Amarjargal 2000). While observing deformation, the same networks can be simultaneously employed to monitor the ionospheric TEC (see papers listed therein Liu et al. 1996, 2001). To simultaneously monitor a large area of the ionosphere, a network of ground-based receivers GPS is ideal to be used. Each satellite transmits two frequency signals, 1575.42 and 1227.60 MHz. Since the ionosphere is a dispersive medium, scientists are able to evaluate the ionospheric effects on the radiowave propagation or the corresponding ray path TEC with measurements of the modulations on carrier phases and code pseudoranges recorded by dual-frequency receivers (cf., Liu et al. 1996). The TEC is defined as the sum (or integration) of the ionospheric electron density along a line-of-sight from a ground-based receiver to the associated GPS satellite at an orbital altitude of about 20200 km (for detail, see Liu et al. 1996). Here, the line-of-sight or slant TEC (STEC) between a GPS satellite and a ground-based receiver can be written as

$$\mathrm{STEC} = (1/40.3)\left[(f_1^2 f_2^2)/(f_1^2 - f_2^2)\right]\left[(L_1 - L_2) - (\delta r + \delta s)\right] \tag{4}$$

where L_1 and L_2 in meter denote the carrier phases of the two frequencies f_1 and f_2 in hertz, and δr and δs are the differential biases for receiver and satellite, respectively. The greatest electron density in the ionosphere usually situates at about a 300-km altitude, which contributes to the heaviest weight in the slant TEC calculation. Based on the spirit of the center of mass, the center of the TEC at about a 350-km altitude is termed the ionospheric point. Therefore, a GPS TEC acts as a space seismometer floating at about 350 km above the Earth's surface and monitors ionospheric disturbances. From recorded GPS broadcast ephemeris, the latitudinal and longitudinal coordinates of each space seismometer can be computed. Assume the ionosphere to be a thin shell at 350 km altitude, the slant TEC along the ray path can be converted, usually using a slant function of the satellite zenith, into the vertical TEC (VTEC, for simplicity hereafter, TEC) at the space seismometer location (Tsai and Liu 1999).

3. SEARCH THE STID ORIGIN

The method of intersecting circles might be the first employed for locating the hypocenter (source, or epicenter) of an earthquake (Lay and Wallace 1995). Scientists calculate the possible circular distance (zone) to the source of seismic waves from each station, which is equal to the product of the propagation speed and the traveling time. When circular zones of three or more stations intersect (i.e., triangulation) at the same location, we then consider the source to be located. The short coming of this method is that the onset time of the earthquake and the propagation speed of the seismic waves should be roughly known in advance.

On the other hand, the ray-tracing technique (Lee and Stewart 1981) and the beam-forming technique (Huang et al. 1999) also have been employed traditionally by seismologists to locate an earthquake source (or hypocenter). In the ray-tracing technique, for a given velocity model, scientists estimate the location of a hypocenter and calculate the arrival time of seismic waves at each seismometer (the forward calculation). From the difference between the calculated and observed arrival times at the seismometers, a new location of the hypocenter is further issued (or given) and tried. When the differences reach the minimum, the iteration process is stopped, and the estimated center is then declared to be the hypocenter. Similarly, scientists can guess the location of a hypocenter but calculate the earthquake onset time from each seismometer (using a backward calculation). The minimum in differences of the calculated onset times is the criterion of the hypocenter location determination. Here, we consider the STID as a seismic wave recorded by a space seismometer orbiting at an altitude of 350 km, and adopt the backward calculation. Assume the average speeds in the vertical and horizontal direction to be V_Z and V_H, respectively. The traveling time to each STID point (i.e., space seismometer "i"), which is the sum of traveling times in the vertical and horizontal directions, can be written as,

$$\Delta t_{i,j} = \Delta Z_{i,j} / V_Z + \Delta S_{i,j} / V_H \quad (5)$$

where the STID at the ionospheric point altitude $\Delta Z_{i,j}$ = 350 km and the horizontal distance from the STID to the trial epicenter $\Delta S_{i,j}$. Since the arrival time t_i at a STID is recorded, the onset time t_{Gi} at the trial epicenter "j" can be computed,

$$t_{Gi,j} = t_i - \Delta t_{i,j} \quad (6)$$

If N points of STIDs are detected, the standard deviation of the computed onset times at the trial center can be written as

$$\sigma_j = [\Sigma (t_{Gi,j} - \mu_j)^2 / N]^{1/2} \quad (7)$$

where μ_j is the associated mean value. The minimum in the standard deviation is the criterion of the location determination of the STID origin/source. The average onset time of the minimum in the standard deviation is used to find when and where the STIDs are activated.

By contrast, for a given onset time, the beam-forming technique (Huang et al. 1999) estimates a hypocenter and computes the speeds by dividing the distances from the hypocenter to the seismometers by the differences between the onset time and observed arrival times at the seismometers. Similarly, when the standard deviation of the computed speeds yields the minimum, the hypocenter is considered to be located. Here we simply guess a onset time t_o and compute the velocity $V_{i,j}$ by dividing the distance from the STID point to the trial epicenter $\Delta S_{i,j}$ by a given traveling time Δt_i (= t_i - t_o) at each STID point,

$$V_{i,j} = \Delta S_{i,j} / \Delta t_i \quad (8)$$

Similarly, for N points of the detected STIDs, the standard deviation of the computed velocities (speeds) at the trial center can be written as

$$\sigma_j = [\Sigma (V_{i,j} - \mu_j)^2 / N]^{1/2} \quad (9)$$

The minimum in the standard deviation is the criterion of the location determination of the STID origin/source. The average speed of the minimum in the standard deviation is considered the STID propagation.

4. OBSERVATION AND INTERPRETATION

A magnitude M 8.0 earthquake occurred in Wenchuan, China (31.0°N, 103.4°E geographic; 24.9°N, 175.5°E geomagnetic) with a depth of 19 km at 0628 UT (universal time) on 12 May 2008. Figure 1 displays the Wenchuan epicenter as well as the locations of 6 GPS receivers and their associated fields of coverage/observation. A high-pass filter with cutoff period less than 10 minutes is applied to analyze the TECs observed at the 6 stations. It can be seen that 5 pronounced fluctuations of STIDs observed at the GPS station kunm at 0635 - 0720 UT which was about 10 minutes after the earthquake occurrence.

Figure 2 illustrates temporal variations of the filtered TEC and the associated distance to the epicenter versus time. A line of the least square fitted of the 5 STID arrival

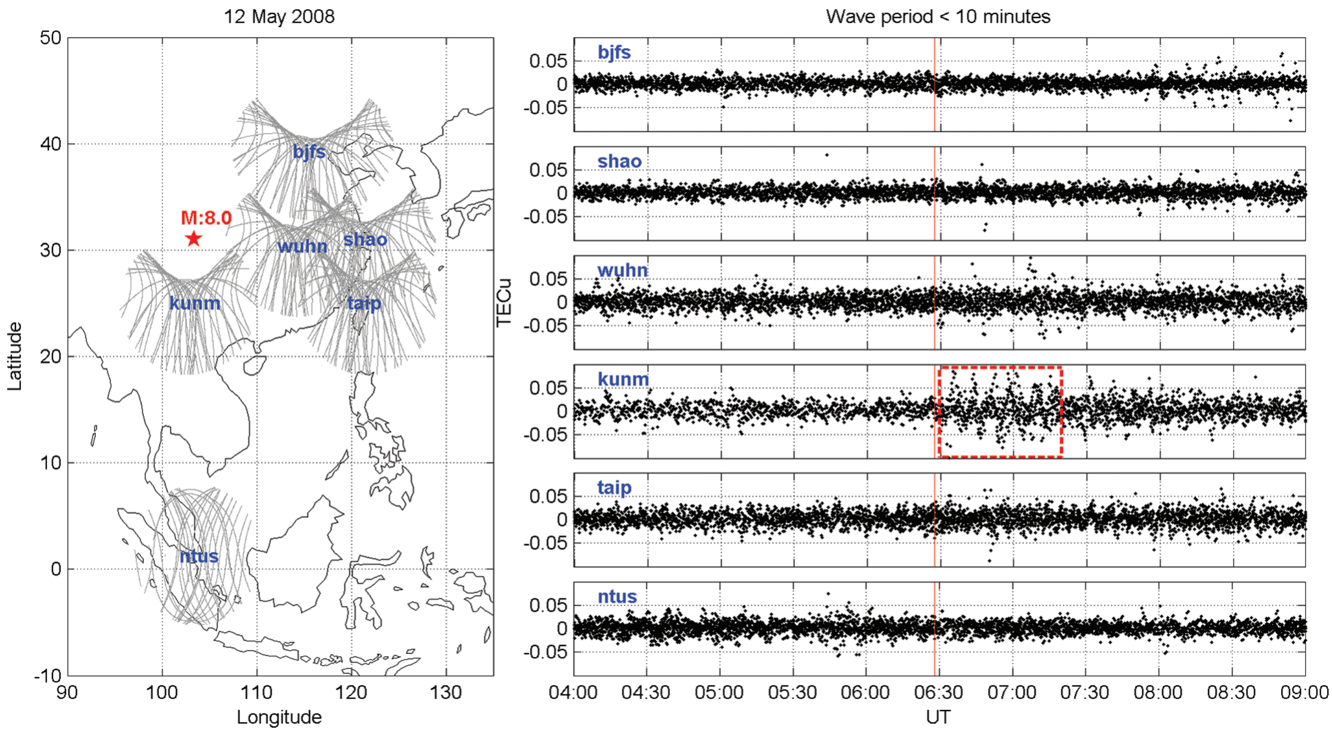

Fig. 1. Locations of the Wenchuan epicenter and 6 ground-based GPD receivers. TEC filtered with a high-pass filter with a cutoff period less than 10 minutes. Pronounced fluctuations of 5 STID signatures were observed by the GPS station kunm. The earthquake magnitude M 7.9 reported by US glological survery (USGS) is later ranked as M 8.0 by China Earthquake Administration (CSA). The red star denotes the epicenter.

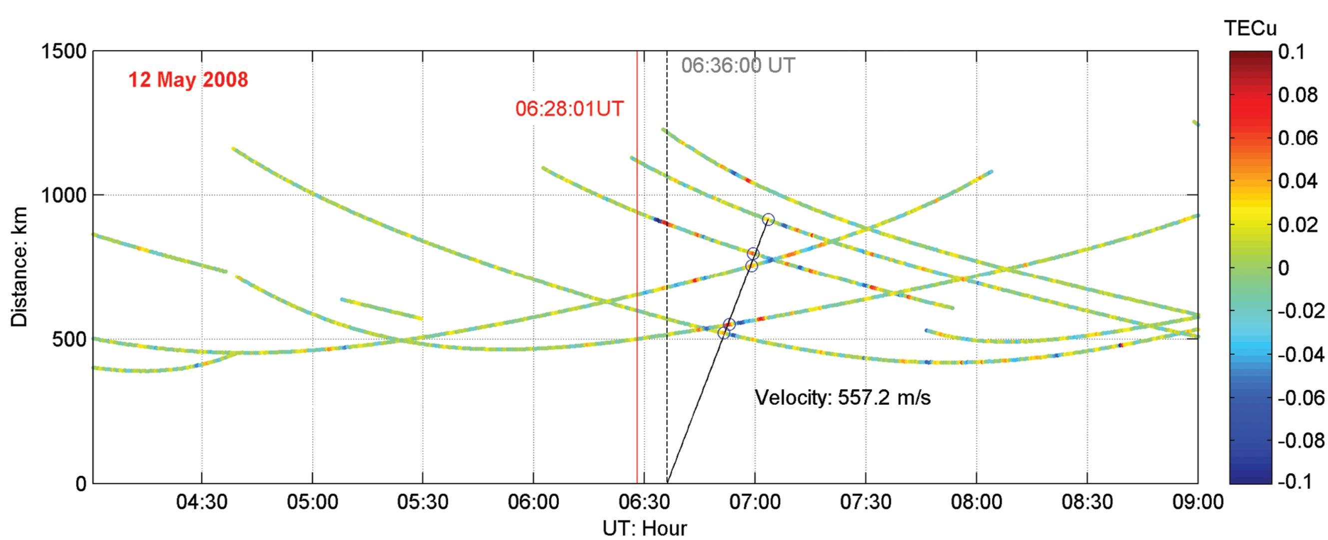

Fig. 2. Temporal variations of the filtered TEC and the associated distance to the epicenter versus that of time. The red vertical line denotes the earthquake onset time (0628 UT). A solid line of the least square fitted of the 5 STID arrival times intersects at 0636 UT.

times intersects at 0636 UT. Since the reported earthquake onset time is 0628 UT, it takes 480 sec (= 8 min) for the STID traveling into the ionosphere. Therefore, the average horizontal and vertical speeds are about 557.2 ± 50 m s^{-1} and 729 (= 350 km/480 sec) m s^{-1}, respectively.

Since the STIDs are assumed to be detected at a fixed altitude of 350 km, we can simply consider their horizontal distances and speeds. Thus, for the circular method, therefore we let the onset time be 0636 UT instead of 0628 UT. Various horizontal speeds 400 - 800 m s^{-1} have been tested. Figure 3 illustrates that when the horizontal speed of 600 m s^{-1} is given, the 5 circles intersect at one location, where is right above (or slightly west of) the Wenchuan epicenter.

In both the ray-tracing and beam-forming calculations, we have tested the trial center within 20 - 33°N and 95 -

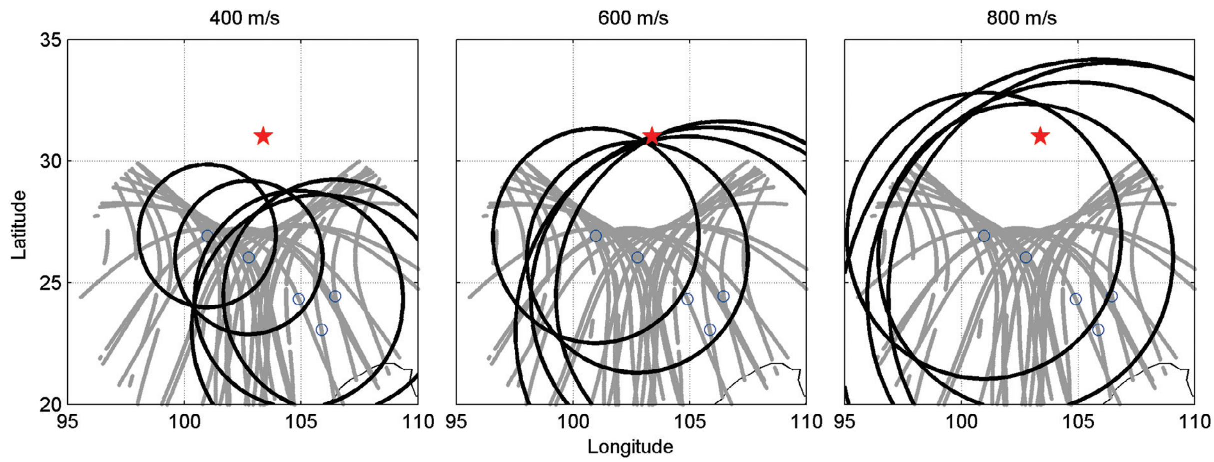

Fig. 3. The circular method: The onset time is assumed to be 0636 UT instead of 0628 UT. Various horizontal speeds 400 - 800 m s^{-1} with a step of 50 m s^{-1} have been tested. The red star and open blue dots denote the epicenter and 5 STID points.

111°E shifting by 0.1°. For the ray-tracing search, we try with the horizontal speed V_H ranging from 200 to 1000 m s^{-1}. The optimal results can be obtained by finding the minimum values of the standard deviation of the calculated onset times, the time difference between the calculated average and reported onset times, as well as the distance between the calculated center (disturbance origin) and the Wenchuan epicenter. It is found that when the horizontal speed 620 m s^{-1}, the contour converges at 30.4°N, 102.9°E where is about 86-km southwest of the Wenchuan epicenter (Fig. 4). Note that the Wenchuan epicenter is within the standard deviation of 25 seconds. The associated onset time is 0628 UT (= 0635 UT-7 minutes of the vertical traveling time).

For the beam-forming technique, we try with the onset time varying from 0600 to 0800 UT and compute the mean speed and standard deviation from each trial center to the 5 STIDs. Figure 5 displays that the onset time at 0638 UT yields the best result (the minimum of the standard deviation) of the STIDs origin being located at 31.1°N, 103.0°E where is about 30 km west of the Wenchuan epicenter. The optimal result of the mean horizontal speed and standard deviation is $V_H = 614 \pm 15$ m s^{-1} traveling away from the STID origin.

5. DISCUSSION AND CONCLUSION

Liu et al. (2006a) observed 2 types of STIDs with traveling speeds of 2.5 km s^{-1} and 370 m s^{-1} triggered by the 24 December 2004 M 9.3 Sumatra earthquake. Liu et al. (2010) found that the STIDs triggered by the M 7.6 Chi-Chi earthquake range from 700 to 900 m s^{-1}. Astafyeva et al. (2009) analyzed STIDs induced by the 4 October 1994 M 8.1 Kurile earthquake and found that starting from about 600 - 700 km away from the epicenter, the disturbance seems to divide into two perturbations which propagate with different velocities, one at about 3 km s^{-1} and the other at about 600 m s^{-1} and suggest that the former perturbation is triggered by acoustic waves launched by a Rayleigh surface wave and the later by the vertical displacements of the ground motion due to the earthquake. Figure 2 shows that the distances of the 5 STIDs to the epicenter are greater than 540 km (= 600 m s^{-1} × 15 min). Artru et al. (2004) and Heki and Ping (2005) show that the acoustic speed is about 300 m s^{-1} from the Earth's surface to the mesosphere at about 90 - 100 km altitude, and speed up to 1000 - 1100 m s^{-1} at 300 km altitude in the ionosphere. Therefore, if the triggered disturbances depart with low elevation angles, they travel nearly horizontally between the troposphere and the mesosphere with speeds of about 300 m s^{-1}, and then both locally and vertically perturb the ionospheric TEC (Liu et al. 2006a). Notably, those disturbances depart with high elevation angles, travel nearly vertically into the thermosphere (ionosphere), and propagate horizontally interacting with the ionized gas, which should travel with average speeds of 600 - 1100 m s^{-1} (Astafyeva et al. 2009; Liu et al. 2010). Based on the above observations and simulations, we speculate that large vertical motions of the Earth's surface near the Wenchuan epicenter excited AGWs in the atmosphere, which propagated obliquely with a moderate elevation angle into the ionosphere as STIDs traveling at 600 m s^{-1}. Although the distance from the epicenter to the GPS station wuhn is not so different, the 5 STIDs are observed only by the GPS station kunm. Scientists hypothesize that the northward (Heki and Ping 2005; Otsuka et al. 2006), and eastward/westward propagating disturbances might be attenuated selectively by interaction between the movements of charged particles in STIDs and the Earth's magnetic fields. Note that the STIDs propagations with a moderate elevation angle in the northward, eastward, and westward directions are perpendicular to the magnetic fields. This once again suggests that AGWs near the Wenchuan epicenter obliquely propagate

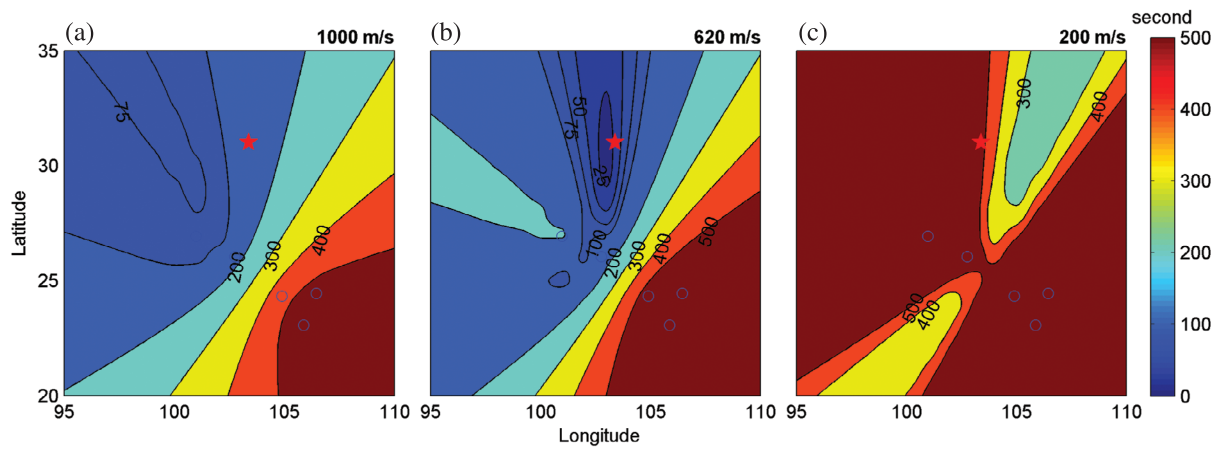

Fig. 4. Contours of standard deviations of the onset time by the ray-tracing technique with horizontal speeds of (a) 1000 m s^{-1}, (b) 620 m s^{-1}, and (c) 200 m s^{-1}.

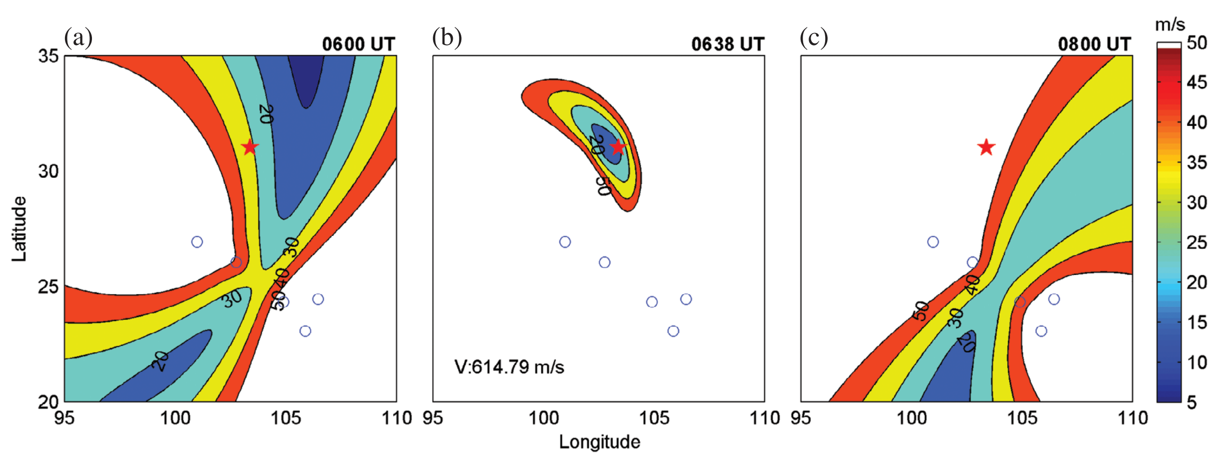

Fig. 5. Contours of the standard deviations of the horizontal speed by the beam-forming technique with onset times of (a) 0600 UT, (b) 0638 UT, and (c) 0800 UT.

with moderate elevation angles into the ionosphere. It is very difficult to obtain ground-based GPS measurements from China. Because no data is available near the epicenter, STIDs induced by the Rayleigh waves cannot be found or identified. Although the data are very limited, the time-distance relationship, the circle method, and the ray-tracing and beam-forming techniques confirm that the STIDs travel with an average speed of 600 m s^{-1} and were induced by the Wenchuan earthquake.

Acknowledgements This research work is partially supported by the National Science Council grant NSC 98-2116-M-008-006-MY3.

REFERENCES

Afraimovich, E. L., N. P. Perevalova, A. V. Plotnikov, and A. M. Uralov, 2001: The shock-acoustic waves generated by earthquakes. *Ann. Geophys.*, **19**, 395-409, doi: 10.5194/angeo-19-395-2001. [Link]

Artru, J., T. Farges, and P. Lognonné, 2004: Acoustic waves generated from seismic surface waves: Propagation properties determined from Doppler sounding observations and normal-mode modelling. *Geophys. J. Int.*, **158**, 1067-1077, doi: 10.1111/j.1365-246X.2004.02377.x. [Link]

Artru, J., V. Ducic, H. Kanamori, P. Lognonné, and M. Murakami, 2005: Ionospheric detection of gravity waves induced by tsunamis. *Geophys. J. Int.*, **160**, 840-848, doi: 10.1111/j.1365-246X.2005.02552.x. [Link]

Astafyeva, E. and E. L. Afraimovich, 2006: Long-distance traveling ionospheric disturbances caused by the great Sumatra-Andaman earthquake on 26 December 2004. *Earth Planets Space*, **58**, 1025-1031.

Astafyeva, E. and K. Heki, 2009: Dependence of waveform of near-field coseismic ionospheric disturbances on focal mechanisms. *Earth Planets Space*, **61**, 939-943.

Astafyeva, E., K. Heki, V. Kiryushkin, E. Afraimovich, and S. Shalimov, 2009: Two-mode long-distance propagation of coseismic ionosphere disturbances. *J. Geophys. Res.*, **114**, A10307, doi: 10.1029/2008JA013853. [Link]

Blanc, E., 1985: Observations in the upper atmosphere of infrasonic waves from natural or artificial sources: A summary. *Ann. Geophys.*, **3**, 673-688.

Calais, E. and J. B. Minster, 1995: GPS detection of ionospheric perturbations following the January 17, 1994, Northridge earthquake. *Geophys. Res. Lett.*, **22**, 1045-1048, doi: 10.1029/95GL00168. [Link]

Calais, E. and S. Amarjargal, 2000: New constraints on current deformation in Asia from continuous GPS measurements at Ulan Baatar, Mongolia. *Geophys. Res. Lett.*, **27**, 1527-1530, doi: 10.1029/1999GL005444. [Link]

Davies, K., 1990: Ionospheric Radio, Peter Peregrinus Ltd., London, 580 pp.

Davies, K. and D. M. Baker, 1965: Ionospheric effects observed around the time of the Alaskan earthquake of March 28, 1964. *J. Geophys. Res.*, **70**, 2251-2253, doi: 10.1029/JZ070i009p02251. [Link]

Ducic, V., J. Artru, and P. Lognonné, 2003: Ionospheric remote sensing of the Denali Earthquake Rayleigh surface waves. *Geophys. Res. Lett.*, **30**, 1951, doi: 10.1029/2003GL017812. [Link]

Heki, K. and J. Ping, 2005: Directivity and apparent velocity of the coseismic ionospheric disturbances observed with a dense GPS array. *Earth Planet. Sci. Lett.*, **236**, 845-855, doi: 10.1016/j.epsl.2005.06.010. [Link]

Huang, B. S., K. C. Chen, H. Y. Yen, and Z. X. Yao, 1999: Re-examination of the epicenter of the 16 September 1994 Taiwan Strait earthquake using the beam-forming method. *Terr. Atmos. Ocean. Sci.*, **10**, 529-542.

Jung, T. K., J. Y. Liu, H. F. Tsai, B. S. Huang, C. H. Lin, S. B. Yu, and Y. S. Yeh, 2006: Ionospheric disturbances triggered by the M_w 7.6 earthquake off the coast of El Salvador on 13 January 2001. *Terr. Atmos. Ocean. Sci.*, **17**, 345-351.

Kelly, M. C., 2009: The Earth's Ionosphere, Academic Press, 2nd Edition, Boston, 556 pp.

Lay, T. and T. C. Wallace, 1995: Modern Global Seismology, Academic Press, San Diego, 512 pp.

Lee, W. H. K. and S. W. Stewart, 1981: Principles and Applications of Microearthquake Networks, Academic Press, New York, 293 pp.

Leonard, R. S. and R. A. Barnes Jr., 1965: Observation of ionospheric disturbances following the Alaska earthquake. *J. Geophys. Res.*, **70**, 1250-1253, doi: 10.1029/JZ070i005p01250. [Link]

Liu, J. Y., H. F. Tsai, and T. K. Jung, 1996: Total electron content obtained by using the global positioning system. *Terr. Atmos. Ocean. Sci.*, **7**, 107-117.

Liu, J. Y., Y. I. Chen, Y. J. Chuo, and H. F. Tsai, 2001: Variations of ionospheric total electron content during the Chi-Chi earthquake. *Geophys. Res. Lett.*, **28**, 1383-1386, doi: 10.1029/2000GL012511. [Link]

Liu, J. Y., Y. B. Tsai, S. W. Chen, C. P. Lee, Y. C. Chen, H. Y. Yen, W. Y. Chang, and C. Liu, 2006a: Giant ionospheric disturbances excited by the M9.3 Sumatra earthquake of 26 December 2004. *Geophys. Res. Lett.*, **33**, L02103, doi: 10.1029/2005GL023963. [Link]

Liu, J. Y., Y. B. Tsai, K. F. Ma, Y. I. Chen, H. F. Tsai, C. H. Lin, M. Kamogawa, and C. P. Lee, 2006b: Ionospheric GPS total electron content (TEC) disturbances triggered by the 26 December 2004 Indian Ocean tsunami. *J. Geophys. Res.*, **111**, A05303, doi: 10.1029/2005JA011200. [Link]

Liu, J. Y., H. F. Tsai, C. H. Lin, M. Kamogawa, Y. I. Chen, C. H. Lin, B. S. Huang, S. B. Yu, and Y. H. Yeh, 2010: Coseismic ionospheric disturbances triggered by the Chi-Chi earthquake. *J. Geophys. Res.*, **115**, A08303, doi: 10.1029/2009JA014943. [Link]

Liu, J. Y., C. H. Chen, C. H. Lin, H. F. Tsai, C. H. Chen, and M. Kamogawa, 2011: Ionospheric disturbances triggered by the 11 March 2011 *M*9.0 Tohoku earthquake. *J. Geophys. Res.*, **116**, A06319, doi: 10.1029/2011JA016761. [Link]

Otsuka, Y., N. Kotake, T. Tsugawa, K. Shiokawa, T. Ogawa, Effendy, S. Saito, M. Kawamura, T. Maruyama, N. Hemmakorn, and T. Komolmis, 2006: GPS detection of total electron content variations over Indonesia and Thailand following the 26 December 2004 earthquake. *Earth Planets Space*, **58**, 159-165.

Row, R. V., 1967: Acoustic?gravity waves in the upper atmosphere due to a nuclear detonation and an earthquake. *J. Geophys. Res.*, **72**, 1599-1610, doi: 10.1029/JZ072i005p01599. [Link]

Tanaka, T., T. Ichinose, T. Okuzawa, T. Shibata, Y. Sato, C. Nagasawa, and T. Ogawa, 1984: HF-Doppler observations of acoustic waves excited by the Urakawa-Oki earthquake on 21 March 1982. *J. Atmos. Terr. Phys.*, **46**, 239-245, doi: 10.1016/0021-9169(84)90150-8. [Link]

Yuen, P. C., P. F. Weaver, R. K. Suzuki, and A. S. Furumoto, 1969: Continuous, traveling coupling between seismic waves and the ionosphere evident in May 1968 Japan earthquake data. *J. Geophys. Res.*, **74**, 2256-2264, doi: 10.1029/JA074i009p02256. [Link]

Amplitude morphology of GPS radio occultation data for sporadic-*E* layers

Wen-Hao Yeh,[1] Cheng-Yung Huang,[2] Tung-Yuan Hsiao,[3] Tsen-Chieh Chiu,[1] Chien-Hung Lin,[4] and Yuei-An Liou[5]

Received 28 April 2012; revised 8 October 2012; accepted 8 October 2012; published 7 November 2012.

[1] Using the Global Positioning System radio occultation (GPSRO) technique, the observation of the global ionosphere becomes possible. The irregularity in the ionospheric sporadic-*E* (*Es*) layer, which is probably caused by wind shear, can be investigated by analyzing the signal-to-noise ratio (SNR) of RO signal. In this study, the relation between the amplitude of RO signals and the electron density profiles of the ionosphere is simulated, and RO data recorded in the time period from mid-2008 to mid-2011 are used for the analysis. Based on the simulation results, the multiple-layer-type (MLT) and the single-layer-type (SLT) *Es* layers which are defined by the shape of SNR, are used to analyze the global distribution of *Es* layer. The seasonal MLT *Es* layer is compared with the seasonal wind shear, which is obtained from the Horizontal Wind Model (HWM07). Furthermore, the seasonal MLT *Es* layer is compared with the SLT *Es* layer, and the global altitude distributions of MLT and SLT *Es* layers are similar while the magnitude distributions are different. Unlike the MLT *Es* layer, the global distribution of the SLT *Es* layer is similar to the distribution of *E* region peak electron density (N_mE), which is related to the solar zenith angle.

Citation: Yeh, W.-H., C.-Y. Huang, T.-Y. Hsiao, T.-C. Chiu, C.-H. Lin, and Y.-A. Liou (2012), Amplitude morphology of GPS radio occultation data for sporadic-*E* layers, *J. Geophys. Res.*, *117*, A11304, doi:10.1029/2012JA017875.

1. Introduction

[2] The Earth's ionosphere is an envelope containing partially ionized gas from about 60 to a thousand kilometers in altitude. The ionospheric *E* region ranges between 90 and 150 km. In the lower *E* region, a thin layer of enhanced electron density, called sporadic-*E* (*Es*) layer, appears sporadically in the altitude range from 90 to 120 km. The *Es* layer has been the subject of much research for many decades [e.g., *Whitehead*, 1970; *Whitehead*, 1989; *Mathews*, 1998] with the wind shear theory being the most likely explanation for the formation of this layer [*Whitehead*, 1961]. *Carrasco et al.* [2007] simulated the effect of winds and electric fields on the formation of the *Es* layer. Vertical shear in the zonal wind is an orientation requirement to establish the *Es* layer [*Kelley*, 2009]. *Pan and Tsunoda* [1999] and *Urbina et al.* [2000] observed quasiperiodic structures with descending echoing layers at altitudes above 100 km. *Pan and Tsunoda* [1999] also used semidiurnal neutral-wind variations to explain the slop sign reversals in the VHF radar observations. Furthermore, the seasonal dependence of the midlatitude *Es* layer is associated with the annual variation of meteor deposition [*Haldoupis et al.*, 2007].

[3] With the advent of Global Positioning System (GPS) technology, the global *Es* layer can be observed by using the radio occultation (RO) technique, which utilizes satellites at low Earth orbit (LEO) to receive GPS signals propagating through the atmosphere and ionosphere. *Hocke et al.* [2001] used data from the GPS/Meteorology experiment (GPS/MET) to find irregularities in the *Es* layer that occur at altitudes of 90–110 km. *Wu et al.* [2005] used German Challenging Minisatellite Payload (CHAMP) data to establish seasonal maps of the *Es* layer. In 2006, six LEO satellites were launched for the FORMosa SATellite Mission −3/ Constellation Observing System for Meteorology, Ionosphere, and Climate (FORMOSAT-3/COSMIC, or F-3). This system provides 2000–2500 profiles of high spatial and temporal resolutions for global analysis per day. *Arras et al.* [2008] used data from CHAMP, Gravity Recovery and Climate Experiment (GRACE), and F-3 to show the influence of the Earth's magnetic field on the *Es* layer. Furthermore, *Arras et al.* [2009] made a comparison between the occurrence of the *Es* layer and wind shear at midlatitudes based on the CHAMP, GRACE, and F-3 data.

[1]Department of Electrical Engineering, National Central University, Chung-Li, Taiwan.
[2]GPS Science and Application Research Center, National Central University, Chung-Li, Taiwan.
[3]Department of Information Technology, Hsing Wu Institute of Technology, New Taipei City, Taiwan.
[4]Department of Earth Science, National Cheng Kung University, Tainan, Taiwan.
[5]Center for Space and Remote Sensing Research, National Central University, Johng-Li, Taiwan.

Corresponding author: C.-Y. Huang, GPS Science and Application Research Center, National Central University, 300 Chung-Da Rd., Chung-Li 32001, Taiwan. (yusn2845@gmail.com)

0148-0227/12/2012JA017875

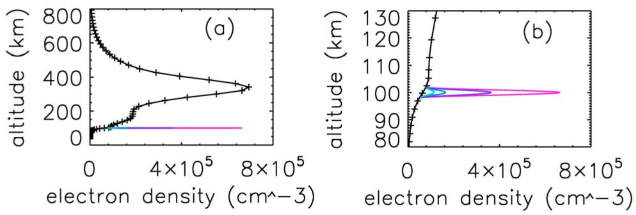

Figure 1. Electron density profiles for simulations. The black profile is the background electron density. The light blue, dark blue, purple, and pink profiles are the maximum electron density of *Es* layer added on the background electron density which are 0×10^5, 0.5×10^5, 1×10^5, 3×10^5, 6×10^5 cm^{-3}, respectively.

[4] In previous studies of the *Es* layer by using RO data, the relation between the *Es* layer electron density and its signature in the RO amplitude profile has been examined [e.g., *Wickert et al.*, 2004; *Pavelyev et al.*, 2007; *Yakovlev et al.*, 2008; *Yakovlev et al.*, 2010; *Zeng and Sokolovskiy*, 2010]. Nevertheless, the statistical analysis with the shape of RO amplitude has not yet received the proper attention. In this study, RO data recorded in the time period from mid-2008 to mid-2011 are used to derive the irregular degree (ID) from the RO signal-to-noise ratio (SNR) data to determine the altitude range and degree of the *Es* layer irregularities. Furthermore, the *Es* layer profiles are separated into the multiple layer type (MLT) and single layer type (SLT) by considering the shape of the SNR profile. The altitude distributions of the MLT and SLT *Es* layers are similar but the magnitude distributions are not. Besides the temporal and spatial analysis of the *Es* layer, the wind shear information as given by the Horizontal Wind Model (HWM07) [*Drob et al.*, 2008] is also used for comparison with the distribution of *Es* layer to examine the correlation between Es layer and wind shear. In Section 2, the RO amplitude profiles affected by SLT and MLT *Es* layers are simulated. In Section 3, the definition of the ID and the separation method of SLT and MLT RO amplitude profiles are described. A comparison of the results and a discussion are displayed and described in section 4, followed by summary.

2. Relation Between Electron Density and Amplitude Profiles

[5] In this study, the *Es* layer profiles are separated into the MLT and SLT. In order to differentiate between these two types of *Es* layers, a ray tracing algorithm is used to retrieve the amplitude profiles from the prescribed electron density profiles. The electron density profiles used for the simulations are shown in Figure 1. The black plus signed line is the background electron density profile obtained from the Thermosphere Ionosphere Electrodynamics General Circulation Model (TIEGCM) result. The light blue, dark blue, purple, and pink lines are the profiles of *Es* layers. The altitude, thickness and horizontal extension of *Es* layer are 90–110 km, 0.5–5 km and 10–1000 km, respectively [*Wu et al.*, 2005]. In this study, the altitude, maximum thickness, and horizontal extension of *Es* layer are set to be 100 km, 4 km and 500 km, respectively. The electron density distribution $N_e(x, y)$ is given by:

$$
\begin{aligned}
&N_e(x,y) = N_b + N_{Es}(x,y)\\
&N_{Es}(x,y) = P(x) + N_{\max}\cos\left[\frac{(x-x_0)\pi}{500}\right]\cos\left\{\frac{(y-y_0)\pi}{4\cos\left[\frac{(x-x_0)\pi}{500}\right]}\right\},\\
&\quad if\ -\frac{\pi}{2} < \frac{(x-x_0)\pi}{500} < \frac{\pi}{2}\ and\ -\frac{\pi}{2} < \frac{(y-y_0)\pi}{4\cos\left[\frac{(x-x_0)\pi}{500}\right]} < \frac{\pi}{2}\\
&P(x) = \sum_{1}^{n} A_n \sin\left(2\pi(x-x_0)\frac{W_n}{500}\right)\\
&N_{Es}(x,y) = 0, else
\end{aligned}
\qquad (1)
$$

where, N_b, N_{Es}, $N_{\max}$, P, and (x_0, y_0) are the background electron density, electron density of *Es* layer, the maximum electron density of *Es* layer, the perturbation function, and the coordinate of the maximum electron density of *Es* layer, respectively. The background electron density profile (N_b) in Figure 1 is result of TIEGCM model. The perturbation function is formed by several sine waves with different amplitudes (A_n) and wave numbers (W_n). One of the N_{Es}, considering the curvature to conform the 100 km in altitude and $P(x)$ is set to be 0, used for simulation is shown in Figure 2 (top). The *Es* layer is often affected by the external forces and irregularities can take place. The effect of gravity waves on the N_{Es} is investigated by introducing gravity-wave-related perturbation. Two different cases of perturbation are examined, and the Earth's curvature is also considered (cf. Figure 2). In Figure 2, the center of the Earth is located at (0,0), (x_0, y_0) is set to be (0,6480.744), and the radius of the Earth is set to be 6380.744 km. In Figure 2 (middle), n is set to be 3, and A_1, A_2,

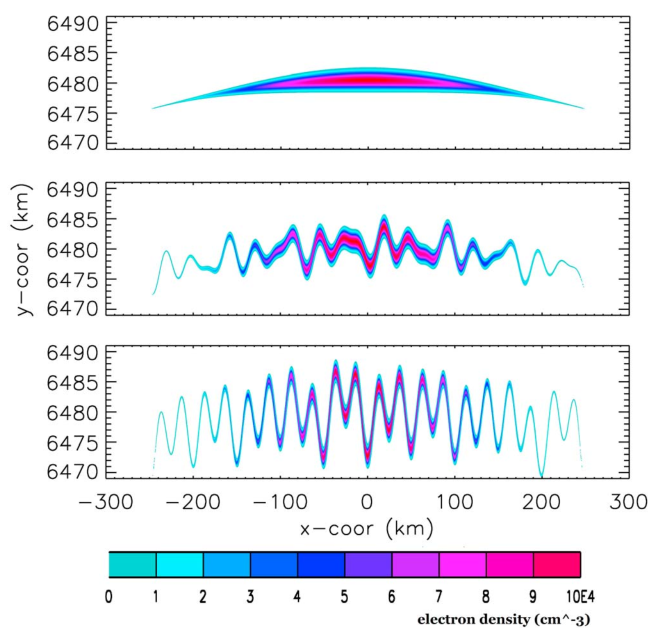

Figure 2. Horizontal distribution of *Es* layers which have (top) no irregularity and (middle and bottom) have irregularities.

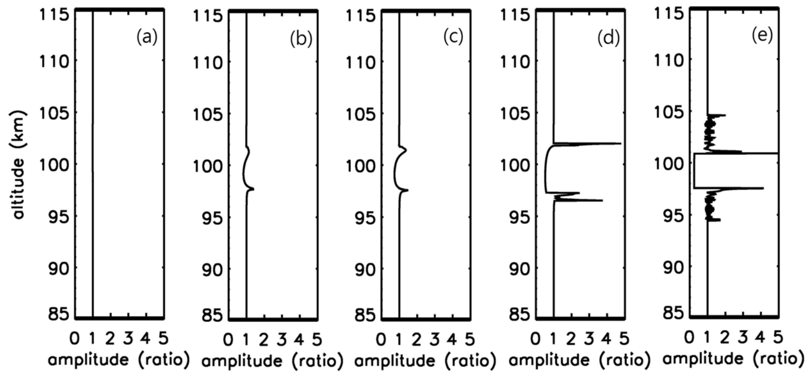

Figure 3. Simulated amplitude profiles by using the background electron density profile and different added electron density of *Es* layer. The shape of the added *Es* layer is like the shape in Figure 2 (top) which has no irregularity. The maximum electron density of *Es* layer added on the background electron density from Figure 3a to Figure 3e are 0×10^5, 0.5×10^5, 1×10^5, 3×10^5, 6×10^5 cm^{-3}, respectively.

A_3, W_1, W_2, and W_3 are set to be 1.2, 1.8, 1, 20, 14, and 8, respectively. In Figure 2 (bottom), n is set to be 4, and A_1, A_2, A_3, A_4, W_1, W_2, W_3, and W_4 are set to be 1.2, 1.8, 1, 5, 6, 10, 8, and 20, respectively. In the simulations, the *Es* layer is located at the tangent point of signal trajectories, and the frequency of the signal is 1.575 GHz (L1). The ray tracing algorithm in W.-H. Yeh et al. (Ray tracing simulation in nonspherically symmetric atmosphere for GPS radio occultation, submitted to *GPS Solutions*, 2012) is used to integrate signal trajectory. The energy flux calculation method in *Sokolovskiy* [2000] is used to estimate amplitude profiles.

[6] The simulations for the profiles of the RO signal amplitude with different maximum electron density of *Es* layer are shown in Figures 3 and 4. The shape of *Es* layer in Figure 2 (top) is used to simulate the amplitude profiles in Figure 3. The simulation results by using $N_{\max} = 0 \times 10^5$, 0.5×10^5, 1×10^5, 3×10^5, and 6×10^5 are shown in Figures 3a–3e, respectively. In the ionosphere, the refractive index decreases as the electron density increases [*Davies*, 1990]. The signal propagating in the ionosphere is bent due to the refractivity gradient. The bent signal trajectory causes a focusing/debunching phenomenon in the amplitude profile. In Figure 3a, the amplitude of signal has no obvious shake, which indicates that the effect of the background profile is very little. The positive/negative humps in Figures 3b and 3c, which are the local maximum/minimum in the profiles, are due to the focusing/debunching of the signal propagating through the *Es* layer. According to the geometrical optics, focusing/debunching of signal occurs if $d^2\,Ne/dh^2$ is positive/negative, where Ne and h are electron density and altitude, respectively. When the electron density of *Es* layer is large, the interference phenomenon will occur in the focusing parts of amplitude profile, and shown in Figures 3d and 3e. The simulation results of the shape of *Es* layer in the first and second panels of Figure 2 are shown in Figures 4a and 4b, respectively. Due to the irregularity of *Es* layer, the refractivity gradient in the signal trajectories is more complex and cause irregular perturbation in amplitude profiles. The irregularity of the *Es* layer in the third panel of Figure 2 is larger than in the second panel. The larger irregularity of *Es* layer often causes the larger irregular degree of irregular amplitude.

[7] Comparing the electron density with the simulated amplitude profiles in Figures 2–4, it is found that the distribution of amplitudes in Figures 3b–3e show an obvious characteristic. Due to the relation between the electron density and amplitude profiles, the distribution of amplitude has one negative hump and its altitude is very close to the altitude of the dense layer of electron density profiles. There are two positive humps (type-I) or two interference portions (type-II) located at the top and bottom of the electron density layer. Four examples of observational amplitude profiles are shown in Figures 5a–5d (left). Figures 5a–5b (left) are type-I and type-II SLT amplitude profiles, respectively. Figure 5c (left) is MLT amplitude profile. The shape characteristics of the

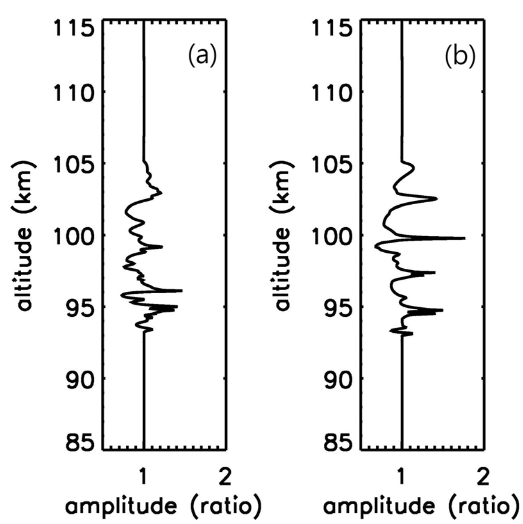

Figure 4. Simulated amplitude profiles by using the background electron density profile and different shape of added *Es* layer. The shape and electron density distribution of added *Es* layer used for Figure 4a and Figure 4b are in the middle and lower panels in Figure 3, respectively.

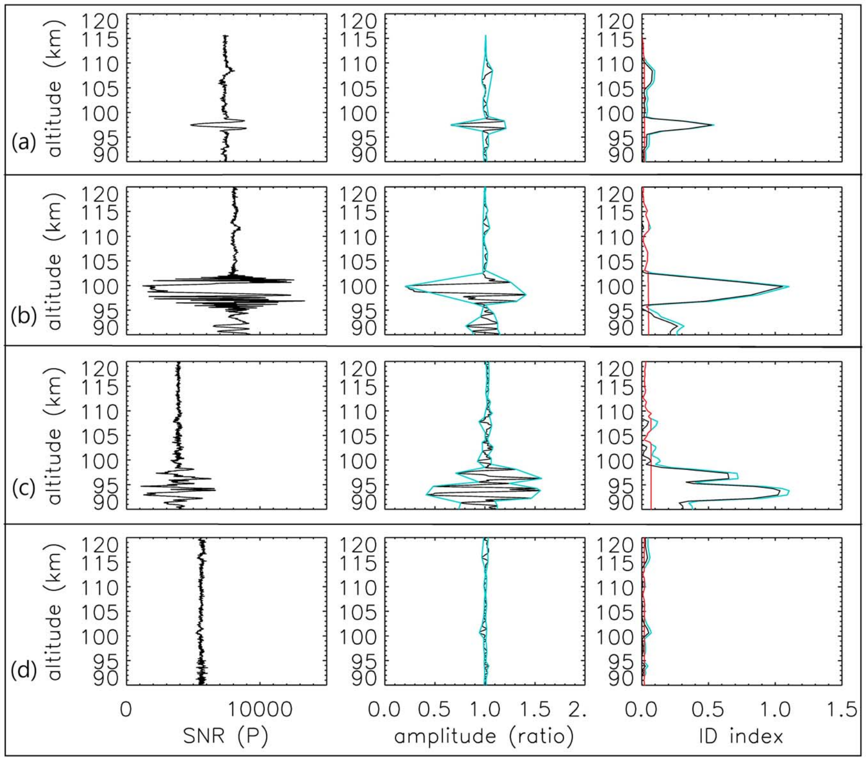

Figure 5. Profiles of SNR, ID index, and intermediate productions (amplitude ratio) of three different type fluctuations: (a) type-I SLT (atmPhs_C004.2010.036.00.30.G07_2010.2640_nc), (b) type-II SLT (atmPhs_C005.2009.244.21.44.G10_2010.2640_nc), (c) MLT (atmPhs_C001.2010.029.01.35. G14_2010.2640_nc), and (d) noisy type (atmPhs_C005.2010.072.00.28.G28_2010.2640_nc).

amplitude profiles in these panels conform to the simulated results. Figure 5d (left) shows that the amplitude profile is not affected by the *Es* layer.

3. Analysis Method

[8] Compare with the simulation and observation results, the large perturbation of amplitude in observation data is caused by ionospheric irregularities. In order to study the irregularities, the ID index is defined and calculated in the following three steps:

[9] (1) Change the SNR to the relative amplitude. The average upper altitude of the high rate (50 Hz) GPS occultation measurement of F-3 is 120 km [*Wickert et al.*, 2009]. Generally, the value of SNR begins to decrease due to the effect of the neutral atmosphere below 40 km in altitude. Therefore, the analysis in this study is conducted from 50 to 120 km in altitude. The average value of SNR from 50 to 120 km is the normalizing factor. The relative amplitude is obtained by dividing SNR with the normalizing factor.

[10] (2) Smooth the relative amplitude profile. The smooth process is used to remove the noise in relative amplitude profiles. The smooth method $f_s = [I + S^T \Gamma S]^{-1} f_u$ [*Feng and Herman*, 1999], where f_s, f_u, I, S, and Γ are the smoothed result, raw data, unitary matrix, constraint smoothing matrix, and diagonal matrix with degrees control element, respectively, is used in this study. The normalized and smoothed relative amplitude profiles are the black lines shown in Figures 5a–5d (middle).

[11] (3) Decompose the amplitude into upper and lower envelopes by using empirical mode decomposition (EMD) [*Huang et al.*, 1998]. It should be noted that in order to avoid distorting the analysis results, the linear connection is replaced with a cubic spline to connect the local maxima/minima for the upper/lower envelopes. The upper and lower envelopes are the blue lines shown in Figures 5a–5d (middle).

[12] (4) Derive pre-ID index by using the value of the upper envelope minus that of the lower envelope. The pre-ID index profiles are the blue lines shown in Figures 5a–5d (right).

[13] (5) Derive ID index profile by using the value of pre-ID index profile without the background profile. In the unaffected portion of the *Es* layer, the background profile is the pre-ID index profile. In the affected portion of the *Es* layer, the background profile is set to be a linear portion between the unaffected upper and lower portions. The background and ID index profiles are represented by the red and black lines shown in Figures 5a–5d (right), respectively.

[14] Comparing the SNR and ID profiles in Figure 5, it is found that the altitude range and the large ID index correspond to that of the large irregularity in the SNR profiles.

[15] The high rate (50 Hz) of L1 GPS occultation SNR data of F-3 recorded from the 181st day of 2008 to the 180th day of 2011 are used for data analysis. We divided the year into four seasons (based on the northern hemisphere): winter is from December to February, spring is from March to May, summer is from June to August, and autumn is from September to November. All data except the SLT data

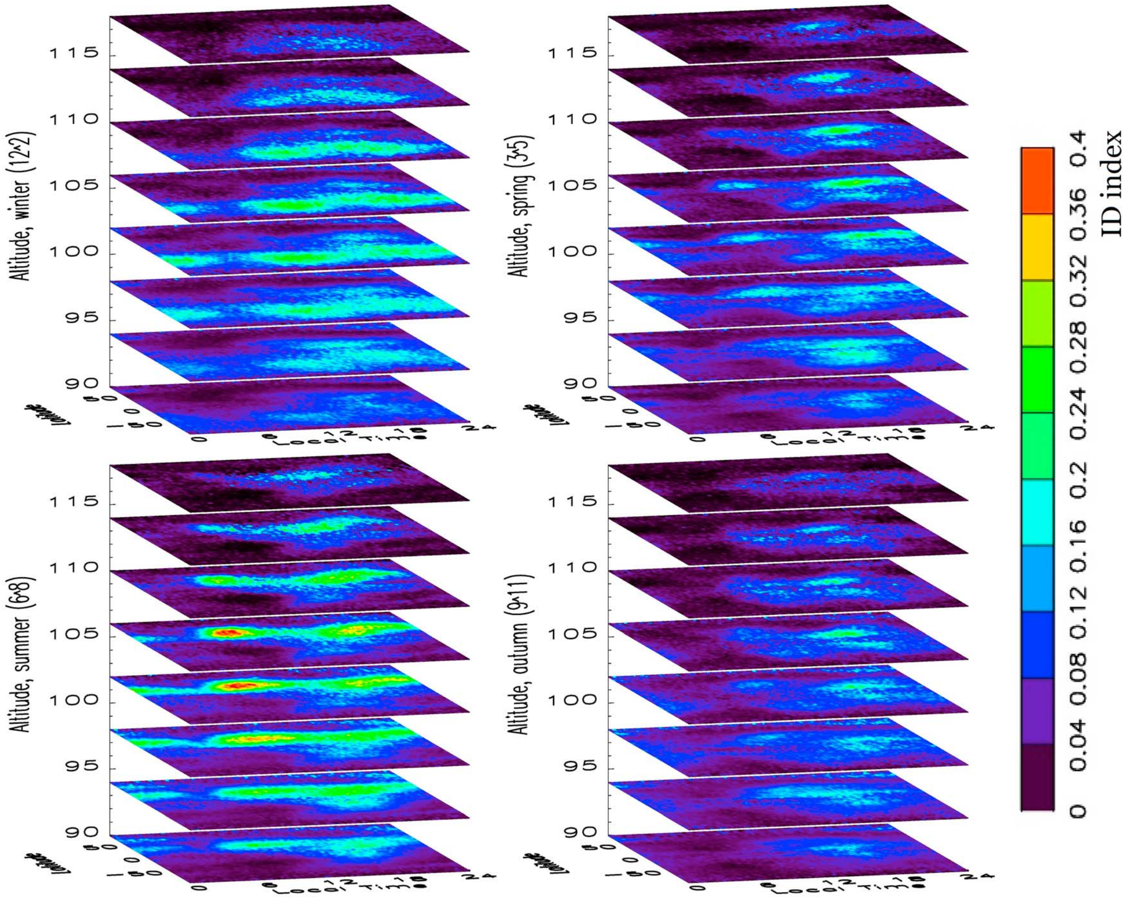

Figure 6. Local time-latitude-altitude analysis of the ID index of the MLT *Es* layer in four seasons.

are used for the 3-dimensional local time-geographic latitude-altitude (LT-Lat-Alt) analysis. We average the individual ID index value over 20 min in local time, 5° in geomagnetic latitude, and 1 km in altitude, while the coordinates of the center are shifted every 4 min and 1° along local time and geomagnetic latitude, respectively.

[16] In addition to data analysis, the SLT data is separated from all RO data. The SNR profile is regarded as type-I SLT profile if it satisfies following conditions: (i) The altitude of the maximum ID (maxID) corresponds to a negative hump; (ii) At the upper and lower altitude of maxID, there are two positive humps near the negative hump at the altitude of maxID. Two ID values correspond to these two positive humps are denoted as ID_S and ID_L. The value of ID_L is larger than ID_s. In this condition, ID_S/ID_L should larger than 2/3; (iii) the nearest negative hump at each upper and lower altitudes of the maxID is smaller than one third of maxID; (iv) except the altitude region of (iii), the ID of the SNR profile is not larger than one third of the maxID. The SNR profile is regarded as type-II SLT profile if it satisfies following conditions: (i) The SNR profile satisfies the *Es* event identified conditions in *Zeng and Sokolovskiy* [2010]; (ii) The standard deviation profile of relative amplitude calculated in 1 km interval has only two local maximum which are larger than 0.2. The value 0.2 is an empirically found threshold to separate the general amplitude and interference amplitude. And the two local maximum indicate two interference portions located at the top and bottom of the electron density layer. The ratio of the SLT and all data is about 1:50. Due to the small amount of SLT data, it cannot be used for LT-Lat-Alt analysis. The local time-latitude (LT-Lat) distribution of maxID and altitude of SLT data are used for analysis. We average the individual ID index value over 28 min in local time, 7° in geomagnetic latitude, while the coordinates of the center are shifted every 4 min and 1° along local time and geomagnetic latitude, respectively.

4. Analysis Results and Discussions

4.1. MLT *Es* Layer Distribution

[17] The 3-dimensional LT-Lat-Alt analysis of all data except for the SLT data for the four seasons is shown in Figure 6. This can be regarded as the analysis of the MLT *Es* layer with 510–570 thousand pieces of data used for analysis for each season. The maximum value of ID index is identified at about 100–108 km in altitude. In summer, in the northern hemisphere, there is a clear semidiurnal pattern of high ID with two ribbons, the morning ribbon (MR) and the afternoon ribbon (AR) that occurs from 90 to 120 km in altitude, which is the range in which the *Es* layer appears [*Arras et al.*, 2008]. The maximum of MR and AR occur around 10:00 and 20:00LT, which agree with *Wu et al.* [2005]. In winter, there is a clear semidiurnal pattern, which is similar to the pattern in summer, also occurs in the southern hemisphere while the maximum

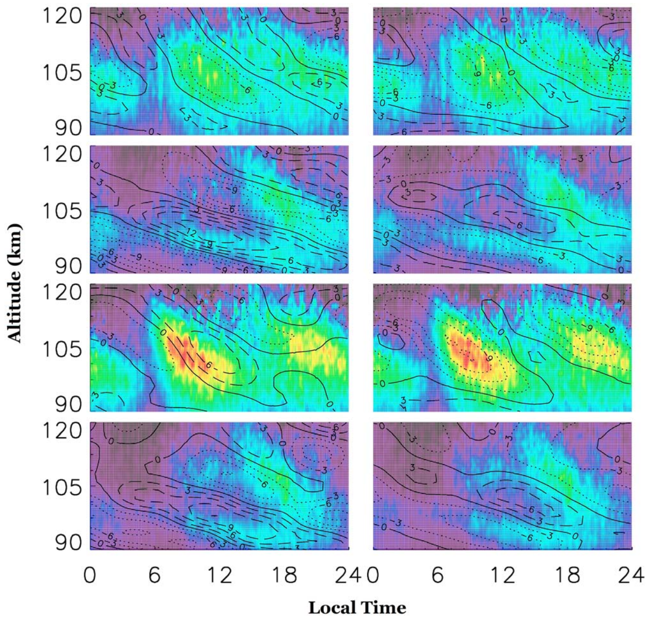

Figure 7. Distribution of the ID index of the MLT *Es* layer and wind shear. The seasons and latitudes in the figure are winter at −40°, spring at 20°, summer at 40°, and autumn at 20° (top to bottom). Color code is similar to Figure 3, which are ID index distributions of the MLT *Es* layer. Contour (left) meridional and (right) zonal wind shear. The zero, negative and positive wind shear are marked by solid, dotted and dashed isolines, respectively, for meridional and zonal wind shear.

MR occurs about one hour later than in summer. In winter/summer, a diurnal pattern occurs in the northern/southern hemisphere with a maximum around 1500LT. The latitude of where patterns occur in southern/northern in winter/summer is about −40°/40°, and in northern/southern in winter/summer is about 15°/−5°, which are agree with *Arras et al.* [2009]. In the northern hemisphere in spring and autumn, the maximum of MR and AR occurrence time is similar to the occurrence time in the southern hemisphere in winter, while in the southern hemisphere the MR and AR occurrence times are closer to noon, about 11:00LT and 17:00LT, respectively. The latitude of where patterns occur in spring/autumn in the northern and southern hemisphere are about 20° and −20°, respectively, which agree with *Arras et al.* [2009]. A comparison of the ID magnitudes in the four seasons shows that the summer maximums agree with *Haldoupis et al.* [2007] and *Arras et al.* [2009].

4.2. Comparison Between Horizontal Wind Shear and MLT *Es* Layer

[18] *Arras et al.* [2009] studied the occurrence frequency of the *Es* layer from 80 to 100 km by using the wind shear information from the Collm Observatory. In this study, HWM07, which is a statistical representation of the horizontal wind fields of the Earth's atmosphere from the ground to the exosphere (0–500 km) [*Drob et al.*, 2008], is used to calculate the wind shear in the *Es* layer region. The distribution of the wind shear in 2010 and ID index distribution for all four seasons are shown in Figure 7. In the figure, the distributions are shown at latitudes of −40, 20, 20, and 40, which are near the latitude where the maximum ID index occurs, in winter, spring, summer and autumn, respectively. The contours in Figure 7 show the mean wind shear from 90 to 120 km in altitude in 2010 for the four seasons as obtained by using HWM07. The zero, negative and positive wind shears are marked by solid, dotted and dashed isolines, respectively, in the meridional and zonal wind shear panels in Figure 7. The color codes indicate the ID index distributions of the MLT *Es* layer. Negative wind shear is required for *Es* layer formation [*Arras et al.*, 2009]. The ID index distributions agree with the negative zonal wind shear for winter and summer, and the negative meridional wind shear for winter. Nevertheless, the agreement with wind shear is not obvious in spring and autumn although the large ID index also distributes in the negative meridional or zonal wind region. The global zonal wind shear distributions at the corresponding altitude of the maxID of the MLT *Es* layer in the four seasons are shown in Figure 8 (right). It is found that in the maxID distributions of the MLT *Es* layer, which are shown in Figure 8 (middle), the high maxID index is related to the high negative zonal wind shear, especially in summer. Compare the middle and right panels of Figure 8 with Figure 7, the distribution of MLT *Es* layer is correlated with the negative wind shear.

4.3. SLT *Es* Layer Distribution

[19] The LT-Lat analyses of maxID and its corresponding altitude of the SLT and MLT *Es* layers are shown in Figures 8 and 9. Due to the lack of the SLT data at high latitudes, we only show the results in latitude ranges from −70° to 70°. The maxID distributions for the four seasons are shown in Figure 8. The semidiurnal and diurnal of the MLT *Es* layer have been described above. Unlike those in the MLT layer, the maxID distributions of the SLT *Es* layer in the four seasons are very similar to one another. Furthermore, the maxID distributions of the SLT *Es* layer are also similar to the distribution of the *E* region peak electron density (N_mE) [e.g., *Nicolls et al.*, 2012], which begins to increase at dawn, reaches its maximum at noon, and then decreases until dusk. The maxID's altitude distributions in the four seasons are shown in Figure 9. It is found that altitude distributions of the SLT and MLT *Es* layers in each season are similar to one another, and are different from the distribution of the altitude of the *E* region peak (h_mE) [e.g., *Nicolls et al.*, 2012].

[20] Based on the similar altitude distributions of the SLT and MLT *Es* layers in Figure 9, it is found that the SLT *Es* layer is almost coexist with the MLT *Es* layer. However, their different maxID distributions indicate that their formation mechanisms are different. From the comparison described in the last subsection and former studies [e.g., *Arras et al.*, 2009], the MLT *Es* layer is probably formed by wind shear, and the SLT *Es* layer, whose maxID distributions in the four seasons are like the distribution of N_mE, is associated with the solar zenith angle. The *Es* layer is formed in the region where the vertical electron velocity is zero and the gradient of vertical velocity is large [*Whitehead*, 1961]. During and after the formation of the *Es* layer, some irregular structures are caused by the effect of certain external forces, such as the wind shear and gravity waves. The irregular structures in

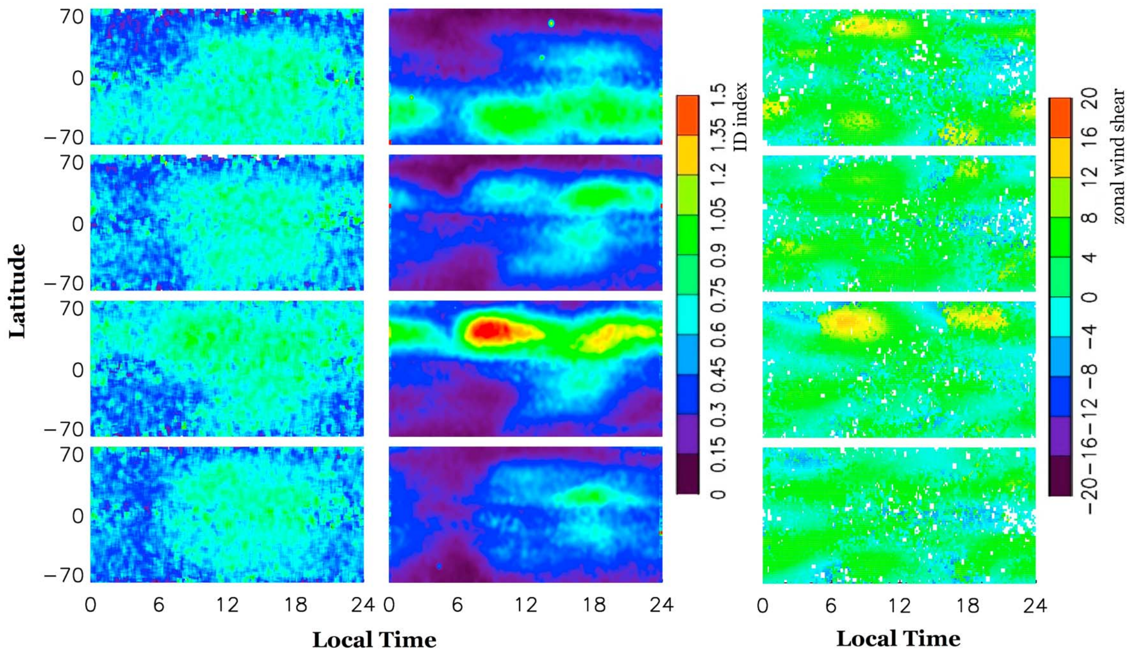

Figure 8. Distributions of maximum irregular degree (maxID) of the (left) SLT and (middle) MLT *Es* layers in four seasons (top to bottom: winter, spring, summer, and autumn). In order to compare two of them more easily, the ID index of the MLT *Es* layer has been multiplied by four. (right) The zonal wind shear distribution at the corresponding altitude of maxID of the MLT *Es* layer in four seasons, which are shown in Figure 6 (right).

the *Es* layer have been observed and simulated in former studies [e.g., *Miller and Smith*, 1978; *Huang and Kelley*, 1996; *Cosgrove and Tsunoda*, 2003]. In contrast to the simulations in this study and the above description, the MLT *Es* layer is caused by irregular structures. Otherwise, the SLT *Es* layer can be regarded as an *Es* layer which has not been influenced by external forces. In the simulations, the amplitude profiles of the SLT *Es* layer are purer than the MLT *Es* layer with only one negative hump with two positive humps or two interference portions on either side. Although the amplitude profile is associated with the vertical gradient of the electron density, the maxID of the SLT *Es* layer can also be indicated by the magnitude of the electron density in the layer. With the smaller solar zenith angle, the ionization rate becomes larger in the *E* region. With a larger electron density in *E* region, a higher electron density is formed in the *Es* layer. Therefore it is reasonable that the maxID distributions of the SLT Es layer are similar to the N_mE distribution. Furthermore, from the above description, the difference between the wind shear and MLT *Es* layer distributions in four seasons shown in Figure 7 can be further explained. In winter and summer, the large irregularities of MLT *Es* layer occur in the large wind shear regions, while it is not the case, although the irregularities still occur in the negative wind shear regions in spring and autumn. In winter and summer, the large wind shear regions contain the regions of *Es* layer and cause the large irregularities in the regions. In spring and autumn, the large negative wind shear regions do not cover the regions of *Es* layer formation, while the small negative wind shear regions do cover the regions of *Es* layer. So, in spring and autumn, the irregularities only occur in the small wind shear regions.

5. Summary

[21] In this study, we have simulated the amplitude profiles of four electron density profiles to confirm the relation

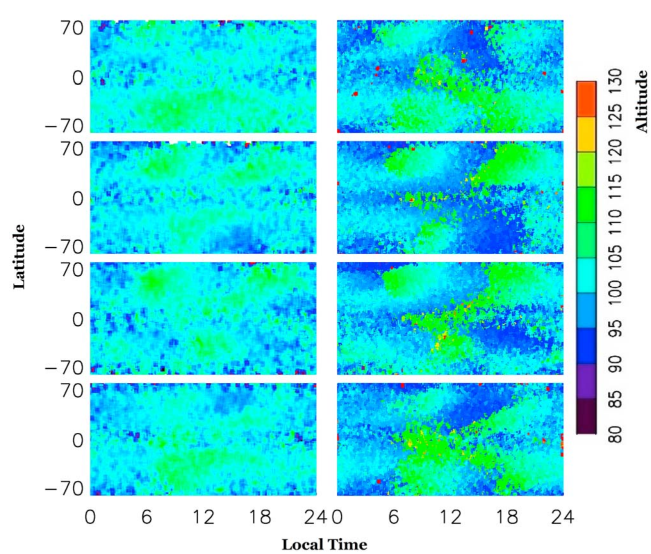

Figure 9. Distributions of altitude of the (left) SLT and (right) MLT *Es* layers in four seasons (top to bottom: winter, spring, summer, and autumn).

between the amplitude and the electron density. Based on the simulation results, it is found that the MLT and SLT *Es* layers can be separated by considering the shape of SNR profiles. A large amount of the F-3 SNR data recorded in three years has been used for the analysis in which the ID index is defined. The distributions of the MLT *Es* layer in the four seasons are in agreement with those obtained in previous studies. The wind shear information obtained from HWM07 in four seasons in 2010 is compared with the global distribution for the MLT *Es* layer. Furthermore, the comparison of the MLT and SLT *Es* layers shows that the maxID distributions of both layers are different while the distributions of the maxID altitude are similar. Unlike the MLT *Es* layer, which is probably formed by wind shear, the SLT *Es* layer is mainly associated with the solar zenith angle.

[22] **Acknowledgments.** The authors would like to thank the support from National Space Organization (NSPO), GPS Science and Application Research Center. The research is supported by grant NSC-100-2119-M-008-011 and NSC-100-2119-M-006-013.

[23] Robert Lysak thanks the reviewers for their assistance in evaluating this paper.

References

Arras, C., J. Wickert, G. Beyerle, S. Heise, T. Schmidt, and C. Jacobi (2008), A global climatology of ionospheric irregularities derived from GPS radio occultation, *Geophys. Res. Lett.*, *35*, L14809, doi:10.1029/2008GL034158.

Arras, C., C. Jacobi, and J. Wickert (2009), Semidiurnal tidal signature in sporadic *E* occurrence rates derived from GPS radio occultation measurements at higher midlatitudes, *Ann. Geophys.*, *27*, 2555–2563, doi:10.5194/angeo-27-2555-2009.

Carrasco, A. J., I. S. Batista, and M. A. Abdu (2007), Simulation of the sporadic *E* layer response to prereversal associated evening vertical electric field enhancement near dip equator, *J. Geophys. Res.*, *112*, A06324, doi:10.1029/2006JA012143.

Cosgrove, R. B., and R. T. Tsunoda (2003), Simulation of the nonlinear evolution of the sporadic-*E* layer instability in the nighttime midlatitude ionosphere, *J. Geophys. Res.*, *108*(A7), 1283, doi:10.1029/2002JA009728.

Davies, K. (1990), *Ionospheric Radio*, Peter Peregrinus, London, doi:10.1049/PBEW031E.

Drob, D. P., et al. (2008), An empirical model of the Earth's horizontal wind fields: HWM07, *J. Geophys. Res.*, *113*, A12304, doi:10.1029/2008JA013668.

Feng, D. D., and B. M. Herman (1999), Remotely sensing the Earth's atmosphere using the Global Positioning System (GPS)—The GPS/MET data analysis, *J. Atmos. Oceanic Technol.*, *16*, 989–1002, doi:10.1175/1520-0426(1999)016<0989:RSTESA>2.0.CO;2.

Haldoupis, C., D. Pancheva, W. Singer, C. Meek, and J. MacDougall (2007), An explanation for the seasonal dependence of midlatitude sporadic *E* layer, *J. Geophys. Res.*, *112*, A06315, doi:10.1029/2007JA012322.

Hocke, K., K. Igarashi, M. Nakamura, P. Wilkinson, J. Wu, A. Pavelyev, and J. Wikert (2001), Global sounding of sporadic *E* layers by the GPS/MET radio occultation experiment, *J. Atmos. Sol. Terr. Phys.*, *63*, 1973–1980, doi:10.1016/S1364-6826(01)00063-3.

Huang, C.-S., and M. C. Kelley (1996), Numerical simulations of gravity wave modulation of midlatitude sporadic *E* layers, *J. Geophys. Res.*, *101*(A11), 24,533–24,543, doi:10.1029/96JA02327.

Huang, N. E., Z. Shen, S. R. Long, M. C. Wu, H. H. Shin, Q. Zheng, N.-C. Yen, C. C. Tung, and H. H. Liu (1998), The empirical mode decomposition and the Hilbert spectrum for nonlinear and non-stationary time series analysis, *Proc. R. Soc. London, Ser. A*, *454*, 903–995, doi:10.1098/rspa.1998.0193.

Kelley, M. C. (2009), *The Earth's Ionosphere: Plasma Physics and Electrodynamics*, 2nd ed., Academic, San Diego, Calif.

Mathews, J. D. (1998), Sporadic *E*: Current views and recent progress, *J. Atmos. Sol. Terr. Phys.*, *60*(4), 413–435, doi:10.1016/S1364-6826(97)00043-6.

Miller, K. L., and L. G. Smith (1978), Incoherent scatter radar observations of irregular structure in mid-latitude sporadic *E* layers, *J. Geophys. Res.*, *83*(A8), 3761–3775, doi:10.1029/JA083iA08p03761.

Nicolls, M. J., F. S. Rodrigues, and G. S. Bust (2012), Global observations of *E* region plasma density morphology and variability, *J. Geophys. Res.*, *117*, A01305, doi:10.1029/2011JA017069.

Pan, J. C., and R. T. Tsunoda (1999), Semidiurnal behavior of quasi-period echoes in the mid-latitude Es region observed with the Chung-Li VHF radar, *Geophys. Res. Lett.*, *26*, 2621–2624, doi:10.1029/1999GL900562.

Pavelyev, A. G., Y. A. Liou, J. Wickert, T. Schmidt, A. A. Pavelyev, and S. F. Liu (2007), Effects of the ionosphere and solar activity on radio occultation signals: Application to CHAllenging Minisatellite Payload satellite observations, *J. Geophys. Res.*, *112*, A06326, doi:10.1029/2006JA011625.

Sokolovskiy, S. V. (2000), Inversions of radio occultation amplitude data, *Radio Sci.*, *35*, 97–105, doi:10.1029/1999RS002203.

Urbina, J., E. Kudeki, S. J. Franke, S. Gonzalez, Q. Zhou, and S. C. Collins (2000), 50 MHz radar observations of mid-latitude *E*-region irregularities at Camp Santiago, Puerto Rico, *Geophys. Res. Lett.*, *27*, 2853–2856, doi:10.1029/2000GL000028.

Whitehead, J. D. (1961), The formation of the sporadic-*E* layer in the temperate zones, *J. Atmos. Terr. Phys.*, *20*, 49–58, doi:10.1016/0021-9169(61)90097-6.

Whitehead, J. D. (1970), Production and prediction of sporadic *E*, *Rev. Geophys.*, *8*, 65–144, doi:10.1029/RG008i001p00065.

Whitehead, J. D. (1989), Recent work on mid-latitude and equatorial sporadic-*E*, *J. Atmos. Terr. Phys.*, *51*(5), 401–424, doi:10.1016/0021-9169(89)90122-0.

Wickert, J., A. G. Pavelyev, Y. A. Liou, T. Schmidt, C. Reigber, K. Igarashi, A. A. Pavelyev, and S. Matyugov (2004), Amplitude variations in GPS signals as possible indicator of ionospheric structures, *Geophys. Res. Lett.*, *31*, L24801, doi:10.1029/2004GL020607.

Wickert, J., et al. (2009), GPS radio occultation: Results from CHAMP, GRACE and FORMOSAT-3/COSMIC, *Terr. Atmos. Oceanic Sci.*, *20*, 35–50, doi:10.3319/TAO.2007.12.26.01(F3C).

Wu, D. L., C. O. Ao, G. A. Hajj, M. de la Torre Juarez, and A. J. Mannucci (2005), Sporadic *E* morphology from GPS-CHAMP radio occultation, *J. Geophys. Res.*, *110*, A01306, doi:10.1029/2004JA010701.

Yakovlev, O. I., J. Wickert, A. G. Pavelyev, S. S. Matyugov, and V. A. Anufriev (2008), Sporadic structures in equatorial ionosphere as revealed from GPS occultation data, *Acta Astronaut.*, *63*, 1350–1359, doi:10.1016/j.actaastro.2008.05.023.

Yakovlev, O. I., J. Wickert, A. G. Pavelyev, V. A. Anufriev, and G. P. Cherkunova (2010), Results of radio occultation measurement of polar ionosphere at links satellite-to-satellite during strong flare solar activity, *Acta Astronaut.*, *67*, 315–323, doi:10.1016/j.actaastro.2010.02.017.

Zeng, Z., and S. Sokolovskiy (2010), Effect of sporadic *E* cloud on GPS radio occultation signal, *Geophys. Res. Lett.*, *37*, L18817, doi:10.1029/2010GL044561.